SYNTHESIS OF COINAGE METAL NANOPARTICLES AS CO-CATALYSTS FOR TiO_2 BASED PHOTOCATALYSTS

Thesis submitted

by

Rupinder Kaur

(Regd. No. 900909011)

In fulfillment of the requirement

for the degree of

Doctor of Philosophy

Under the supervision of

Dr. Bonamali Pal

(Professor and Head)

School of Chemistry and Biochemistry

Thapar University

Patiala – 147 004

Punjab, India

July, 2014

Certificate

This is to certify that thesis entitled "***Synthesis of Coinage Metal Nanoparticles as Co-catalysts for TiO_2 Based Photocatalysts***", being submitted by Miss Rupinder Kaur in the fulfillment of the requirement for the award of Degree of Doctor of Philosophy to the School of Chemistry and Biochemistry, Thapar University, Patiala, is a record of candidate's own work carried out by him under my supervision and guidance. The matter presented in this thesis has not been submitted in part or full for the award of any degree in any other University or Institute.

(Supervisor)

Dr. Bonamali Pal
Professor and Head
School of Chemistry and Biochemistry
Thapar University, Patiala - 147 004
Punjab (India)

Candidate's Declaration

I, hereby declare that the work presented in the thesis entitled "***Synthesis of Coinage Metal Nanoparticles as Co-catalysts for TiO_2 Based Photocatalysts***" in fulfillment of the requirement for the award of the Degree of Doctor of Philosophy, School of Chemistry and Biochemistry, Thapar University, Patiala, is an authentic record of my own work carried out under the supervision of Dr. Bonamali Pal, Associate Professor, School of Chemistry and Biochemistry, Thapar University, Patiala, India. The matter embodied in this thesis has not been submitted in part or full to any other university or institute for the award of any degree in India or Abroad.

Rupinder Kaur

(Supervisor)

Dr. Bonamali Pal
Professor and Head
School of Chemistry and Biochemistry
Thapar University, Patiala - 147 004
Punjab (India)

Dedicated

To My

Parents

Acknowledgements

Through this section of the thesis, I would like to convey my heartiest thanks to all those who support and encouraged me in many ways for the accomplishment of this study and made it an unforgettable journey for me.

First and foremost, praises and thanks to the almighty God, the most merciful and compassionate, for His blessings throughout my research work to complete this project successfully.

I would like to extend my sincerest gratitude to my supervisor, Dr. Bonamali Pal, Professor and Head, School of Chemistry and Biochemistry, Thapar University, Patiala for giving me the valuable opportunity to work under his worthy guidance. His immense knowledge, constructive ideas, innovative way of teaching, effort, time and patience for giving me useful comments and suggestions on manuscript writing and research presentations were priceless. He has always supported, inspired, encouraged and challenged me in many ways for making me confident and enhancing my professional growth. He gave me the opportunities to present my research work in several conferences and other professional gatherings, through which my public speaking skills have improved immensely. I will always remain thankful to him for preparing me for my future career and without his inspiration; I could not be able to achieve so much today. I attribute the level of my doctoral degree to his motivation, encouragement and sustainable effort.

I express my special regards to Dr. Satnam Singh, Associate Professor, School of Chemistry and Biochemistry, Thapar University, Patiala for his ever-helping attitude and good wishes.

I would like to thanks the members of my doctoral committee for their insightful comments, advices and scientific discussions.

I am indebted to my all respected teachers who touched my life and enlighten my path with their incredible knowledge. Special thanks to faculty of the School of Chemistry and Biochemistry for their supportive nature.

I would like to thank other staff of the School of Chemistry and Biochemistry, Thapar University, Patiala for the constant official help and cooperation.

I sincerely acknowledge to the Department of Science and Technology, Government of India, for providing the financial support under Women Scientist Fellowship Scheme (WOS-A).

This word 'Thank you' seems insufficient for my friends who expressed their constant moral support, care and understanding towards me and provide a stimulating and fun filled environment. I am greatly thankful to Miss Mandeep Kaur, Mr. Rohit Singh, Mr. Inderpreet Singh Grover and Mr. Bhupender Pal Thakur for their precious friendship and for making this journey easier. I am also thankful to Miss Nidhi Gupta, Miss Anila Monga, Mrs. Jaspreet Kaur, Miss Navjot Kaur and Mr. Akul Sen Gupta for their timely help.

I would also like to thanks Dr. B. K. Chudasama and Ms. Chandani (School of Physics and Material Science, Thapar University, Patiala) for Zeta potential and conductance analysis, Vipul Singh and Sanjeev Gupta (Thapar Center for Industrial Research and Development) for surface charge analysis. I would extend my thanks to SAI labs, Thapar University, Patiala, Sophisticated Analysis Instrumentation Facility (SAIF), Punjab University, Chandigarh, SAIF IIT Bombay, and Central Salt & Marine Chemicals Research Institute for SEM and TEM analysis.

Words fail me to express my regards to my family for their encouragement and inspiration throughout my research work which keep me lifting up during hard phases of my life. I would always remain indebted to my loving mother, Mrs. Jasbir Kaur and father, Mr. Harjeet Singh, who always remained besides me as a source of motivation. I owe everything to them. My special thanks to my brother, Harjot, sister (Minnie), my grandma, grandpa and little cute angel Rajveer, for their unconditional love and support to overcome the tough conditions.

Besides this, I thank to the persons who knowingly and unknowingly helped me during the successful completion of this project.

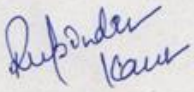

Rupinder Kaur

Table of Contents

List of Abbreviations

UV	Ultraviolet
Vis	Visible
DLS	Dynamic light scattering
SEM	Scanning electron microscopy
XPS	X-ray photon spectroscopy
HPLC	High pressure liquid chromatography
GC	Gas chromatography
GC-MS	Gas chromatography - mass spectrometry
TEM	Transmission electron microscopy
XRD	X-ray diffraction
SAED	Selected area electron diffraction
HRTEM	High resolution transmission electron microscopy
BET	Brunauer Emmett Teller
EDX	Energy dispersive X-ray spectroscopy
JCPDS	Joint committee on powder diffraction standards
SA	Salicylic acid
PNP	*p*-nitrophenol
PAP	*p*-aminophenol
m-CNB	m-chloronitrobenzene
m-CAB	m-chloroaminobenzene
DNB	m-Dinitrobenzene
PDA	m-Phenylenediamine
BZ	Benzaldehyde
NBZ	Nitrobenzaldehyde
BA	Benzoic acid
VB	Valence band
CB	Conduction band
SC	Semiconductor

NS	Nanosphere
NR	Nanorod
NW	Nanowire
NPs	Nanoparticles
SPR	Surface plasmon resonance
PCA	Photocatalytic activity
PS	Photocatalytic reaction system
SNS	Small nanospheres
MNS	Medium nanospheres
LNS	Large nanospheres
ANS	Chemical aggregated nanospheres
PAP	Au photodeposited particles
PNS	Polygonal nanospheres
PCO	Photocatalytic oxidation
PDR	Photocatalytic degradation rate
TT	Truncated nanospheres
EDA	Ethylenediamine
EG	Ethylene glycol
PVP	Polyvinyl pyrollidone
a.u.	Arbitrary unit
ca.	Calculated amount
wt%	Weight percentage
o-	Ortho
m-	Meta
p-	Para
S/V	Surface to volume
CCA	Co-catalytic activity
ANS	Agglomerated nanospheres
RI	Refractive index
MeOH	Methanol
DMSO	Dimethylsulphoxide

DMF	Dimethlyformamide
PrOH	Propanol
CCl_4	Carbon tetrachloride
TiO_2	Titanium oxide
DP	Dipole moment
D	Debye
MW	Molecular weight
wt%	Weight percent
ml	Millilitre
min	Minute
mol	Mole
mM	Milli molar
nm	Nanometre
mM	Milimolar

List of Symbols

e^-	Electron
h^+	Hole
$OH^\bullet$	Hydroxyl radical
E_g	Band gap
Å	Angstrom
α	Absorption coefficient
A	Absorbance
°	Degree
λ	Wavelength
%	Percentage
µ	Micro
ζ	Zeta potential
τ_{av}	Average lifetime
h	Hour
E_o	Reduction potential
g	Gram
mg	Milligram
E_f	Fermi energy
V	Volt
s	Second
L	Length
W	Width
I	Current
V	Voltage
MΩ	Mega ohm
eV	Electron volt
R	Resistance
S	Siemens
υ	Frequency

Abstract

The work presented in this thesis enlightens the importance of coinage metal nanoparticles (NPs) as co-catalysts for the enhancement of TiO_2 photocatalysis. Main emphasis has been given on synthesis of various shapes and sizes of coinage metal nanostructures such as rods, spheres, truncated triangles, wires, etc., and their implication as co-catalyst towards the improvement in the heterogeneous photocatalytic systems, which cannot be achieved through simple conventional approach. This whole work has been divided into eight chapters:

Chapter 1: Introduction and Characterization Techniques

The first chapter provides the brief introduction on the role of coinage metal nanoparticle as co-catalysts for the improvement of TiO_2 photocatalytic reactions. Specific attention has been paid to the impact of catalyst-co-catalyst structure-activity interactions for enhancing the photocatalytic rate. A brief description of various techniques used for the characterization of optical, electrokinetic, co-catalytic and catalytic properties of metallic nanostructures and metal-TiO_2 composites has also been incorporated.

Chapter 2: Size and Shape Dependent Attachments of Au Nanostructures to TiO_2 for Optimum Reactivity of Au-TiO_2 Photocatalysis

This chapter demonstrates the effects of AuNPs of various sizes and shapes on its co-catalytic activity imparted to TiO_2 during photocatalytic oxidation of salicylic acid. The TiO_2 photoactivity is remarkably improved with the decreasing size (9.5 ± 0.06 to 3.5 ± 0.25 nm) and increasing the surface to volume (S/V) ratio (0.629 to 1.95 nm^{-1}) of spherical Au co-catalysts loading. The Au nanorod (aspect ratio = 2.8 ± 0.12 and S/V = 0.54 nm^{-1}) attachment to TiO_2 significantly decreased the photoactivity compared with the highly active quantum size (3.5 ± 0.25 nm) Au co-catalysts loading. The interaction of AuNPs of various morphologies with TiO_2 induces the photoexcited charge transfer process in varied extent, leading to diverse photocatalytic activity. Zeta potential/surface charge and conductance measurement of aqueous dispersions of TiO_2, AuNPs and salicylic acid was carried out to investigate the interaction among the various components in the photoreaction system.

Chapter 3: Co-catalytic and Electro-kinetic Properties of Au Nanostructures Dispersed in Solvents of Varying Dipole Moments

The influence of electrokinetic parameters; surface charge and zeta potential on the optical absorption band and co-catalytic activity of Au nanospheres (AuNS) dispersed in polar solvents i.e., methanol (MeOH), propanol (PrOH), dimethylformamide (DMF), and dimethyl-sulphoxide (DMSO) has been considered in detail here. The narrow intense surface plasmon resonance (SPR) absorption band of AuNS (520 nm) becomes broadened and a SPR band at > 970 nm is appeared, whose absorption intensity varies from 0.05 to 0.13 a.u with the extent of aggregation in solvents of varying dipole moment from 1.66 D to 3.96 D while no such alteration in SPR band occurs for AuNS dispersion in non-polar CCl_4 as confirmed by DLS and TEM analysis. The effective electronic charge ca. +4306 µequ./l present over AuNS surface in water suspension is highly reduced to +512 µequ./l in photoreaction (TiO_2 + salicylic acid + AuNS) mixture and the zeta potential (+50.32 mV) and conductance (1673 µS) of AuNS in water has been decreased to +24.06 mV and 1480 µS in methanol, respectively. The co-catalytic activity of aggregated AuNS (formed in polar solvents) varied in a diverse extent depending on its degree of agglomeration, where the non-aggregated aqueous AuNS + TiO_2 mixture displayed higher degradation efficiency ($r = 9.990\times10^{-3}$ mM/min) of salicylic acid than that ($r = 9.172\times10^{-3}$ mM/min) of aggregated AuNS in MeOH + TiO_2 mixture under UV light irradiation.

Chapter 4: Electro-kinetic and Catalytic Sensitivity of Au Nanorods Agglomerated in Solvents of Varying Dipole Moment and Refractive Index

In continuation of chapter-3, this chapter deals with the impact of dipole moment (1.66 to 3.96 D) and refractive index (1.333-1.422) of the dispersion solvent on the optoelectronic, adsorption, co-catalytic and catalytic properties of Au nanorods (AuNRs). AuNRs (Length ≈ 53 nm and Width ≈ 20 nm) also undergo agglomeration to a varied extent (size 50-180 nm) as a function of the dipole moment of the solvent, similar to AuNS aggregation. The electrostatic interaction of AuNRs with its surface adsorbed solvent dipoles leads to alteration of the their ionic state, absolute electronic charge and zeta potential (+49.79 mV in H_2O, +8.99 mV in DMF and -4.65 mV in MeOH dispersion). This interaction distinctly modifies the adsorption behavior of polar molecules like *p*-nitrophenol and salicylic acid on AuNRs surface, as evidenced by the measured changes in their electro-kinetic parameters. As a result, we observe a substantial difference in catalytic and co-catalytic activities of AuNRs dispersed in various solvents (such as PrOH, DMSO, DMF, etc.) because the catalytic properties of AuNRs are strongly dependent on the type of solvent in which they are dispersed. The reduction of *p*-nitrophenol to *p*-aminophenol by

AuNR-H_2O exhibits the highest k = 5.28×10^{-2} min^{-1} as compared to the lowest k = 1.0×10^{-2} min^{-1} with AuNR in DMF. Similarly, the co-catalytic activity of AuNR-TiO_2 mixture for the photo-oxidation of salicylic acid is found to be higher (k = 8.4×10^{-2} min^{-1}) in H_2O than in DMF (k = 5.2×10^{-2} min^{-1}) due to the severe agglomeration of the NRs in the latter.

Chapter 5: Improved Surface Properties and Catalytic Activity of Polymorphic Facets of Photoetched Au Nanostructures Formed by Variable Energy Laser Exposure

Many anisotropic Au nanostructures with versatile crystal facets have been prepared in a single step by different energy (λ = 457.9, 488 and 514.7 nm) laser exposure and studied their optical, electrokinetic and catalytic properties. The surface morphology of photoetched AuNPs was monitored by variable energy laser beam follows an exponential ($A = A_0 e^{-kt}$) disintegration rate as a function of particles geometric size and shape. A variety of many irregular Au nanomorphology such as multifaceted spherical (5-20 nm), low aspect ratio rod, oval egg shaped, ice cubes (~7 nm), truncated triangle (~7-8 nm), pentagonal (~12 nm), nanocapsules, square types (~8 nm) and polygonal nanospheres (~8-12 nm) like particles were formed after laser exposure. The percentage decomposition of AuNRs (aspect ratio = 2.8) is found to increase as 59 % > 69% > 72% with increased energy of laser exposure; 2.41 eV (514.7 nm) > 2.50 eV (488 nm) > 2.71 eV (457.9 nm) as determined from the decrease in SPR band absorption during laser illumination. The formation of small clusters on laser irradiation results in the decrease of zeta potential from +49.79 to +12.71 mV and conductance values. Catalytic reduction of *p*-nitrophenol to *p*-aminophenol and m-dinitrobenzene to m-phenylenediamine with photofragmented Au nanostructures is ~ 15-20% is higher than bare Au particles.

Chapter 6: Co-catalysis Effect of Different Morphology of Ag Nanostructures for the Photocatalytic Oxidation Reaction by Ag-TiO_2 Photocatalysis

This chapter highlights the comparative co-catalytic efficiency of different shapes of prepared AgNPs of a size much bigger as well as smaller than titanium for the Ag-TiO_2 photocatalysis. Quantum sized Ag nanospheres (4–8 nm), nanorod (length 70-75 nm and width 30-38 nm), polygonal nanosphere (80-120 nm) and truncated triangles (side length 70-140 nm) are prepared by solvothermal process. The co-catalytic activities of these Ag nanostructures were investigated by mixing them with TiO_2 for the photocatalytic degradation of aqueous salicylic (0.5 mM) and benzoic acid (0.5 mM) under UV light (125 W-Hg arc, 10.4 mW/cm^2) irradiation. The Ag co-catalysis effect imparted to TiO_2 follows as polygonal nanosphere > nanorod > truncated triangle

> small nanosphere due to the formation of many Ag-TiO_2 interfaces by a single large-sized Ag nanoparticle than smaller one. As the surface coverage of Ag particles by TiO_2 decreases, the Ag-TiO_2 photoactivity is decreased accordingly. The efficient adsorption of salicylic acid to TiO_2 surface through -COOH and -OH groups render its higher photodegradation rate (1.8-2.7×10^{-2} μmol/min) than benzoic acid (1.5-2.5×10^{-2} μmol/min) having one chelating -COOH group. Zeta potential and conductance measurement of photoreaction mixture were carried out to investigate the ionic interaction-adsorption of reactant substrates over Ag-TiO_2 surface.

Chapter 7: Copper Nanostructures of Various Morphologies for Superior Catalytic and Co-catalytic Activities

This chapter describes the improvement in the photocatalytic rate of TiO_2 by utilizing different morphologies of CuNPs in comparison with bare TiO_2. The Cu nanospheres of three different sizes ≈ 3-20 nm were synthesized employing long chain fatty acid surfactant (lauric acid) and polyvinyl pyrollidone as capping agent. Nanorods of length ≈ 600-700 nm and width ≈ 15-20 nm and nanowires with dimensions, length ≈ 4-6 μm and width ≈ 60-80 nm were prepared by solvothermal process and characterized by UV-vis spectrophotometer, DLS, SEM and TEM analysis. Both co-catalytic and catalytic activities of various Cu nanomorphologies were evaluated for the photooxidation of acetic acid by CuNPs-TiO_2 mixture, and for the reduction of nitroaromatics (nitrobenzene, m- chloronitrobenzene and m-nitrotoluene), respectively. A significant increase in the catalytic reduction (30 to 50%) was found with decreasing size (20 to 3 nm) and increasing the surface to volume ratio (0.34 to 1.73 nm^{-1}) of nanospheres, analyzed through UV-vis, HPLC and GC-MS measurements. The photocatalytic activity for acetic acid oxidation under UV irradiation and reduction reaction using varied morphologies was gradually improved with the increasing exposed surface area per particle as ≈ 1278295 nm^2 for nanowires > nanorods (≈ 352154 nm^2) and nanospheres (≈ 1076.02 nm^2).

Chapter 8: Comparative Co-catalytic Account of Coinage Metal Nanoparticles (Au, Ag and Cu) for TiO_2 Photocatalysis under Visible Light Irradiation

A comparative report on the nature of the coinage metal NPs (Au, Ag and Cu) co-catalysts for enhancement of the catalytic activity of TiO_2 under visible light irradiation has been described here. Coinage metal nanospheres of similar sizes (3-5 nm) were prepared using sodium citrate as a capping agent and characterized through UV-vis spectrophotometer, DLS and TEM analysis. These NPs were impregnated onto TiO_2 to produce metal-TiO_2 nanocomposites, operating

efficiently under visible light owing to the surface plasmon resonance effect of metallic particles. The comparative impact of Au, Ag and Cu-TiO_2 nanocomposites was evaluated by utilizing them for the photodegradation of benzaldehyde and nitrobenzaldehyde. Ag-TiO_2 was found to exhibit highest photoactivity relative to Au and Cu-TiO_2 composites. Notably, very low resistance and thus high conductance in Ag-TiO_2 (2.7×10^{-7} S) in contrast to Au (2.5×10^{-7} S) and Cu-TiO_2 (2.7×10^{-7} S) composites highlights the importance of interface in conduction. The difference in work function, redox potential, e^--h^+ recombination time, oxidation state of the M-TiO_2 nanocomposite dictates their varied co-catalytic activity.

Chapter 1

Introduction and Literature

1.1 Co-catalysis

The term "catalysis" cannot be understood only as a way to accelerate chemical reactions, indeed it comprises a broad field combining physical, inorganic, organic and biochemical reaction systems which can either be homogeneous, heterogeneous or photochemical in order to achieve high turnover [1-30]. The most basic definition of a catalyst, as mentioned systems is to function as promoters without being consumed, specific in nature, needed in a minute amount and lowers down the activation barrier to enhance the activity, selectivity and productivity of a reaction. Catalysis can be traced back to ancient times by considering the fermentation process which is an example of bio-catalysis. The first industrially catalyzed reaction was the oxidation of SO_2 to SO_3 where NO used as homogeneous catalyst, the classical reaction occurred in the gas phase. But, a major drawback of such homogenous catalysis was that it was difficult to recover the catalyst from the reaction medium [27]. So, in order to overcome the serious issue in term of recycle and reuse, heterogeneously catalyzed processes constitute the basis for a large number of chemical technologies employed, nowadays as they demonstrated a great potential for the ease of separation, continuous processing and catalyst recycling. Many commercially important heterogeneous catalysts comprise supported noble metal nanoparticles (NPs), metal oxides, metal chalcogenides, such as Ni powder used for hydrogenation of unsaturated organics, Co for the production of petroleum, dyes, and electronics, V_2O_5 in the contact process for the conversion of SO_2 to SO_3, TiO_2 for the elimination of pollutants, etc [1-22].

Since there are many catalysts which are not so effective on their own, but they work in conjunction with some other promoters and these promoters are known as "co-catalysts". ***Co-catalysts*** *can be understood as the components that make the catalytic process feasible, activate the catalyst or modify its action***.** In simple words, "***co-catalysts in the union of a catalyst could modify the specificity, activity and rate of a reaction through catalyst-co-catalyst interactions".*** All the biological activities (digestion, respiration, etc.) in a human body are a result of enzyme (catalyst)-co-enzyme (co-catalyst) interactions. In chemical industry, synthesis of ammonia needs Fe as a catalyst and Molybdenum as a co-catalyst for enhancing the productivity. There are many industrially important reactions which need catalysts as well as co-

catalysts for higher yield, enhanced productivity and improved rate. *The most common and important example of this interaction is the photocatalysis (heterogeneous catalysis) in which the co-catalysts were employed to enhance the activity of semiconductor*.

1.2 What is photocatalysis?

Photocatalysis is an important stream of chemistry to develop environmental friendly photochemical conversion processes for synthesizing useful substances. *Photocatalysis, a heterogeneous catalytic system is a combination of photochemistry and catalysis that can be illustrated as a catalytic reaction which is initiated only in the presence of photons of light [31-36]*. For example, chlorophyll is a natural photocatalyst in photosynthesis, whereas semiconductor (SC) materials are artificial photocatalysts. Photocatalysis has been exploited for various environmental processes such as deodorization [36-38], water purification, solar energy conversion [39], and organic synthetic reactions [40]. Many researchers have put their effort on degradation and mineralization of a variety of toxic substances by photocatalytic oxidation reactions. A photocatalytic reaction system (PS) usually comprises of metal oxides or metal chalcogenide SC characterized by an electronic band structure with valence band (VB) and conduction band (CB) separated by a bandgap (E_g) [23-36]. Different types of semiconductors were used as photocatalyst, for eg., ZnO [19], TiO_2 [5,6, 11-15, 23-28, 31-36], ZnS [22, 41], CdS [21], CdSe [42], ZnSe [43], WO_3 [20], etc. In this study, we have chosen TiO_2 semiconductor as an area of our research interest.

1.2.1 Why TiO_2 photocatalyst ?

TiO_2 (titanium dioxide) is an attractive, most active and highly suitable material due to its abundance, low toxicity, high photocatalytic activity (PCA) and have found applications in hydrogen evolution from photocatalytic water splitting, photovoltaic's [25-27], solar cells, solar fuels, and environmental cleaning, etc [36-38]. TiO_2 exhibits notable resistance to corrosion and photocorrosion especially in harsh aqueous environments. Its VB hole has a strong oxidation potential towards environmental toxic substances. Literature reveals that TiO_2 SC is an excellent photocatalyst that can mineralize a large range of refractory organic pollutants including harmful herbicides, dyes, pesticides and various phenolic compounds under UV irradiation [23-28, 31-36]. All these features, so far, make TiO_2 superior for energy and environmental applications. Every year thousands of papers have been published on TiO_2 photocatalysis, describing the treatment of hazardous materials, environmental pollutants, destruction of harmful bacteria,

organic transformations, etc. A general mechanism of TiO_2 PS has been discussed in next section.

1.2.2 Mechanism of TiO_2 photocatalysis

When the photon of energy higher or equal to the E_g is absorbed by a TiO_2 particle, an electron from the VB is promoted to CB with simultaneous generation of hole (h^+) and electron (e^-) which may either resulting in recombination as heat, or it can react with other adsorbed species as shown in scheme 1. The hole will oxidize the adsorbed species, such as organic compounds, water or hydroxyl ions as given in following equations:

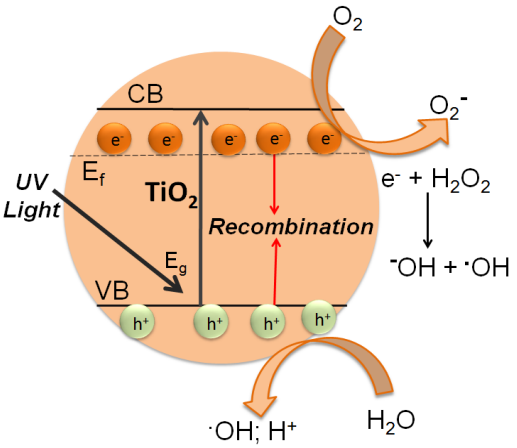

Scheme 1. Mechanism of TiO_2 photocatalysis.

$$TiO_2 + h\nu \rightarrow e^- + h^+$$

$$e^- + h^+ \rightarrow \text{heat}$$

$$h^+ + H_2O_{ads} \rightarrow {}^{\bullet}OH + H^+$$

$$h^+ + OH_{ads} \rightarrow {}^{\bullet}OH$$

$${}^{\bullet}OH + R \rightarrow CO_2 + H_2O$$

The electrons can also react with the compounds present in the solution such as oxygen and hydrogen peroxide. The electrons can be absorbed by the oxygen to form superoxide or they may react with oxygen together with hydrogen to create hydrogen peroxide. It can then react with hydrogen peroxide to create hydroxyl radicals and hydroxyl ions [5,6,11-15,23-28,31-36].

$$e^- + O_{2ads} \rightarrow O_2^-$$

$$2e^- + O_{2ads} + 2H^+ \rightarrow H_2O_2$$

$$e^- + H_2O_{2ads} \rightarrow {}^{\bullet}OH + OH^-$$

Mostly, this single component SC system exhibit relatively low photocatalytic efficiency (<5%) since the majority of the photogenerated charge carriers (e^--h^+) undergo recombination as shown in scheme 1. Therefore, some controlled measures should be taken for delaying e^--h^+ pair recombination in order to achieve high PCA.

1.2.3 Improvement in photocatalytic systems

This charge carrier (e^--h^+) recombination is an undesired process as it hinders the efficacy of a PS and several ways have been adopted to enhance the PCA. Various strategies like coupling

with a narrow band gap semiconductor [25], metal ion/non-metal ion doping [44,45], surface sensitization by organic dyes or metal complexes [46], noble metal deposition [47-50], metal NPs loading [51, 52], etc. have been employed with the aim of improving charge separation and for acquiring higher quantum efficiency during photocatalytic reaction. *Modification of TiO_2 surface with noble metals (Rh, Pt, Ag, and Au)* ***as co-catalysts*** *has been investigated as a far better technique to increase the PCA. So, here we are dealing with the* ***metal NPs (Au, Ag and Cu) loading on TiO_2 for the improvement of PS.***

1.2.3.1 Role of noble metal NPs co-catalyst in photocatalytic system

Metal NP co-catalysts were known to improve the catalyst (TiO_2) activity by playing a mediating role in storing and shuttling of photogenerated electrons from the SC to an acceptor, acts as a sink for photoinduced charge carriers and hence, promote interfacial charge-transfer processes [9,24,48,53-55]. Generally noble metals (e.g. Au, Ag, Cu, Pt, etc.) with Fermi level (E_f) lower than SC catalyst have been deposited on the SC surface for enhanced charge separation. As the Fermi levels of noble metals are lower than that of TiO_2, electrons from CB can be easily

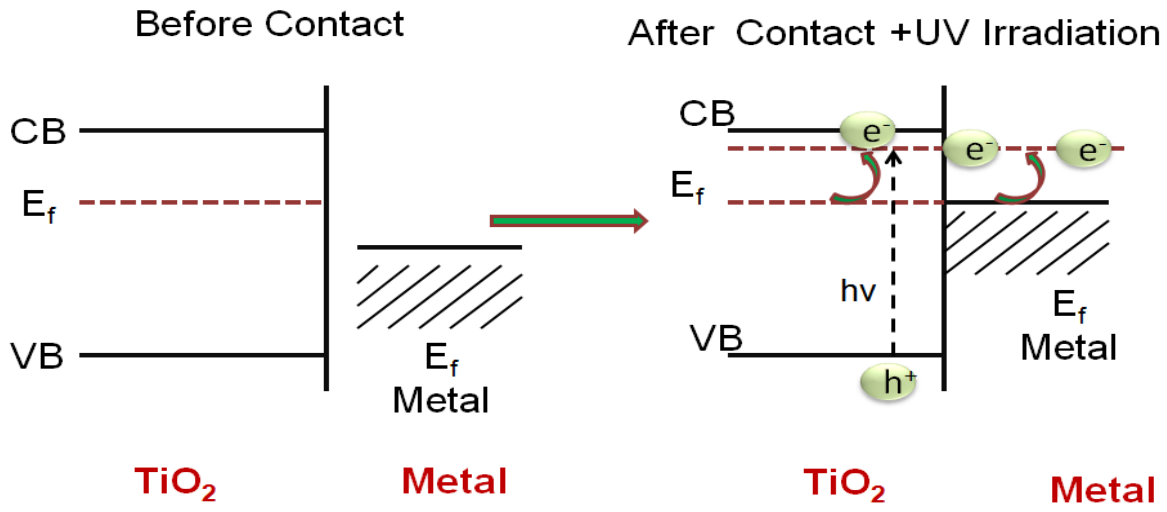

Scheme 2. Fermi level equilibration in metal-TiO_2 composite.

transferred to metal NPs, while VB holes remain free on the TiO_2 and this greatly reduce the possibility of electron-hole recombination and resulting in efficient separation (scheme 2). *Therefore, the coupling of SC catalyst with metal NP co-catalyst provides a unique pathway for maximizing the efficacy of PS as metal acts as a sink for photoinduced charge carriers, exhibiting a shift in the E_f to more negative potential and promotes interfacial charge-transfer processes* [53-55].

Literature reveals that when the SC and metal NPs come in contact, the photogenerated electrons are distributed between TiO_2 and metal NPs [9,24,48,53-55]. The transference of electrons from the excited TiO_2 into metal continues until the two systems attain equilibration as shown in scheme 2. The electron accumulation increases the E_f of metal NP to more negative potentials and the resultant E_f of the composite system shifts closer to the CB of the SC. The negative shift in the E_f signifies better charge separation and more reductive power for the composite system. *The charge transport at this metal co-catalyst–photocatalyst junction is strongly dependent upon the interfacial contact area, work function, Fermi level positions and metal reduction potential values.* The interfacial contact area, in turn is highly influenced by geometric confirmation of metal NP. As a result, interfacial properties can be easily modulated by tuning the size and shape of metal NP co-catalyst because the shift in band edge, barrier height and space charge layer, are strongly dependent on the energetics of metal NP–SC interface area (scheme 3).

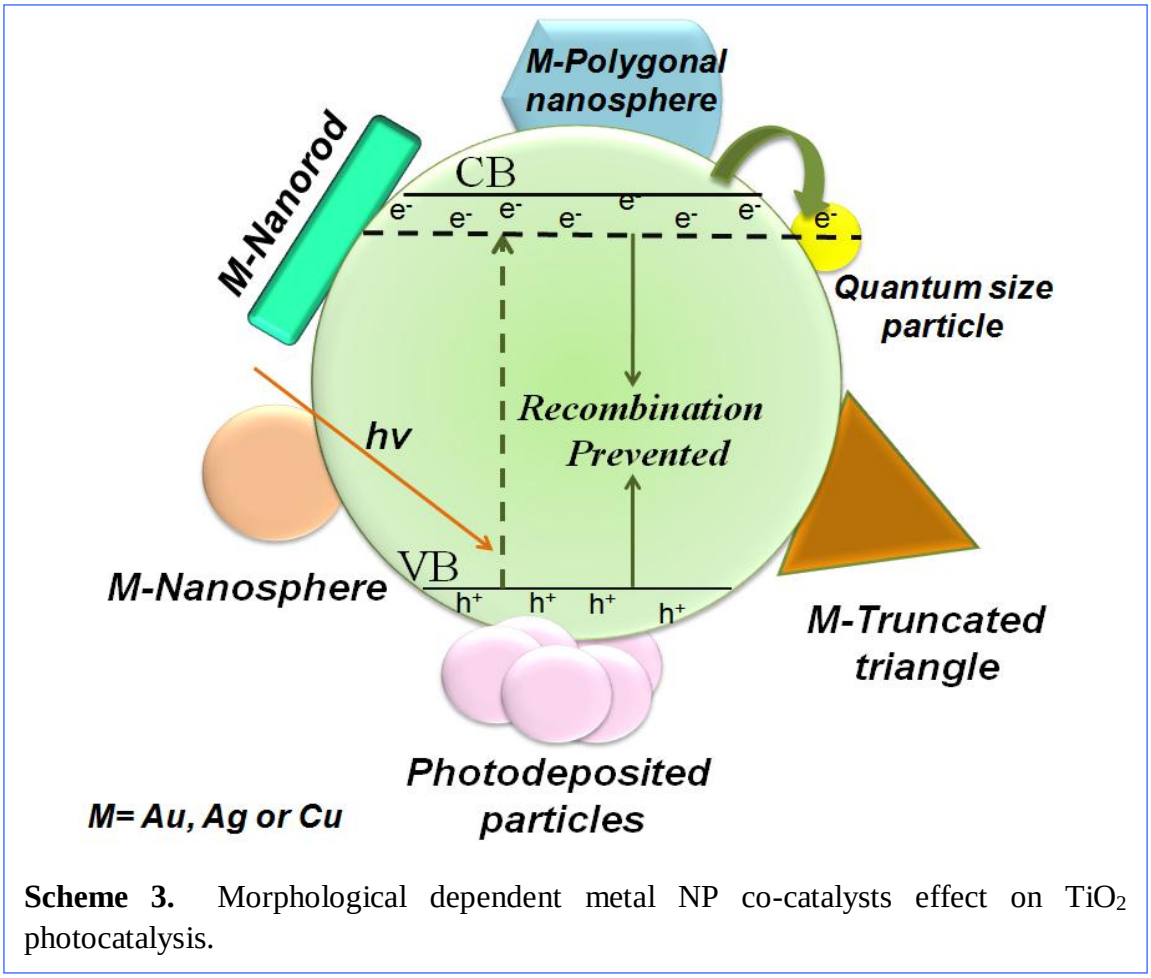

Scheme 3. Morphological dependent metal NP co-catalysts effect on TiO_2 photocatalysis.

The loading of metal NPs co-catalyst on TiO_2 has been accomplished by various techniques such as wet impregnation, in-situ deposition, photodeposition, co-precipitation, etc. These conventional methods are also known as in-situ growth methods, where the metal NPs are synthesized inside the TiO_2 and yield relatively larger spherical metal island deposits or aggregated morphologies of metal NPs onto TiO_2 surface which obscure the effect of size and shape dependent activity of metal co-catalysts (photodeposited particles, scheme 3). Therefore, conventional approach has offered limited control on the nature of the final NPs produced. *Moreover, large metal islands on TiO_2 resulting in the blocking of active sites of semiconductor, hinder the light absorption and hence results in the decrease of photocatalytic activity. Notably, it is impossible to study the morphological effect imparted by metal NPs co-catalysts onto photocatalyst activity by adopting the conventional methods.*

So, it would be highly desirable to have full control of the design and fabrication of specific catalyst-co-catalyst interfacial junctions with specific metal NPs geometries in order to tune activity and selectivity of PS. In this context, cost effective modified approach known as ex-situ approach should be implemented where the NPs of variety of shapes and sizes were first synthesized and purified, and then loaded over TiO_2 as shown in scheme 3. It includes various synthetic routes for preparation of NPs with controllable sizes and diverse morphologies, which leads to new characteristics. Scheme 3 displayed the attachments of various sizes i.e., quantum sized particles, photodeposited large metal islands/ aggregated particles and different shapes such as sphere, polygonal nanosphere, truncated triangle and rod of metal NPs to TiO_2. The interfacial contact area between the metal NPs and SC is varied dependent on morphology of NPs and highly influence the rate of charge transfer in composite system, hence have an effect on the PCA. *This modified approach takes into account the* ***comparative aspects of various shapes and sizes*** *of metal NPs co-catalyst loading on TiO_2 surface as shown in scheme 3.*

(a) Influence of NP co-catalyst size

The two main principles which cause the properties of nanomaterials to differ notably from other bulk materials are increased relative surface area and quantum size effects [56] as shown in figure 1. These factors can modify or enhance the physicochemical, optical, electrokinetic and catalytic characteristics of NPs. Literature reveals [56] that a particle of size 30 nm has 5% of its atoms on surface, 10 nm has 20%, and 3 nm has 50% exposed surface atoms which can efficiently participate in a chemical reaction as shown in figure 1a. Figure 1b illustrates the

enhanced surface area for NPs, i.e., if a bulk material is subdivided into individual NPs, the total volume remains the same, but the collective surface area would greatly increased, hence showed a profound effect in catalytic activity. It was believed that for small NPs, electronic effects are likely to be more dominating as the clusters lose their metallic character and begin to display discrete energy levels and electronic band separations owing to quantum confinement [57-60].

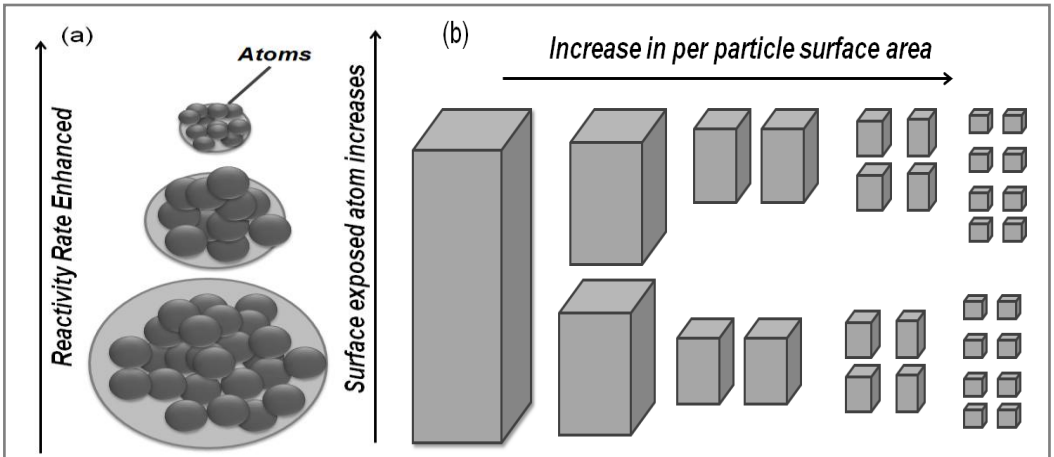

Figure 1. Quantum Size Effect.

Haruta et al. [29,61,62] observed interesting size effect on catalytic activity for oxidation reactions with Au catalysts, a metal that almost inactive in its bulk state, but extremely active in its NP form. Since then the remarkable growth of interest in the catalysis by metal NPs have been emerged [63-66]. The catalytic activity for the reduction of aromatic nitro compounds with metal NPs was seen to increase with decreasing particle size [66]. The smaller particles are found to be more active owing to the larger numbers of surface active atoms available for catalysis. It has been reported that large sized NPs surface is characterized by large terraces of identical surface atoms because of less surface heterogeneity [67-69]. But decrease in the NPs size would result in the more surface heterogeneity due to modified surface atom statistics, which in turn likely to hike the surface roughness [67-69]. Furthermore, quantum sized particles are composed of large number of coordinatively unsaturated surface atoms which increase the surface roughness and promotes the chemisorption of the reactant molecules and thereby smoothen the progress of the reaction [67]. While the large sized particles are terminated primarily by low-index, high-coordination surfaces related to lower surface roughness [67]. Ornelas et al. studied the hydrogenation of styrene using different types of Pd NPs and showed that higher activity was

obtained with smaller NPs, which suggests that the uncoordinated sites promote the catalytic reaction [70].

Whereas in case of heterogeneous catalysis, there are only a few examples in which modified approach has been employed to analyze the activity and selectivity of specific catalysts with respect to the size of the NPs co-catalyst. Somorjai and co-workers [71,72] tested the performance of Pt NPs with sizes ranging from 0.8–5.0 nm for the hydrogenation and hydrogenolysis of pyrrole. They found that the conversion selectivity shifted from n-butylamine formation with larger particles to the formation of pyrrolidine with smaller particles. Moreover, with methylcyclopentane, the smaller Pt NPs were found to favored the hydrogenolysis to 2-methylpentane, while the larger Pt NPs yielded primarily benzene at high temperatures [73]. It was investigated that the hydrogenation of neat o-, m-, and p- xylene catalyzed by C-nanotube-supported metallic Rh NPs become faster and more stereoselective with decreasing the particle size. Jin et al. studied the size dependence activity of Pd nanocubes and confirmed that upon reducing the size of the Pd nanocrystals from 18 to 6 nm, catalytic activity was increased by a factor of approximately ten [74]. Subramanian et al. [48] observed -60 mV shift in flat band potential using 3 nm AuNPs as compared to -20 mV shift for 8 nm AuNPs. Kaur et al. [51] investigated a considerable improvement in the TiO_2 photocatalytic oxidation with decreasing size (9.5 to 3.5 nm) of the spherical Au co-catalyst and was ascribed to the surface-to-volume ratio of the NPs, which assist in the formation of Au–TiO_2 interface. It is interesting to know that the effective amount (0.01 wt%) of Au atom required for maximum PCA of TiO_2 is 100 times less than the conventional prerequisite of 1–2 wt% metal deposition [51].

Therefore, as a consequence of cost effective modified approach, different sizes of metal NPs can be easily synthesized and employed to tune the size dependent co-catalytic activity for TiO_2 photocatalysis.

(b) Impact of NP Shape

Catalytic as well co-catalytic activity of NPs cannot be explained solely on the basis of size factor, another important parameter which should be taken into account is the geometric shape of the nanocrystal [8-18]. Every shape has its own characteristic property, have varied number of atoms on the corners and edges, dissimilar surface to volume ratio, high and low index planes, exposed crystallographic facets as shown in figure 2, etc. The atomic arrangement within the spherical shape is quiet different as compared to rod or wire and hence, interact in a dissimilar

manner and would result in varied catalytic rate. This raises the possibility that the use of metal NPs of varied morphologies could catalyze different reactions with different competence.

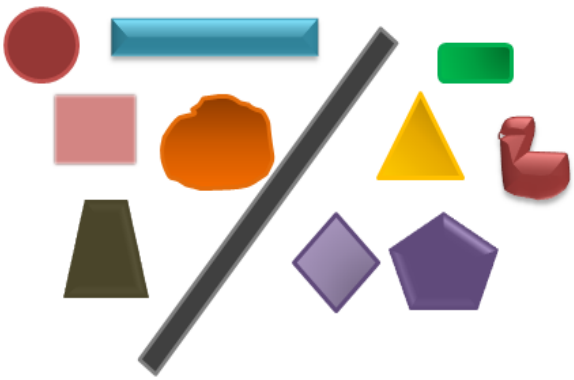

Figure 2. Various morphologies of metal nanoparticles.

Different shapes of NPs possess varied crystallographic facets and would expect to show diverse reactivities and selectivities. For example, Xu et al. [75] have observed that Ag nanocubes with {100} facets were 14 times more reactive than nanoplates, and 4 times more active than spherical NPs for the oxidation of styrene. Similarly, Cuenya et al. [76] reported that the Ag nanocubes and nanowires with {100} facets found to display better selectivities than nanospheres composed of {111} facets for the selective epoxidation of ethylene. Nanocubes of Pt with {100} planes were found to display enhanced selectivity for the conversion of benzene to cyclohexane, while a mixture of cyclohexane and cyclohexene were obtained using cuboctahedron Pt NPs with {100} and {111} facets [77]. Narayanan et al. [8,12,78] examined the rate of conversion of hexacyanoferrate (III) with thiosulfate ions using various shapes of Pt NPs which follow the sequence as Pt nanocubes [with (100) facets] <Pt nanospheres <Pt nanotetrahedra [terminated by (111) surfaces]. The kinetic parameters of this electron-transfer reaction were also found to correlate with the fraction of the resulting low-coordination surface atoms.

A plentiful of studies showed the distinct behavior of NPs shape on the catalytic performance but much less research elucidates the role played by the NPs morphology as a co-catalyst towards the TiO_2 PCA. One can clearly observe from the scheme 3 that various NP morphologies such as rod, sphere, truncated triangle, polygonal nanospheres etc. exhibit different catalyst-co-catalyst interactions as discussed above and would result in varied PCA. In this respect Kaur et al. [51, 52] investigated the differences in the co-catalytic behavior imparted by Au and AgNPs of varied morphologies for the enhancement in TiO_2 PS and have been discussed in chapter 2 and 6, respectively.

Unfortunately, reports in the area making an effective use of modified approach for TiO_2 photocatalysis are still limited and need more exploration. So, in this thesis, emphasis has been

given on the synthesis of various shapes and sizes of ***coinage metal NPs*** *and their utility as co-catalyst for the improvement in the TiO_2 PS. The synthesized coinage metal NPs were also used as catalyst to correlate their shape and size effect.*

1.3 Why Coinage (Au, Ag and Cu) metal nanoparticles?

Although coinage metals are expensive yet they are extensively studied because of their non corrosive nature and their characteristic surface plasmon resonance (SPR) band which make their study accessible in visible region [79-84]. The optical properties of coinage metal NPs arising due to the SPR have been received noteworthy research attention in recent years because of their potential applications in diverse areas such as photonic circuits, biological sensors, surface enhanced Raman spectroscopy, photochromics, photoluminescence, bio-imaging, etc.

SPR is the optical feature of metal NPs and can be defined as the resonance energy produced when the frequency of photons of the incident light matches with the frequency of the coherent oscillation of conduction electrons confined at the surface of the metal NPs (Scheme 4). The electric fields of the incoming light polarizes the free conduction electrons with respect to the much heavier ionic core of a spherical NP and the negative charge of conduction electrons move under the influence of external fields. The resultant displacements of the negative charges cause a net charge difference at the nanoparticle boundaries which in turn, give rise to a linear restoring force to the system. As a consequence, a dipolar oscillation of the electrons is created and this is known as the surface plasmon oscillation [79]. This resonance frequency can be easily determined from absorption spectroscopy and depends on a few factors such as particle size, shape, nature of the surrounding medium and by manipulating these variables, metal nanostructures are of potential interest, can be designed to exploit the entire solar spectrum [79-85]. For many metals such as, Pt, Rh, Pb, In, Hg, Cd and Sn etc., the surface plasmon frequency lies in the UV part of the spectrum and these NPs do not display strong color effects. But the coinage metals such as Au, Ag and Cu are exceptional. Coinage metal NPs are also known as

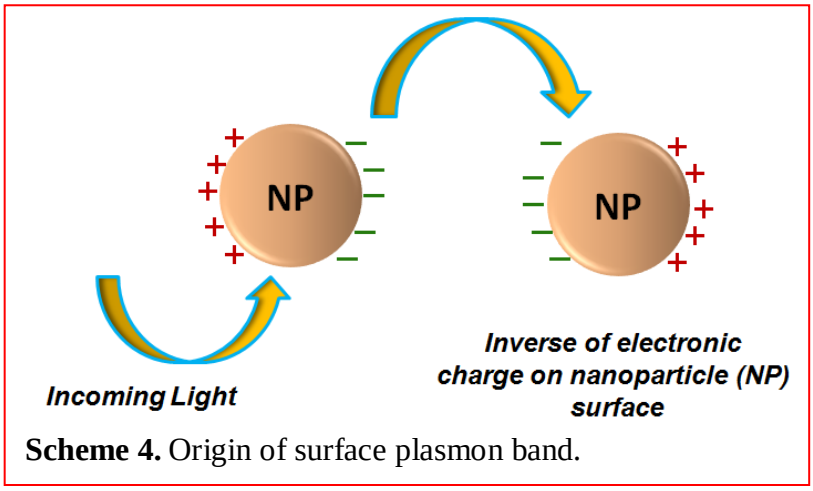

Scheme 4. Origin of surface plasmon band.

electron banks that lend out electrons at appropriate time, and store them for chemical species at other times and show their application in thermal catalysis, electronic devices, separation technology, and as a biocatalyst in many medicines to cure diseases and *photocatalysis.*

1.4 Research gap and objectives

Based on the above literature review, following important issues are the research gaps which need to be taken under consideration.

1.4.1 Morphological dependent co-catalytic effect: Generally, the metal-SC catalysts have been prepared by precipitation deposition, wet-impregnation, doping and photoreduction methods under UV light irradiation which results in the formation of spherical aggregated nanodeposits on TiO_2 surface and hence, restricts catalyst-co-catalyst structure-activity interactions. Many efforts have been employed to investigate optical and structural properties of coinage metal NPs of different dimensions, but the correlation of catalyst-co-catalyst interactions dependent on nature, size, shape of co-catalyst and their spatial alignments to achieve the best information in TiO_2 photocatalysis is still essential for finding better efficient catalytic materials. It is believed that the addition of different morphologies of NPs to the SC suspension can significantly influence the overall energetics of the PS depending on interfacial contact area between the two that effects adsorption of substrate and expected to show different reactivities and selectivities as discussed above. Moreover, surface area, surface to volume ratio, per particle surface area, number of exposed surface atoms, and density of the active corners correlates with strong surface activity as a function of particle shape.

1.4.2 Fate of NPs in organic reactions: Mostly nanocrystals are synthesized in aqueous media and used in many organic and inorganic reactions employing polar solvents that lead to their disordered arrays due to the dipole-dipole interactions [86] and mask the true catalytic activity of NP. During random aggregation process, the net surface charge and zeta potential (ζ) [87] of NPs get modified depending on aggregated cluster size and attached polar/non-polar surface active agents that influence the adsorption/or interaction of reacting substrate and thereby effect the catalytic and co-catalytic activity. In this regard, chapter 3 and 4 deals with way of AuNPs arrangement/agglomeration in various polar solvents and relate their catalytic and co-catalytic activity in order to tune the kinetics of Au catalyzed organic reactions.

1.4.3 Co-catalytic efficiency of CuNPs: CuNPs are known to be extremely sensitive to arid atmosphere, and therefore there are several problems related to the stability, oxidation resistance

and shape dependent co-catalytic activity that need to be solved.

1.4.4 Comparative catalytic influence of coinage metal on reaction rate: Nature of the metal imparts a characteristic impact on the pace of the reaction rate and can be explained by the difference in their work functions, E_f, SPR and interaction/ adsorption behavior with the substrate. Moreover, the execution of these coinage metal NPs onto TiO_2 (UV light active catalyst) drive the catalyst to do efficiently work in the visible light as a function of their SPR band. So, it is valuable to investigate the comparative activity of coinage metal NPs to know which metal is playing an efficient role and this comparative account has been discussed in details in chapter 8.

1.5 Objectives

1. Synthesis of coinage metal (Au, Ag and Cu) nanoparticles and the effect of different solvents on their aggregation.
2. Characterization of nanoparticles using structural, microscopic and spectroscopic techniques.
3. To study size & shape dependent catalytic activity as a co-catalyst for the metal-TiO_2 photocatalytic degradation of model compounds, e.g., salicylic acid, benzoic acid and acetic acid.
4. To evaluate efficiency of the synthesized metal nanoparticles.

1.6 Characterization Techniques

Various considerable synthetic strategies have been adopted to sophisticatedly prepare various shapes and sizes of coinage metal NPs and have been discussed in respective chapters. The instrumental techniques which have been used to characterize nanomaterials to get an idea of their size, geometric shape, and surface area, chemical and physical details have been listed below.

1.6.1 UV-vis spectrophotometer

UV-vis absorption spectrum is a preliminary technique to characterize NPs because the absorption spectra give tentative information about the NP shape and size distribution. It is based on the principle of absorption of light with suitable energy by sample molecules, which result in the promotion of an electron to a higher energy level. Analysis has been done on **Analytikjena Specord 205** instrument by taking ≈ 2.5 ml colloidal NP solution in a 3.5 ml quartz cuvette within the range of 190−1100 nm.

1.6.2 UV-vis diffuse reflectance spectrophotometer

The absorbance of solid powders was carried on **Avantes Diffuse Reflectance Spectrophotometer.** 2-5 mg of sample was taken on a glass slide and the light source probe was placed over the sample to record its absorbance/ reflectance spectra by using $BaSO_4$ as a reference. This technique was used to understand the Eg between the VB and CB of the powdered samples. Bandgap calculations of as prepared samples were done by using Tauc equation [88,89].

$$\alpha h\nu = A(h\nu - Eg)^n$$

Where α is the absorption coefficient of the material, which represents the absorption ability of a material for a certain wavelength; h is the Planck constant; ν is the frequency of light; A is a constant, which depends on temperature, photo energy and phonon energy; Eg is the band gap; the exponent n is a characteristic of the type of electrons transition process (n = 1/2 for a direct allowed transition & n = 2 for an indirect allowed transition process). As TiO_2 is indirect band gap semiconductor, hence the band gap was determined by extrapolating the linear portion of the plot of $(\alpha h\nu)^2$ versus hν.

1.6.3 Time resolved spectroscopy

Time resolved spectroscopy is the study of charge dynamic processes in metal-SC composites. The time resolve luminescence spectra was recorded using Nitrogen laser (excitation at 390 nm) pulsed in operation (5-7 ns pulse width) coupled with **Tektronix TDS-1012 oscilloscope.** Sample was prepared by making a thick paste of TiO_2 powder (~50 mg) and metal-TiO_2 with a few drops of acetone to make it as a solid mass. Thereafter, stub having solid mass was suspended vertically for laser pulsation (excited at 390 nm) and an average lifetime was recorded and calculated using following equation [90].

$$\tau_{av} = (a_1\tau_1 + a_2\tau_2)/ a_1 + a_2$$

1.6.4 Zeta potential measurements

The zeta potential is crucial in determining the stability of a colloidal NP suspension. All the particles in suspension exhibit some surface charge or zeta potential, the measurement and knowledge of which is significant for predicting stability and interactions among the reacting substrates. **Zeta potential (ζ)** measurements were carried out by means of **Brookhaven 7610 instrument** and sample was prepared by adding 1.5 ml sample in a 3.5 ml glass cuvette. It represents the surface charge of a particle which arises due to the potential difference between the particle's surface and the surrounding medium.

1.6.5 Dynamic light scattering

It provides the hydrodynamic size of the NPs and was done by taking ≈ 1.5 ml of the dispersed particles in a cuvette by means of **Brookhaven 7610 instrument.**

1.6.6 Surface charge measurements

Surface charge density of NPs has been measured by **Mutek-PCD03pH**, using 300 ml aqueous suspension containing 1.66×10^{15} atoms/ml.

1.6.7 X-ray diffraction analysis

Structural and phase identification of the composites was carried out with Cu-Kα (k = 1.54060 A°) radiation operated at 45 kV within the range of 10-90° on **PANalytica X' pert PRO X-ray diffractometer.** XRD samples were prepared by grinding dried M-TiO_2 powder in a pestle and mortar to form fine powders.

1.6.8 Scanning electron microscopy (SEM)

SEM was used to obtain information about the surface morphology of the sample. SEM images provide information in terms of topography, morphology (size, shape and arrangement) and composition of the sample surface. **JSM-7600F (0.1–30 KV) SEM instrument** was used for surface morphology analysis of sample by treating powder with an ultrathin coating of electrically conducting Au material, which was lodged on the sample by low-vacuum sputter coating. After that, conducting material was mounted rigidly on a specimen holder called a specimen stub for surface analysis.

1.6.9 Energy dispersive X-ray (EDX) spectrophotometer

This technique was used to study the chemical composition of the selected points or areas of the sample. It was also helpful in identifying materials and contaminants and even in distinguishing their relative concentrations on the surface of the sample. EDX analysis was carried on **JSM-7600F.**

1.6.10 Transmission electron microscopy (TEM)

TEM is a valuable tool to study the structural details and statistical distribution of sizes and shapes of the particles in sample. The specimens were prepared by depositing a drop of a dilute aqueous suspension of NPs on carbon-coated copper grids and allowing the solvent to evaporate. Low magnification **TEM (Hitachi 7500 model**) was performed at operating voltages of 20-200 kV with 2.4 A˚ resolutions and High Resolution-TEM (HR-TEM) was carried at with resolution 2 A˚ operating at voltage 120 kV **on JEOL, JEM 2100 at** Sophisticated Analysis

Instrumentation Facility (SAIF) centre, Panjab University, Chandigarh, India; IIT-Mumbai, India and at Central Salt and Marine Chemicals Research Institute, Bhavnagar, Gujarat, India.

1.6.11 Surface area analysis

BET surface area analysis was carried out in order to measure the surface area of the powdered samples. The analysis of the porous surface was carried out by N_2 adsorption/desorption techniques at 77 K. Adsorption isotherms were determined using a **Smartsorb 92/93** instrument where 100 mg of samples are regenerated at 150 °C for 1 h.

1.6.12 X-ray photoelectron spectroscopy

XPS is a spectroscopic technique that measures the elemental composition; chemical state and electronic state of the elements exist within a material. X-ray photoelectron spectroscopy **(XPS, PHI 5200 mode)** was performed using an Al Kα x-ray source in a chamber with base pressure of $\sim 10^{-10}$ Torr.

1.6.13 Current-voltage (I-V) characteristic

The samples were doctor bladed onto soda lime glass substrates. Then the samples were cut into 1×1 cm^2 area and silver paste was applied at two opposite ends for electrical contact. Controlled potential was applied at a bias step of 0.03V to the samples and resulting current was measured using a computer controlled **KEITHLEY source meter** (KI 2400.)

1.6.14 Ar ion LASER

High energy laser was used to fragment the nanoparticles in a variety of shapes with reduced size and much exposed area. Au nanospheres and nanorods were irradiated with laser ion beam of different energies. Ar ion continuous laser (**Stellar-Pro, MODU LASER with multiline configuration**) having energies in the range of 40-120 W and controllable monochromatic wavelengths i.e. 514, 488 and 458 nm was used for photodistortion of NPs.

1.6.15 High Performance Liquid chromatography (HPLC) was carried out by using **Agilent, 1120 Compact LC technologies** with C-18 column (250 mm × 4.5 mm). The mobile phase used for the analysis was methanol and water in ratio of 65:35 or 70:30 with a flow rate of 1 ml/min at 220 and 254 nm wavelengths for the detection of oxidized or reduced products. 20 µl of the reaction mixture was injected into the loop after filtration by cellulose filter of 0.22 µm. This technique is based on the principle of adsorption in which analyte molecules are separated on the basis of their interaction with the mobile and the stationary phase.

1.6.16 Gas chromatography (GC)

The CO_2 evolution was determined by injecting 1 ml of the gaseous mixture from the reaction vessel into the gas chromatography using Propak-Q column, **NUCON-5765** (30 mm × 0.32 mm × 12.00 µm) with nitrogen as carrier gas (30 ml/min) and Thermal Conductivity Detector (TCD). Column oven was maintained at 40 °C while injector and detector were at 70 and 80 °C, respectively.

1.6.17 Gas chromatography-mass spectroscopy (GC-MS) was carried out on **Shimadzu, GC-2010 and GC-MS-QP 2010 plus** with RTX-5Sil-MS column (30 mm × 0.25 mm × 0.25 µm) to confirm the products/intermediates. As obtained aqueous solution of substrate after final UV-light exposure was centrifuged, filtered through cellulose filter (0.22 µm) and then extracted three times with dichloromethane. Residue thus obtained was redissolved in methanol. Helium was used as a carrier gas with a flow of 1ml/min through capillary column. Injector was maintained at 240 °C. Oven was programmed at 60 °C to 300 °C at 6 °C/min rise of temperature.

1.7 Photocatalytic reaction setups

1.7.1 Photocatalytic reactor with Hg (UV) light source

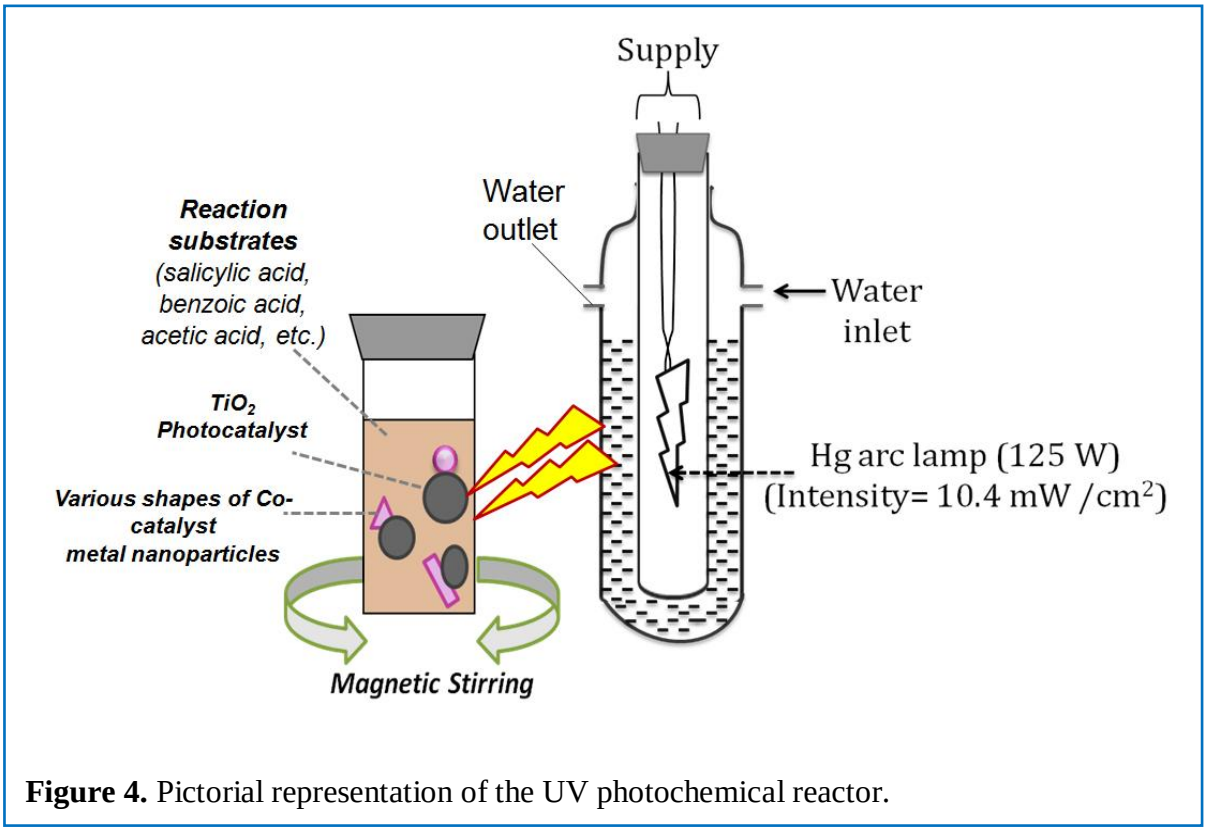

Figure 4. Pictorial representation of the UV photochemical reactor.

It is composed of a UV light source (125 W) of low pressure mercury vapor lamp that emit mainly at 254 nm. The Hg lamp (125 W; intensity 10.4 mW/cm^2) connected to power cords was set inside a water-jacketed quartz tube (figure 4). A continuous flow of cold water was circulating in the outer

jacket to make sure that it remains cool for a longer time. A maximum amount of 5 ml reaction sample was taken in 15 ml capacity test tube that is placed at a distance of 2-3 cm from light source under continuous magnetic stirring. The distance between magnetic stirrer and lamp was minimized to get optimum flux. The whole set up was placed in a wooden box to prevent the UV exposure as a safety purpose.

1.7.2 Catalytic Reaction

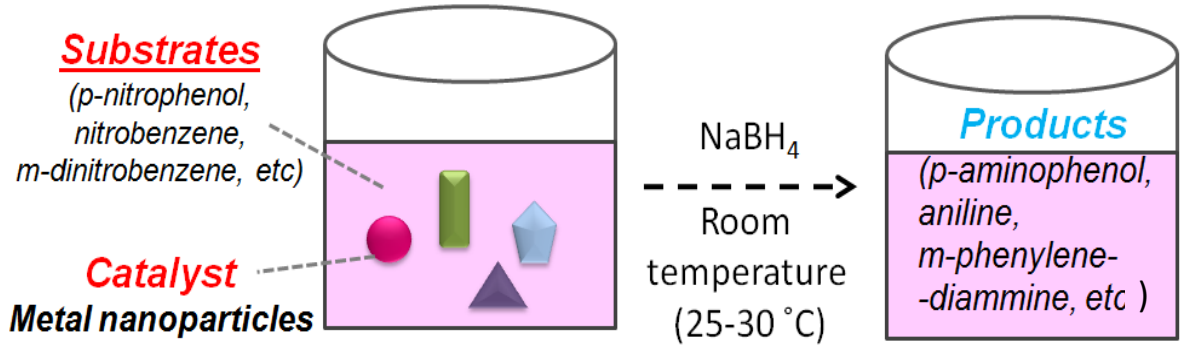

Figure 5. Experimental setup for catalytic reduction reaction using metal nanoparticles.

Catalytic activity with various metal nanomorphlologies was carried out by adding requisite amount of ice-cold $NaBH_4$ solution to aqueous solution of nitro aromatic compounds such as p-nitrophenol, nitrobenzene, m-dinitrobenzene, etc. at room temperature (25-30˚C, figure 5). The extent of reduction was monitored by measuring the absorption spectra of the reaction mixture at regular intervals and also analyzed by high–performance liquid chromatography. Reaction intermediates were investigated using GC-MS analysis.

1.7.3 Sunlight as a visible light source

The experiment under sunlight irradiation was carried out by constantly stirring 10 ml of substrate solution in a 25 ml capacity beaker (exposed area = 12.56 cm^2) with 20 mg catalyst. The whole arrangement was placed under the direct sunlight exposure at the terrace between 12.00 noon – 4.00 pm (figure 6). Sunlight intensity (flux) was measured by using Lux meter. The reaction samples were analyzed with UV-visible spectrophotometer for

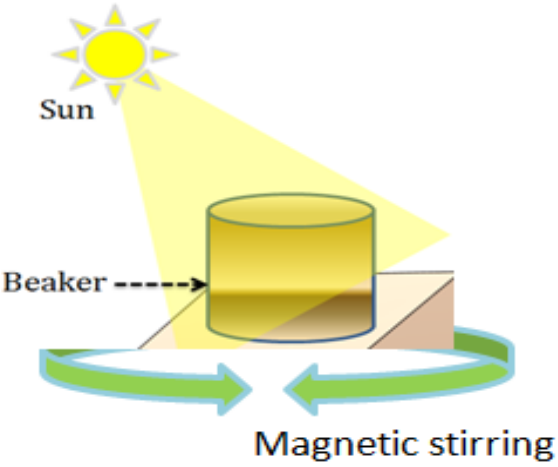

Figure 6. Design of experimental setup under sunlight irradiation.

different time intervals.

1.8 References

[1] F. Boccuzzi, A. Chiorino, M. Manzoli, D. Andreeva, T. Tabakova, L. Ilieva and V. Iadakiev, Catal. Today, 75 (2002) 169.

[2] R.J. Tayade, R.G. Kulkarni and R.V. Jasra, Ind. Eng. Chem. Res., 45 (2006) 5231.

[3] A. Boisen, S. Dahl, J.K. Norskov and C.H. Christensen, J. Catal., 230 (2005) 309.

[4] I.M.L. Billas, A. Chatelain and W.A. De Heer, Science, 265 (1994) 1682.

[5] J. Yang, D. Wang, H. Han and C. Li, Acc. Chem. Res., 46 (2013) 1900.

[6] D.Y.C Leung, X.L. Fu, C.F. Wang, M. Ni, M.K.H. Leung, X.X. Wang and X.Z. Fu, ChemSusChem., 3 (2010) 681.

[7] S. Trasatti, J. Electroanal. Chem., 39 (1972) 163.

[8] R. Narayanan, Molecules, 15 (2010) 2124.

[9] H. Choi, W.T. Chen and P.V. Kamat, ACS Nano, 6 (2012) 4418.

[10] J. Zeng, Q. Zhang, J. Chen and Y. Xia, Nano Lett., 10 (2010) 30.

[11] J.K. Norskov, T. Bligaard, B. Hvolbaek, F.A. Pedersen, I. Chorkendorff and C.H. Christensen, Chem. Soc. Rev., 37 (2008) 2163.

[12] R. Narayanan and M.A. El-Sayed, Langmuir, 21 (2005) 2027.

[13] A. Primo, A. Corma and H. Garcia, Phys. Chem. Chem. Phys., 13 (2011) 886.

[14] B.R. Cuenya, Acc. Chem. Res., 46 (2013) 1682.

[15] S. Schauermann, N. Nilius, S. Shaikhutdinov and H.J. Freund, Acc. Chem. Res., 46 (2013) 1673.

[16] S.E. Allen, R.R. Walvoord, R.P. Salinas and M.C. Kozlowski, Chem. Rev., 113 (2013) 6234.

[17] X. Yang, Z. Wu, M.M. Debusk, D.R. Mullins, S.M. Mahurin, R.A. Geiger, M. Kidder and C.K. Narula, J. Phys. Chem. C, 116 (2012) 23322.

[18] S. Linic, P. Christopher and D.B. Ingram, Nat. Mater., 10 (2011) 911.

[19] F. Sheng, C. Xu, Z. Jin, J. Guo, S. Fang, Z. Shi and J. Wang, J. Phys. Chem. C, 117 (2013) 18627.

[20] X. Luo, F. Deng, L. Min, S. Luo, B. Guo, G. Zeng and C. Au, Environ. Sci. Technol., 47 (2013) 7404.

[21] H. Kim, J. Kim, W. Kim and W. Choi, J. Phys. Chem. C, 115 (2011) 9797.

[22] J. Zhang, Y. Wang, J. Zhang, Z. Lin, F. Huang and Jiaguo Yu, ACS Appl. Mater. Interfaces, 5 (2013) 1031.

[23] H. Wang, T. You, W. Shi, J. Li and L. Guo, J. Phys. Chem. C, 116 (2012) 6490.

[24] A. Takai and P.V. Kamat, ACS Nano, 5 (2011) 7369.

[25] N. Serpone and A.V. Emeline, J. Phys. Chem. Lett., 3 (2012) 673.

[26] E. Grabowska, A. Zaleska, S. Sorgues, M. Kunst, A. Etcheberry, C. Colbeau-Justin and H. Remita, J. Phys. Chem. C, 117 (2013) 1955.

[27] W.Y. Teoh, J.A. Scott and R. Amal, J. Phys. Chem. Lett., 3 (2012) 629.

[28] C.L. Pang, R. Lindsay and G. Thornton, Chem. Rev., 113 (2013) 3887.

[29] M. Haruta, Gold Bull., 37 (2004) 27.

[30] M.D. Blankschien, L.A. Pretzer, R. Huschka, N.J. Halas, R. Gonzalez and M.S. Wong, ACS Nano, 7 (2013) 654.

[31] A.L. Linsebigler, G. Lu and J.T. Yates, Chem. Rev., 95 (1995) 735.

[32] K. Hashimoto, H. Irie and A. Fujishima, Jpn. J. Appl. Phys., 44 (2005) 8269.

[33] M.A. Mahmood , S. Baruah, A.K. Anal and J. Dutta, Environ. Chem. Lett., 10 (2012) 145.

[34] A. Kumar and N. Mathur, J. Colloid Interf. Sci., 300 (2006) 244.

[35] M. Ni, M.K.H. Leung, D.Y.C. Leung and K. Sumathy, Renew. Sust. Energ. Rev., 11 (2007) 40.

[36] R. Daghrir, P. Drogui and D. Robert, Ind. Eng. Chem. Res., 52 (2013) 3581.

[37] S.Y. Lee and S.J. Park, J. Ind. Eng. Chem., 19 (2013) 1761.

[38] L. Zhang, T. Kanki, N. Sano and A. Toyoda, Sep. Purif. Technol., 31 (2003) 105.

[39] G. Liu, L.C. Yin, J. Wang, P. Niu, C. Zhen, Y. Xie and H.M. Cheng, Energy Environ. Sci., 5 (2012) 9603.

[40] M.A. Henderson, N.A. Deskins, R.T. Zehr and M. Dupuis, J. Catal., 279 (2011) 205.

[41] S.K. Mehta, S. Kumar, S. Chaudhary and K.K. Bhasin, Nanoscale Res. Lett., 4 (2009) 1197.

[42] S. Chen, X. Zhang, Y. Zhao and Q. Zhang, Bull. Mater. Sci., 33 (2010) 547.

[43] W.G. Lee, Y.K. Kim, J.K. Kim, N. Starzhinskiy, V. Ryzhikov and B. Grinyov, Radiat. Meas., 43 (2008) 502.

[44] H. Shi, T. Zhang, T. An, B. Li and X. Wang, J. Colloid Interf. Sci., 380 (2012) 121.

[45] R. Asahi, T. Morikawa, T. Ohwaki, K. Aoki and Y. Taga, Science, 293 (2001) 269.

[46] E. Grabowska, H. Remita and A. Zaleska, Physicochem. Probl. MI., 45 (2010) 29.

[47] M.V. Dozzi, A. Saccomanni and E. Selli, J. Hazard. Mater., 211 (2012) 188.

[48] V. Subramanian, E. Wolf and P.V. Kamat, J. Phys. Chem. B, 105 (2001) 11439.

[49] K. Loganathan, P. Bommusamy, P. Muthaiahpillai and M. Velayutham, Environ. Eng. Res., 16 (2011) 81.

[50] A. Kumar and N. Mathur, Appl. Catal. A: Gen., 275 (2004) 189.

[51] R. Kaur and B. Pal, J. Mol. Catal. A: Chem., 355 (2012) 39.

[52] R. Kaur and B. Pal, Colloids Surf. A., 441 (2014) 155.

[53] A. Wood, M. Giersig and P. Mulvaney, J. Phys. Chem. B, 105 (2001) 8810.

[54] S. Chen and R.W. Murray, J. Phys. Chem. B, 103 (1999) 9996.

[55] S. Chen, R.S. Ingram, M.J. Hostetler, J.J. Pietron, R.W. Murray, T.G. Schaaff, J.T. Khoury, M. M. Alvarez and R.L. Whetten, Science, 280 (1998) 2098.

[56] S. Chaturvedi, P.N. Dave and N.K. Shah, J. Saudi Chem. Soc., 16 (2012) 307.

[57] O.M. Wilson, M.R. Knecht, J.C. Garcia-Martinez and R.M. Crooks, J. Am. Chem. Soc., 128 (2006) 4510.

[58] F. Zaera, ChemSusChem, 6 (2013) 1797.

[59] C.N.R. Rao, G.U. Kulkarni, P.J. Thomas and P.P. Edwards, Chem. Eur. J., 8 (2002) 1.

[60] G.J. Hutchings and M. Haruta, Appl. Catal. A, 291 (2005) 2.

[61] M. Haruta, Chem. Rec., 3 (2003) 75.

[62] X. Xie, Y. Li, Z.Q. Liu, M. Haruta and W. Shen, Nature, 458 (2009) 746.

[63] S. Sarkar, A.K. Sinha, M. Pradhan, M. Basu, Y. Negishi and T. Pal, J. Phys. Chem. C, 115 (2011) 1659–1673.

[64] N. Pradhan, A. Pal and T. Pal, Langmuir, 17 (2001) 1800.

[65] N.R. Jana, T.K. Sau and T. Pal, J. Phys. Chem. B, 103 (1999) 115.

[66] S. Panigrahi, S. Basu, S. Praharaj, S. Pande, S. Jana, A. Pal, S.K. Ghosh and T. Pal, J. Phys. Chem. C, 111 (2007) 4596.

[67] H. Song, R.M. Rioux, J.D. Hoefelmeyer, R. Komor, K. Niesz, M. Grass, P.Yang and G.A. Somorjai, J. Am. Chem. Soc., 128 (2006) 3027.

[68] H. Harle, W. Metka, H.R.Volpp and Wolfrum, J. Phys. Chem. Chem. Phys., 1 (1999) 5059.

[69] R.V.V. Hardeveld and F. Hartog, Surf. Sci., 15 (1969) 189.

[70] C. Ornelas, J.R. Aranzaes, L. Salmon and D. Astruc, Chem. Eur. J., 14 (2008) 50.

[71] J.N. Kuhn, W. Huang, C.K. Tsung, Y. Zhang and G.A. Somorjai, J. Am. Chem. Soc., 130 (2008) 14026.

[72] C.K. Tsung, J.N. Kuhn, W. Huang, C. Aliaga, L.I. Hung, G.A. Somorjai and P. Yang, J. Am. Chem. Soc., 131 (2009) 5816.

[73] S. Alayoglu, C. Aliaga, C. Sprung and G.A. Somorjai, Catal. Lett., 141 (2011) 914.

[74] M. Jin, H. Liu, H. Zhang, Z. Xie, J. Liu and Y. Xia, Nano Res., 4 (2011) 83.

[75] R. Xu, D. Wang, J. Zhang and Y. Li, Chem. Asian J., 1 (2006) 888.

[76] B.R. Cuenya, J.R. Croy, S. Mostafa, F. Behafarid, L. Li, Z. Zhang, J.C. Yang, Q. Wang and A.I. Frenkel, J. Am. Chem. Soc., 132 (2010) 8747.

[77] K.M. Bratlie, H. Lee, K. Komvopoulos, P.D. Yang and G.A. Somorjai, Nano Lett., 7 (2007) 3097.

[78] M.A. Mahmoud, R. Narayanan and M.A. El-Sayed, Acc. Chem. Res., 46 (2013) 1795.

[79] S.K. Ghosh and T. Pal, Chem. Rev., 107 (2007) 4797.

[80] S.T. Kochuveedu, Y.H. Jang and D.H. Kim, Chem. Soc. Rev., 42 (2013) 8467.

[81] X. Zhou, G. Liu, J. Yu and W. Fan, J. Mater. Chem., 22 (2012) 21337.

[82] K.L. Kelly, E. Coronado, L.L. Zhao and G.C. Schatz, J. Phys. Chem. B, 107 (2003) 668.

[83] K.P. Rice, E.J. Walker, Jr., M.P. Stoykovich and A.E. Saunders, J. Phys. Chem. C, 115 (2011) 1793.

[84] Md. A.Al-Mamun, Y. Kusumoto, T. Zannat, Md. S. Islam, Appl. Catal. A: Gen., 398 (2011) 134.

[85] M. Achermann, J. Phys. Chem. Lett., 1 (2010) 2837.

[86] J. Liao, Y. Zhang, W. Yu, L. Xu, C. Ge, J. Liu and N. Gu, Colloids Surf. A., 223 (2003) 177.

[87] C.J. Orendorff, T.M. Alam, D.Y. Sasaki, B.C. Bunker and J.A. Voigt, ACS Nano, 3 (2009) 971.

[88] Y.F. Zhu, J. Zhang, L. Xu, Y. Guo, X.P. Wang, R.G. Du and C.J. Lin, Phys. Chem. Chem. Phys., 15 (2013) 4041.

[89] B. Subramanian, C. Sanjeeviraja and M. Jayachandran, J. Cryst. Growth, 234 (2002) 421.

[90] J. Li and J. Xia, Phys. Rev. B, 62 (2000) 12613.

Chapter 2

Size and Shape Dependent Attachments of Au Nanostructures to TiO_2 for Optimum Reactivity of Au-TiO_2 Photocatalysis

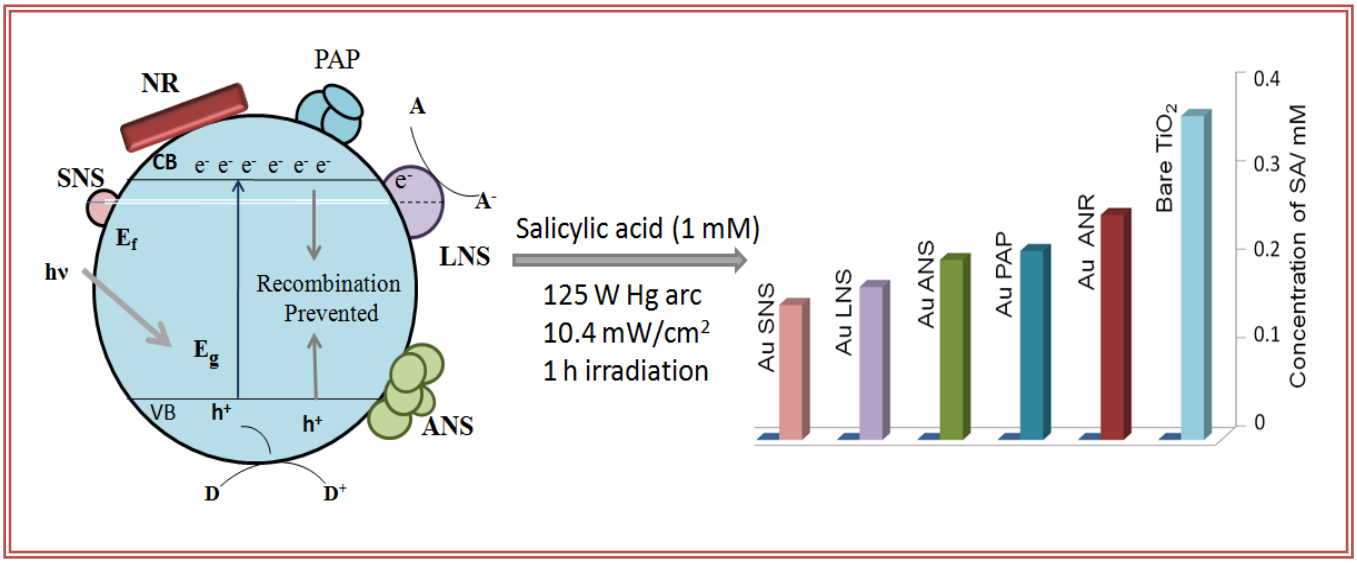

2.1 Introduction

The deposition of transition metals co-catalysts, Pt, Rh, Au, Cu and Ag onto TiO_2 catalyst usually improves the photocatalytic activity (PCA) which strongly depends on the extent, nature and the work function of the metals [1-5]. Also, several strategies have been employed to improve the PCA by tailoring size and shape of titania and metal nanostructure [3-11]. After photoexcitation, the electron migrates to the metal where it gets trapped and e^-/h^+ recombination is reduced. The hole is then free to migrate to the surface where oxidation of the organics takes place. Conventional metal deposition techniques [9-14] generally lead to the growth of aggregated spherical particles and hence, the key effect of various sizes and shapes of metal nanoparticles (NPs) co-catalysts for photocatalytic reactions could not be determined. Metal NPs in the size regime 1-10 nm exhibit characteristic size and shape dependent properties due to better charge transfer that cannot occur in bulk materials because the exposed surface atoms are 50 times less than quantum size particles [15-18]. Consequently, the size and shape specific activity of Au, Ag, Cu and Pt, NPs are studied both as catalysts and co-catalysts for variety of thermal and photoreactions, respectively [12-19]. This size effect of metal NPs on the enhanced PCA of TiO_2 has been ascribed to the Fermi energy shifts to the more negative direction for smaller NPs, leading to decrease the potential difference between the conduction band of TiO_2 and the Fermi level of the metal NPs [20-24]. Hence, facilitates electron accumulation in the metal NPs and shifts the apparent Fermi level of metal NPs close to the bottom of the conduction band of TiO_2. As a result, Fermi level equilibrium takes place quickly and rapid electron transfer from TiO_2 to metal NPs occurs for improved photooxidation reaction by photoexcited hole. *However, there have been very few comparative studies in the literature on the use of specific metal NPs co-catalyst of unlike shapes and size dependent attachments on the PCA of TiO_2* [22-27]. *Therefore, it is worth to study the Au-TiO_2 nanoassembly as a*

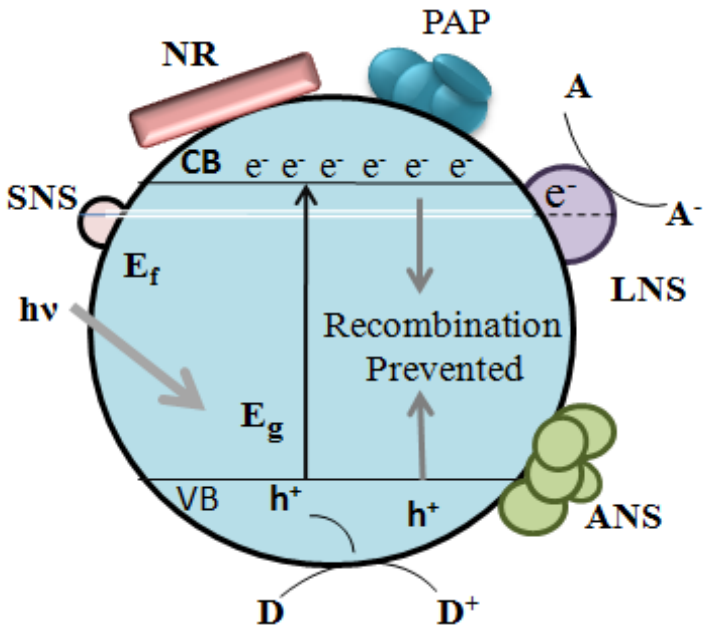

Scheme 1. Various morphology of Au nanoparticles-TiO_2 junctions.

function of their interface geometry, the role of Au nanoparticles (AuNPs) morphology, their aggregation and spatial attachments effect compared to that of bare TiO_2. The loading of AuNPs e.g., small nanosphere (SNS, size ≈ 3.5), medium size nanosphere (MNS, size > 5 nm), large nanosphere (LNS, size ≈ 9.5 nm), chemically aggregated nanosphere (ANS), nanorod (NR) and Au photodeposited particles (PAP), onto TiO_2 as shown in scheme I (MNS not shown here) would alter the PCA of TiO_2 in different extent. Thus, the observed change in PCA could be attributed to the prevailing effect of size and shape dependent co-catalytic activity of AuNPs imparted to TiO_2. This is due to photoexcited charge transfer processess at the Au-TiO_2 interface which can be caused in photocatalytic test reaction.

2.2 Experimental

2.2.1 Materials and methods

Chloroauric acid ($HAuCl_4.3H_2O$), sodium borohydride ($NaBH_4$), ascorbic acid ($C_6H_8O_6$), methanol (CH_3OH) and salicylic acid (SA) were obtained from Loba chemie, India. Commercially available P25-TiO_2 is a gift sample from P-25 Degussa, Germany. Silver nitrate ($AgNO_3$), cetyltrimethylammoniumbromide (CTAB) was purchased from Fischer Scientific and Sigma Aldrich, respectively. All the chemicals were used as-received without any further purification. Deionized water was obtained using an ultrafiltration system (Milli-*Q*, Millipore) with a measured conductivity above 35 mho cm^{-1} at 25 ˚C.

2.2.2 Synthesis of various Au nanostructures

The AuNPs of different sizes and shapes were synthesized [28-30] by seed-mediated approach in aqueous media at 0˚C. The Au seeds were first prepared by adding 250 µl (0.01 M) $HAuCl_4$ to 9.5 ml (0.1 M) cetyltrimethylammonium bromide (CTAB), followed by reduction with 600 µl (0.01 M) $NaBH_4$ solution under magnetic stirring for two minutes. The growth solution was prepared by treating a mixture of 500 µl (0.01 M) $HAuCl_4$, 9.5 ml (0.1 M) CTAB and 75 µl (0.01 M) $AgNO_3$ with 55 µl ascorbic acid (0.1 M). Then, 12 µl of above Au seed solution was introduced into the growth solution. Similarly, Au nanorod has been synthesized by the same seed approach method at 70˚C. The AuNPs were repeatedly washed with deionized water under four cycles of centrifugation at 8500 rpm for 10 minutes and then used for photocatalytic reactions. Chemical aggregation of Au nanospheres [31,32] was carried out by the addition of 100 µl CH_3OH to 100 µl Au-MNS in a test tube and then the solvent was vacuum evaporated and used for photoreaction. For surface plasmon resonance (SPR) absorption study, the aggregation of the Au-MNS (SPR band 563 nm and size > 5 nm) was carried out by direct addition of 1.5 ml CH_3OH (or CCl_4) to 1.5 ml of aqueous Au-MNS particles which showed 557 nm and 974 nm peaks.

Photodeposition of 0.02 wt.% Au onto TiO_2 (P25, Degussa, size ~ 20-30 nm) was carried out in a test tube using 5 ml deaerated aqueous suspension of CH_3OH, 50 mg TiO_2 and $HAuCl_4.3H_2O$ for 1 hour light irradiation under stirring.

2.2.3 Photocatalytic activity

The photoreaction was carried out in a test tube containing 5 ml salicylic acid (SA, 1 mM), 50 mg TiO_2 and desired amount (50 to 300 µl) of various AuNPs suspension under UV irradiation (125W Hg-arc lamp, 10.4 mW/cm^2 and λ_{max} = 253.6 nm) and magnetic stirring for different time periods at 30°C temperature.

2.2.4 Characterization

The AuNPs are characterized by their SPR band and TEM (Hitachi 7500, 200 KV) size and shape analysis. The unreacted SA was measured by UV-visible spectrophotometer (at λ_{max} = 298 nm) and HPLC (C18 column, 50% CH_3OH) analysis. Zeta potential measurement was done by using Brookhaven Instrument corporation 90plus/BI-MAS instrument. The solution containing Au-SNS (200 µl) or TiO_2 (200 µl form 50 mg per 5 ml water suspension) and water (1.3 ml) was taken in a cuvette for the zeta potential measurement. Similarly, 200 µl of the reaction mixture (1 mM-5 ml SA+ 50 mg TiO_2 + 100 µl Au-SNS) was added to 1.3 ml of water and analyzed for surface charge measurement. Table 1 shows the calculation for Au atoms as given below.

Table 1. Calculation for the Amount of Au atoms.

512 µl Au solution (0.01M, $HAuCl_4$) contains	**0.98 mg Au**
10 ml (10,000 µl) of AuNPs solution contains	0.98 mg Au
1 µl AuNPs contains	0.98×10^{-4} mg Au
1 µl AuNPs contains	2.996×10^{14} atoms
10 µl AuNPs contains	2.996×10^{15} atoms
25 µl AuNPs contains	7.489×10^{15} atoms
50 µl AuNPs contains	1.497×10^{16} atoms
100 µl AuNPs contains	2.996×10^{16} atoms

2.3 Results and discussion

2.3.1 Optical studies

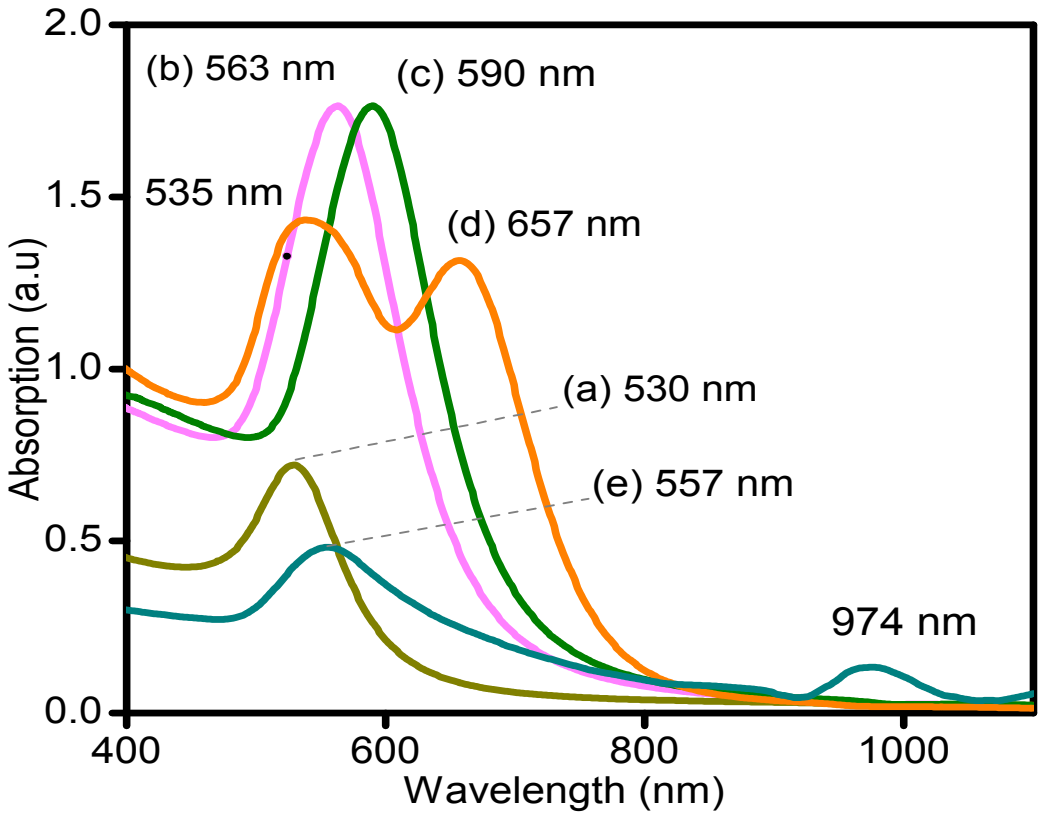

Figure 1. Optical absorption spectra of various Au nanostructures showing different surface plasmon bands: (a) SNS (size ≈ 3.5 nm), (b) MNS (size >5 nm), (c) LNS (size ≈ 9.5 nm), (d) NR (aspect ratio ≈ 2.8) and (e) ANS in methanol.

The SPR band is the most important characteristic property of AuNPs to identify its shape and size. The interaction of light with the AuNPs results in the oscillating electric field which causes the conduction-electrons to oscillate in resonance with the light's frequency coherently and develop the SPR resonance. The resonance condition is determined from absorption and scattering spectroscopy and is found to depend on the shape, size, and dielectric constants of both the metal and the surrounding material [33]. Figure 1 showed the characteristic SPR bands at 530, 563 and 590 nm for Au-SNS, and Au-MNS and Au-LNS of three different particle sizes, respectively [34-36]. The characteristic SPR bands 535 and 657 nm are seen for transverse and longitudinal absorption band of AuNR, respectively [33,34]. As the shape or size of the nanoparticle changes, the surface geometry changes that led to a shift in the electric field density on the surface. This causes a change in the oscillation frequency of the electrons, generating different cross-sections for the optical properties including absorption and scattering. Chemical aggregation of Au-MNS (563 nm) by CH_3OH

addition leads to the evolution of a red-shifted SPR band at 974 nm along with a band at 557 nm. This has been demonstrated to the formation of linear coagulation of AuNPs in polar CH_3OH which was absent on the addition of non-polar (CCl_4) solvent [31,32]. Table 2 displayed the different physical and optical properties of these various Au nanostructures.

Table 2. Physical and optical properties of various Au nanostructures.

S.No.	Various Au nanostructures	Measured SPR band	Average size (particles considered)	Expected Size	Surface area	Surface to Volume ratio
1.	SNS	530 nm	3.5 ± 0.25 nm (20)	3.5 - 37 nm (Ref. 36)	333.44 nm^2	1.95 nm^{-1}
2.	MNS	563 nm	-	80-100 nm (Ref. 34)	-	
3.	LNS	590 nm	9.5 ± 0.06 nm (10)		2058.61 nm^2	0.629 nm^{-1}
4.	PAP	-	6 - 10 mm (8)	-	-	-
5.	ANS	557 and 974 nm	10 - 20 nm (12)	-	-	-
6.	NR	535 and 657 nm	Aspect ratio: 2.8 ± 0.12 (12)	-	757.80 nm^2	0.54 nm^{-1}

Table 3. Calculation for Au wt%.

Amount of AuNPs	Amount of Au present in AuNPs	Au wt% with respect to 50 mg TiO_2
50 µl	0.0049 mg Au	0.01
100 µl	0.0098 mg Au	0.02
200 µl	0.0196 mg Au	0.04
300 µl	0.0294 mg Au	0.06
1 µl AuNPs solution = 0.098 µg Au		

2.3.2 TEM analysis

The TEM images in figure 2a reveal that the average size of the monodisperse Au-SNS is 3.5 ± 0.25 nm corresponding to SPR band 530 nm which is found to be red-shifted as compare to broad absorption band at 520 nm of Au nanospheres having size range 3.5 ± 0.7 nm [36]. It has been also reported that the Au nanospheres of size range between 3.5 and 37 nm exhibit SPR bands within 520-530 nm [36]. The evolution of such red-shifted and intense absorption peak of these small AuNPs in our study can be attributed to the improper nucleation and growth of spherical shape particles. In fact, the TEM image of figure 2a does not show perfect spherical particles that may change the resonance condition/absorption of light during interaction with electromagnetic radiation. Hence, the apparent reason for highly red shifted SPR band compared to the expected value for size < 10 nm AuNPs in water might be due to shape and/or aggregation effects of the AuNPs. Similarly, the AuNS size corresponding to SPR band 563 nm and 590 nm is expected to be about 80-100 nm as reported [36,37] elsewhere which is not obtained in our case. Although the size of Au-MNS is not determined, but the size of Au-LNS (SPR band 590 nm) is measured to be 9.5 ± 0.06 nm as shown in the TEM images of figure 2b. It seems that the particles are slightly elongated, hence the progressive red shift is observed with increasing the particle size due to their anisotropic shape. The TEM images in figure 2c revealed that Au nanorods (AuNRs) formed are in growth stage and do not show uniform size and shape. The average length, 23.6 nm and aspect ratio, 2.8 ± 0.12 of AuNR are (figure 2c) formed along with some cubical shape crystals. It is observed (figure 2d) that coagulated chain like assembly of Au-MNS (> 5 nm) is formed by CH_3OH addition. It was interpreted by the effect of strong dipole–dipole interactions of asymmetrically distributed charges on AuNPs surface in polar solvents and the existence of dipole moments can lead to the linear assembly of Au nanospheres (AuNS) [31,32]. Aggregated Au deposits (black) of size ranging 6-10 nm are seen (figure 2e) onto

Table 4. Calculation Au atom to TiO_2 ratio.

TiO_2 used	**Amount of AuNPs**	**No. of Au atoms**	**TiO_2 :Au atom**
50 mg = 3.773×10^{20} molecules	50 µl	1.497×10^{16}	25200 : 1
	100 µl	2.996×10^{16}	12500 : 1
	200 µl	5.992×10^{16}	6290 : 1
	300 µl	8.988×10^{16}	4198 : 1
1 µl AuNPs = 2.996×10^{14} Au atoms			

TiO_2 (gray) after Au (0.02 wt%, table 3) photodeposition. Figure 2f showed the AuNRs attachment to TiO_2 particles due to the electrostatic interaction between the two colloidal particles in suspension.

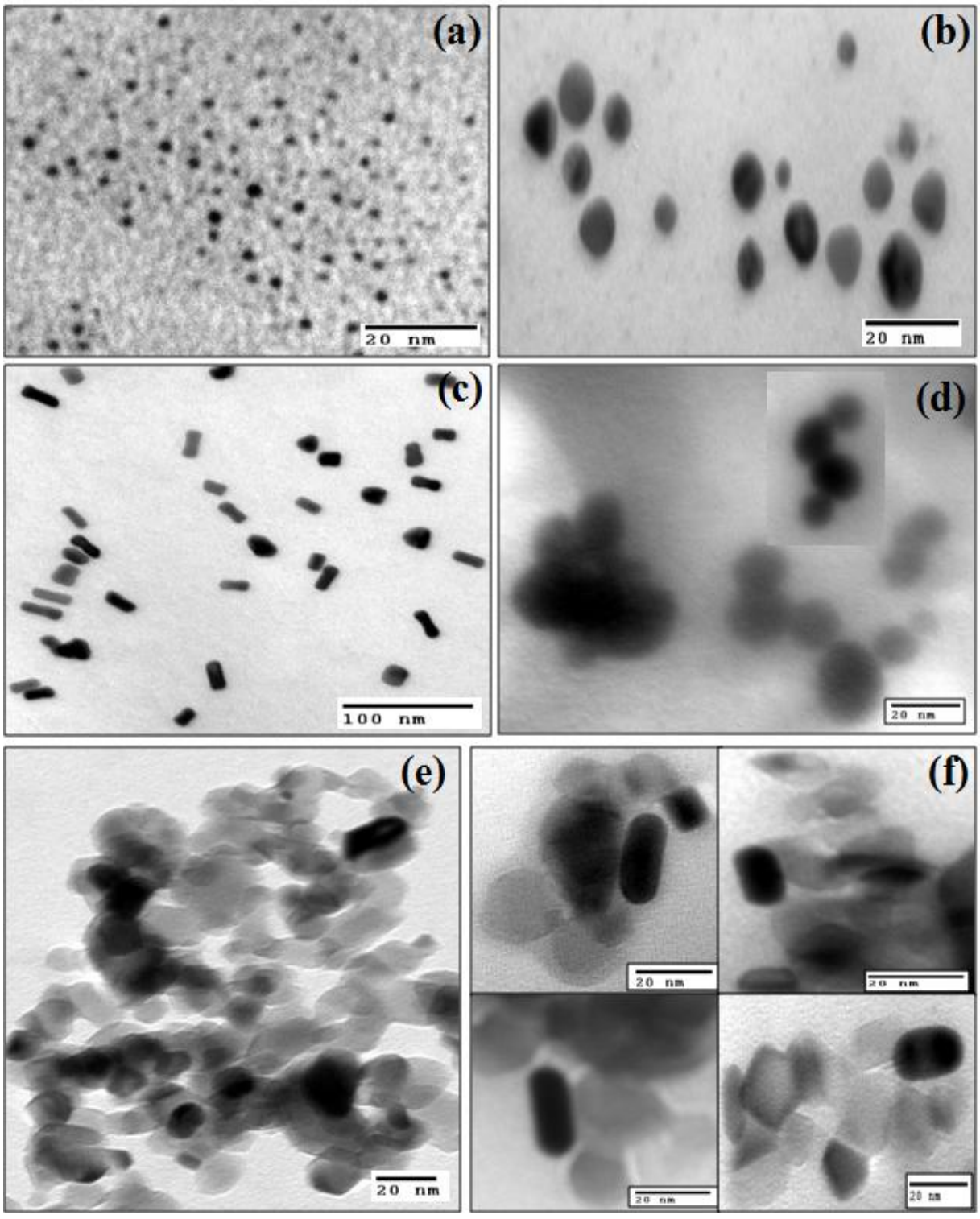

Figure 2. TEM images of (a) Au small nanospheres, SNS, (b) Au large nanospheres, LNS, (c) Au nanorod, NR, (d) coagulated chain like Au nanospheres, ANS, (e) 0.02 wt% Au photodeposited, PAP onto TiO_2 and (f) NR-TiO_2 nanoassembly.

2.3.3 Photocatalytic activity

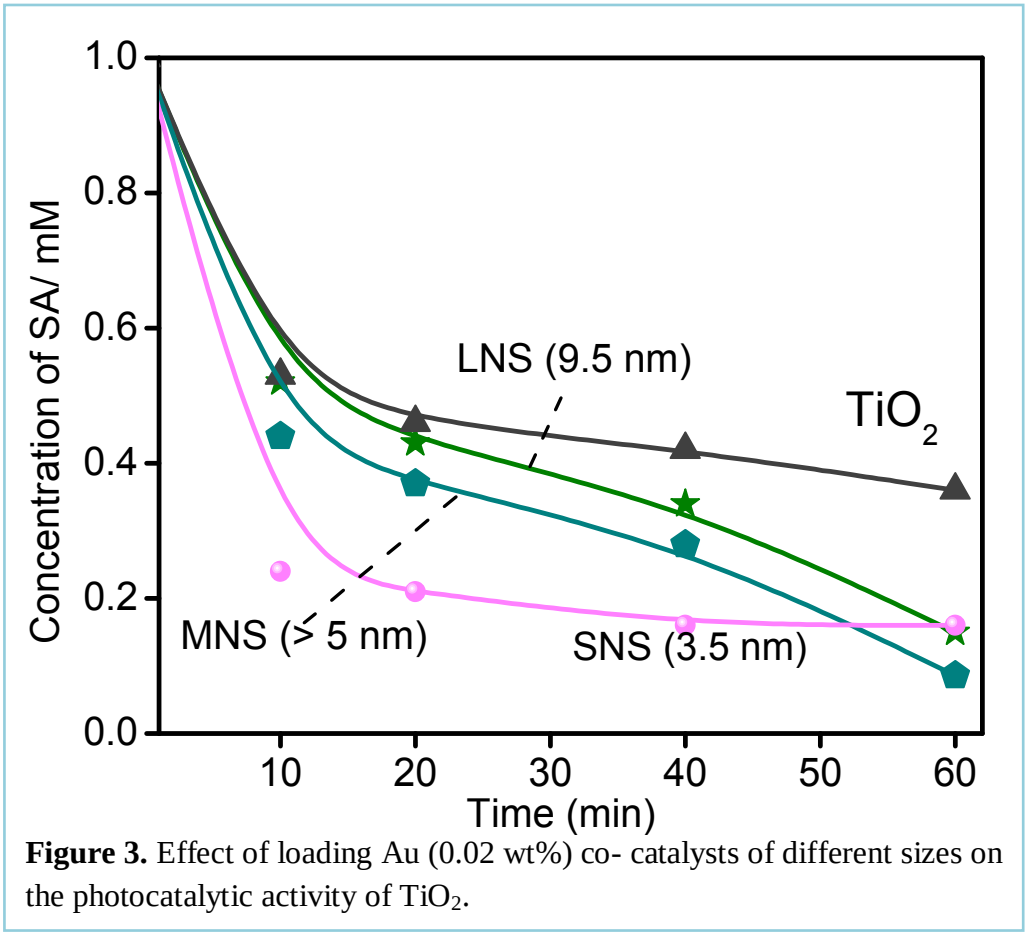

Figure 3. Effect of loading Au (0.02 wt%) co- catalysts of different sizes on the photocatalytic activity of TiO_2.

Figure 3 showed the influence of Au co-catalysts size on the PCA of TiO_2 by the addition of 100 µl =2.996 × 10^{16} atoms, (~ 0.02 wt% of TiO_2, table 3) Au-SNS, Au-MNS and LNS where ratio of TiO_2 particles to Au atoms (12,500:1, table 4) was kept same. It is observed that with decreasing size of AuNPs from 9.5 nm to > 5 nm and 3.5 nm, the SA photodegradation rate (PDR) is rapidly enhanced in comparison to bare TiO_2. During SA photodegradation, the Au-SNS exhibited highest PCA, whereas Au-MNS of size > 5 nm and Au-LNS of size ≈ 9.5 nm imparted nearly similar co-catalytic efficiency to TiO_2. Although the added AuNS and TiO_2 are not permanently connected, it is presumed that an electrostatic interaction due to intrinsic surface charge of colloidal particles may occur which facilitate the conduction of photoexcited electron from TiO_2 to AuNS and thereby, increased the PDR by valence band holes. It has been found that the measured zeta potential +50.32 mV for Au-SNS and -2.80 mV for TiO_2 aqueous solution is reduced to a value of +30.34 mV after mixing them. This fact indicates surface charge neutralization in some extent due to electrostatic interaction between the two unlike nanoparticles. Similar trend is also observed in the experimental reaction mixture of Au-SNS, TiO_2 and salicylic acid. Otherwise, the improvement of PCA

would not have been possible if the AuNPs are not in good electrical contact to TiO_2 or separated from each other by an insulating medium.

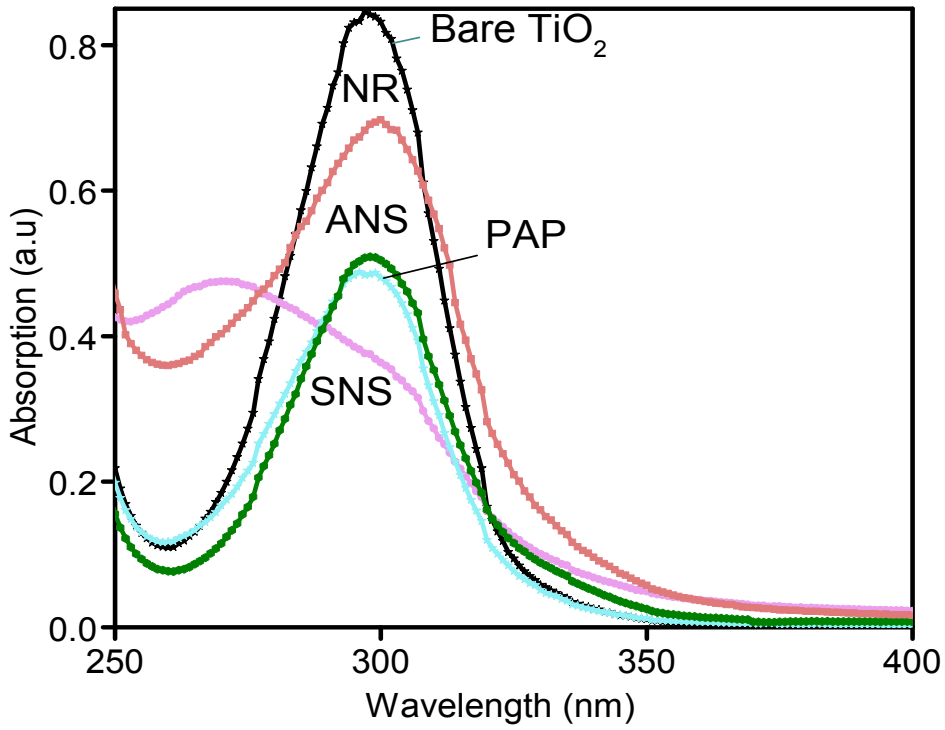

Figure 4. Changes in absorption spectra of salicylic acid (1 mM, abs: 2.78) during 1 h photodegradation by bare TiO_2 and different Au (0.02 wt%)-TiO_2 nanostructures.

Figure 4 displayed the changes of absorption intensity of SA (1 mM, absorption = 2.78 a.u) during its photooxidation by the addition of 100 µl AuNPs of different morphology to TiO_2 suspension under 1 h light irradiation. Smallest Au-SNS addition almost completely degrades SA (abs. 0.35) as compared to the lowest (abs. 0.86) photoactivity of bare TiO_2. The AuNR loading exhibited lower PCA (abs 0.69) of TiO_2 than the Au-PAP (abs. 0.47) and ANS (abs. 0.50) deposition. The effect of various attachments of Au co-catalysts onto TiO_2 for the degradation of SA for different time periods was shown in figure 5. The degradation rate was found to be higher in first 10 min because of the strong adsorption of salicylic acid due to chemisorption at the TiO_2 particle interface forming [38,39] inner-sphere titanium(IV)-salicylate surface complex. This is supported by the fact that the conductance of Au-SNS (1673 µS) and TiO_2 (57 µS) aqueous solution is highly reduced to 19 µS (experimental reaction mixture) after SA (263 µS) addition due to the complexation through negative charges of –COOH and –OH groups attachments to TiO_2 surface.

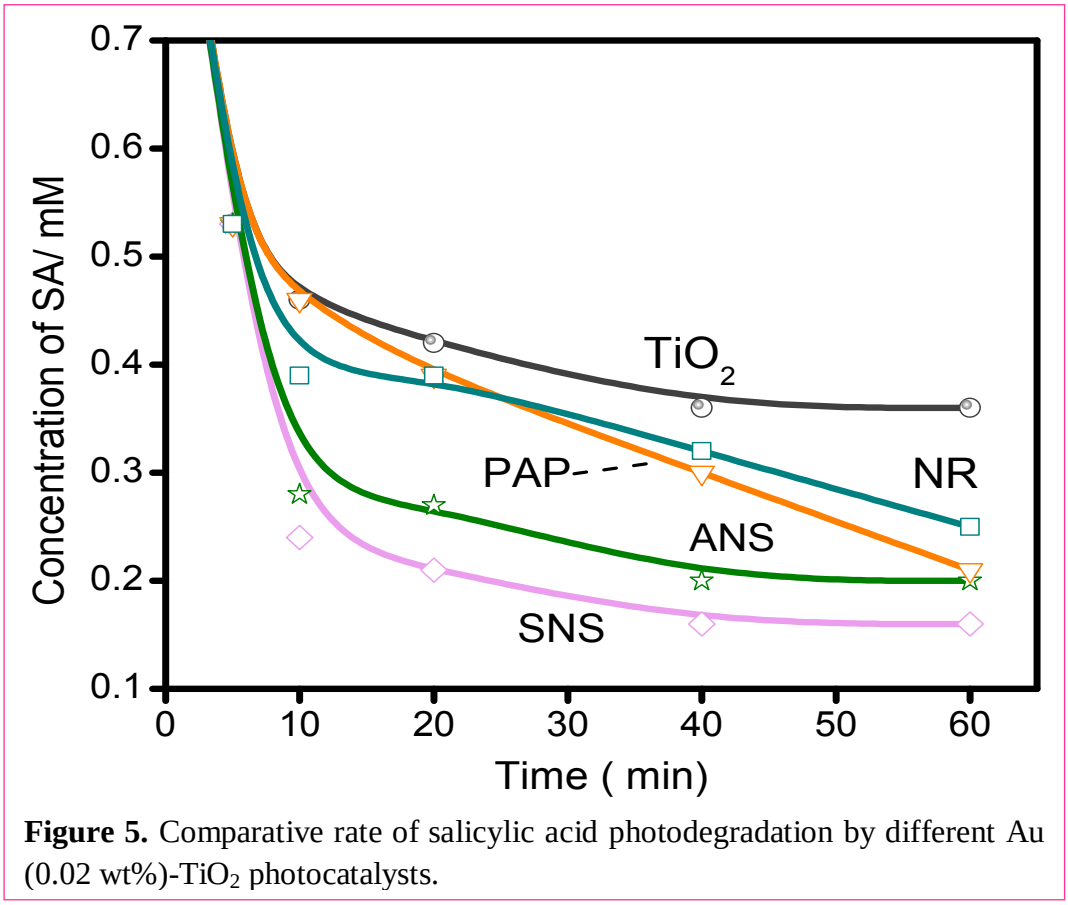

Figure 5. Comparative rate of salicylic acid photodegradation by different Au (0.02 wt%)-TiO_2 photocatalysts.

The PDR of SA is gradually improved after the loading of NR, PAP, ANS and SNS AuNPs onto TiO_2 photocatalyst. The Au-ANS and PAP displayed lower PDR in comparison to the bare quantum size Au-SNS addition. One can observe that the AuNR loaded TiO_2 significantly retarded the PDR of SA as compared to highly active Au-SNS (≈ 3.5 nm) loading. This may be due to the constraint of charge accumulation and mobility of the photoexcited electrons in AuNR for having lesser S/V ratio (0.54 nm^{-1}) than Au-SNS (1.95 nm^{-1}). There is an exponential (1^{st} order reaction, $C = C_0 e^{-kt}$) decrease in SA concentration with reaction time in all the systems which is a characteristic of first order reaction. The PDR of SA is very less after 20-60 min reactions and SA does not completely degraded even after 3 h light irradiation, indicating the photooxidation process follows the first order rate law.

Chemisorption, surface charge and thermal catalysis of various AuNPs may also influence the TiO_2 reactivity during initial hours of light irradiation. The average surface area per particles of Au-SNS, Au-LNS and AuNR are found to be 333.44, 2058.62 and 757.8 nm^2, respectively, and their co-catalytic activity does not follow the same order. However, their S/V ratio are gradually decreased as 1.95 (Au-SNS) > 0.629 (Au-LNS) > 0.54 nm^{-1} (AuNR) can reasonably explain the impartment of decreasing co-catalytic activity to TiO_2 catalyst along with the shape effect. The quantum yield of SA degradation at the maximum emission

line, 253.6 nm of Hg arc lamp has been found to improve from 0.67 % of bare TiO_2 to 0.9 % upon Au-SNS (3.5 ± 0.25 nm) loading. The photooxidation of SA due to only 253.6 nm UV exposure is verified to be insignificant as compared to photoirradiated bare TiO_2 catalyst. Hence, the fluctuation in the PCA of TiO_2 can be interpreted [21-26] due to the effect of large variation in S/V ratio and difference in percentage of surface active atoms of AuNPs of different size and shape because the amount (0.02 wt%) of Au loading is kept the same. As a result, the diverse rate of photoinduced charge transfer processes took place at the unlike nature of Au-TiO_2 nanojunctions.

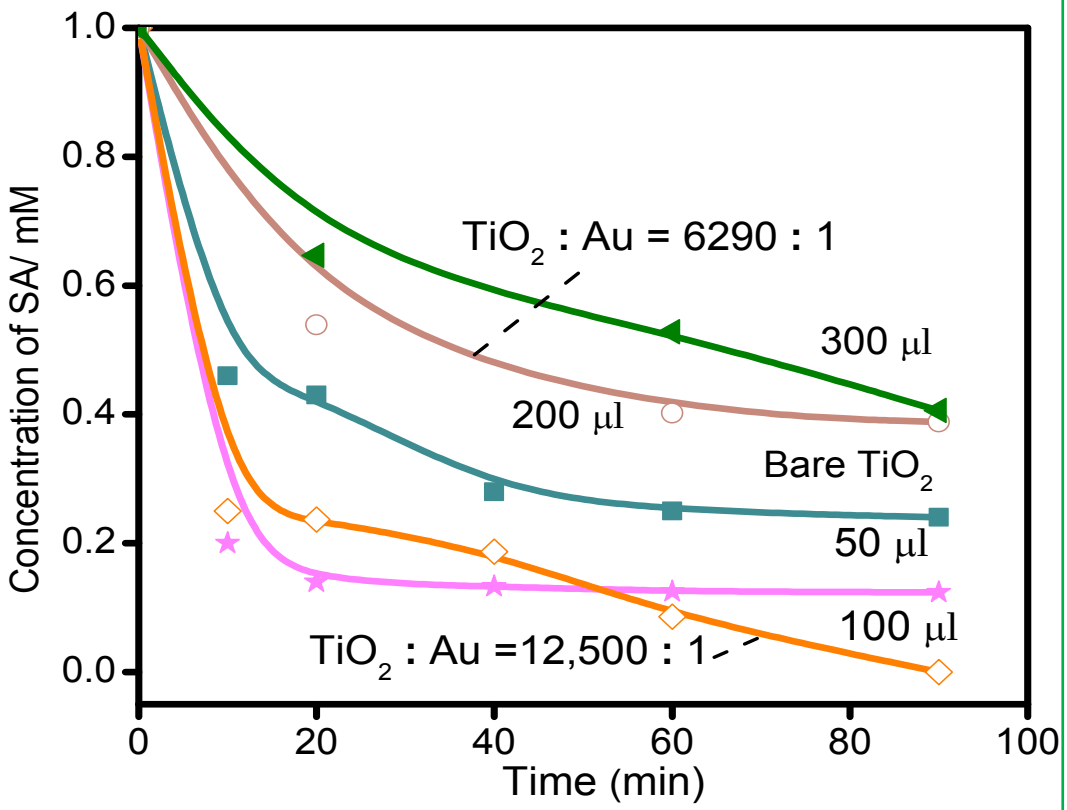

Figure 6. Effect of varying amount of Au nanosphere (SNS, size ≈ 3.5 nm) addition on the photodegradation rate of 1 mM salicylic acid by TiO_2.

In fact, because of the high electronegativity of AuNPs, the Fermi level can be shifted to more negative potentials as a function of its different size and shape [20,21]. Thereby, the equilibration of the Fermi-level between the AuNPs and TiO_2, favours electron accumulation over small Au nanocrystals, hence, the photoexcited hole could be liberally utilized for the enhanced photooxidation. This was supported [40-42] by the results of higher photocurrent, photovoltage and increasing charge separation as found in the Au-TiO_2 nanostructures. Moreover, Wood et al. [20] also proved the substantial electron accumulation on the Ag, Au, and Cu islands during metal-ZnO photocatalysed reactions. Figure 6 showed the influences of

varying amount of Au-SNS loading on PCA of TiO_2. It is observed that upto certain concentration (ca. 50-100 µl = 0.01-0.02 wt%) of AuNPs, addition, the PDR is highly increased and thereafter gradually reduced with the increasing (> 100 µl) amount of Au-SNS loading as compared to bare TiO_2 activity. Above the optimum (> 0.02 wt%) AuNPs (Au-SNS, Au-LNS, AuNR, Au-PAP, ANS), the PCA decreases because once negatively charged, AuNPs become attractive for hole, recombine with photogenerated electron in large extent [25,26]. The presence of large number of electron rich AuNPs and same concentration of photoexcited TiO_2 in the reaction mixture, the recombination rate is probably enhanced because of the increase in frequency of interaction with decreasing ratio (12,500 : 1 to 6290 : 1) of TiO_2 to Au atom. Rather than facilitating charge transport and reducing the charge recombination, the Au-SNS may act as the electron-hole recombination centre and retards the quantum efficiency. Moreover, the presence of large number of AuNPs may also slow down mass transport and reduce the PDR. Hence, the optimum amount of metal loading is always beneficial for the maximum photoactivity of TiO_2.

This chapter has considered various parameters such as size, shape, and optimum amount of AuNPs addition to TiO_2 for achieving better catalyst-co-catalysts interactions in order to tune the photocatalysis rate. It has been proven that Au-TiO_2 interface plays a significant role in the photocatalytic reactions dependent on the morphological aspects of nanoparticles which has not been attained through conventional methods.

2.4 References

[1] M. I. Litter, Appl. Catal. B: Environ., 23 (1999) 89.

[2] P.V. Kamat, J. Phys. Chem. B, 106 (2002) 7729.

[3] M. Murdoch, G.I.N. Waterhouse, M.A. Nadeem, J.B. Meston, M.A. Keane, R.F. Howe, J. Llorca and H. Idriss, Nature Chem., 3 (2011) 489.

[4] A.J. Bard and M.A. Fox, Acc. Chem. Res., 28 (1995) 141.

[5] S. Ikeda, N. Sugiyama, B. Pal, G. Marci, L. Palmisano, H. Noguchi, K. Uosaki and B. Ohtani, Phys. Chem. Chem. Phys., 3 (2001) 267.

[6] Z. Kasarevic-Popovic, D. Behar and J. Rabani, J. Phys. Chem. B, 108 (2004) 20291.

[7] P.V. Kamat, Chem. Rev., 93 (1993) 267.

[8] M. Bellardita, M. Addamo, A.D. Paola and L. Palmisano, Chem. Phys., 339 (2007) 94.

[9] X. Chen and S.S. Mao, Chem. Rev., 107 (2007) 2891.

[10] J. Li, Y. Yamada, K. Murakoshi and Y. Nakatoa, Chem. Commun., 21 (2001) 2170.

[11] P.D. Cozzoli, E. Fanizza, R. Comparelli, M.L. Curri and A. Agostiano, J. Phys. Chem. B, 108 (2004) 9623.

[12] C. Yogi, K. Kojima, T. Hashishin, N. Wada, Y. Inada, E.D. Gaspera, M. Bersani, A. Martucci, L. Liu, and T.K. Sham, J. Phys. Chem. C, 115 (2011) 6554.

[13] J. Lee and W. Choi, J. Phys. Chem. B, 109 (2005) 7399.

[14] M.C. Hidalgo, M. Maicu, J.A. Navio and G. Colon, Catal. Today, 129 (2007) 43.

[15] M. Haruta, Catal. Today, 36 (1997) 153.

[16] J.D. Grunwaldt, C. Kiener, C. Wogerbauer and A. Baiker, J. Catal., 181 (1999) 223.

[17] S. Eustis and M.A. El-Sayed, Chem. Soc. Rev., 35 (2006) 209.

[18] M. Haruta, Chem. Rec., 3 (2003) 75.

[19] A. Schatz, O. Reiser and W.J. Stark, Chem. Eur. J., 16 (2010) 8950.

[20] A. Wood, M. Giersig and P. Mulvaney, J. Phys. Chem. B, 105 (2001) 8810.

[21] V. Subramanian, E.E. Wolf and P.V. Kamat, J. Am. Chem. Soc., 126 (2004) 4943.

[22] J. Zeng, Q. Zhang, J. Chen and Y. Xia, Nano Lett., 10 (2010) 30.

[23] R. Narayanan and M.A. El-Sayed, Nano Lett., 4 (2004) 1343.

[24] C. Burda, X. Chen, R. Narayanan and M.A. El-Sayed, Chem. Rev., 105 (2005) 1025.

[25] M. Mrowetz, A. Villa, L. Prati and E. Elena Selli, Gold Bull., 40 (2007) 154.

[26] R. Narayanan and M.A. El-Sayed, J. Phys. Chem. B, 109 (2005) 12663.

[27] N.S. Patil, B.S. Uphade, P. Jana, R.S. Sonawane, S.K. Bhargava, and V.R. Choudhary, Catal. Lett., 94 (2004) 89.

[28] J. Kimling, M. Maier, B. Okenve, V. Kotaidis, H. Ballot, and A. Plech, J. Phys. Chem. B, 110 (2006) 15700.

[29] B. Nikoobakht and M.A. El-Sayed, Chem. Mater., 15 (2003) 1957.

[30] X. Huang, S. Neretina and M.A. El-Sayed, Adv. Mater., 21 (2009) 4880.

[31] J. Liao, Y. Zhang, W. Yu, L. Xu, C. Ge, J. Liu and N. Gu, Colloids Surface A, 223 (2003) 177.

[32] J.H. Liao, K.J. Chen, L.N. Xu, C.W. Ge, J. Wang, L. Huang and N. Gu, Appl. Phys. A, 76 (2003) 541.

[33] K. Lance Kelly, E. Coronado, L.L. Zhao and G.C. Schatz, J. Phys. Chem. B, 107 (2003) 668.

[34] L.M. Liz-Marzan, Langmuir, 22 (2006) 32.

[35] W. Ni, X. Kou, Z. Yang and J. Wang, ACS NANO, 2 (2008) 677.

[36] N.R. Jana, L. Gearheart and C.J. Murphy, Langmuir, 17 (2001) 6782.

[37] W. Haiss, N.T.K. Thanh, J. Aveyard and D.G. Fernig, Anal. Chem., 79 (2007) 4215.

[38] A.E. Regazzoni, P. Mandelbaum, M. Matsuyoshi, S. Schiller, S.A. Bilmes and M.A. Blesa, Langmuir, 14 (1998) 868.

[39] J.A. Anderson, Catal Today, 175 (2011) 316.

[40] Y. Nakato, K. Ueda, H. Yano and H. Tsubomura, J. Phys. Chem,. 92 (1988) 2316.

[41] V. Subramanian, E. Wolf and P.V. Kamat, J. Phys. Chem. B, 105 (2001) 11439.

[42] T. Bora, H.H. Kyaw, S. Sarkar, S.K. Pal and J. Dutta, Beilstein J. Nanotechnol., 2 (2011) 681.

Chapter 3

Co-catalytic and Electro-kinetic Properties of Au Nanospheres Dispersed in Solvents of Varying Dipole Moments

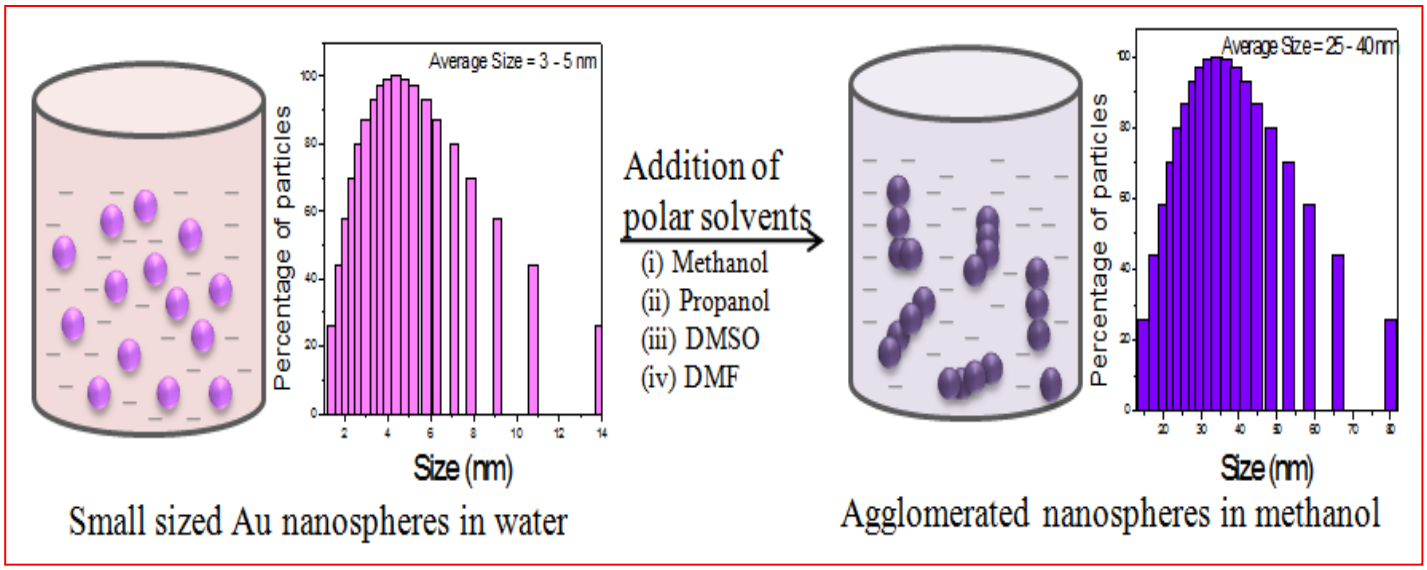

3.1 Introduction

Coinage metal (Au, Ag and Cu) nanostructures of different shapes e.g., spheres [1-3], cubes [4], boxes, pyramids [5], plates [6], decahedrons, rods [7], bars [8], cages [9] and wires [10] are found to exhibit tunable optical, electronic and catalytic properties [11-14]. Because of very small size (1-50 nm) and different geometrical shapes, a large fraction of atoms reside on the surface, hence, they exert strong affinity towards adsorption of reacting substrates and absorption of electromagnetic radiation which in-turn shows characteristic plasmon resonance band [15-17]. Haruta and co-workers [18,19] demonstrated for the first time that metal oxide-supported Au catalysts of size 2-5 nm showed unusually high catalytic activities as compared to the bulk. After that extensive research is carried out about the size and shape dependent optoelectronic and catalytic properties of Au nanoparticles (AuNPs) for various applications [20-22]. Luis M. Liz-Marzan [17] studied the influence of particle size, shape, the presence of a capping shell and the dielectric properties of the surrounding medium on the optical properties of metal nanoparticles (NPs). However, these small AuNPs are extremely unstable and tend to agglomerate owing to high surface charge and hence, it becomes difficult to measure the precise absorption and catalytic properties of these small size particles. Therefore, many surface capping agents such as glutathiol, cyclodextrins, polymers, xanthates, thioethers, disulfides, alkyl thiols, mercapto silane and amino acids etc. have been used to stabilize AuNPs [23-25]. However, due to presence of capping agent over AuNPs surface, the catalytic activity, optoelectronic and other physicochemical properties are masked or blocked to a certain extent. As a result, the functionality of AuNPs is also affected by various electrokinetic parameters such as; surface charge, zeta potential, conductivity, pH, dipole moment and ionic strength of the dispersion medium.

The potential difference between the dispersion medium and the stationery layer of the fluid attached to the dispersed particle is known as zeta potential (ζ) [26,27] responsible for the stability of colloidal system. It arises due to preferential adsorption of either positive or negative charge ions on the NP surface from the surrounding medium [28-30]. Kim et al. [27] observed that the ζ ca. -52.72 mV of Au nanospheres in water was reduced to -41.38 mV by capping with benzyl mercaptan due to close interparticle interaction between them. This high ζ of AuNPs in water arises due to symmetric distribution of like charges that makes a stable Au colloid suspension due repulsive interaction among them. The reduction in ζ from $+47.6 \pm 3.3$ mV to

+10.9 ± 4.1 mV during addition of 10^{-5} M adipic acid in Au nanorod aqueous suspension occurs because of the electrostatic interactions between the positively charged nanorods and negatively charged adipic acid [31]. Liao et al. [32] observed the chain like aggregation of Au nanospheres (AuNS) on changing the surrounding water medium to ethanol and found that dipole-dipole interaction and asymmetric distribution of the charges were responsible for such linear aggregation of AuNPs.

The efficiency of such AuNPs co-catalysts as a function of its degree of agglomeration in polar solvents can be studied and compared for the Au-TiO_2 photocatalysis. Goodman and co-workers [33] have demonstrated the influence of AuNPs deposition on the catalytic activity of TiO_2 catalyst. The size dependent co-catalytic activity of AuNPs in TiO_2 photocatalysis for the improved photoactivity is also reported [34,35]. Therefore, it is useful to study the colloidal stability, surface charge of Au co-catalyst and their degree of aggregation can be attuned by the nature and polarity of solvents used for their synthesis. *In this context, we investigated the zeta potential, surface charge, pH and conductance of small AuNS dispersed in water, methanol, propanol, dimethlyformamide, and dimethyl-sulfoxide and carbon tetrachloride and studied their influence on the relative optical absorption and co-catalytic activity (CCA) for the oxidative degradation of salicylic acid (SA) as a test reaction because SA is strongly adsorbed and formed surface complex over TiO_2 surface.*

3.2 Experimental section

3.2.1 Chemicals and materials

Chloroauric acid ($HAuCl_4.3H_2O$), sodium borohydride ($NaBH_4$), ascorbic acid ($C_6H_8O_6$), methanol (MeOH), propanol (PrOH), dimethylsulphoxide (DMSO), dimethlyformamide (DMF), carbon tetrachloride (CCl_4) and salicylic acid (SA) were obtained from Loba chemie, India. Commercially available P25-TiO_2 is a gift sample from P-25 Degussa, Germany. Silver nitrate ($AgNO_3$), cetyltrimethylammoniumbromide (CTAB) was purchased from Fischer Scientific and Sigma Aldrich, respectively. All the chemicals were used as-received without any further purification. Deionized water was obtained using an ultrafiltration system (Milli-*Q*, Millipore) with a measured conductivity above 35 mho cm^{-1} at 25 $^{\circ}$C.

3.2.2 Preparation of Au nanospheres

The AuNS were synthesized by seed-mediated approach in aqueous media as reported [2,3]. It comprised the addition of 250 μl (0.01 M) $HAuCl_4$ to 9.5 ml (0.1 M) CTAB, followed by

reduction with 600 µl (0.01 M) $NaBH_4$ solution under magnetic stirring for 2 min and resulted in the formation of gold seeds. This seed solution (ca. 12 µl) was introduced in the mixture of 500 µl (0.01 M) $HAuCl_4$, 9.5 ml (0.1 M) CTAB and 55 µl ascorbic acid (0.1 M) at 0°C. The pink coloured solution showing surface plasmon band at 520 nm indicates the formation of spherical AuNPs. The AuNPs were washed with deionized water under centrifugation at 8500 rpm for 10 min.

3.2.3 Dispersion of Au nanospheres in various solvents

As synthesized AuNS was dispersed in MeOH, PrOH, DMF, DMSO and CCl_4 to examine their optical and co-catalytic behavior. For surface plasmon absorption analysis, 1.5 ml aqueous suspension of AuNS (4.494×10^{17} atoms) was added to 1.5 ml above polar or non-polar (CCl_4) solvent and also measured their pH. The sharp change in colour of AuNS (pink to light purple or blue) has been noticed within few seconds after addition of polar solvents due to the aggregation of AuNS. The AuNS after agglomeration (ANS) in various dispersion solvents (ANS-solvents) are abbreviated as ANS-MeOH, ANS-PrOH, ANS-DMF ANS-DMSO and non-aggregated AuNS in water and carbon tetrachloride are referred as AuNS-water, AuNS-CCl_4, respectively, for further discussion throughout the chapter.

3.2.4 Co-catalytic activity of Au nanospheres for Au-TiO_2 photocatalysis

The calculated amount (100 µl = 2.996×10^{16} atoms) of AuNS were added to various polar or a non-polar solvent (100 µl) which were then centrifuged, vacuum dried and finally dispersed in 100 µl of water. These AuNS-water and ANS-solvents were added into a mixture of TiO_2 and SA aqueous suspension to evaluate their co-catalytic efficiency for the photocatalytic oxidation of SA. The photocatalytic reaction was carried out by taking 5 ml SA (1 mM), 50 mg TiO_2 and calculated amount (10-100 µl) of AuNS (polar solvents dispersion) under UV irradiation (125 W Hg-arc lamp, λ_{max} = 253.6 nm and 10.4 mW/cm^2) and magnetic stirring for different time periods. The commercially available P25-TiO_2 (size 30-50 nm, surface area ~50m^2/g, 70% anatase and 30% rutile phase) is used in photocatalytic experiment. The concentration of SA was measured with UV-spectrophotometer at λ_{max} = 298 nm.

3.2.5 Structural and electrokinetic properties analysis

The size and shape of AuNS was analysed by TEM (Hitachi 7500, 2Å, 120 KV). Zeta potential and dynamic light scattering (DLS) particle size distribution analysis was carried out by means of Brookhaven 7610 instrument and sample was prepared by adding 1.5 ml polar or non polar

solvent (MeOH/ PrOH/ DMF/ DMSO/ CCl_4) to vacuum dried AuNS (1.5 ml, 4.494×10^{17} atoms). Zeta potential measurement of the photocatalytic reaction mixture (1 mM, 5 ml SA + 50 mg TiO_2) with or without AuNS (100 µl) addition was carried out by taking 200 µl of reaction mixture into a 1.3 ml of water. Surface charge density (Mutek-PCD03pH) analysis was carried out using 300 ml aqueous suspension of AuNS containing 1.66×10^{15} atoms/ml. Similarly, reaction mixture (1 mM, 5 ml SA + 50 mg TiO_2) with and without AuNS in 300 ml aqueous slurry has been used for the surface charge measurement. Different physicochemical, optical and electrokinetic parameters of Au nanostructures are summarized in Table 1.

3.3 Results and discussion

3.3.1 Optical properties of Au nanostructures

Figure 1a showed the surface plasmon resonance (SPR) absorption band of AuNS of size ~ 3-6 nm dispersed in polar solvents of dipole moments (DP) as 1.85D for water, 1.70D for MeOH, 1.66D for PrOH, 3.82D for DMF, and 3.96D for DMSO etc. The AuNS-water exhibits a sharp and narrow SPR band at 520 nm having particle size in the range of $\approx 3.5 \pm 0.25$ nm as reported by N. R. Jana et al [2,3]. After addition of 1.5 ml of different polar solvents to 1.5 ml AuNS (4.494×10^{17} Au atoms) in water, a red shift in the SPR band from 520 nm to 540-557 nm is observed. The intensity of these SPR absorption band is decreased and becomes flatten with the appearance of SPR band at 970-984 nm of varied absorption intensity is always noticed in all polar solvents. However, there is no such red shifted new SPR band (> 970 nm) appears for AuNS-CCl_4 dispersion in comparison to AuNS-water as seen in the inset figure 1a.

The AuNS dispersion in DMF, DMSO and PrOH almost completely suppress the absorption intensity of SPR band at 520 nm and the spectra are nearly levels-off. This difference in the absorption spectral intensity is ascribed to the nature of solvent and their polarity difference. DMF and DMSO being polar aprotic solvents showed a little absorption as compared to polar protic solvents MeOH and PrOH which displayed higher absorption intensity of AuNS SPR band. The SPR band at > 970 nm gradually red-shifted from 971 to 984 nm (figure 1b) and its absorption intensity is generally decreased with the increasing solvent polarity/ or DP as 1.70D (MeOH) ≈ 1.66D (PrOH), 3.82D (DMF), and 3.96D (DMSO) however, no such red shifted band is seen in water dispersion as shown in the enlarged view (900-1100 nm scale) of figure 1b. Furthermore, changes in the refractive index (RI) of AuNS (ca. 500 µl) has also been measured (Atago refractometer) in order to verify the extent of AuNS aggregation on varying the amount

(100-500 µl) of MeOH, PrOH and DMF addition, and a linear increase in the RI has been observed (figure 2). The RI of the AuNS (500 µl) ≈ 1.3349 enhanced to 1.3457, 1.3753 and 1.3901 on the addition of 500 µl of MeOH, PrOH and DMF, whose individual RI is 1.3354, 1.3374 and 1.4248, respectively. Such influence of solvent RI on the position of SPR band was also observed by Lee and co-workers [36]. They found change in the position of SPR band toward longer wavelength after introducing the Ag nanoparticles on substrates with high refractive indexes. Templeton et al. [37] showed the effect of solvent RI on the SPR band of alkanethiolate monolayer-protected gold clusters (size = 5.2 nm)

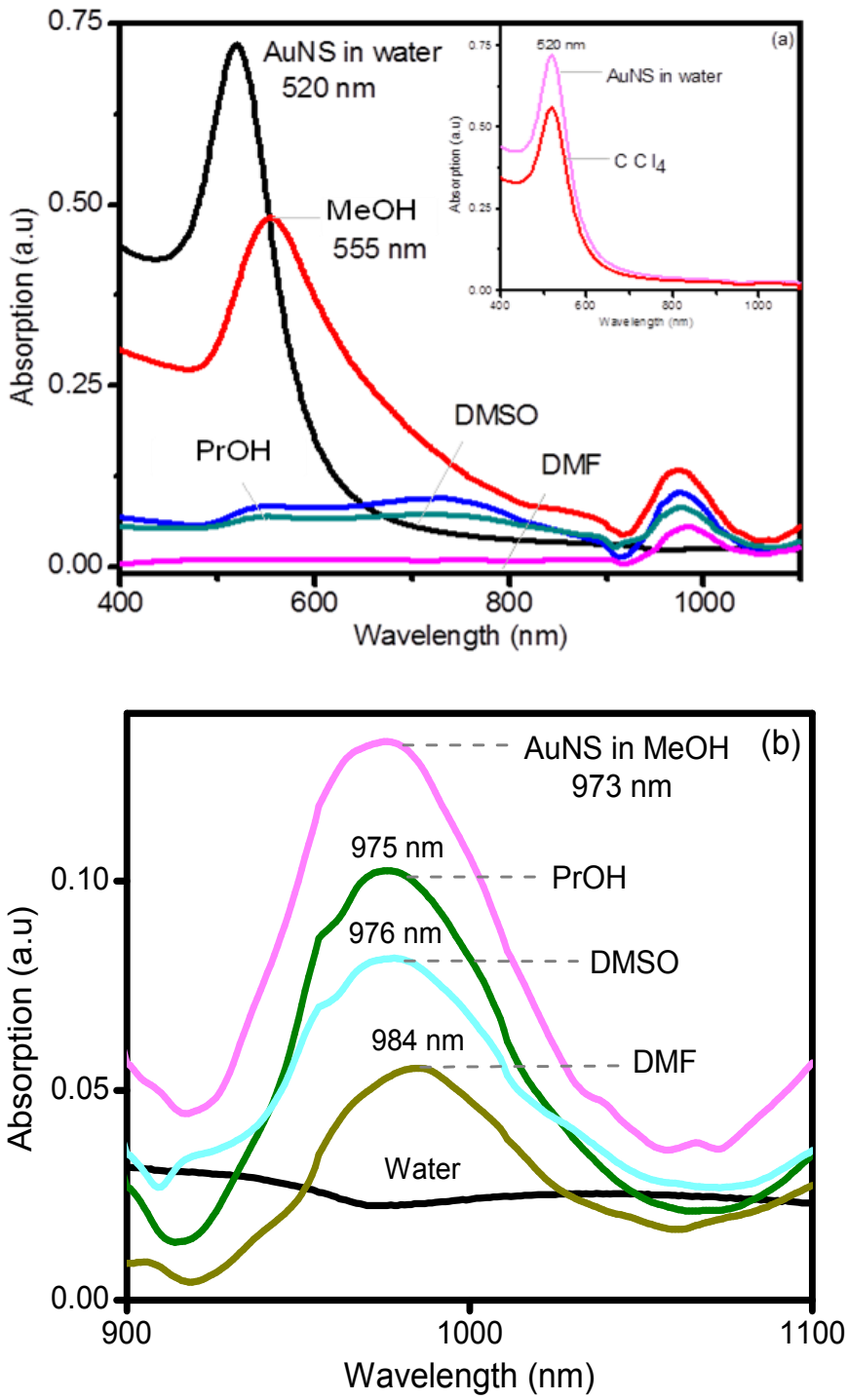

Figure 1. Influence of surface plasmon band of Au nanospheres (size = 3.5 nm) dispersed in (a) water, MeOH, PrOH, DMSO, DMF and CCl_4 solvent (inset), and (b) enlarged view (900 to 1100 nm) shows the formation of new surface plasmon absorption band of Au nanospheres in different polar solvents.

and revealed 8 nm red shift as the solvent RI was varied from 1.33 to 1.55 by transferring AuNPs into appropriate solvents e.g., hexane, tetrahydrofuran, benzene etc.

Thus, the cause for this red shifting, flattening (at 520 nm) and evolution of SPR band (at > 970 nm) is the polarity/ DP and RI of individual solvent. These optical changes, i.e., increase in the plasmon linewidth are due to change in the particle size distribution or orientation and surface morphology of AuNS that causes light scattering and plasmon oscillation in different manner [11]. J. Liao et al. also observed the second absorption band at the longer wavelength > 970 of the spectrum after the addition of ethanol to AuNS and interpreted the results on the basis of Mie Scattering theory [32]. According to this theory, this new SPR band at the longer wavelength is associated with the longitudinal mode of the electronic plasma oscillation along the long axis of the agglomerated Au nanospheres chain [38].

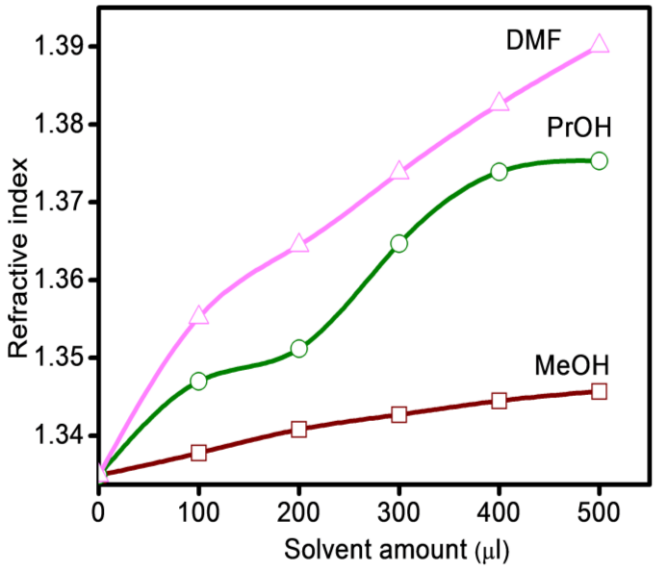

Figure 2. Changes in the refractive index of AuNS on adding varying amount (100-500 µl) of various polar solvents.

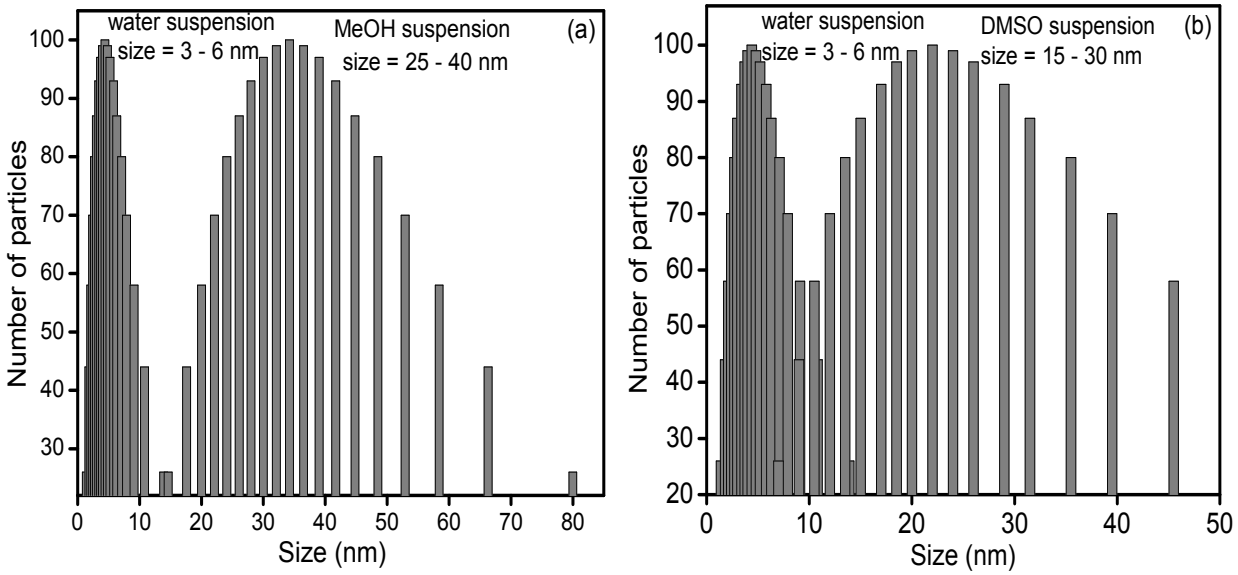

Figure 3. DLS particle size distribution of Au nanospheres dispersion in (a) water and methanol and (b) water and DMSO.

Whereas, the non aggregation of AuNS in water and CCl_4 was interpreted by the dipole–dipole interactions among the symmetrically distributed charges that cause repulsion amongst AuNPs. The charge equilibrium between the particles has not been disturbed on the addition of non-polar CCl_4 having zero DP and no charged entity. However, addition of polar solvents disturbed or reverse the charge equilibrium between the species carrying alike charge and results in the attraction between NPs, hence, responsible for their aggregation. In order to confirm this phenomenon of AuNPs agglomeration in polar solvents, dynamic light scattering (DLS) of AuNS dispersed in water, methanol and DMSO was analyzed. The average size ca. 3-6 nm distribution of AuNS in water was found to significantly increase to 25-40 nm in MeOH suspension and 15-30 nm in DMSO dispersion as shown in figure 3. This fact indicates that the coagulation of AuNS particles took place on changing the dispersion media from water to polar MeOH (figure 3a) and DMSO (figure 3b) solvents as a function of their polarity. Therefore, the evolution of new SPR band (at > 970 nm) can be ascribed to the agglomeration of AuNS in polar solvents which does not occur in non-polar CCl_4 dispersion.

3.3.2 Structural morphology of Au nanostructures

The surface morphology of AuNS dispersed in water, DMSO, and MeOH was verified by TEM size and shape analysis as shown in figure 4 and 5. The AuNS-water has been found to be monodispersed with average size 3.5 ± 0.25 nm (figure 4a). On addition of 1.5 ml DMSO to 1.5 ml of AuNS in water, the growth in the size of AuNS begins and finally agglomeration took place in different extent. They begin to link together (marked area in figure 4) or merged into one another to grow into bigger nanoparticles assembly that resembles chain like aggregation as seen in figure 4b and 4c. It seems that inter-particle distance between the AuNS is decreased in DMSO dispersion and nanospheres fused to large clusters consisting of many AuNS particles as noticed in figure 4d. Similar behavior of AuNS coagulation has also been observed on the addition of MeOH as revealed by the TEM images of figure 5. Individual ANS-MeOH dispersion is seen to be relatively bigger in size (figure 5a-d) than AuNS-water dispersion (figure 4a). Figure 5b and d displayed aggregated clusters formed by many AuNS and a few chain like arrangements consisting of 3 to 5 AuNS. The average AuNS particle size increases to a large extent from ~ 3.5 nm (in water) to ~ 25 nm (in DMSO) and ~ 35 nm (MeOH) that is also in accordance with the DLS particle size distribution in figure 3 discussed above. On account of the negative ions adsorbed on the AuNS particle surface, linear coagulation is most probably caused

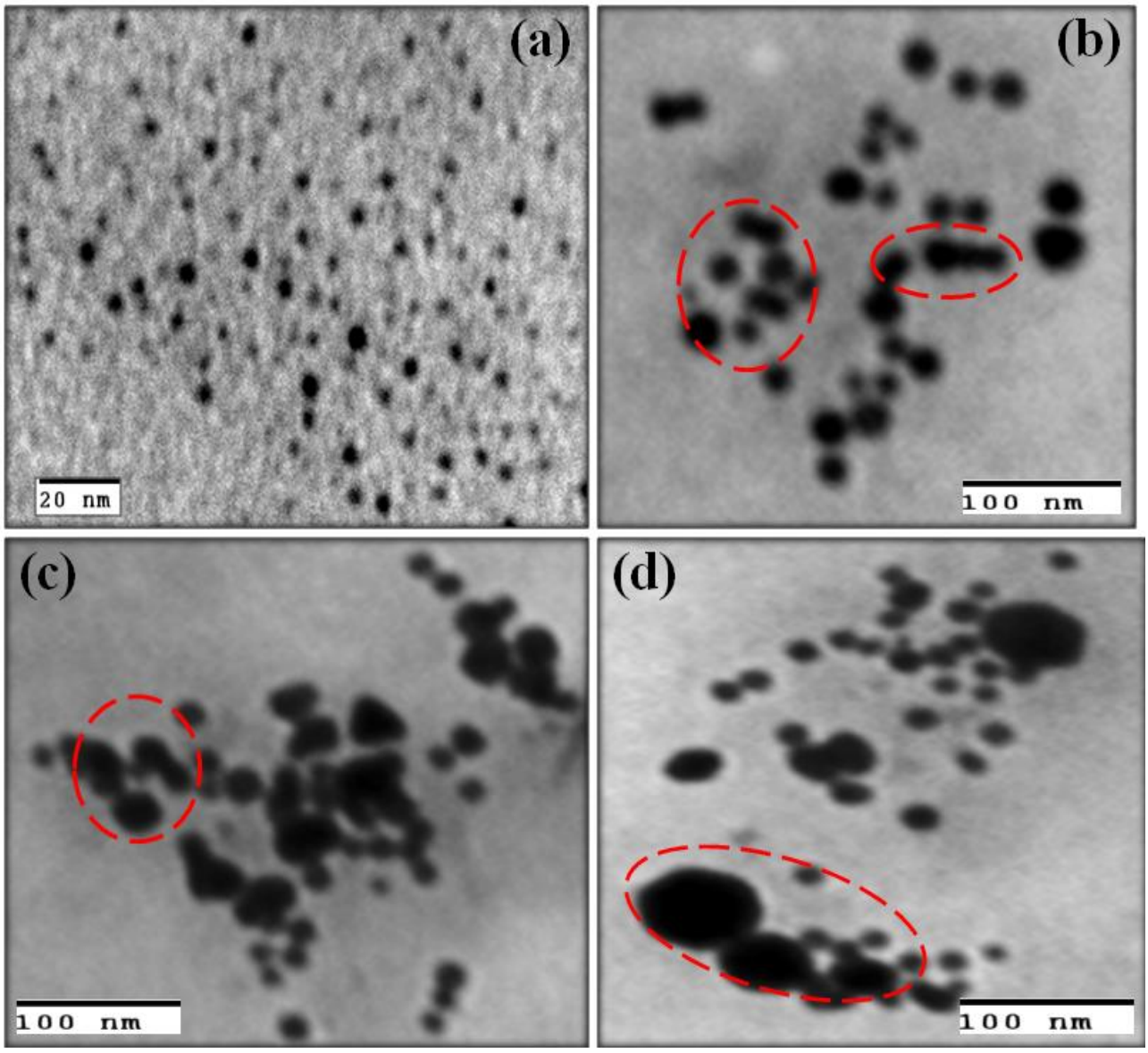

Figure 4. TEM images of (a) bare Au nanospheres in water (b) marked area representing the chain like aggregation of Au nanospheres in DMSO and (c) and (d) forming large size aggregates in DMSO.

by the effect of dipole–dipole interactions due to the asymmetrically distributed charges on the particle surface. When the dipole–dipole interaction is strong enough to overcome the thermal energy and the electrostatic repulsion between the colloidal particles, the existence of dipole moments can lead to linear assembly [32].

3.3.3 Electrokinetic properties of Au nanospheres in different polar solvents

The zeta potential is a key parameter governing the electrokinetic behavior of particles in colloidal solution due to the effective surface potential that arises close to the solid-liquid interface i.e., between the nanoparticle surface and surrounding medium.

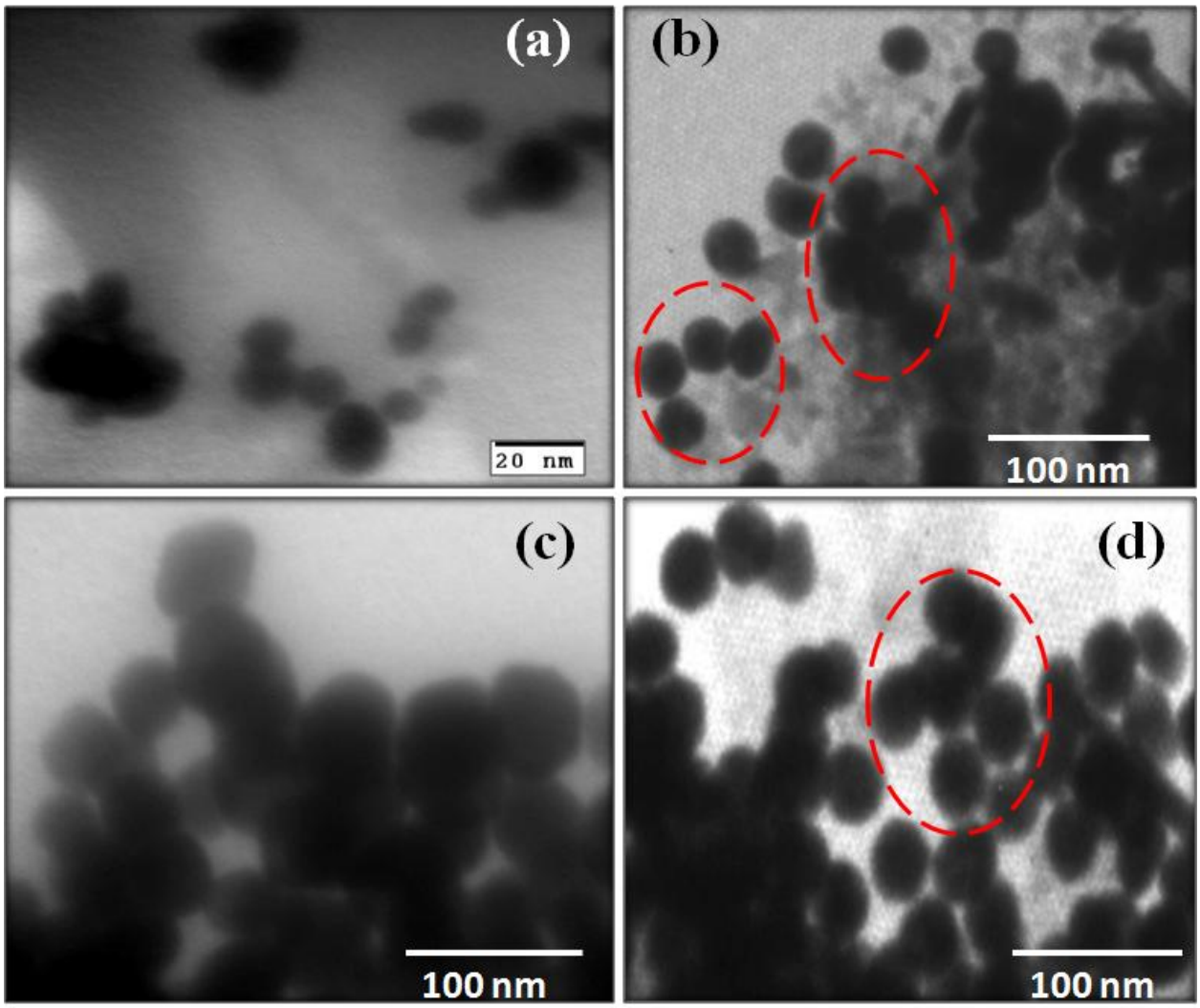

Figure 5. TEM images of various aggregated Au nanospheres (a-d) formed in methanol dispersion.

A double layer is formed at the interface of the particle; the first layer (the Stern-layer) contains immobilized ions which are directly adsorbed to the surface. This layer is surrounded by a second more diffuse layer of mobile ions attracted by the surface charge. The potential difference between the surface of tightly bound layer developed at the surface of the colloidal particle due to the adsorption of ions and the electroneutral region of the solution is known as zeta potential (ζ). The variation in the values of ζ determines the electrostatic repulsion or attraction between the AuNS particles due to the change in the electronic charge of surrounding media with polar

solvents of different DP. As a result, the surface charge of AuNS is varied that prevents or promotes particle attraction and adhesion as a function of the polarity of the dispersion medium. Literature values for the ζ of citrate coated gold nanoparticles are in the range of -29 to -50 mV

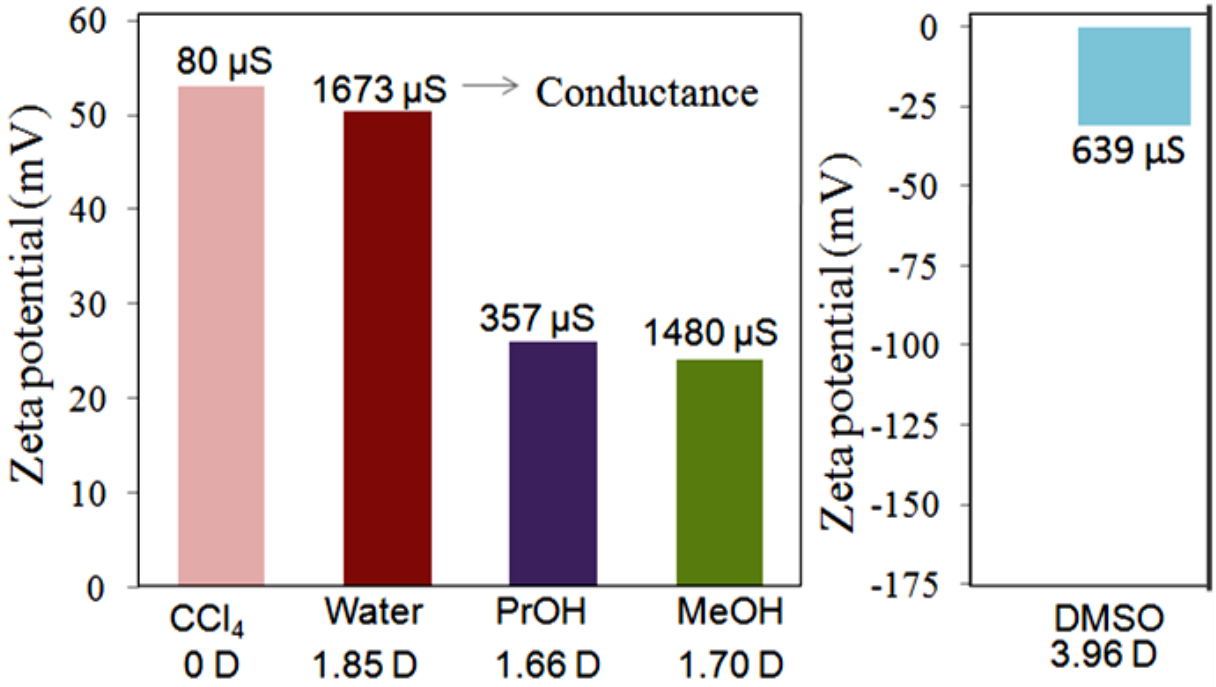

Figure 6. Variation in zeta potential and conductance (over the bar) of Au nanospheres dispersion in polar solvents of different dipole moment (below).

indicating the electrostatic stabilization of the particles [27]. Sau et al. [39] measured ζ values for CTAB-coated gold nanocrystals in the range +49 mV to +71 mV, depending on nanoparticle shape and size.

Figure 6 shows the variation of ζ and conductance of AuNS suspensions in polar and non polar (CCl_4) solvents as a function of their dipole moments. The measured ζ value ca. +50 mV at pH = 6.4 for AuNS in water is found to reduce to +24.06 mV (at pH = 7.62) in MeOH, +26.01 mV (at pH = 7.54) in PrOH and -31.88 mV (at pH = 7.84) in DMSO dispersion, respectively. It is very important to know that AuNS in non-polar CCl_4 dispersion, the ζ value +53 mV is measured to be almost same (+50 mV) as water suspension. As CCl_4 having zero DP does not carry any charge and hence, there is no influence of electric potential difference on the AuNS particle surface. It is evident that AuNS in solvents of varying polarity (DP = 1.46 D to 3.96 D), neutralization of surface charge in some extent causes the reduction in the inter-particle repulsion between the particles of like charge. As a result, the colloidal particles come closer to one

another, coalesces to form bigger aggregates and thus, the stability of the AuNS colloidal suspension is decreased. It had been reported by Martin Moskovits and co-workers [40] that the metal nanoparticles are highly stabilized in aqueous solution because of the presence of double layer charge surrounding each nanoparticle that produces a coulomb barrier to prevent aggregation and stabilize the colloid suspension.

In order to confirm this fact of electronic charge disparity on the surface of AuNS particle, the conductance of each AuNS suspension in various solvents is measured. The conductance of solution is dependent upon the concentration and mobility of the charged ions/species present in solution. The conductance 1673 µS of AuNS-water is determined to be highest that decreases with the ionic dipoles of solvents having different polarity/ DP. Whereas in non-polar CCl_4 dispersion, the conductance of AuNS is reduced to 80 µS indicating absence of any dipolar ionic charge on CCl_4 as compared to highly polar water molecules. Moreover, increase in carbon chain length/ or bigger dipole having hetero atom also can act as barrier for the conductance of ions leading to a gradual decrease in conductance value (figure 6) of ANS-MeOH (1480 µS), ANS-DMSO (639 µS), and ANS-PrOH (357 µS), etc.

3.3.4 Electro-kinetic properties of photocatalytic reaction mixture

The synthesized AuNS in water suspension and its aggregated morphology formed in various

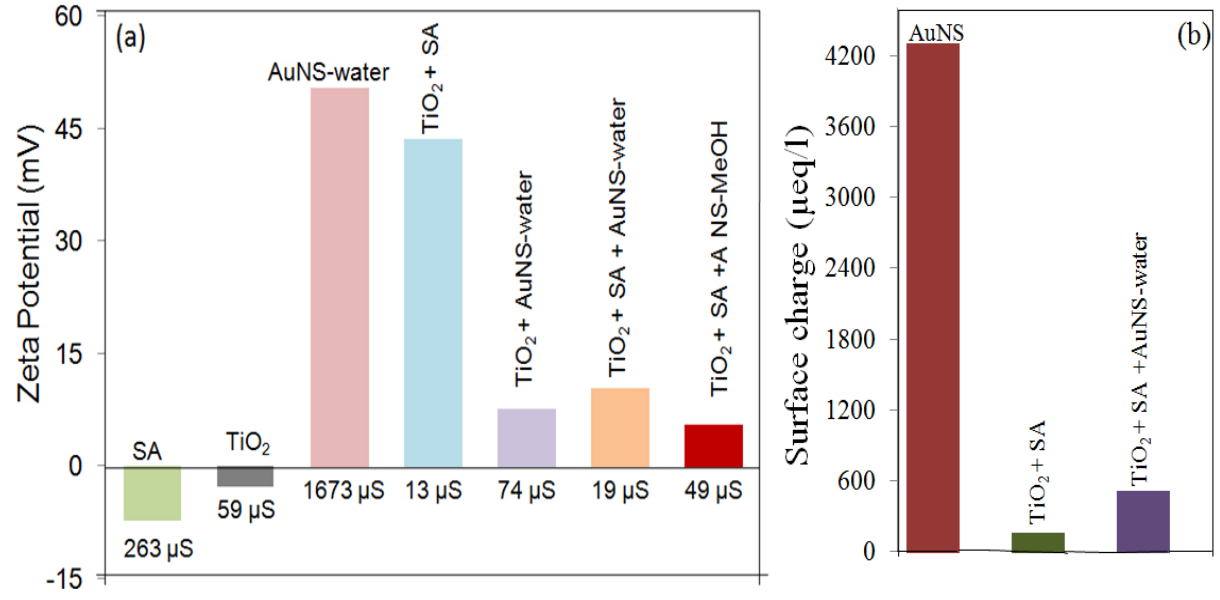

Figure 7. (a) Variation in zeta potential and conductance (mentioned below) and (b) surface charge of different reaction mixtures TiO_2, SA and AuNS etc.

polar solvents (ANS-solvents) are utilized to study the relative co-catalytic activity imparting to

Au-TiO_2 photocatalysis for salicylic acid oxidation. The photocatalytic oxidation (SA oxidation) process utilizing AuNS and ANS-solvents as co-catalyst have been investigated in terms of electrokinetic parameters such as surface charge, zeta potential, pH, and conductance for the very first time. Figure 7a shows the difference in the ζ and conductance values of the reaction mixture (TiO_2 + SA) with and without the addition of AuNS-water and ANS-solvents. The ζ ca. +43.51 mV for TiO_2 + SA reaction system has been found to be higher and opposite charge than TiO_2 (-2.80 mV) and SA (-7.07 mV) aqueous suspension alone. This high ζ indicates the stability of the reaction mixture due to the complexation through negative charges of –COOH and -OH groups of bidentate salicylate to TiO_2 surface as evident by the conductance measurements. The high conductance 263 µS of SA aqueous solution and 59 µS of TiO_2 water slurry alone is notably reduced to 13 µS in TiO_2 + SA reaction mixture.

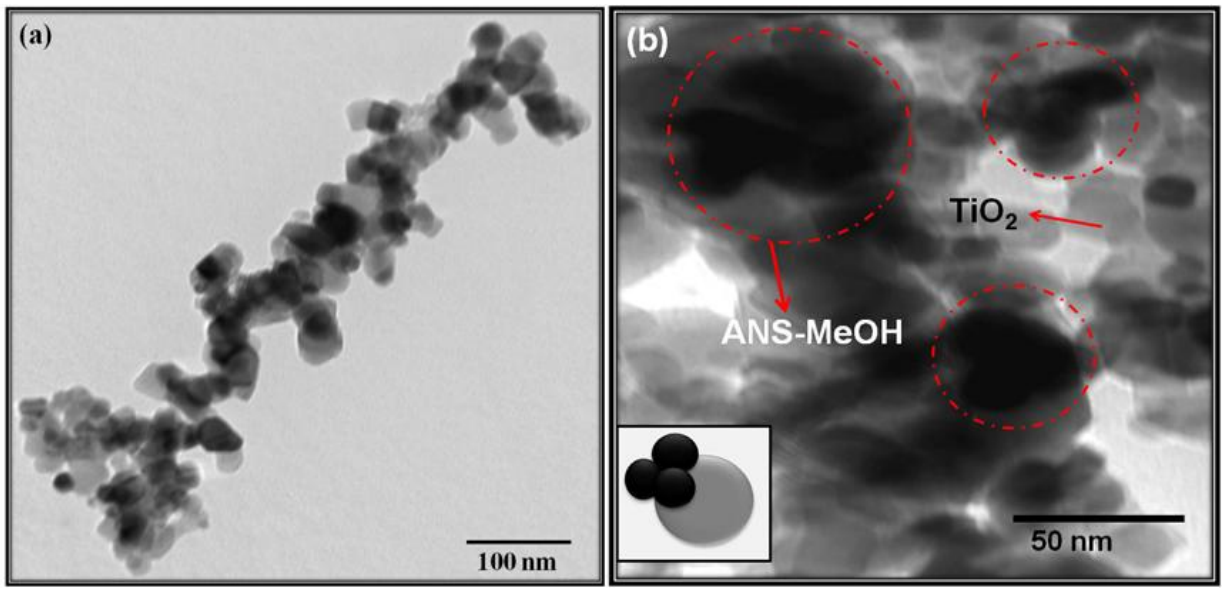

Figure 8. (a) TEM images of AuNS-water (3-6 nm)-TiO_2 mixture and (b) ANS-MeOH (size= 25-40 nm) mixed with TiO_2 in aqueous suspension.

Furthermore, the complexation results in the decrease of free H^+ ions in the reaction media (TiO_2 + SA at pH=6.13) in comparison to TiO_2 (pH=5.81) and SA (pH=3.29) alone which reflects from its pH value (changes from acidic to alkaline) and responsible for the charge reversal. The ζ value of +43.51 mV for TiO_2 + SA reaction mixture is further reduced to +10.38 mV and +5.46 mV after addition of AuNS-water having ζ value +50.32 mV and +24.06 mV for ANS-MeOH, respectively. This fact dictates the strong affinity of AuNS for electrostatic adsorption to TiO_2 surface which in-turn will govern the photocatalytic oxidation rate of SA. For further

confirmation about this AuNS-TiO_2 interionic interaction/adsorption, the effective surface charge of AuNS, TiO_2+SA and TiO_2+SA+AuNS-water suspension was determined. The high positive surface charge ca. +4306.2 µequ./litre of AuNS-water (pH = 6.4) has been significantly decreased to +512.5 µequ./litre in TiO_2+SA+ AuNS aqueous mixture (pH = 6.14) despite having lower surface charge ca. +161.1 µequ./litre of TiO_2+SA mixture (pH = 6.13) alone as displayed in figure 7b. This reduction in the surface charge affects the distribution of ions in the interfacial region, resulting in an increased concentration of counterions, and brings the two particles to come in contact through inter-ionic attractions. The strong ionic interaction/adsorption between AuNS-water (size = 3-6 nm) and TiO_2 (size = 30-50 nm) suspension is further verified by the TEM images of aqueous mixture containing either 100 µl AuNS-water (2.996×10^{16} atoms) or ANS-MeOH, and 50 mg TiO_2 as shown in figure 8a and 8b. It can be seen that larger spherical aggregates of Au nanospheres (formed in MeOH, size = 30-40 nm, encircled in red) appears to be present over the TiO_2 surface, indicating proper attachment of AuNS-water or ANS-MeOH (black colored) with TiO_2 particles (gray contrast) that may improve the TiO_2 photoactivity. This close association of TiO_2 and AuNS was again verified by measured ζ and conductance values as given in figure 7a. It has been found that the zeta potential + 50.32 mV and conductance 1673 µS of AuNS in water are notably reduced to 7.68 mV and 74 µS respectively, after addition of TiO_2 that evidencing strong inter-ionic attraction between themselves.

3.3.5 Co-catalytic activity of AuNS nanostructures obtained in different polar solvents

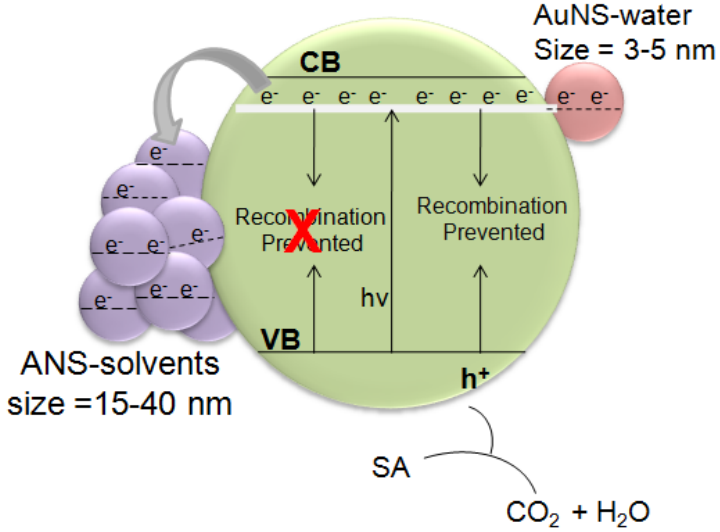

Scheme 1. Co-catalysis effect of AuNS-water and ANS-solvents attached to TiO_2 for the photocatalytic oxidation of salicylic acid.

The AuNPs of various shapes and sizes have been extensively used as co-catalysts to enhance the photocatalytic activity of TiO_2 catalyst. It has been demonstrated that AuNPs store a fraction of electrons captured from photoexcited semiconductor [33,34,41-44] and hence, the double-layer charging between the metal and semiconductor has been shown to play a role in stabilizing the stored electrons within the metal nanoparticles. Most of the photocatalytic reactions have been achieved by depositing the metal ions on the catalyst surface (TiO_2) which leads to the metal/TiO_2 schottky barrier and the low Fermi level of the metal drive the photogenerated electron from TiO_2 conduction band (CB) to the metal phase, leaving the valence band (VB) holes freely available for oxidation of substrate [33,34]. However, herein the efficiency by the AuNS is due to the rapid interfacial charge transfer

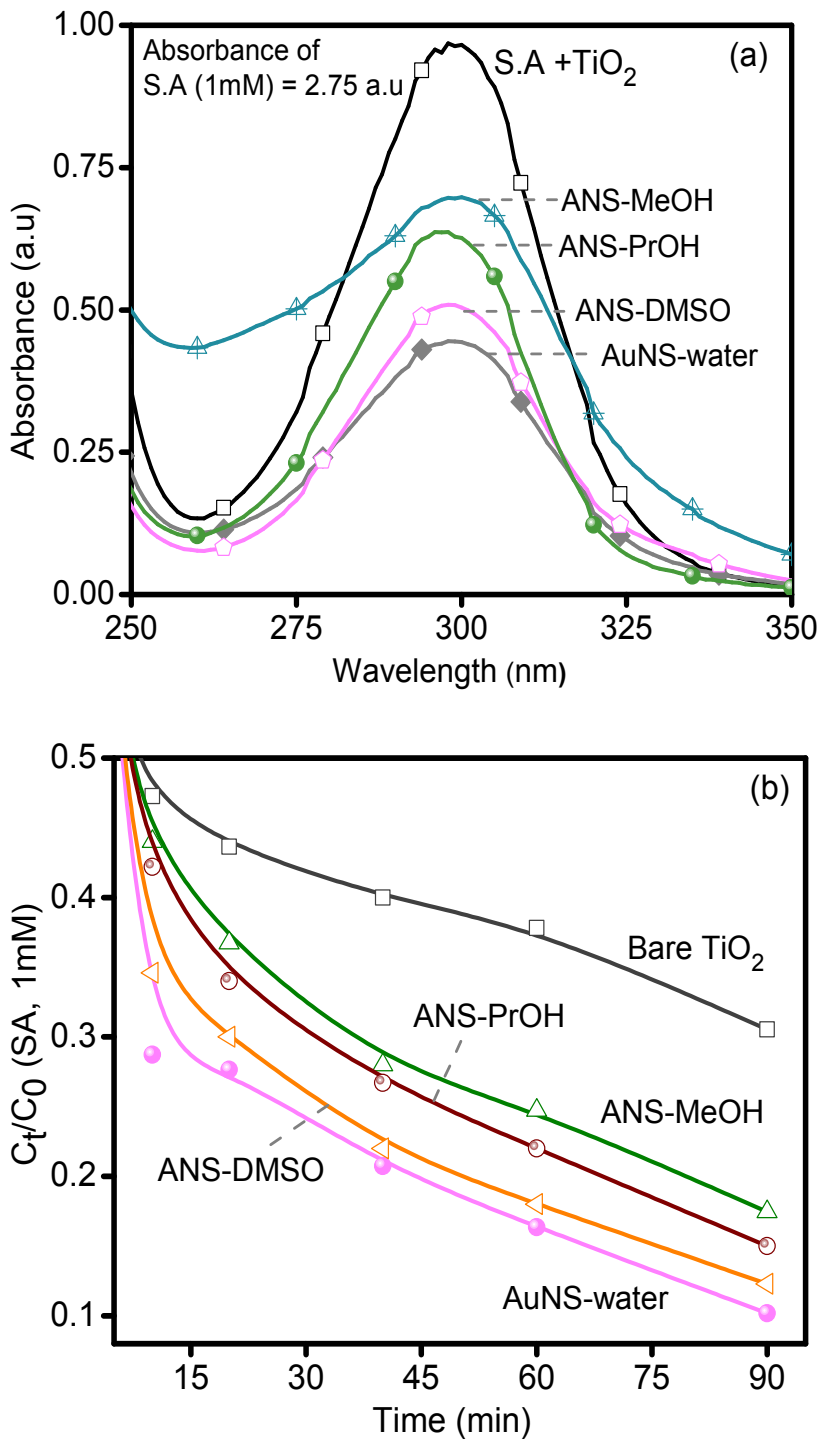

Figure 9. Changes in the absorption spectra (λ_{max} = 298 nm) and (b) time course of salicylic acid (1 mM) photooxidation by AuNS-water and various ANS-solvents addition on TiO_2 under UV irradiation.

between reacting species (TiO_2 and AuNS) due to the temporary ohmic contact, when reacting substrates come in close vicinity to each other during continuous stirring under UV irradiation and has already been discussed in our previous result [45]. Scheme 1 shows the pictorial representation about the difference in the co-catalysis activity of non-aggregated AuNS-water and aggregated AuNS (ANS-solvents) imparting to TiO_2 for the photooxidation of SA under UV irradiation. The smaller Au nanospheres (AuNS-water, size = 3-5 nm) induce greater shift in the Fermi energy level than the larger agglomerated particles (ANS-solvents, size = 15-40 nm), hence, the catalytic efficiency of TiO_2 [44,45] is expected to vary depending on the rate of photoexcited electron transfer process from TiO_2 to AuNPs surface under UV light irradiation. The co-catalytic efficiency of AuNS-water and ANS-MeOH, ANS-PrOH, and ANS-DMSO has been comparatively studied for the UV induced photooxidation of SA (1 mM) by TiO_2 (50 mg, P-25 Degussa). Figure 9a shows the changes in the absorption intensity of SA (1 mM) during its photooxidation by addition of 100 µl (AuNS = 0.0098 mg of Au = 0.02 wt% Au to that of TiO_2) of various ANS-solvents to TiO_2 suspension under 1 h UV light irradiation. The absorption intensity (2.6 a.u) of 1 mM SA decreases in a varied extent by bare and different Au-TiO_2 heterojunction.

The AuNS-water (size ≈ 3.5 ± 0.25) addition to TiO_2 appreciably degrades SA (abs. 0.45 a.u) as compared to bare TiO_2 (abs. 0.96 a.u) alone. The CCA imparted by ANS-DMSO (abs. 0.51 a.u) has been found to higher as compared to (abs 0.69 a.u) ANS-MeOH (abs 0.69 a.u) and ANS-PrOH (0.63 a.u) suspension. This difference in the photooxidation efficiency of SA by various ANS-solvents mixed TiO_2 suspension could be ascribed to the effect of agglomerated size of AuNS formed in polar solvents because almost same amount (100 µl = 2.996×10^{16} Au atoms) of aggregated AuNS are added to TiO_2 and SA suspension. In a similar way, the time course of photocatalytic degradation of 5 ml (1 mM) SA by 100 µl (2.996×10^{16} atoms) with different ANS-solvent co-catalysts (obtained in MeOH, PrOH and DMSO dispersion) addition to TiO_2 as compared to bare and AuNS-water mixed TiO_2 suspension has been displayed in figure 9b. The highest photodegradation rate ($r = 9.990 \times 10^{-3}$ mM/min) has been achieved by AuNS-water and TiO_2 mixture as compared to $r = 7.710 \times 10^{-3}$ mM/min of bare TiO_2 photoactivity during 90 min UV irradiation. It is observed (table 1) that addition of ANS-MeOH to TiO_2 exhibited lower photoactivity ($r = 9.172 \times 10^{-3}$ mM/min) as compared to ANS-PrOH ($r = 9.442 \times 10^{-3}$ mM/min) and ANS-DMSO ($r = 9.771 \times 10^{-3}$ mM/min) addition, respectively. The highest rate of SA

Table 1. Various physicochemical, optical, electrokinetic and catalytic properties of AuNS dispersed in various solvents.

AuNS in different solvents and their (dipole moment / D)	SPR band (size/ nm)	pH of AuNS dispersion	Zeta potential (mV)	Conductance (μS) (Surface charge/ μequ./l)	Photoxidation rate of SA (mM/min)
Water (1.85)	520 nm (3-6 nm)	6.4	50.32	1673 (+4306.2)	9.990×10^{-3}
Methanol (1.70)	555 and 973 nm (25-40 nm)	7.62	24.06	1480 (+2468.4)	9.172×10^{-3}
Propanol (1.66)	975 nm	7.54	26.01	357	9.442×10^{-3}
DMSO (3.96)	976 nm (15-30 nm)	7.84	-31.88	639	9.771×10^{-3}
CCl_4 (0.00)	526 nm	---	53	80	---

photodegradation was achieved by the AuNS-water and TiO_2 suspension followed by various ANS-solvent systems depending on its agglomeration in different polar solvents. The ANS-solvent clusters immobilized on the surface of TiO_2 results in the low density of the reaction sites for the absorption of UV light, therefore, photoproduction of hole and electrons at the surface would decrease and hence, lowered the reactivity to a varied extent depending on the AuNS co-catalysts aggregation or cluster size as shown in scheme 1. The zeta potential, surface charge, pH and conductance measurements provide evidence for the variation in the CCA of aggregated and non aggregated NPs as discussed. Furthermore, the effect of varying concentration (10 μl to 100 μl) of AuNS-water addition to TiO_2 for the photodegradation of SA during 90 min of light irradiation has been carried out as shown in figure

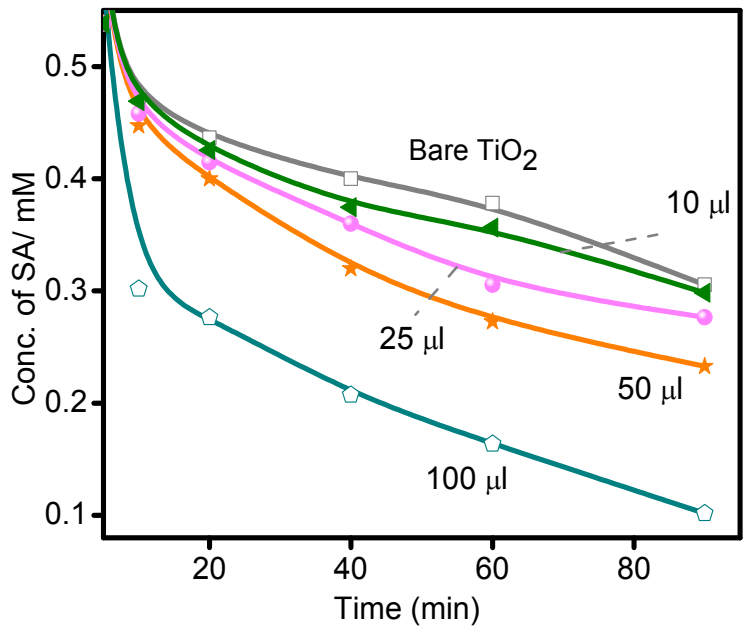

Figure 10. Effect of different amount of AuNS-water addition onto TiO_2 for the rate of salicylic acid (1 mM) photodegradation under UV irradiation.

10. It has been observed that on increasing the amount of AuNS (2.996×10^{15} to 2.996×10^{16} atoms) co-catalyst addition onto TiO_2 (50 mg), the rate of photocatalytic oxidation of SA is highly enhanced as compared to bare TiO_2.

The photocatalytic degradation rate undergoes an exponential decrease in SA concentration as $C = C_0 e^{-kt}$ with irradiation time follows the first order kinetic reaction as typically observed in many photocatalytic reactions [46-51]. The SA photooxidation rate was found to be higher during first 20 min due to the formation of titanium(IV)-salicylate surface complex [43]. It is because of the ionic adsorption of salicylic acid onto larger numbers of AuNS (100 µl)-TiO_2 particle interface. In addition, the adsorption behavior by the ANS-polar solvents was also carried out in comparison with AuNS-water. Thus, it is shown that ANS-solvents of different dipole moments displayed less adsorption and hence less co-catalysis effect to TiO_2 photocatalysis than quantum size AuNS-water dispersion because of the limitation of photoexcited charge transfer process and Fermi energy equilibration of ANS-solvents co-catalyst particles as discussed above. This phenomenon was further supported by the zeta potential and conductance measurements as discussed above.

This chapter gives a new insight for tuning the reaction rate as a function of solvents polarity. As the extent of aggregation in various solvents is different and hence by using appropriate aggregated structure, yield and selectivity of a reaction can be easily manipulated. Moreover, this method offers an economic route for catalysis.

3.4 References

[1] J. Kimling, M. Maier, B. Okenve, V. Kotaidis, H. Ballot and A. Plech, J. Phys. Chem. B, 110 (2006) 15700.

[2] N.R. Jana, L. Gearheart and C. Murphy, J. Chem. Mater., 13 (2001) 2313.

[3] N.R. Jana, L. Gearheart and C. Murphy, Langmuir, 17 (2001) 6782.

[4] M. Eguchi, D. Mitsui, H.L. Wu, R. Sato and T. Teranishi, Langmuir, 28 (2012) 9021.

[5] M.J. Guffey, R.L. Miller, S.K. Gray and N.F. Scherer, Nano Lett., 11 (2011) 4058.

[6] X. Huang, X. Qi, Y. Huang, S. Li, C. Xue, C.L. Gan, F. Boey and H. Zhang, ACS Nano., 4 (2010) 6196.

[7] J. Perez-Juste, I. Pastoriza-Santos, L.M. Liz-Marzan and P. Mulvaney, Coord. Chem. Rev., 249 (2005) 1870.

[8] Q. Zhang, C.H. Moran, X. Xia, M. Rycenga, N. Li and Y. Xia, Langmuir, 28 (2012) 9047.

[9] S.E. Skrabalak, J. Chen, Y. Sun, X. Lu, L. Au, C.M. Cobley and Y. Xia, Acc. Chem. Res., 41 (2008) 1587.

[10] P.R. Sajanlal, T.S. Sreeprasad, A.S. Nair and T. Pradeep, Langmuir, 24 (2008) 4607.

[11] K.L. Kelly, E. Coronado, L.L. Zhao and G.C. Schatz, J. Phys. Chem. B, 107 (2003) 668.

[12] P.V. Kamat, J. Phys. Chem. B, 106 (2002) 7729.

[13] J. Zeng, Q. Zhang, J. Chen and Y. Xia, Nano Lett., 10 (2010) 30.

[14] R. Narayanan and M.A. El-Sayed, Langmuir, 21 (2005) 2027.

[15] S. Eustis and M.A. El-Sayed, Chem. Soc. Rev., 35 (2006) 209.

[16] P. Mulvaney, Langmuir, 12 (1996) 788.

[17] L.M. Liz-Marzan, Langmuir, 22 (2006) 32.

[18] G.J. Hutchings and M. Haruta, Appl. Catal. A., 291 (2005) 2.

[19] M. Haruta, Gold Bull., 37 (2004) 27.

[20] M.C. Daniel and D. Astruc, Chem. Rev., 104 (2004) 293.

[21] J. Hu, Z. Wang and J. Li, Sensors, 7 (2007) 3299.

[22] I.O. Sosa, C. Noguez and R.G. Barrera, J. Phys. Chem. B, 107 (2003) 6269.

[23] T. Huang, F. Meng and L. Qi, J. Phys. Chem. C, 113 (2009) 13636.

[24] O. Tzhayik, P. Sawant, S. Efrima, E. Kovalev and J.T. Klug, Langmuir, 18 (2002) 3364.

[25] I. Pastoriza-Santos, J. Perez-Juste and L.M. Liz-Marzan, Chem. Mater., 18 (2006) 2465.

[26] B. Mukherjee and J.W. Weaver, Environ. Sci. Technol., 44 (2010) 3332.

[27] T. Kim, K. Lee, M. Gong and S.W. Joo, Langmuir, 21 (2005) 9524.

[28] P.R. Chandran, M. Naseer, N. Udupa and N. Sandhyarani, Nanotechnology, 23 (2012) 015602.

[29] C.E. McNamee, M. Matsumoto, P.G. Hartley, P. Mulvaney, Y. Tsujii and M. Nakahara, Langmuir, 17 (2001) 6220.

[30] A. Elbadawy, T.P. Luxton, R.G. Silva, K.G. Scheckel, M.T. Suidan and T.M. Tolaymat, Environ. Sci. Technol., 44 (2010) 1260.

[31] C.J. Orendorff, P.L. Hankins and C.J. Murphy, Langmuir, 21 (2005) 2022.

[32] J. Liao, Y. Zhang, W. Yu, L. Xu, C. Ge, J. Liu and N. Gu, Colloids Surf. A., 223 (2003) 177.

[33] D.W. Goodman, Catal. Lett., 99 (2005) 1.

[34] V. Subramanian, E.E. Wolf and P.V. Kamat, J. Am. Chem. Soc., 126 (2004) 4943.

[35] M. Jakob, H. Levanon and P.V. Kamat, Nano Lett., 3 (2003) 353.

[36] S.M. Lee, M. Kim and K.C. Choi, IEEE Photonic.Tech. L, 24 (2012) 882.

[37] A.C. Templeton, J.J. Pietron, R.W. Murray and P. Mulvaney, J. Phys. Chem. B, 104 (2000) 564.

[38] P.K. Jain, K.S. Lee, I.H. El-Sayed and M.A. El-Sayed, J. Phys. Chem. B, 110 (2006) 7238.

[39] T.K. Sau and C.J. Murphy, Langmuir, 21 (2005) 2923.

[40] M. Moskovits, J. Phys. Chem. B, 109 (2005) 14755.

[41] A. Wood, M. Giersig and P. Mulvaney, J. Phys. Chem. B, 105 (2001) 8810.

[42] H. Choi, W.T. Chen and P.V. Kamat, ACS Nano, 6 (2012) 4418.

[43] A.E. Regazzoni, P. Mandelbaum, M. Matsuyoshi, S. Schiller, S.A. Bilmes and M.A. Blesa, Langmuir, 14 (1998) 868.

[44] P.V. Kamat, J. Phys. Chem. C, 111 (2007) 2834.

[45] R. Kaur and B. Pal, J. Mol. Catal. A: Chem., 355 (2012) 39.

[46] M. Tamimi, S. Qourzal, A. Assabbane, J.-M. Chovelon, C. Ferronato and Y. Ait-Ichou, Photochem. Photobiol. Sci., 5 (2006) 477.

[47] V. Tiwari, J. Jiang, V. Sethi and P. Biswas, Appl. Catal. A- Gen., 345 (2008) 241.

[48] I.K. Konstantinou, T.M. Sakellarides, V.A. Sakkas and T.A. Albanis, Environ. Sci. Technol., 35 (2001) 398.

[49] A. Fujishima, T.N. Rao and D.A. Tryk, J. Photoch. Photobio. C, 1 (2000) 1.

[50] X.Z. Li and F.B. Li, Environ. Sci. Technol., 35 (2001) 2381.

[51] K.A. Connelly and H. Idriss, Green Chem., 14 (2012) 260.

Chapter 4

Electro-kinetic and Catalytic Sensitivity of Au Nanorods Agglomerated in Solvents of Varying Dipole Moment and Refractive index

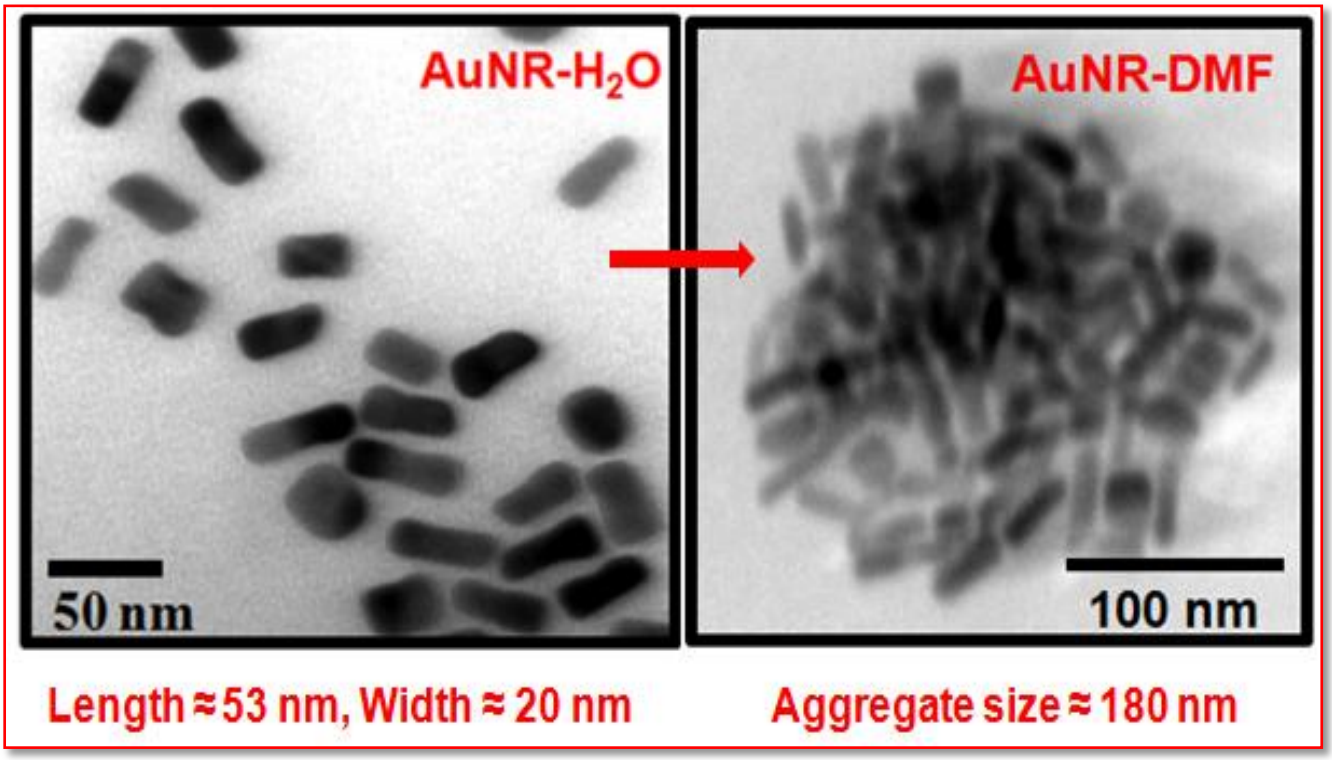

4.1 Introduction

The self-assembly of Au nanoparticles (AuNPs) generally occur due to vander-Waals forces, dipole moment, hydrogen bonding and binding via surface active agents such as alkyl thiols, amino acids, hydroxyl, carboxylic group and other chelating agents [1-11]. Several reports exist in the literature on ordered assembly of AuNPs such as necklace like Au nanorods (AuNRs) structure, nanorod-nanosphere and bipyramid-nanosphere, end-to-end and parallel attachment by the addition of glutathione and cysteine [12], etc. The pH-dependent AuNRs assembly was attained by using deprotonated adipic acid form side-to-side assemblies consisting of 20-200 NR at pH~8 [13] and Au particles were found to spontaneously organize into a linear chain like aggregates in ethanol due to the dipole-dipole interaction in the polar solvents [1]. Various liquid crystalline ordered structures with nematic, smectic, and columnar phases have been observed for rod and plate shaped nanocrystals [14]. Surface passivation of rod-shaped AuNPs can promote end-to-end assembly instead of side-to-side liquid crystalline assembly [14]. Thus, it is evident that the AuNPs aggregation and their plasmonic properties could be well-tuned by adjusting the experimental conditions. During the self-assembly process, the net surface charge and zeta potential (ζ) developed over AuNPs surface is dependent on aggregated cluster size and attached polar/non-polar surface active agents could influence the adsorption/ or interaction of reacting substrate and thereby modify the catalytic activity. For example, the ζ of AuNRs was reduced from +47.6 ± 3.3 mV to +10.9 ± 4.1 mV by the addition of 10^{-5} M adipic acid due to electrostatic interactions between the positively charged nanorods and negatively charged deprotonated adipic acid [13]. Replacement of the CTAB surface group of AuNRs with phosphocholine lipid resulted in side-to-side assembly and the ζ potential of the composite was decreased from +39.4 ± 2.8 mV to+11.1 ± 1.6 mV due to charge pairing [15].

Nanocrystals synthesized in colloidal solution require capping agents to limit their growth and to passivate dangling bonds, and many organic and inorganic reactions employing polar solvents lead to random or chaotic arrays of AuNRs and thus, affecting their catalytic activity. Catalysis using AuNPs of different sizes and shapes make them attractive for chemical reactions because of their high surface area-to-volume ratio and more active surface atoms located on their corners and edges [16-19]. For example, Au nanocages with fine intrinsic electrical connection across their entire surface are proven to be a better catalyst than small Au solid nanoparticles for redox reaction [20]. Tetrahedral Pt NPs are most active relative to the spherical NPs in catalyzing the Suzuki reaction between phenylboronic acid and iodobenzene [21]. Moreover, it is well proven that noble metal deposits as a co-catalyst

over TiO_2 particles exhibit size-dependent shift in the Fermi level and thereby influencing the TiO_2 photoactivity [22,23].

In spite of the large volume of research on the theoretical and experimental aspects of optical properties of AuNPs assembly, little attention has been paid to assess the electro-kinetic and catalytic properties of aggregated/assembled AuNRs in polar solvents of varying dipole moments [12-16]. *So in continuation of chapter-3, the present chapter focuses on the effect of AuNRs aggregation in polar solvents (methanol, propanol, dimethylsulphoxide, and dimethylformamide typically used in Au catalyzed reactions) on the electro-kinetic properties and catalytic activity for the reduction of p-nitrophenol to p-aminophenol, and co-catalytic effect of AuNRs–TiO_2 composite on photo-oxidation of salicylic acid under UV light irradiation.*

4.2 Experimental section

4.2.1 Materials

Chloroauric acid ($HAuCl_4.3H_2O$), sodium borohydride ($NaBH_4$), ascorbic acid, methanol (MeOH), propanol (PrOH), dimethylsulphoxide (DMSO), dimethlyformamide (DMF), carbontetrachloride (CCl_4), salicylic acid (SA), *p*-nitrophenol (PNP) and *p*-aminophenol (PAP) were obtained from Loba chemie, India. Commercially available titanium oxide (TiO_2) is a gift sample from P-25 Degussa, Germany. Silver nitrate ($AgNO_3$) was purchased from Fischer Scientific. Cetyltrimethylammoniumbromide (CTAB) was purchased from Sigma Aldrich. All these chemicals were used without further purification. Deionized water was obtained using an ultrafiltration system (Milli-*Q*, Millipore) with a measured conductivity above 35 mho cm^{-1} at 25 °C

4.2.2 Preparation and dispersion of AuNRs in various solvents

The AuNRs were synthesized according to the previously reported method with certain modifications [24,25]. 250 µl of (0.01 M) $HAuCl_4$ was added to 10 ml (0.1 M) CTAB, followed by reduction with 600 µl (0.01 M) $NaBH_4$ solution under magnetic stirring for 2 min, which results in the formation of gold seeds. This above formed solution (ca. 12 µl) was introduced to the mixture of 500 µl (0.01 M) $HAuCl_4$, 10 ml (0.1 M) CTAB, 75 µl (0.01 M) $AgNO_3$, 55 µl ascorbic acid (0.1 M) and it was kept undisturbed overnight. The formed AuNRs were repeatedly washed with deionized water under four cycles of centrifugation at 8500 rpm for 10 min. For surface plasmon absorption and pH measurements, 1.5 ml aqueous suspension of AuNRs was dispersed in 1.5 ml polar (methanol, propanol, DMF and DMSO) and non-polar (CCl_4) solvent. The sharp change in color of colloidal solution of nanorods (light purple to blackish) was noticed within a few seconds, due to aggregation with polar

solvents. The AuNRs after agglomeration (ANR) in various dispersion solvents (ANR-solvents) are denoted as AuNRs-H_2O, AuNRs-CCl_4, ANR-MeOH, ANR-PrOH, ANR-DMF and ANR-DMSO for further discussion.

4.2.3 Co-catalytic activity of bare and aggregated AuNRs mixed with TiO_2 (Au-TiO_2)

Various polar or non-polar solvents (100 µl) were added to AuNRs (100 µl), centrifuged and vacuum dried to remove the excess solvent and were finally dispersed in 100 µl water. The photocatalytic reaction was carried out by taking 5 ml SA (1 mM), 50 mg TiO_2 and calculated amount (10-100 µL) of AuNRs (formed by spreading out in various polar solvents) under UV irradiation (125 W Hg-arc lamp, λ_{max} = 253.6 nm and 10.4 mW/cm^2) and magnetic stirring for different time periods. The concentration of SA was determined using UV-vis spectrophotometer at λ_{max} = 298 nm.

4.2.4 Catalytic activity of AuNRs

Catalytic activity with various aggregated morphologies of AuNRs (ca. 100 µl) was examined by adding 1 ml of ice-cold $NaBH_4$ solution (0.42 M) to 7 mL PNP (0.2 mM). Catalytic reduction of PNP to PAP was monitored by measuring the absorption spectra (λ_{max} = 400 nm for nitrophenolate ion and 298 nm for PAP) of the reaction mixture at regular intervals and also analyzed by high–performance liquid chromatography (HPLC, Agilent, 1120 Compact LC, 254 nm, using C–18 column and MeOH: H_2O (65:35) as mobile phase) at a flow rate of 1ml/min.

4.2.5 Structural and electro-kinetic parameter analysis

The size and shape of AuNRs was analyzed by TEM (Hitachi 7500, 2Å, 120 KV). The ζ and dynamic light scattering (DLS) particle size distribution analysis was carried out by means of Brookhaven 7610 instruments and sample was prepared by adding 1.5 ml water to vacuum dried AuNRs (1.5 ml, 4.494×10^{17} atoms) in various solvents (MeOH/ PrOH/ DMF/ DMSO/ CCl_4). ζ measurement of the photocatalytic reaction mixture (1 mM, 5 ml SA + 50 mg TiO_2) with or without AuNRs (100 µl) addition was carried out by taking 200 µl of reaction mixture into a 1.3 ml of water. Surface charge density (Mutek-PCD03pH) of AuNRs has been measured by using 300 ml aqueous suspension containing 1.66×10^{15} Au atoms/ml. Similarly, the reaction mixture (1 mM, 5 ml SA + 50 mg TiO_2) with and without NR in 300 ml aqueous slurry was used for the surface charge measurement.

4.3 Results and discussion

4.3.1 Optical properties of AuNRs in polar and non-polar solvents

Figure 1a shows the alterations in the surface plasmon resonance band (SPR, transverse band ~ 532 nm and longitudinal band ~ 698 nm) of AuNRs after the addition of polar and non-polar solvents of different dipole moments (0–3.96 D). It can be seen that the absorption intensity (1.03 a.u) at SPR = 698 nm of AuNRs-H_2O suspension was appreciably dropped down (0.52–0.27 a.u.) and a small peak at > 1050 nm characteristic to aggregation appears, whose intensity depends on the solvent polarity [1,26]. Whereas, no such changes in the SPR were observed for non-polar solvent (CCl_4) and water dispersion as seen in figure 1b. This variation in the plasmonic resonance of AuNRs is sensitive to the refractive index (RI) and therefore it is significant to understand the dependence of plasmonic resonance on the RI of the surrounding medium. Figure 2a illustrates a linear increase in the RI of AuNRs (1.333 to 1.4227) on the successive addition (0-1500 µl) of different polar solvents. DMSO and DMF with higher polarity (3.96 and 3.82 D) showed a maximum enhancement in the RI (~1.4227) as compared with almost no change (RI~1.334) after CCl_4 addition. Figure 2b shows the dependence of RI and SPR (698 nm) absorption intensity of AuNRs on solvent polarity.

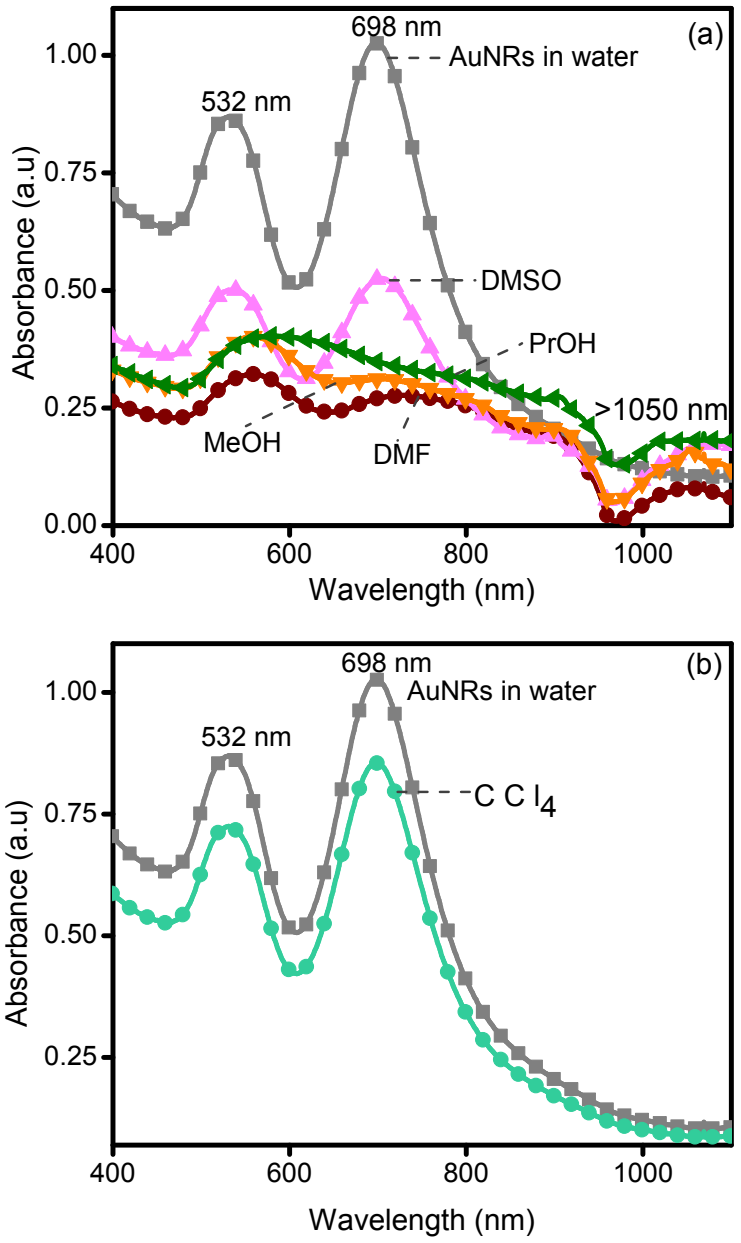

Figure 1. Optical absorption spectra of Au nanorods (a) in various polar and (b) non-polar solvents.

Highly polar solvents (DMF and DMSO) decrease the absorption intensity to a larger extent while non-polar solvent (CCl_4) does not show any variation in the absorption intensity. Higher change in the RI by surrounding medium increases the wavelength of the longitudinal resonance and show red shift with an increase in the size or aspect ratio of rods. The observed variation in SPR and RI could occur, probably due to increasing particle diameter, nanorod plasmon coupling through nanorod-nanorod interactions or by increasing local refractive index (RI), etc. [27-30] that influences the light scattering behavior. The DLS particle size analysis of AuNRs dispersion (figure 3) in various solvents revealed a significant increase in the hydrodynamic size to ~180-200 nm in DMF (figure 3a), 90-120 nm in MeOH and 120-150 nm in DMSO dispersion (figure 3b) as compared to 50-70 nm in H_2O suspension. Light-scattering measurements generally assume particles to be spherical and often fail to produce accurate estimates when the particle shape (NR) is anisotropic, hence DLS measurements have been used to monitor the variations in AuNRs agglomeration, not to evaluate any spatial parameters [31].

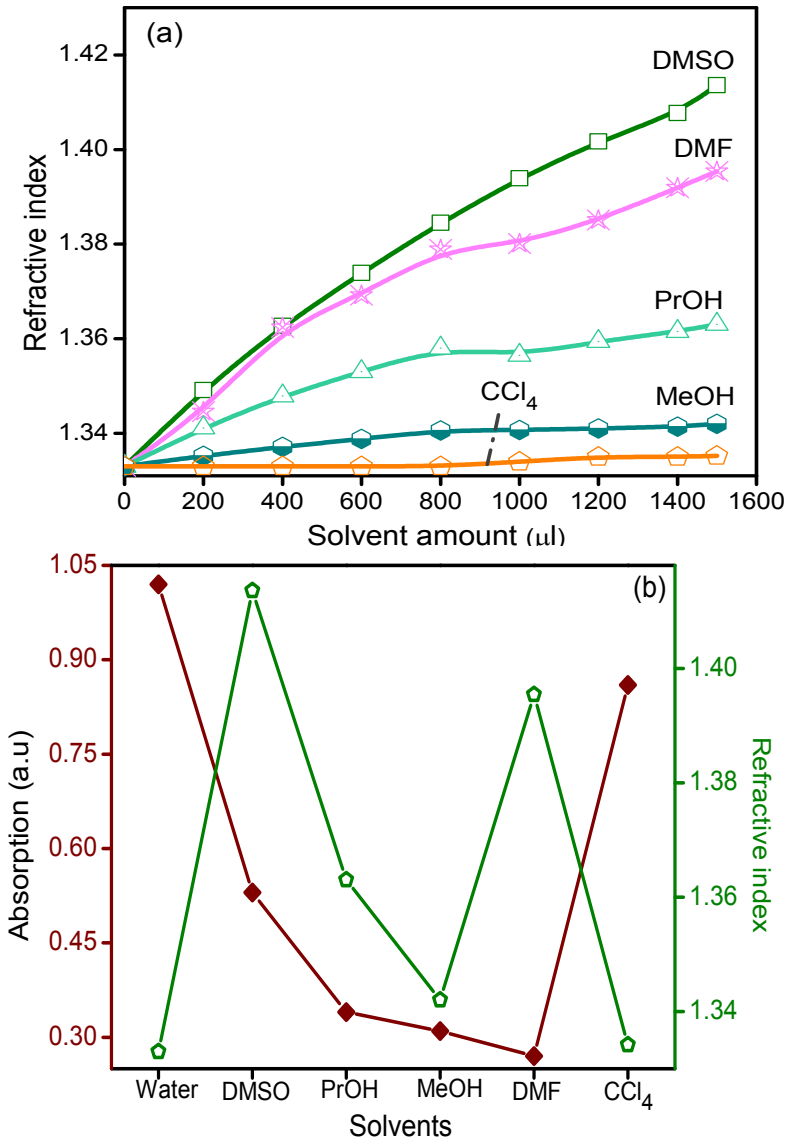

Figure 2. Variation in refractive index on polar solvent addition (b) Variation in the absorption intensity (left axis) and refractive index (right axis) as a function of solvent polarity.

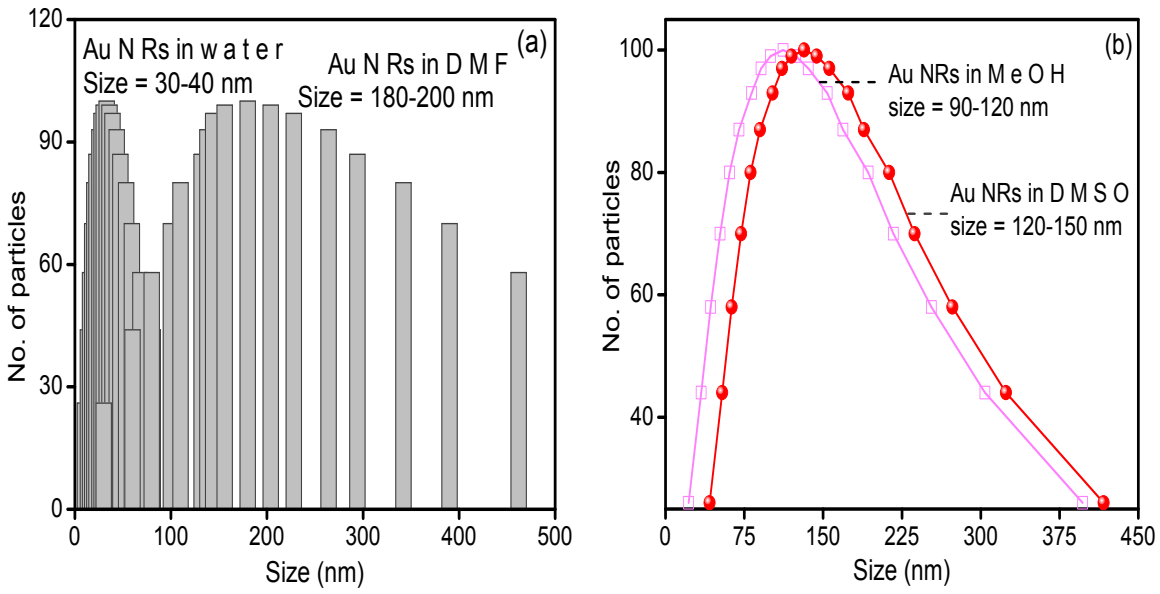

Figure 3. Particle size distribution of Au nanorods dispered in (a) water and DMF and (b) methanol and DMSO.

4.3.2 Structural morphology of Au nanorods

Figure 4a corresponds to the TEM images of homogenous dispersion of AuNRs in the water having length ≈ 53 nm and width ≈ 20 nm (aspect ratio ≈ 2.5). MeOH addition resulted in the decrease of inter particle distance among the adjacent NRs and showed parallel alignment to a little extent (figure 4b). Formation of small groups of NR with random or haphazard arrangement (figure 4c) and a large clump of aggregate (figure 4d) relative to distantly positioned rods in aqueous media are also seen in MeOH dispersion. Figure 4e-f illustrates the close assembly of AuNRs in DMF dispersion and clearly evident that NRs organize themselves in a globular shaped structure having cluster size ~ 200 nm (figure 4f), resembling honeycomb like morphology. These differences in the degree of agglomeration in MeOH and DMF, as evidenced by TEM measurements, can be attributed to the difference in their dipole moments and is entirely different from regular self assembled nanostructures.

AuNRs in aqueous media with cationic surfactant (CTAB) acquire net positive charge on their surface which helps in balancing the repulsive and attractive interactions between particles thereby, preventing their aggregation. Whereas, polar solvents results in the asymmetric distribution of adsorbed charge on the particles surface and generate the dipole moment. The dipole-dipole interactions between the two individual AuNRs results in a dimer, and hence, once the thermal energy and the columbic repulsion is suppressed causes assembling/clustering of particles [1].

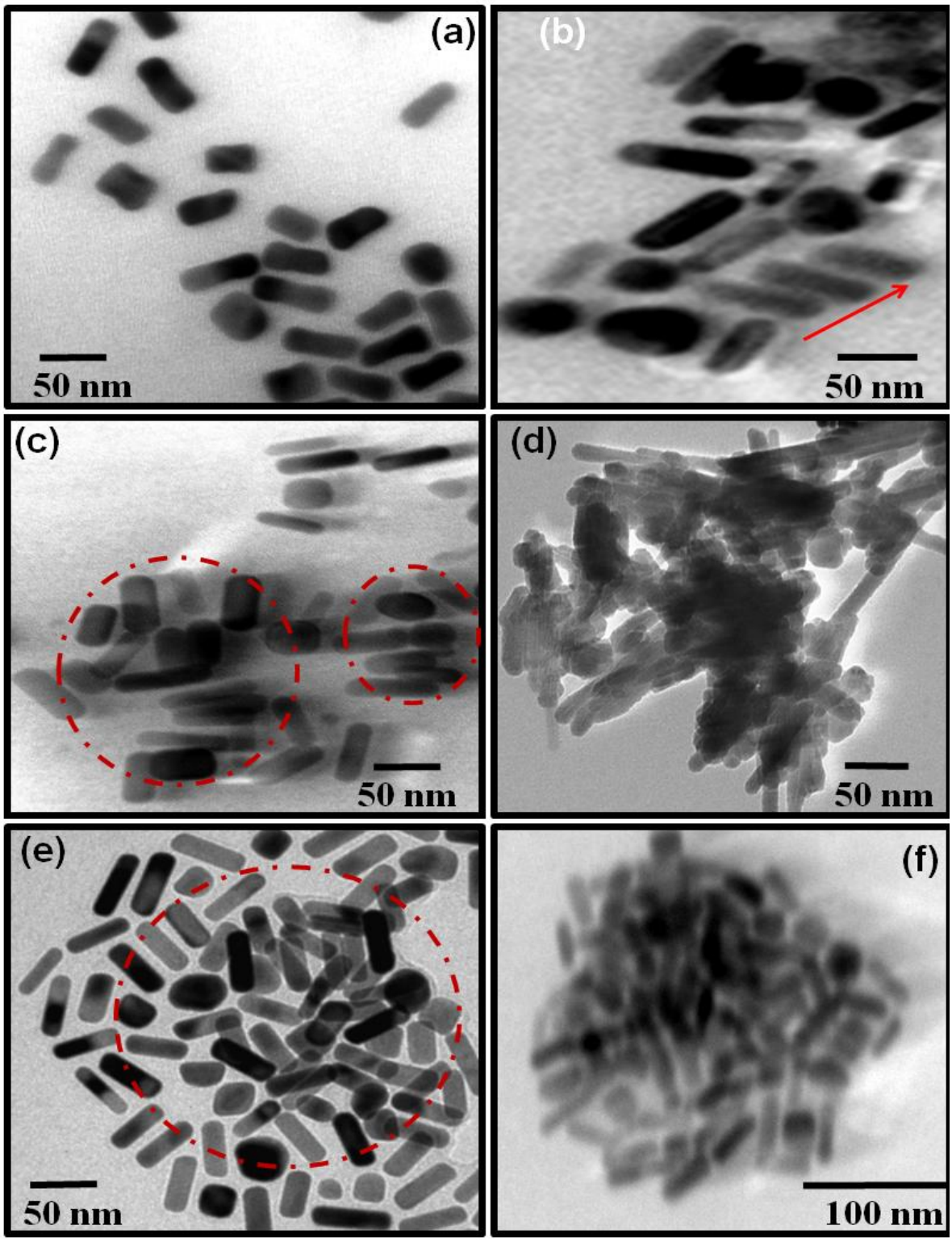

Figure 4. TEM images of (a) Au nanorods in water, (b) marked area representing the parallel alignment of Au nanorods in methanol, (c) and (d) clump of nanorods in methanol, (e) and (f) forming large size aggregates in DMF.

According to Onsager's theory, this type of particle clustering depending on the solvent nature is irreversible and leads to much lowering of the surface energy after the elimination of highly curved surfaces of individual rods and is an enthalpy-favorable process [32]. An increase in the pH of colloidal AuNRs (6.1, aqueous media to 7.3 in DMF) on the addition of polar solvents has also been observed [33] which leads to the formation of larger aggregated size on increasing pH of Au colloidal dispersion.

4.3.3 Electrokinetic properties of AuNRs in polar solvents

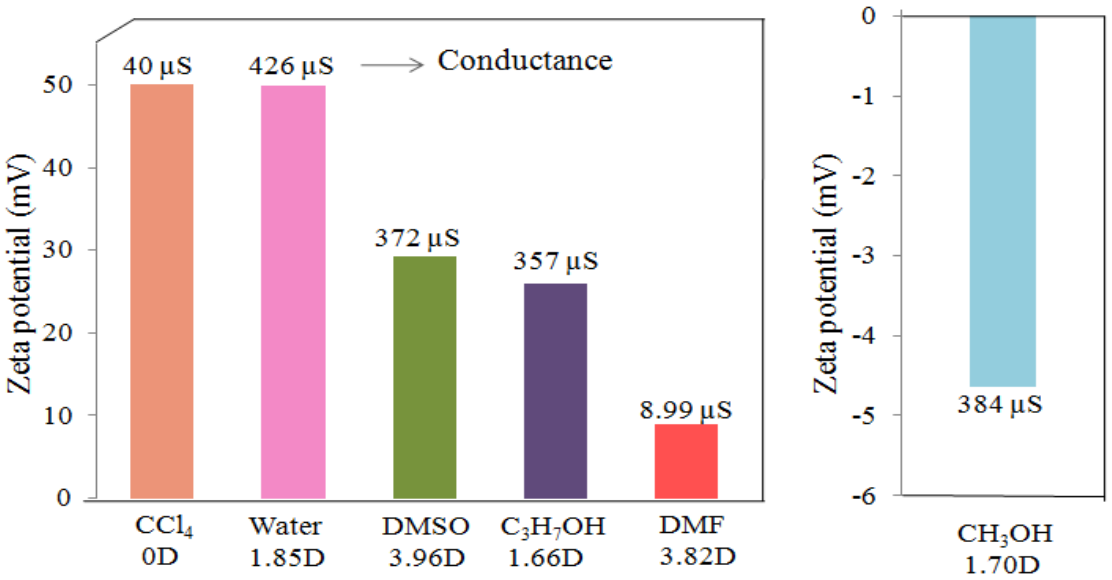

Figure 5. Zeta potential and conductance of Au nanorods dispersed in solvents of varying dipole moment.

Interactions between the AuNRs and solvents not only alter the optical properties but also result in modification of the charge distribution at their interface and hence affect their electrokinetic properties. ζ represents the surface charge of a particle which arises due to the potential difference between the particle's surface and the surrounding solvent. Figure 5 illustrates that highest ζ ca. +49.79 mV at pH=6.1 exhibited by the AuNRs in aqueous suspension has been dropped down ≈ +8.99 to -4.65 mV in polar solvents, whereas non-polar CCl_4 solvent suspension does not show any appreciable change in ζ (+50 mV) value. Conductance of AuNRs in aqueous dispersion (426 µS) has also been lowered down to 8.99 µS in DMF. The marked reduction in ζ and conductance of AuNRs signifies the unstable system and is attributed to the solvent nature with varying polarity (DP = 1.46 D to 3.96 D) that bring about the neutralization of surface charge to a different extent and results in the reduction of inter-particle repulsion between the particles of like charges. As a result, the colloidal particles come closer to one another and coalesce to form bigger aggregates.

Whereas CCl_4 being a non-polar solvent, does not carry any charge and hence, there is no influence of electric potential difference on the NR surface. Martin Moskovits and co-workers [34] reported that the metal NPs are highly stabilized in aqueous solution because of the presence of double layer charge surrounding each nanoparticle that produces a coulomb barrier to prevent aggregation and thus stabilizes the colloidal suspension.

4.3.4 Electrokinetic and catalytic properties of AuNRs-H_2O and ANR-solvents

It is a well proven fact that catalysis using NPs depend on their shape, size, number of surface active atoms, nature of charged species, which create some unbalanced forces over the particle surface and facilitates the adsorption of the reactant species for a reaction to proceed.

Table 1. Electrokinetic properties and rate constant (k) of co-catalytic and catalytic reaction mixture in different polar solvents.

S.No.	AuNRs dispersion in various solvent-dipole moment (zeta potential, mV)	Zeta potential, ζ / mV (Conductance, μS)		SA oxidation (k/ min^{-1})	PNP reduction (k/ min^{-1})
		PNP	TiO_2 +SA		
		+ AuNRs in various solvents			
1.	H_2O-1.85D (+49.79)	29.78 (275)	31.88 (17)	8.4×10^{-2}	5.28×10^{-2}
2.	MeOH-1.70D (-4.65)	22.32 (259)	16.88 (50)	5.9×10^{-2}	2.69×10^{-2}
3.	PrOH-1.66D (26.01)	24.46 (220)	14.56 (15)	7.7×10^{-2}	2.33×10^{-2}
4.	DMSO-3.96D (8.99)	20.32 (234)	10.98 (14)	----	1.74×10^{-2}
5.	DMF-3.82D (29.22)	17.79 (229)	6.88 (10)	5.2×10^{-2}	1.0×10^{-2}

As the surface charge of AuNRs-H_2O (pH = 6.1) is measured to be positive (+2712.5 μeq/litre), an electronic attraction with the negatively charged nitrophenolate ions may help in better PNP adsorption over AuNRs surface. Thus it is evident from the measured ζ (+49.79 mV) of AuNRs-H_2O which is significantly decreased to +29.78 mV after addition of aqueous PNP (0.2 mM) having ζ = -8.77 mV. ANR addition to aqueous PNP solution also gradually reduced the ζ value from +29.78 to 17.79 mV (ANR-DMF) as a function of the agglomerated size of ANR formed, owing to the difference in solvent polarity as seen in table 1. Typically $–NO_2$ group reduction occurs with the transfer of hydride from BH_4^- to NPs surface, followed by adsorption of nitrophenolate ions and finally, hydride ion transfer from NP surface to the adsorbed (PNP) species [35]. Therefore, the reduction process is highly dependent on surface area, nature of electronic charge, and the geometric morphology of AuNPs.

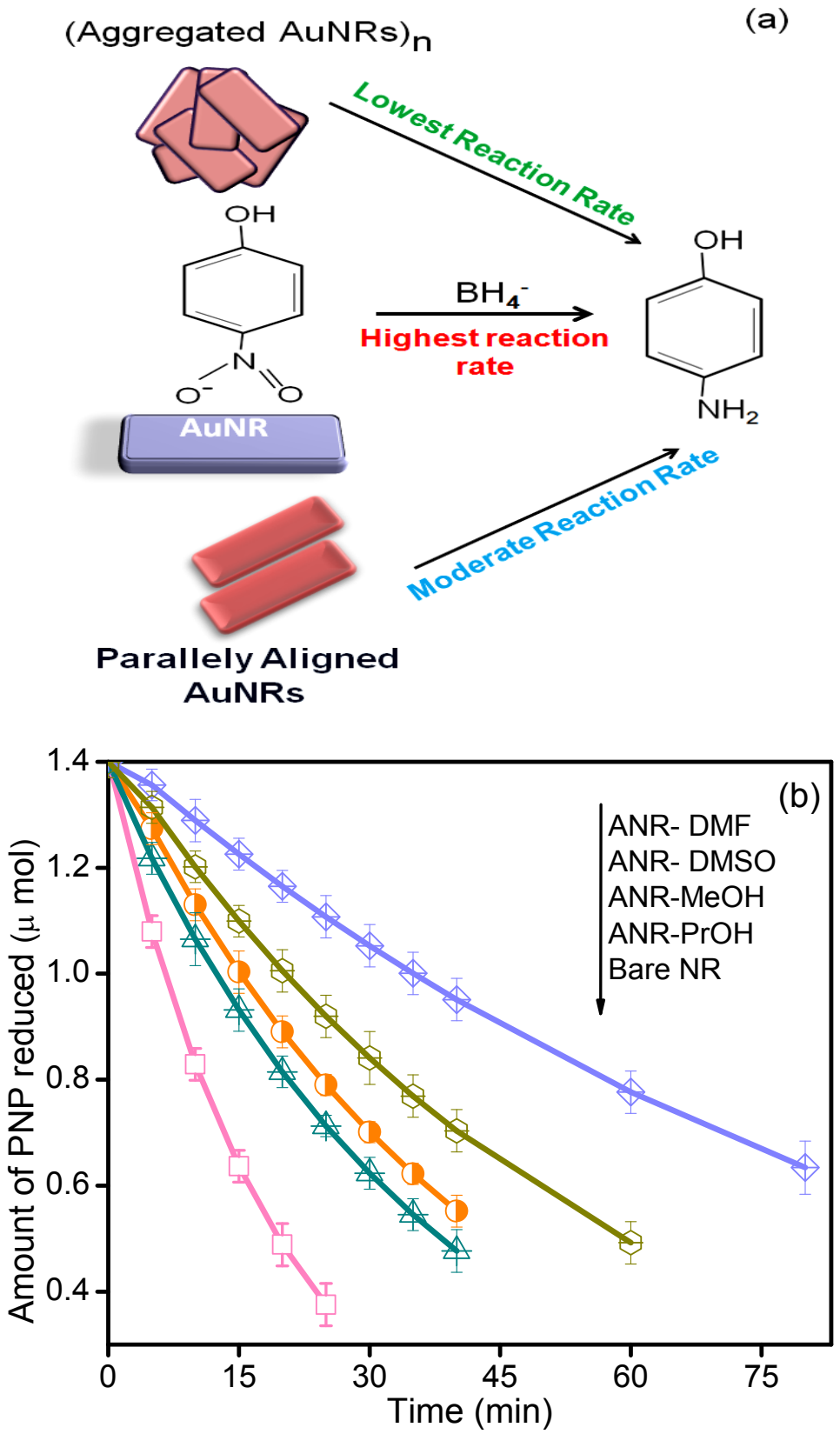

Figure 6. (a) PNP reduction by $NaBH_4$ in the presence of different shape and sizes of agglomerated Au nanoparticles catalyst, and (b) time course for the reduction of PNP by various aggregated morphologies at various time intervals.

Thus, aggregation of AuNRs may likely to hinder the electron transfer process and further affect the adsorption and catalytic activity for PNP reduction by ANR as shown in figure 6a. Time course reduction of PNP to PAP formation is shown in figure 6b. It indicates a linear decrease of PNP concentration, like pseudo-first-order kinetics ($C/C_0 = e^{-kt}$) equation, where AuNRs-H_2O addition (100 µl = 2.996×10^{16} atoms) showed a complete reduction of PNP within 25 min (highest k= 5.28×10^{-2} min^{-1}) as compared to 80 min (lowest k =1.0×10^{-2} min^{-1}) by ANR-DMF as shown in table 1. Accordingly, PAP yield (70%) and selectivity by AuNRs-H_2O is also found to be gradually reduced as (54%) ANR-MeOH> (48%) ANR-PrOH> (27%) DMSO> (12%) ANR-DMF (figure 7), with increasing extent of agglomeration in polar solvents as quantified by HPLC analysis.

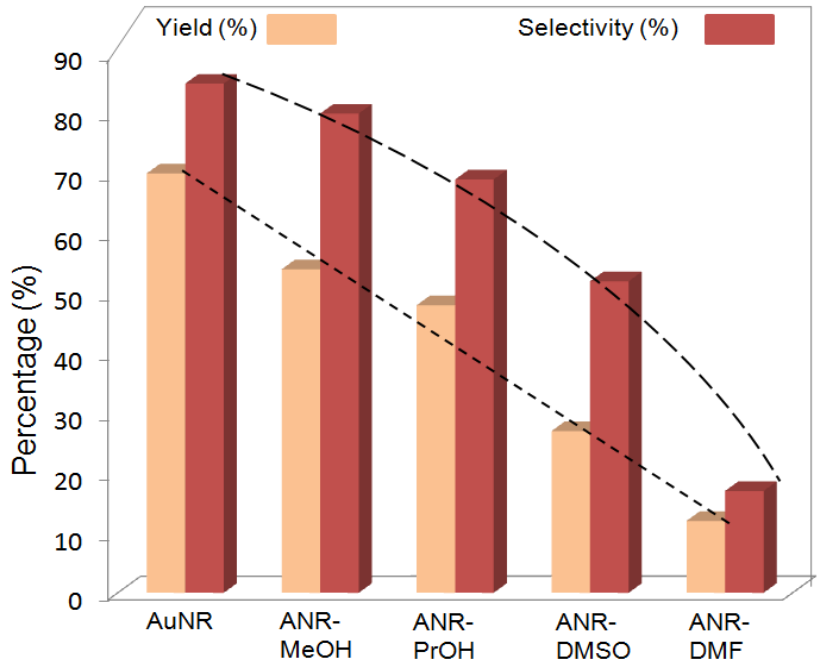

Figure 7. Yield and selectivity of PAP formation as a function of extent of aggregation.

4.3.5 Co-catalytic activity of AuNRs and ANR

The presence of metal NP co-catalyst on photo-catalyst (TiO_2) particles enhance the photocatalytic efficiency of TiO_2 through achieving efficient charge separation by preventing e^--h^+ pair recombination, which is sensitive to the size and shape of NP [22,23,36-38]. As discussed above, polar solvent dipolar interactions tend to align NRs in irregular or haphazard arrays of size ≈100-200 nm (confirmed from TEM) that create disparity in the distribution of ionic dipoles over the particle surface.

This disparity further influences adsorption/ desorption behavior among the reacting substrates and hence, affects the co-catalytic activity. ζ and conductance measurements revealed that ζ of TiO_2 (-2.80 mV) and SA (-7.07 mV) aqueous suspension was enhanced to ζ +43.51 mV for TiO_2 + SA aqueous mixture, reflecting stability of the reaction system. Moreover, higher conductance value 263 µS of SA solution is notably reduced to 13 µS after mixing of TiO_2 slurry (59 µS) to SA suspension, indicating the formation of SA-TiO_2 surface complexation through negative charges of –COOH and -OH groups of bidentate salicylate to TiO_2 surface [36]. The highly positive surface charge +2712.5 µeq/litre of AuNRs-H_2O (pH = 6.1) has also been significantly reduced to +255.0 µeq/litre in TiO_2+SA+AuNRs-H_2O (pH = 5.47) despite having low surface charge +161.1 µeq/litre in case of TiO_2+SA mixture (pH = 6.13). Similarly, the observed ζ value of +49.59 mV for AuNRs-H_2O and -4.65 mV for ANR-

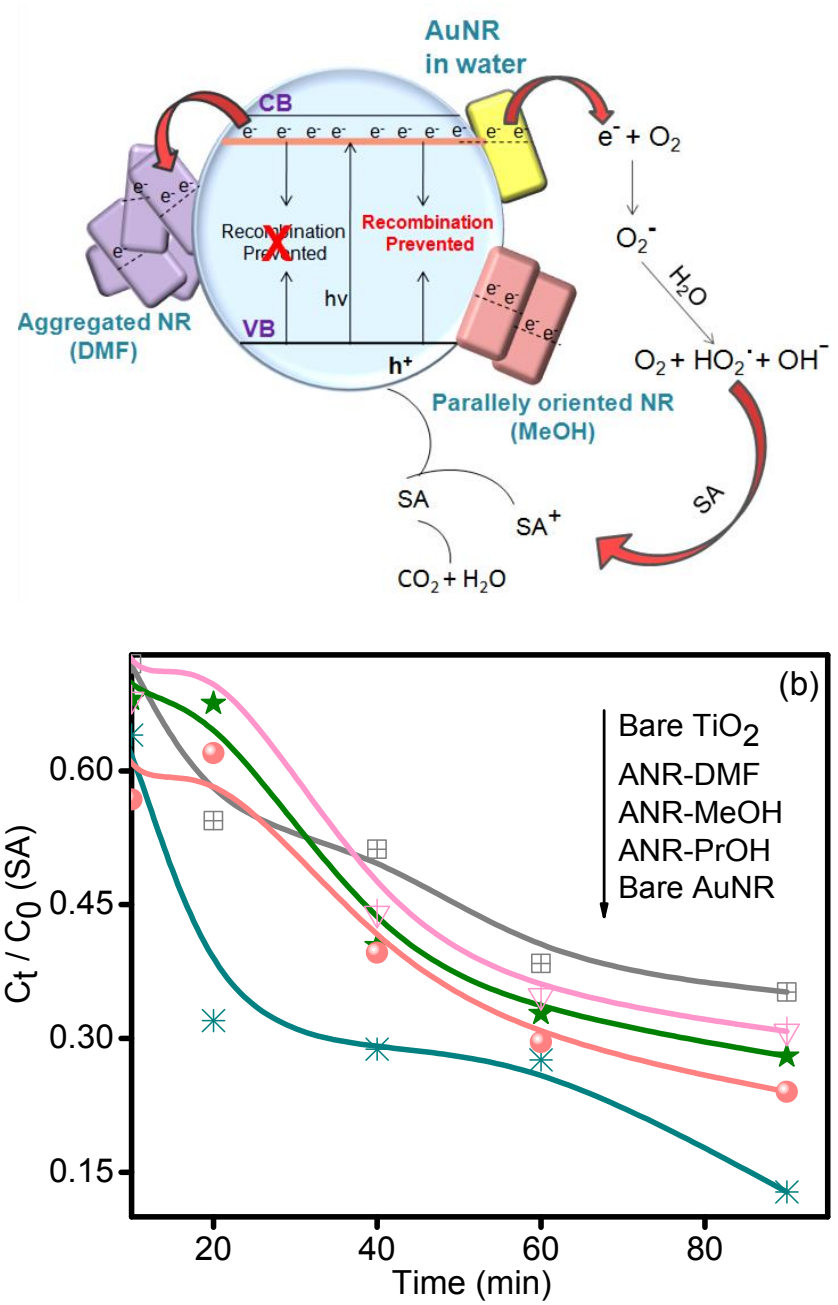

Figure 8. (a) Schematic representation of various agglomerated Au morphologies onto TiO_2 for tuning the rate of photocatalytic reaction (b) time course of salicylic acid photooxidation by bare and various ANR (formed in polar solvents)-TiO_2 under UV irradiation.

MeOH aqueous suspension were also dropped down to +31.88 mV and +16.88 mV, respectively, after their addition to SA + TiO_2 photoreaction system as described in table 1. Figure 8a demonstrates difference in the photocatalytic rate imparted by TiO_2 on mixing with AuNRs-H_2O and ANR-solvents for photooxidation of SA under UV irradiation as a function of NRs arrangement in polar solvents. Complete time course for SA oxidation with various ANR-solvent morphologies are shown in figure 8b. Concentration of SA is found to be exponentially ($C = C_0 e^{-kt}$) decreased with UV irradiation time (0 to 90 min) and the obtained SA degradation rate is found to be highest, $k = 8.4\times10^{-2}$ min^{-1} after AuNRs-H_2O mixing into SA+ TiO_2 suspension as compared to $k = 4.8\times10^{-2}$ min^{-1} for bare TiO_2 activity during 90 min UV irradiation. However, ANR mixing always retard the TiO_2 photoactivity (e.g., $k = 5.2\times10^{-2}$ min^{-1} for ANR-DMF) depending on the size of agglomerated moiety formed in polar solvents as shown in table 1. This variation in the catalytic reduction rate can be attributed to the nature of agglomerated AuNRs size of the cluster formed as a function of solvent dipole moments. Increase in the surface roughness, differences in the distribution of surface active atoms over the assembled moieties, nature of ionic interactions among the reacting substrates as a function of solvent polarity are the cause for discrepancy in the catalytic and co-catalytic behavior of AuNRs-water and ANR-solvents.

Solvent polarity is found to influence the optical, electrokinetic, structural, catalytic and co-catalytic properties of AuNRs. Since most of the Au catalyzed reactions utilize organic media, which in-turn results in the formation of aggregated morphologies and hence, true catalytic activity of single nanorods get hampered. But, alternatively by choosing an appropriate aggregated moiety (formed as a function of solvent dipole moment), one can easily tune the optimum catalytic activity.

4.4 References

[1] J. Liao, Y. Zhang, W. Yu, L. Xu, C. Ge, J. Liu and N. Gu, Colloids Surf. A., 223 (2003) 177.

[2] X. Hu, W. Cheng, T. Wang, E. Wang and S. Dong, Nanotechnology, 16 (2005) 2164.

[3] K.G. Thomas, S. Barazzouk, B.I. Ipe, S.T.S. Joseph and P.V. Kamat, J. Phys. Chem. B, 108 (2004) 13066.

[4] N. Varghese, S.R.C. Vivekchand, A. Govindaraj and C.N.R. Rao, Chem. Phys. Lett., 4 (2008) 340.

[5] S.T.S. Joseph, B.I. Ipe, P. Pramod and K.G. Thomas, J. Phys. Chem. B, 110 (2006) 150.

[6] H. Nakashima, K. Furukawa, Y. Kashimura and K. Torimitsu, Chem. Commun., (2007) 1080.

[7] H. Zhang, K.H. Fung, J. Hartmann, C.T. Chan and D. Wang, J. Phys. Chem. C, 112 (2008) 16830.

[8] A. Pescaglini, U. Emanuele, A.O. Riordan and D. Iacopino, J. Phys. Conf. Ser., 307 (2011) 1.

[9] B. Ozturk, C. Blackledge and B.N. Flanders, Appl. Phys. Lett., 88 (2006) 073108-1.

[10] S. Sun, C.B. Murray, D. Weller, L. Folks and A. Moser, Science, 287 (2000)1989.

[11] N. Wangoo, K.K. Bhasin, S.K. Mehta and R. Suri, J. Colloid Interf. Sci., 323 (2008) 247.

[12] S. Zhang, X. Kou, Z. Yang, Q. Shi, G.D. Stucky, L. Sun, J. Wang and C. Yan, Chem. Commun., (2007) 1816.

[13] C.J. Orendorff, P.L. Hankins and C.J. Murphy, Langmuir, 21 (2005) 2022.

[14] T.K. Sau and C.J. Murphy, Langmuir, 21 (2005) 2923.

[15] C.J. Orendorff, T.M. Alam, D.Y. Sasaki, B.C. Bunker and J.A. Voigt, ACS Nano, 3 (2009) 971.

[16] S.K. Ghosh and T. Pal, Chem. Rev., 107 (2007) 4797.

[17] B.R. Cuenya, Acc. Chem. Res. 46 (2013) 1682.

[18] M.A. Mahmoud, R. Narayanan and M.A. El-Sayed, Acc. Chem. Res., 46 (2013) 1795.

[19] S. Schauermann, N. Nilius, S. Shaikhutdinov and H.J. Freund, Acc. Chem. Res., 46 (2013) 1673.

[20] J. Zeng, Q. Zhang, J. Chen and Y. Xia, Nano Lett., 10 (2010) 30.

[21] R. Narayanan and M.A. El-Sayed, J. Phys. Chem. B, 109 (2005) 12663.

[22] A. Wood, M. Giersig and P. Mulvaney, J. Phys. Chem. B, 105 (2001) 8810.

[23] V. Subramanian, E.E. Wolf and P.V. Kamat, J. Am. Chem. Soc., 126 (2004) 4943.

[24] J.P. Juste, I.P. Santos, L.M. Liz-Marzan and P. Mulvaney, Coord. Chem. Rev., 249 (2005) 1870.

[25] B. Nikoobakht and M.A. El-Sayed, Chem. Mater., 15 (2003) 1957.

[26] R. Kaur and B. Pal, Colloids Surf. A., 441 (2014) 155.

[27] P.K. Jain, S. Eustis and M.A. El-Sayed, J. Phys. Chem. B, 110 (2006) 18243.

[28] P. Galletto, P.F. Brevet, H.H. Girault, R. Antoine and M. Broyer, J. Phys. Chem. B, 103 (1999) 8706.

[29] H. Chen, X. Kou, Z. Yang, W. Ni and J. Wang, Langmuir, 24 (2008) 5233.

[30] S. Kubo, A. Diaz, Y. Tang, T.S. Mayer, I.C. Khoo and T.E. Mallouk, Nano lett., 7 (2007) 3418.

[31] S. Park, N. Sinha and K.H. Schifferli, Langmuir, 26 (2010) 13071.

[32] N.R. Jana, Angew. Chem. Int. Ed., 43 (2004) 1536.

[33] P.R. Chandran, M. Naseer, N. Udupa and N. Sandhyarani, Nanotechnology, 23 (2012) 1.

[34] M. Moskovits and B. Vlckova, J. Phys. Chem. B, 109 (2005) 14755.

[35] S. Wunder, F. Polzer, Y. Lu, Y. Mei and M. Ballauff, J. Phys. Chem. C, 114 (2010) 8814.

[36] A.E. Regazzoni, P. Mandelbaum, M. Matsuyoshi, S. Schiller, S.A. Bilmes and M.A. Blesa, Langmuir, 14 (1998) 868.

[37] P.V. Kamat, J. Phys. Chem. C, 111 (2007) 2834.

[38] R. Kaur and B. Pal, J. Mol. Catal. A: Chem., 355 (2012) 39.

Chapter 5

Improved Surface Properties and Catalytic Activity of Polymorphic Facets of Photoetched Au Nanostructures Formed by Variable Energy Laser Exposure

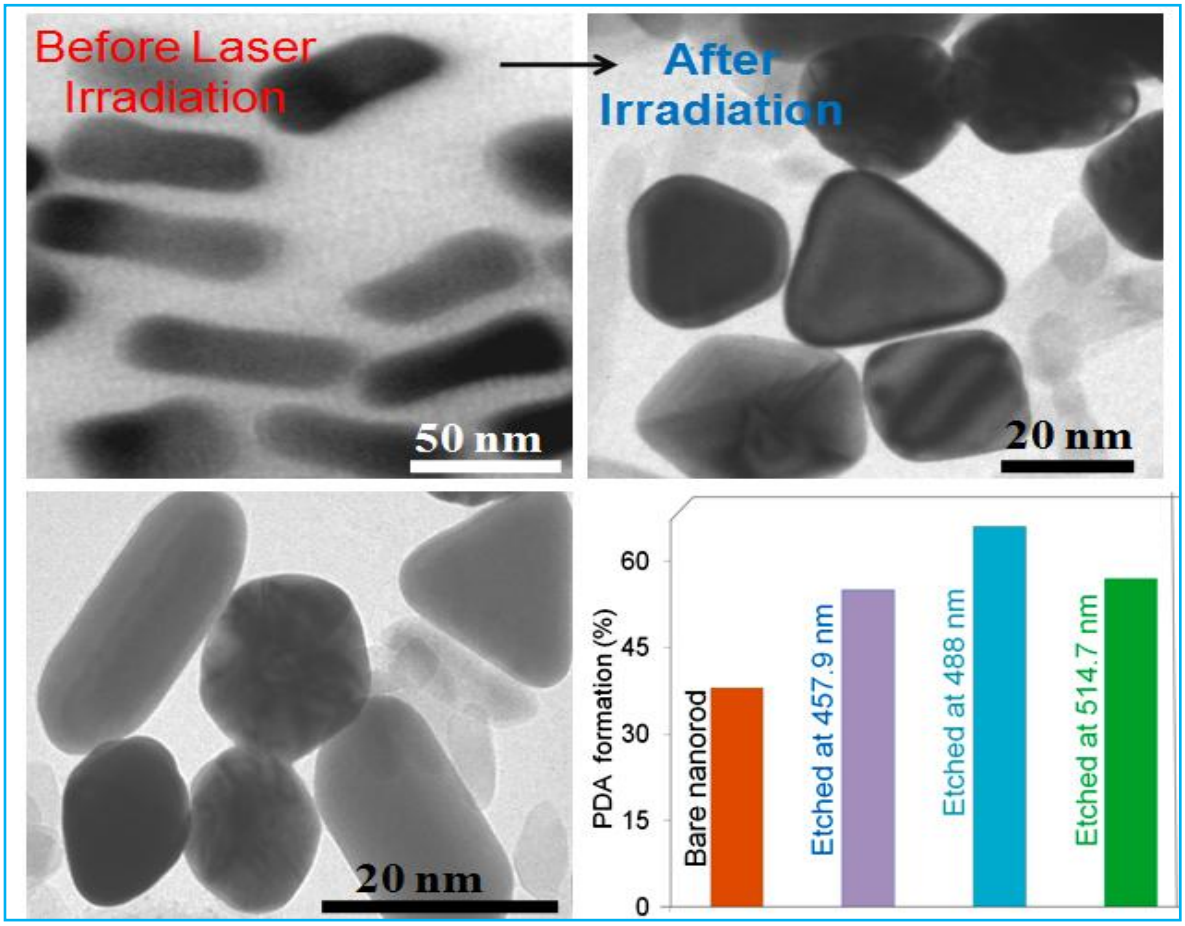

5.1 Introduction

The emergent opto-electronic [1-4] and catalytic properties [5,6] of metal nanoparticles (NPs) with various shapes are attracting a great deal of research importance, relative to their bulk counterparts. In nanocatalysis, structure-reactivity relationship is manifested in terms of NPs morphology determined by the high and low index planes, exposed crystallographic facets, number of atoms on the corners and edges, high density of atomic ledges, kinks, and dangling bonds that could considerably modify the catalytic property [5-10]. For example, studies have shown that high-index planes such as {210}, {410} and {557} of Pt generally exhibit much higher catalytic activity than that of the {111}, {100}, and {110} planes because these planes have high density of atomic steps and kinks which serve as active sites for breaking of chemical bonds [10]. The Ag nanocubes exposing more reactive {100} plane showed much improved activity than nanospheres and nanoplates having {111} plane [8].

Hence, multistep chemical procedures have been adopted [10-14] to synthesize Au nanocrystals (prisms, boxes, and cages, etc.) containing high index lattice planes and asymmetric facets possessing more surface exposed atoms for enhanced catalytic activity [10-17]. Like throwing a chalk or stone on the ground with different thrust would result into a number of small irregular pieces having new surface active atoms, edges and corners as shown in scheme 1. There is no such viable cost effective and single step mechanical process exists for the preparation of the different geometric morphology of metallic NPs except the laser mediated photo-thermal melting of Au nanostructure. Koda et al. [18] reported the AuNPs fragmentation into nanodots by 532 nm laser pulses and explained their results by slower heat transfer of the laser energy into the surrounding solvent which led to the melting and vaporization of the nanoparticles. Kamat et al. [19] demonstrated the photo-fragmentation of relatively large (40-60 nm) Ag colloids to smaller sized particles (5 nm diameter) on excitation with 355 nm picosecond laser pulses. Chang et al. [20] studied the photon-induced shape transition of the Au nanorod by different wavelength (532 and 1064 nm) of laser irradiation.

All previous studies explained the mechanism and optical properties of photofragmented Au morphology; however, their usage in catalysis applications was not explored. *These decomposed AuNPs over non-fragmented becomes especially significant when a large number of particles in a finely divided state offer more catalytic sites having fresh surface active atoms and enlarged per particle surface area.* These AuNPs have uneven or imbalance forces which in turn influence the electronic charge distribution that may alter the surface charge, zeta potential and conductance, therefore, the extent of interaction or

adsorption of reacting substrates with fragmented AuNPs could influence the industrial catalytic processes (scheme 1).

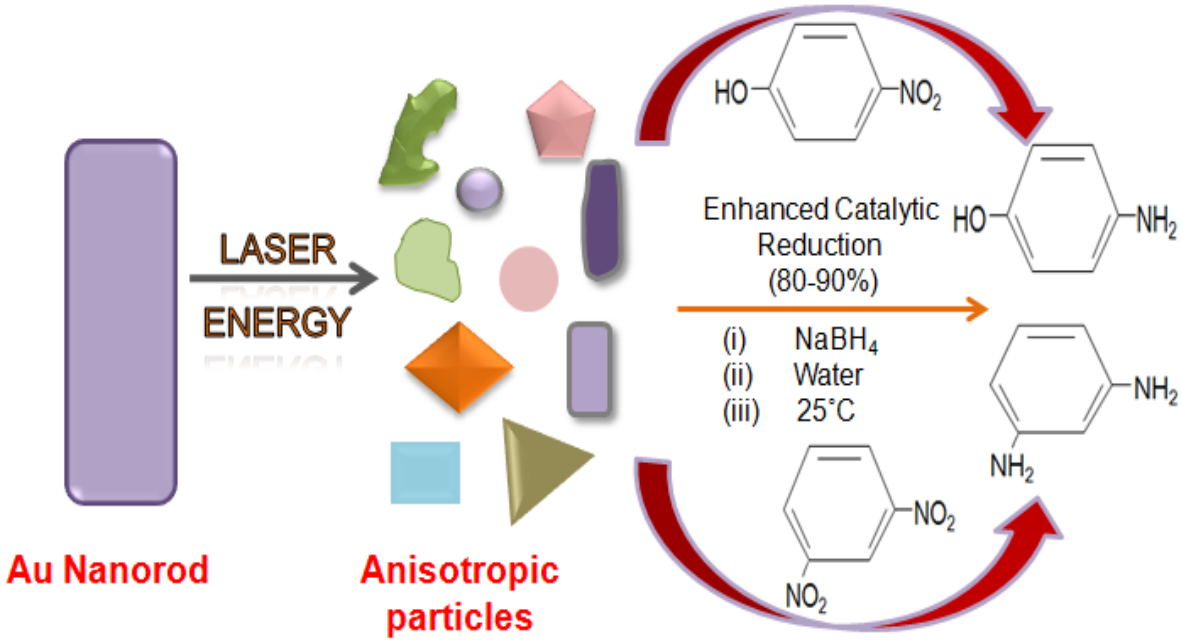

Scheme 1. Photodistortion of Au nanorod into irregular shaped particles by different energy laser exposure and their utilization in nitro aromatic reduction reactions.

Hence, we studied the impact of different wavelengths (457.9, 488 and 514.7 nm) of Ar ion laser irradiation for the fragmentation of AuNPs as a function of laser energy, illumination time and geometric shape and determined their various electro-kinetic properties and catalytic activity for reduction of p-nitrophenol and m-dinitrobenzene as compared with bare Au nanostructures before laser exposure.

5.2 Chemicals and materials

5.2.1 Material and methods

Chloroauric acid ($HAuCl_4.3H_2O$), sodium borohydride ($NaBH_4$), ascorbic acid ($C_6H_8O_6$), Silver nitrate ($AgNO_3$), *p*-nitrophenol (PNP) and *p*-aminophenol (PAP) were obtained from Loba Chemie, India. Cetyltrimethylammoniumbromide (CTAB), m-Dinitrobenzene (DNB) and m-Phenylenediamine (PDA) was purchased from Sigma Aldrich. All these chemicals were used as-received without any further purification. Deionized water was obtained using an ultrafiltration system (Milli-*Q*, Millipore) with a measured conductivity above 35 mho cm^{-1} at 25 ˚C.

5.2.2 Synthesis of Au nanospheres and nanorods

Au nanospheres (S-1) were synthesized via. well-known chemical route [21] comprising the addition of 250 µl (0.01 M) $HAuCl_4.3H_2O$ to 9.5 ml (0.1 M) CTAB, followed by reduction

with 600 µl (0.01 M) $NaBH_4$ solution under magnetic stirring for two minutes. Then, 12 µl of above solution was introduced into the mixture of 500 µl (0.01 M) $HAuCl_4.3H_2O$, 9.5 ml (0.1 M) CTAB and 55 µl ascorbic acid (0.1 M) at 0°C. The Au nanorod (R-1) was synthesized by seed mediated approach as reported [22, 23] i.e., by mixing 0.25 mM $HAuCl_4.3H_2O$, 0.368 g CTAB and 1 ml (0.01 M) ice cooled $NaBH_4$ solution in 10 ml aqueous solution that results in the formation of Au seeds. Further, $HAuCl_4.3H_2O$ (0.5 mM), CTAB (300 mg), 225 µl $AgNO_3$ (5 mM), 0.1 M ascorbic acid (250 µl) and 100 µl of Au seeds were added in 10 ml aqueous media in a separate beaker for the synthesis of AuNR. In a similar manner, NRs of different aspect ratio (R-2) was also prepared by varying the Au content (calculated from $HAuCl_4.3H_2O$) i.e, 0.0113 mg Au in seed and 0.98 mg Au in growth solution which was finally reduced to AuNRs. The obtained AuNPs and NRs were repeatedly washed with deionized water under four cycles of centrifugation at 8500 rpm for 10 minutes and then used for optical, structural, photoetching and catalytic analysis.

5.2.3 Laser irradiation and electro-kinetic analysis of Au nanostructures

S-1, R-1 and R-2 colloidal solutions (2 ml contains = 2.99×10^{18} Au atoms) were irradiated with monochromatic Ar ion laser light (Stellar-Pro-L Select 300) of different wavelengths ca. 457.9 nm (λ_1 = 2.71 eV), 488 nm (λ_2 = 2.5 eV)**,** and 514.7 nm (λ_3 = 2.41 eV) for various time intervals (0 to 32 h), respectively (table 1). Colloidal Au nanosphere suspension (ca. 2.99×10^{18} Au atoms) was placed in a 5 ml test tube kept at 15 cm away from the Ar ion laser beam (diameter of laser spot ~ 2 mm) under continuous magnetic stirring. This S-1 and R-1 AuNPs irradiated with λ_1, λ_2, and λ_3 are abbreviated as S-1@λ_1, R-1@λ_1, R-1@λ_2, and R-1@λ_3, respectively. The progress of etching of AuNPs on laser treatment has been analyzed by the changes in surface plasmon resonance band absorption intensity and TEM (Hitachi 7500, 2Å, 120 KV) shape analysis. The electrokinetic studies (zeta potential and conductance) were carried out by means of Brookhaven 7610 instrument by dispersing 20 µl (2.99×10^{16} atoms) etched and non etched Au nanoparticles in 1.5 ml aqueous solution.

5.2.4 Catalytic reaction

The catalytic reduction of *p*-nitrophenol and m-dinitrobenzene was carried out by adding 1 ml of 0.42 M ice-cold $NaBH_4$ solution to 7 ml of 0.2 mM PNP and/ or DNB, and the solution was vigorously stirred for 5 min at 25˚C. Calculated amount (20 µl = 2.99×10^{16} atoms) of the fragmented and non-fragmented S-1 and R-1 was added to initiate the reduction. The reduction process of PNP to PAP and DNB to PDA was monitored by measuring the absorption spectra (PNP-λ_{max} = 400 nm) and analyzed by high–performance

liquid chromatography (HPLC, Agilent, 1120 Compact LC, 254 nm, using C–18 column and MeOH: H_2O (70:30) as mobile phase) with a flow rate of 1ml/min.

5.3 Results and discussion

5.3.1 Optical properties of laser irradiated AuNPs

The impact of monochromatic laser irradiation of three different wavelengths (λ_1, λ_2, and λ_3) on the changes in the surface plasmon resonance (SPR) band of S-1 (533 nm, size ≈ 10-15 nm) and NR, R-1 (transverse band = 526 nm, longitudinal band = 642 nm and aspect ratio ≈ 2.8) at various time intervals are shown in figure 1.

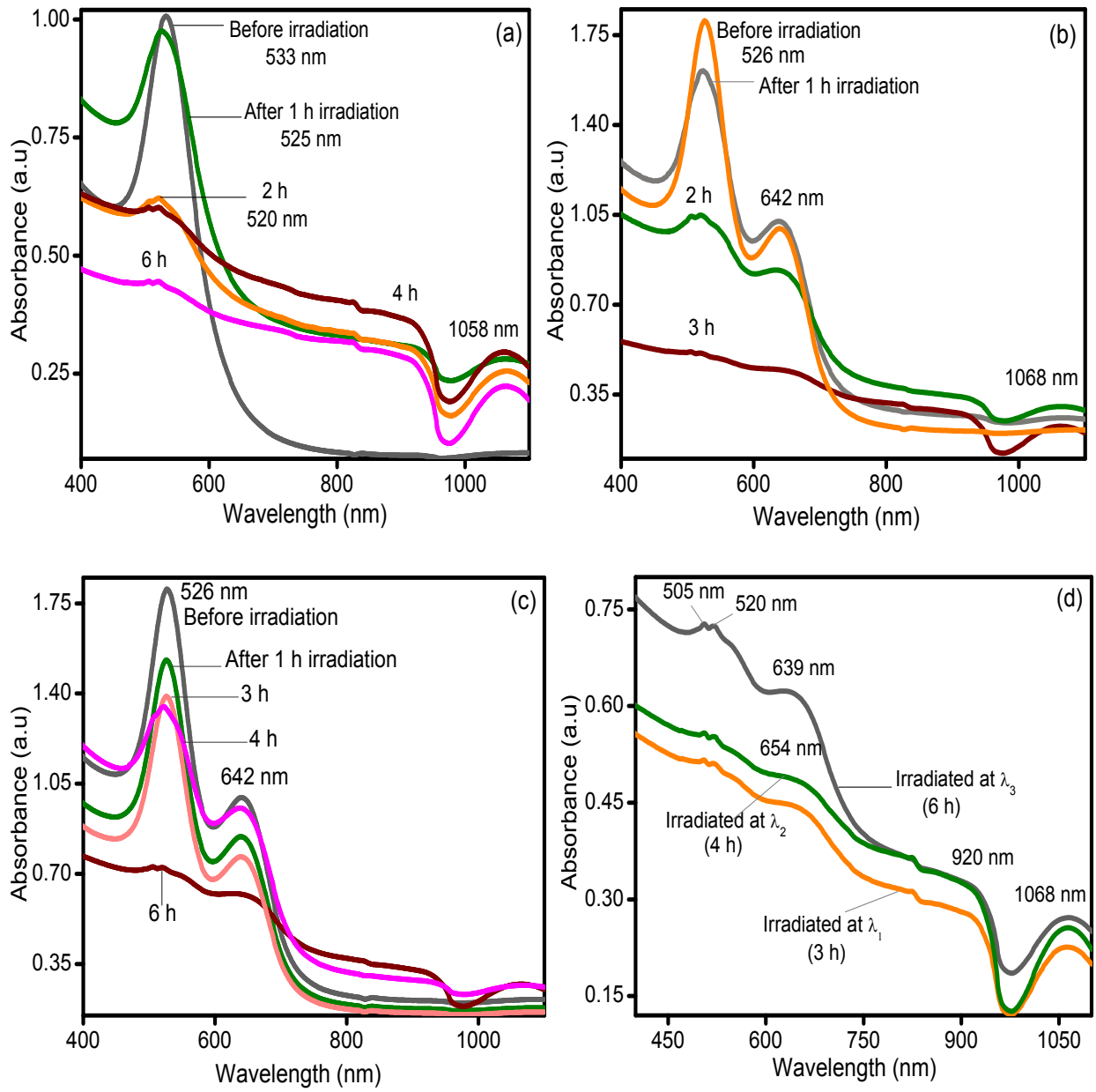

Figure 1. SPR absorption spectral changes of (a) Au nanospheres and (b) Au nanorods after laser irradiation with 457.9 nm, (c) 514.7 nm and (d) comparative variation of SPR band absorption intensity of Au nanorods during laser exposure with 457.9, 488 and 514.7 nm at various time intervals.

The transverse SPR band is blue shifted from 533 to 520 nm for S-1 and 526 to 518 nm for R-1 and becomes flattened with a relative decrease in the absorption intensity on increasing irradiation time from 0 to 6 h for S-1@λ_1 (fig. 1a), R-1@λ_1 (fig. 1b), and λ_3 (fig. 1c), respectively. The SPR band intensity after laser exposure is found to be always reduced than the parent AuNPs because of the smaller distorted Au particles without SPR absorption have been formed during the irradiation process [24]. Always a negative absorption ~ 970 nm and appearance of a low intense band at ~ 1060 nm have been noticed after laser irradiation with all wavelengths (λ_1, λ_2, λ_3). The photodistorted particles possess modified crystal faces with rough surfaces allowing surface electronic modes to differ over the surface of the nanostructure and results in anisotropic light absorption and scattering. The SPR band at ~ 1060 nm is due to the instantaneous aggregation of small NPs formed after laser irradiation. The oscillating electrons in one particle feel the electric field due to the oscillation of the free electrons in a second particle, which can lead to a collective plasmon oscillation of the aggregated system. Link et al. [4] has also shown that aggregation of AuNPs leads to another plasmon absorption at longer wavelengths when the individual NPs are electronically coupled to each other. Mafune et al. [25] observed that the heated nanoparticle fragmented into smaller nanoparticles with releasing atoms and clusters, promoting the coalescence of the melt colloids that grow to form assembled clusters during 532 nm laser exposures.

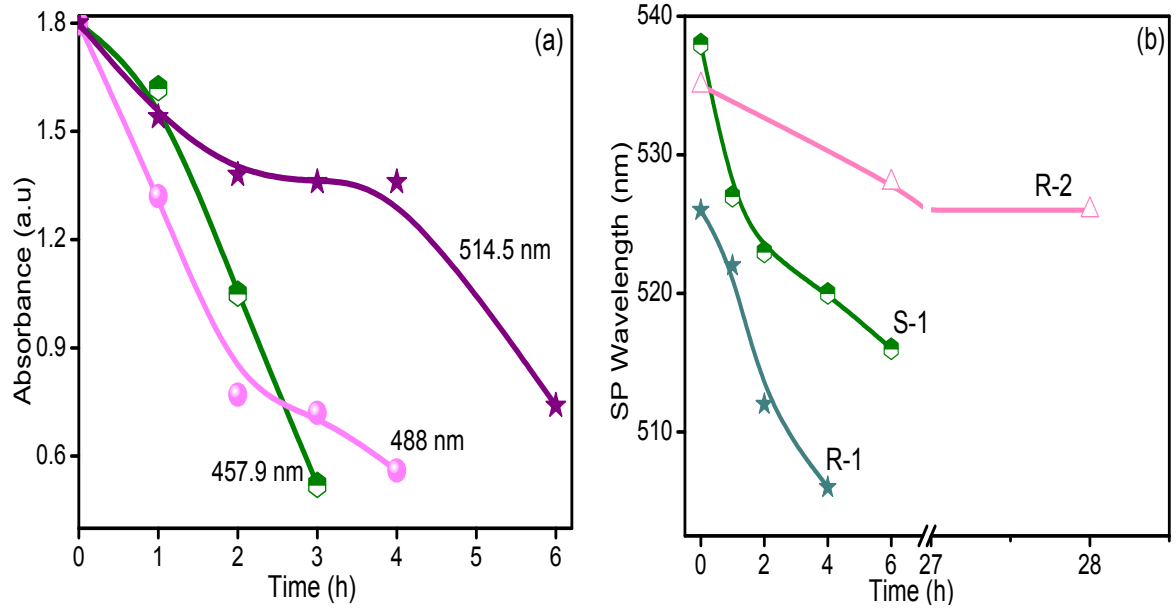

Figure 2. Effect of different energy laser irradiation on the SPR band absorption decay during Au nanorod (R-1) photoetching and (b) influence of AuNPs shape on the SPR band wavelength shifts as a function of laser (457.9 nm) exposure time.

Figure 1d demonstrates the comparative variation in the SPR absorption of R-1 during final hour exposure on irradiating with λ_1, λ_2 and λ_3 laser energies. It is seen that SPR absorption decreased to a maximum limit with highest energy exposure (λ_1 = 2.7 eV), whereas some distinct SPR bands are still visible with lower energy (λ_2 = 2.54 eV and λ_3 = 2.41 eV) irradiation. All these spectral changes i.e., the decrease of the peak height and the increase of the peak width by laser irradiation implies that the parent NPs are decomposed into smaller NPs in accordance with the Drude theory [25]. Furthermore, the broadening and absorptive dissipation of the resonance plasmon band is due to the difference in the surface scattering of conduction electrons that strongly dependent on the geometric dimensions of the nanoparticles. The localized electric field of the SPR band is also very sensitive to refractive index change [26], however, the measured refractive index (1.3323) of R-1 remains almost same even after irradiation at different laser wavelengths, indicating that SPR band shift might occur due to the surface morphological change of AuNPs upon laser illumination.

Figure 2a depicts the relative influence of different laser energies (λ_1, λ_2 and λ_3) on the decomposition rate of R-1, where R-1@λ_1 took only 3 h while low energy laser beams (λ_2 and λ_3) exposure need 4 and 6 h, respectively, for the complete flattening of transverse SPR absorption band (526 nm) as compared to initial absorption 1.8 a.u. for bare R-1. The exponential decay of SPR absorption of R-1 as a function of laser beam energy denoting the 1st order photofragmentation kinetics ($A_t = A_o e^{-kt}$), where A_t is the absorbance decay at time t and A_o is the initial absorbance of AuNPs before irradiation. The absorption decay rate constants (k) increase from 1.47×10^{-3} min^{-1} to 1.89×10^{-3} min^{-1} upon increasing laser energy from 2.41 eV (λ_3) to 2.7 eV (λ_1), irradiation, respectively. It is believed that the different energy laser beams excite the metallic electrons to a variable extent and results in the alternation in photodissolution rate of AuNPs and hence, higher energy beam (λ_1) results in the fast dissolution by 3 h irradiation only.

Figure 2b illustrates the influence of disintegration rate of S-1, R-1 and R-2 (transverse band = 560 nm, longitudinal band = 727 nm, and aspect ratio ≈ 3.6, has not been shown here) by 2.71 eV (457.9 nm) laser exposure as a function of AuNPs dimension. Again an exponential decrease (blue-shift) in the SPR band wavelength has been examined with increasing irradiation time (0 to 28 h) resembling the first-order ($\lambda_{SPR} = \lambda_{SPR}^{0} e^{-kt,}$) photoetching kinetics of AuNPs, where λ_{SPR} is the shift in SPR band wavelength after laser exposure time t and λ^{0}_{SPR} is the initial SPR band λ_{max} of AuNPs. The rate constant is determined to be the highest (k = 1.382 h^{-1}) for R-1 followed by 0.586 h^{-1} for S-1 and lowest for R-2 (0.015 h^{-1}), respectively. Furthermore, larger aspect ratio ~ 3.6 Au nanorod, R-2

taking longer time (28 h) laser exposure than 4 h for lower aspect ratio ~ 2.8, R-1 for their complete disintegration. Such difference in the photoetching kinetics can be interpreted to the disparity in breaking of many Au-Au metallic bonds depending on the dimension and per-particle mass of various Au nanostructures.

Table 1. Details of laser photoetched AuNPs and rate constants for catalytic reduction.

S.No.	Various Au nanostructures (Irradiation wavelength / nm)	Irradiation time (h)	Observed TEM particles shape and size	Rate constant k (min^{-1}) PNP reduction	Rate constant k (min^{-1}) DNB reduction
1.	Bare S-1	0	Spheres ≈ 15-20 nm	6.6×10^{-3}	2.1×10^{-2}
2.	S-1 (λ_1 = 457.9)	6	Quantum sized spheres (≈ 2-5 nm)	7.1×10^{-3}	2.4×10^{-2}
3.	Bare R-1	0	Length ≈ 20-27 nm Width ≈ 7-10 nm Aspect ratio ≈ 2.8	3.2×10^{-3}	1.8×10^{-2}
4.	R-1 (λ_1 = 457.9)	3	Small rods (aspect ratio≈ 2.1), Uneven particles and polygonal nanospheres (10-15 nm)	6.0×10^{-3}	2.0×10^{-2}
5.	R-1 (λ_2 = 488)	4	Polygonal nanospheres (15-20 nm)	6.6×10^{-3}	1.88×10^{-2}
6.	R-1 (λ_3 = 514.7)	6	Square shape, pentagonal, ice cube and irregular shapes (8-10 nm)	5.5×10^{-3}	1.94×10^{-2}

5.3.2 TEM size and shape analysis

Figure 3a showed the TEM images of R-1 (average length 20-27 nm and width 7-10 nm) having aspect ratio ≈ 2.8 prior to irradiation was reduced to lower aspect ratio 2.5 (length ≈ 18-22 nm and width ≈ 8-10 nm) and 2.0 (length ≈ 12-17 nm and width ≈ 6-8 nm) after 1 h and 2 h laser exposure with λ_1 as seen in figure 3b and 4a, respectively.

A variety of shapes such as polygonal multifaceted particles of sizes ~ 5-20 nm, (encircled in red, figure 3b), small nanorods of low aspect ratio, some spherical particles (15-20 nm) with modified geometrical faces are seen in the TEM image. On further irradiation upto 3 h (figure 4b), R-1 transforms to very small spheres, oval egg shaped particles, and irregular morphology which seems to be formed on the melting of longitudinal end of R-1 (marked in red), suggesting the gradual dissolution or removal of atomic layers from AuNPs surface.

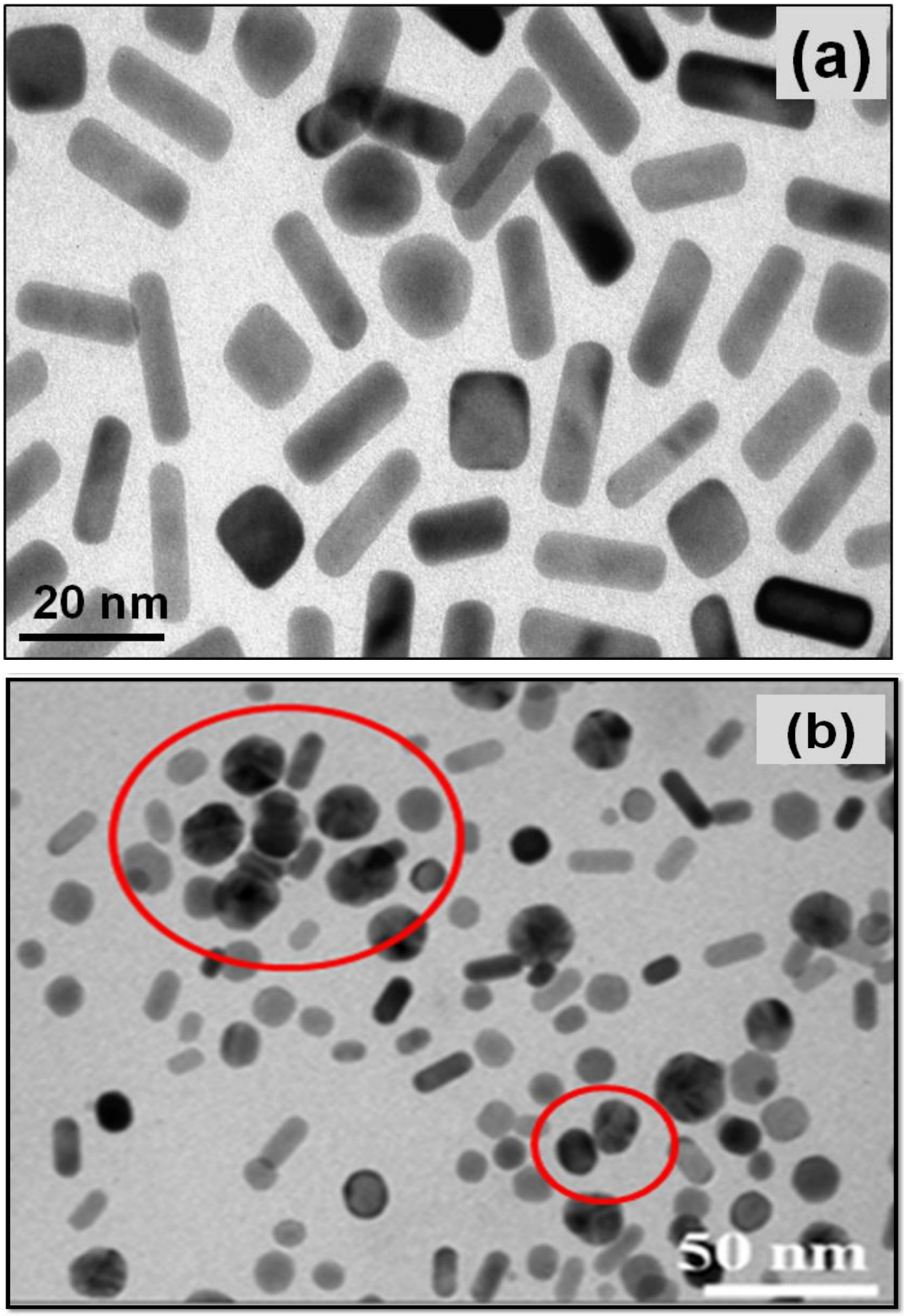

Figure 3. TEM images of Au nanorods (aspect ratio ≈ 2.8) (a) before laser irradiation and after (b) 1 h photoetching with 457.9 nm laser irradiation.

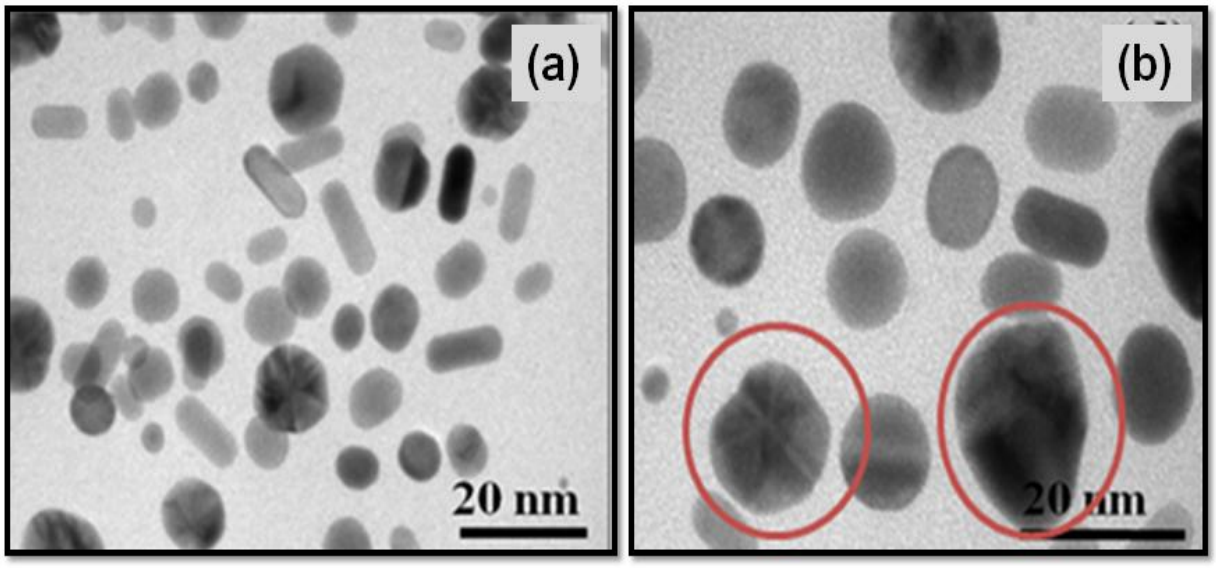

Figure 4. TEM images of Au nanorods after (a) 2 h and (b) 3 h photoetching with 457.9 nm laser irradiation.

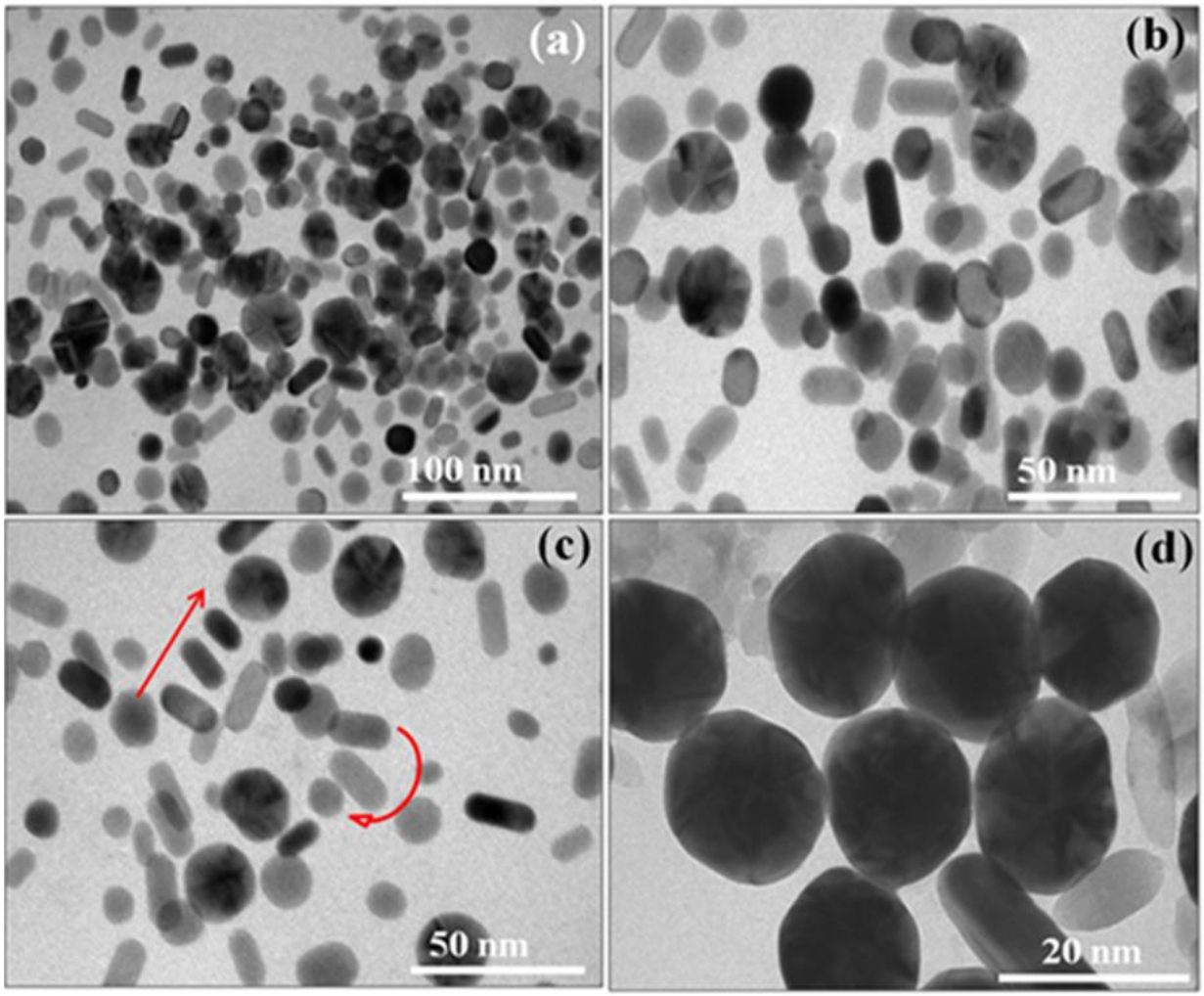

Figure 5. TEM images of photoetched Au nanorod after (a-b) 2 h (c) 3 h and (d) 4 h laser (488 nm) irradiation.

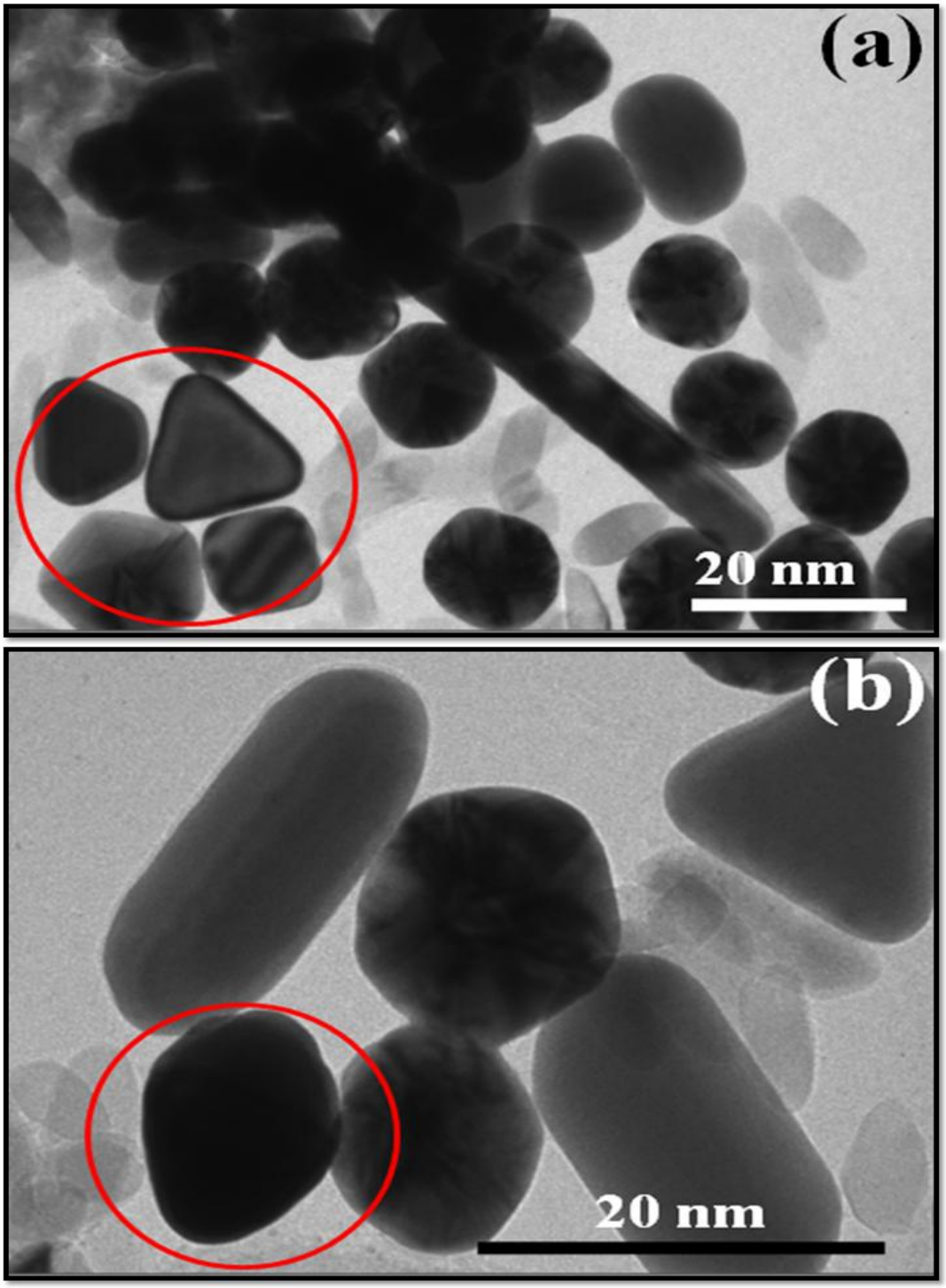

Figure 6. TEM morphologies of photofragmented Au nanorods after 6 h laser (514.7 nm) irradiation.

Such laser induced formation of cylinders or spheres, bent and twisted Au nanorods and a variety of irregularly shaped Ag particles are also reported by Link et al. [4] and Kaempfe et al. [27] Influence of λ_2 on the morphological changes of R-1 at different time (0 to 4 h) of irradiation has been displayed in figure 5. The R-1 aspect ratio (≈ 2.8) progressively reduced to ≈ 2.5 (length $\approx$ 19-24 nm and width $\approx$ 7-9 nm) and 2.1 after 2 h and 3 h laser exposure, respectively, as shown in figure 5a to 5c. The event of fragmentation can be comprehend in

figure 5c where a large NR disintegrates into smaller NR and spherical particle (indicated by arrow) on the dissipation of laser energy and it resembles the breakdown of blackboard chalk on employing different thrust as per scheme 1.

The formation of polygonal anisotropic Au nanostructures (size ≈ 15-20 nm) looks like football shape having round edges and corners formed on irradiating R-1@λ_2 for 4 h (figure 5d). Multiple shaped particles (encircles area in red) such as ice cubes like structure (~ 7 nm), truncated triangle (~ 7-8 nm), pentagonal (~ 12 nm), nanocapsules, square particle (~ 8 nm) and polygonal nanospheres (~ 8-12 nm) has been seen in figure 6 as a result of R-1 irradiation @λ_3. Each of this shape has its characteristic property with different geometric faces formed in a single step on laser exposure without employing any external chemicals. Different laser energies excite the particles to a varied extent and hence results in anisotropic shapes.

5.3.3 Electrokinetic properties of AuNPs

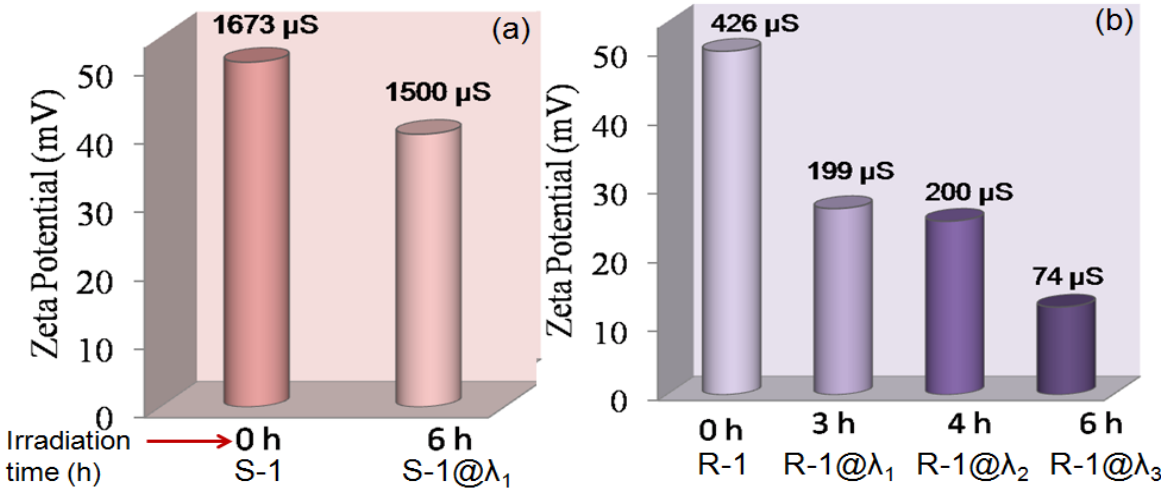

Figure 7. Variation in zeta potential and conductanc of bare and photofragmented Au nanostructures (a) spherical and (b) nanorod by different energy of laser exposure at various time intervals.

Zeta potential (ζ) is a function of surface charge determines electrostatic repulsive interaction between colloidal particles and commonly used to predict dispersion stability [28]. Figure 7 shows the variation in the ζ and conductance of AuNPs on irradiating with three different laser beams during their final hours of exposure. A general decrease in ζ and conductance value of various nanostructures has been observed, ζ of the S-1 (≈ +50.32 mV) has been lowered down to +39.8 mV (S-1@λ_1) in figure 7a and ζ for R-1 (≈ +49.79 mV) is reduced to +26.98, +25.15 and +12.71 mV (figure 7b) on irradiating with 457.9, 488 and 514.7 nm, respectively. This lowering in the ζ can be assigned to the attraction interaction among the

NPs resulting in the formation of small aggregated moieties. As conductance is associated with the movement of ionic/ electronic species and hence, decrease in its value (426 to 74 μS) confirming (figure 7b) the phenomenon of agglomeration.

Another probable reason may be the decrease in the net electronic charge on the smaller AuNPs surface due to the adsorption of the ionic species from the surrounding media or due to the formation of hydro-oxide layer or on the NP surface. Au atoms at the surface of the particles are coordinatively unsaturated, that is, highly unstable states are available to donate electron density and form Au^{+3}, may be one of the causes for the aggregation and thereby altering the various electro-kinetic parameters.

5.3.4 Catalytic reduction of p-nitrophenol and m-dinitrobenzene

Au nanostructures (2.99×10^{16} Au atoms) before and after laser irradiation have been used for the selective reduction of PNP (figure 8a) and DNB (figure 9) by $NaBH_4$ to PAP and PDA, respectively. As the amount of $NaBH_4$ (410 μmol) greatly exceeds 1.4 μmol of PNP which is higher than 0.0049 μmol of Au catalyst, PNP reduction must occur due to Au catalysis irrespective of $NaBH_4$ concentration.

An exponential decrease in the amount of PNP (figure 8a) with gradual increase in PAP formation by various AuNPs was observed at different reaction time. It

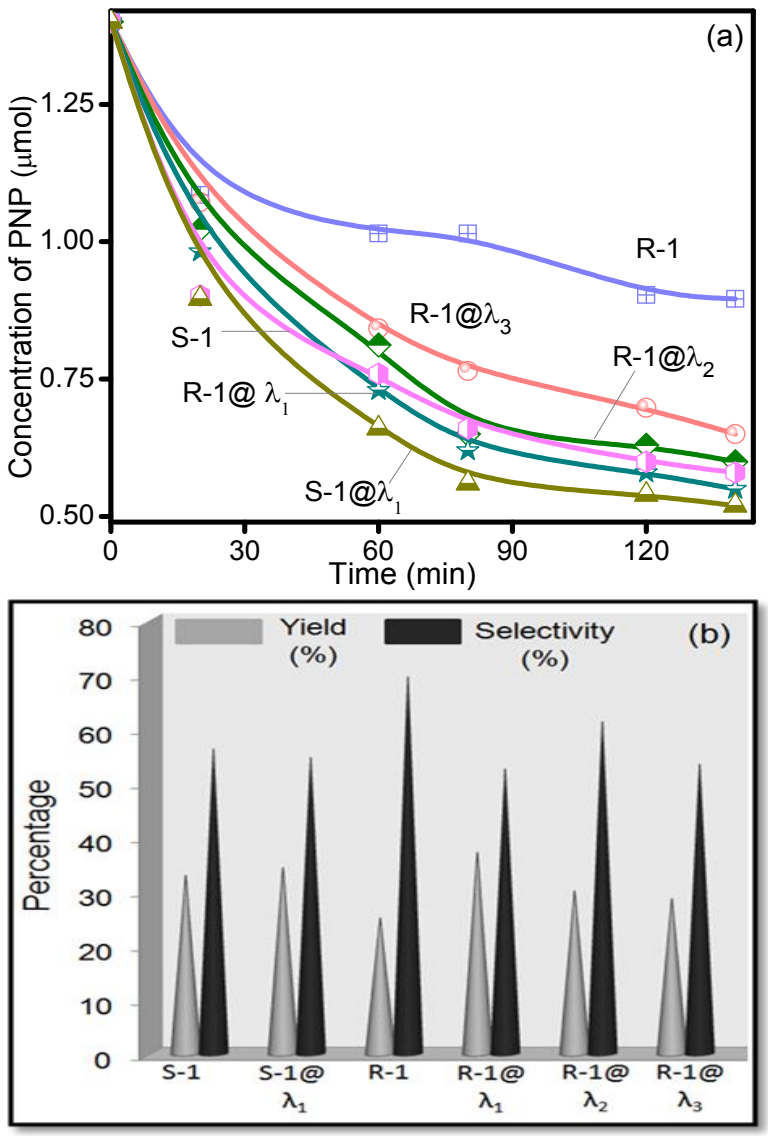

Figure 8. Catalytic activity for PNP reduction by various polymorphic AuNPs (S-1 and R-1) formed after three different wavelengths of laser exposure: (a) reduction rate and (b) yield and selectivity of PAP formation.

follows the pseudo-first-order kinetics ($C = C_0 e^{-kt}$), where the rate constants k for PNP reduction by different Au catalysts was significantly improved after laser treatment with different wavelength of laser irradiation. It is found that photofragmented AuNPs, S-1@λ_1 (k = 7.1×10^{-3} min^{-1}) and R-1@ λ_1 (k = 6.0×10^{-3} min^{-1}) always displayed enhanced PNP reduction with the extent of AuNPs photoetching rate by increasing energy of laser exposure as compared to bare S-1 (k = 6.6×10^{-3} min^{-1}) and R-1 (k = 3.2×10^{-3} min^{-1}) AuNPs of without laser treatment as shown in table 1.

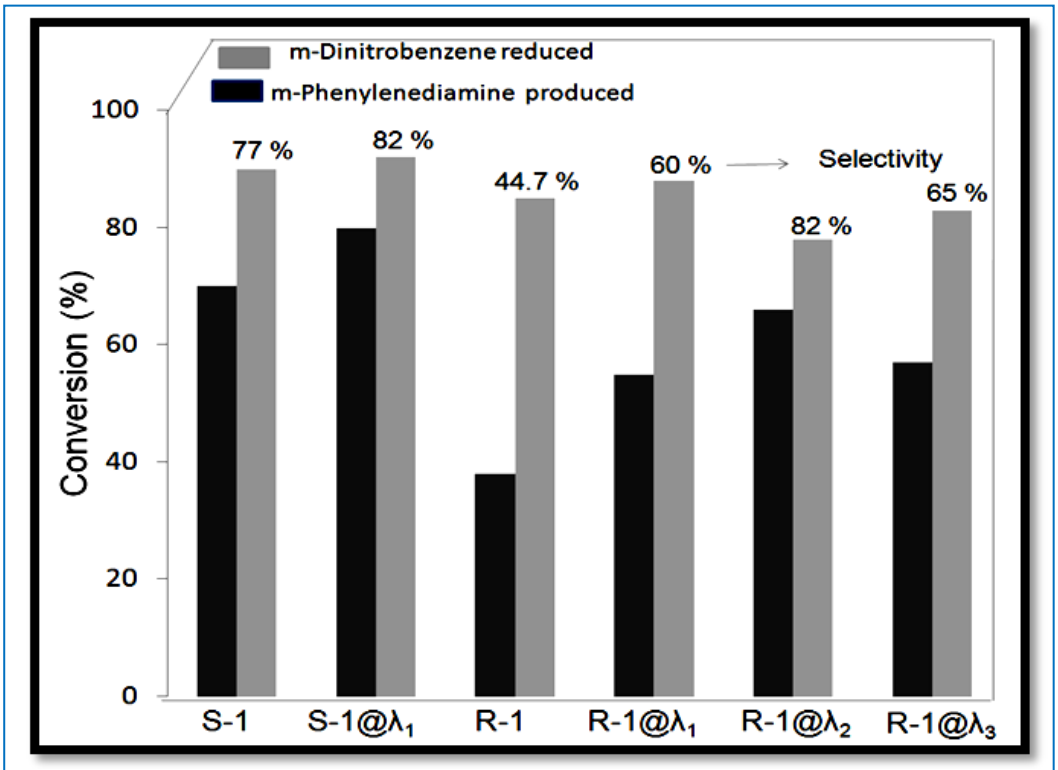

Figure 9. Catalytic reduction of m-dinitrobenzene (DNB, 0.2 mM) to m–pheneylenediamine (PDA) by bare and photofragmented AuNPs obtained after different energy of laser irradiation.

Also percentage yield of PAP formation is appreciably increased as 40% (R-1@λ_1) > 30% (R-1@λ_2) > 28% (R-1@λ_3) by photoetched AuNPs treated with decreasing laser energy relative to 25% of bare R-1 particles and selectivity varied in the range of 50-70% (figure 8b) as quantified by HPLC analysis. Similarly, the amount of DNB reduced ~ 92 % for S-1@λ_1 and ~ 88% for R-1@λ_1 is quite higher relative to 88% and 82% for bare S-1 and R-1 catalysts, respectively, as shown in figure 9. The improved PDA yield ~ 80% and 66 % has been observed by laser photoetched particles (S-1@λ_1 and R-1@λ_1) as compared to ≈ 38 % for S-1 and ≈ 55 % for R-1 particles and PDA selectivity (44-82%) varied in the same extent as quantified by HPLC analysis (figure 10). Thus, the catalytic activity was found to be highly improved by the photosplited AuNPs as a function of dimensions, high surface to

volume ratio, different geometric facets or surface exposed planes of Au nanocatalysts obtained by various energy of laser irradiation at different time intervals. In contrary to high catalytic performance, the zeta potential of the photoetched AuNPs drop down after laser irradiation representing unstable agglomerated system. The irradiation directs the renewal of NPs surface by the removal of adsorbed foreign material, leads to high surface charged particles and the neutralization of these charged species via. electronic interactions results in the lowering of zeta potential.

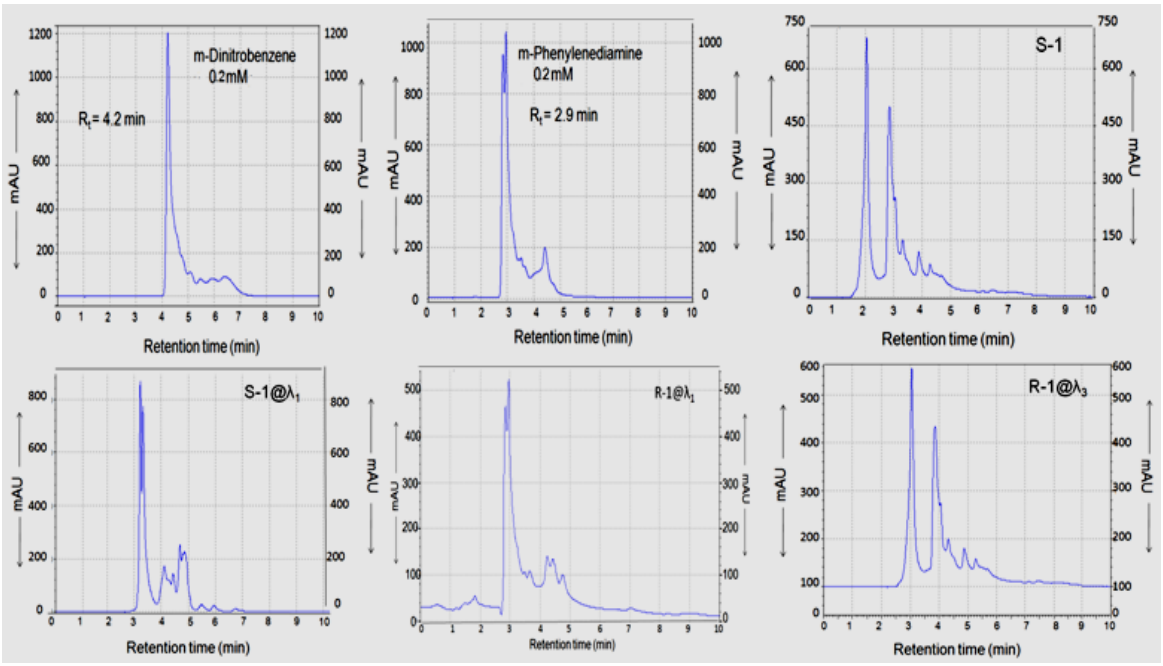

Figure 10. HPLC chromatograms of m-dinitrobenzene reduction to m-phenylenediamine using various Au catalysts after 1 h.

The quantum sized AuNPs (1-2 nm, S-1@λ_1) with rough and uneven surfaces with large number of low-coordinated Au atoms located at the edges and corners of AuNPs offer more adsorption and catalytic sites. In addition, photoetched Au particles being smaller in size (≈ 3-5 times) with higher per-particle surface area (765.84 nm^2), exposed fresh surface atoms and high surface to volume ratio (S/V = 0.64 nm^{-1}, R-1@λ_2) in comparison to bare nanorods (R-1) with lesser surface area (672 nm^2), S/V ratio (0.52 nm^{-1}) are believed to be the cause of high catalytic activity. Theoretically calculated molecular ratio of AuNPs to PNP/DNB molecules suggests that ~ 289 molecules of PNP/DNB are reduced by a single non-irradiated Au particle. However, as number of fragmented AuNPs (1 particle splits into 3 or more) is increased after laser exposure though atomic concentration remains constant, the catalytic reactivity of photoetched AuNPs is enhanced by almost threefold, i.e., ~ 867 molecules can take part in thermal catalysis with a much faster reduction rate by effective usage of nanoscale Au catalysts. Literature reveals [29] that the transfer of hydride from BH_4^- to a

nanoparticle surface followed by adsorption of nitrophenolate ions and reduction of the nitro group is achieved with hydride transfer from the surface to the adsorbed species. Hence, the mechanism depends on the nature of the surface of the adsorbent, i.e., nanoparticles and adsorption constant of both of the species.

Thus, laser irradiation provides a cost effective facile route for the synthesis of multiple shaped particles in a single step. These small sized and anisotropic photo-fragmented AuNPs exhibits superior properties because of the emergence of new surfaces/edges/corners etc. As a consequence of laser irradiation, geometric shape, dimensionality, size, percentage of surface active atoms, surface area, surface to volume ratio, etc., has been drastically enhanced which displayed alteration in optical and electrokinetic properties and highly enhanced catalytic activities.

5.4 References

[1] K.S. Lee and M.A. El-Sayed, J. Phys. Chem. B, 110 (2006) 19220.

[2] A. Moores and F. Goettmann, New J. Chem., 30 (2006) 1121.

[3] P.K. Jain, K.S. Lee, I.H. El-Sayed and M.A. El-Sayed, J. Phys. Chem. B, 110 (2006) 7238.

[4] S. Link and M.A. El-Sayed, J. Phys. Chem. B, 103 (1999) 8410.

[5] R. Narayanan and M.A. El-Sayed, J. Phys. Chem. B, 109 (2005) 12663.

[6] B.R. Cuenya, Acc. Chem. Res., 46 (2013) 1682.

[7] C.Y. Chiu, P.J. Chung, K.U. Lao, C.W. Liao and M.H. Huang, J. Phys. Chem. C, 116 (2012) 23757.

[8] R. Xu, D.S. Wang, J.T. Zhang and Y.D. Li, Chem. Asian J., 1 (2006) 888.

[9] N.M. Andoy, X. Zhou, E. Choudhary, H. Shen, G. Liu and P. Chen, J. Am. Chem. Soc., 135 (2013) 1845.

[10] N. Tian, Z.Y. Zhou, S.G. Sun, Y. Ding and Z.L. Wang, Science, 316 (2007) 732.

[11] Y. Chen, X. Gu, C.G. Nie, Z.Y. Jiang, Z.X. Xie and C.J. Lin, Chem. Comm., 33 (2005) 4181.

[12] S.E. Skrabalak, J. Chen, Y. Sun, X. Lu, L. Au, C.M. Cobley and Y. Xia, Acc. Chem. Res., 41 (2008) 1587.

[13] M. Hu, J. Chen, Z.Y. Li, L. Au, G.V. Hartland, X. Li, M. Marquez and Y. Xia, Chem. Soc. Rev., 35 (2006) 1084.

[14] P.R. Sajanlal, T.S. Sreeprasad, A.K. Samala and T. Pradeep, Nano Reviews, 2 (2011) 5883.

[15] M.A. Mahmoud, R. Narayanan and M.A. El-Sayed, Acc. Chem. Res., 46 (2013) 1795.

[16] Y. Lee, A. Loew and S. Sun, Chem. Mater., 22 (2010) 755.

[17] J. Zeng, Q. Zhang, J. Chen and Y. Xia, Nano Lett., 10 (2010) 30.

[18] A. Takami, H. Kurita and S. Koda, J. Phys. Chem. B, 103 (1999) 1226.

[19] P.V. Kamat, M. Flumiani and G.V. Hartland, J. Phys. Chem. B, 102 (1998) 3123.

[20] S.S. Chang, C.W. Shih, C.D. Chen, W.C. Lai and C.R. Chris Wang, Langmuir, 15 (1999) 701.

[21] R. Fenger, E. Fertitta, H. Kirmse, A.F. Thuemann and K. Rademann, Phys. Chem. Chem. Phys., 14 (2012) 9343.

[22] J.P. Juste, I.P. Santos, L.M. Liz-Marzan and P. Mulvaney, Coord. Chem. Rev., 249 (2005) 1870.

[23] B. Nikoobakht and M.A. El-Sayed, Chem. Mater., 15 (2003) 1957.

[24] Z. Peng, T. Walther and K. Kleinermanns, J. Phys. Chem. B, 109 (2005) 15735.

[25] F. Mafune, J. Kohno, Y. Takeda and T. Kondow, J. Phys. Chem. B, 106 (2002) 8555.

[26] N. Ahamad, A. Bottomley and A. Ianoul, J. Phys. Chem. C, 116 (2012) 185.

[27] M. Kaempfe, H. Hofmeister, S. Hopfe, G. Seifert and H. Graener, J. Phys. Chem. B, 104 (2000) 11847.

[28] T. Kim, K. Lee, M.S. Gong and S.W. Joo, Langmuir, 21 (2005) 9524.

[29] S. Sarkar, A.K. Sinha, M. Pradhan, M. Basu, Y. Negishi and T. Pal, J. Phys. Chem. C, 115 (2011) 1659.

Chapter 6

Co-catalysis Effect of Different Morphology of Ag Nanostructures for the Photocatalytic Oxidation Reaction by Ag-TiO_2 Photocatalysis

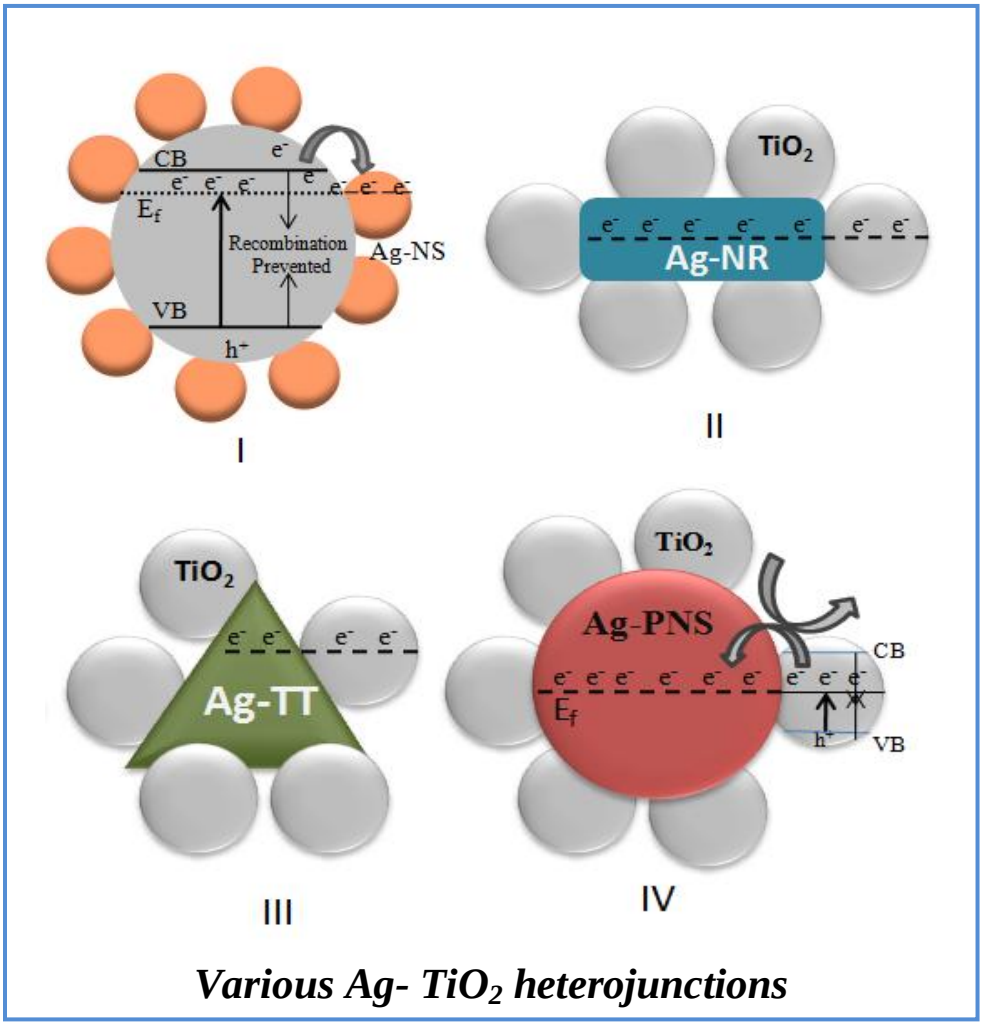

Various Ag- TiO_2 heterojunctions

6.1 Introduction

Metal-semiconductor nanocomposites have been widely employed to enhance the overall photocatalytic efficiency as metal facilitates the storing and shuttling of photogenerated electrons from the semiconductor to an acceptor and hence, exhibiting a shift in the Fermi level to more negative potential [1-4]. Studies have shown that transition metal (Pt, Au, Ag, Cu, etc.) loaded or doped semiconductors [5-9] allows the extension of the light absorption of wide band gap semiconductors to the visible light and results in enhanced quantum yield. Zheng et al. [8] prepared noble-metal plasmonic photocatalysts, M@TiO_2 (M = Au, Pt, Ag) by employing in situ method and evaluated photocatalytic properties under visible light by monitoring the oxidation of benzene to phenol.

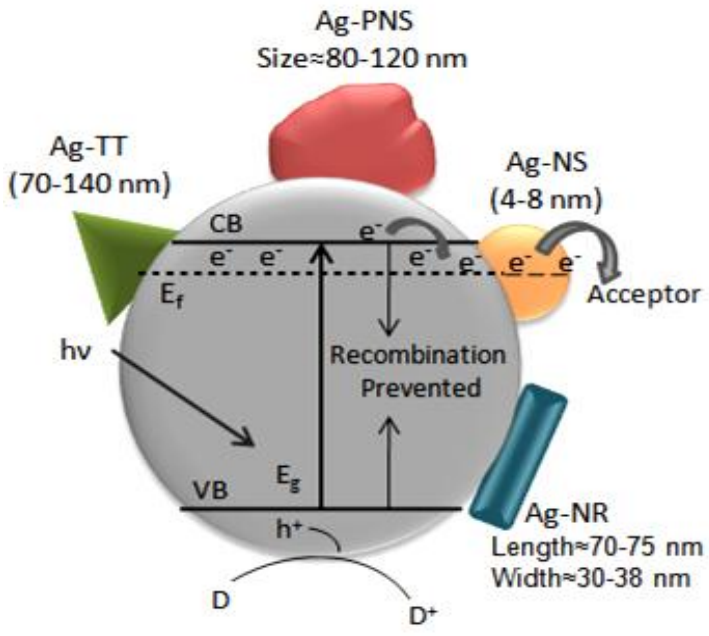

Scheme 1. Design of various Ag nanostructures addition to TiO_2 photocatalyst.

The metal-semiconductor catalysts have been traditionally prepared [1,10] by precipitation deposition, wet-impregnation and photoreduction methods under UV irradiation, results in the formation of spherical aggregated nanodeposits on TiO_2 surface and hence, restricts morphological dependent co-catalytic effect as already discussed in previous chapters. It has been proposed that addition of dissolved transition metal ions to the semiconductor suspension can significantly influence the overall energetics of the photocatalytic process [11-13] such as modification of TiO_2 with $[Pt_3(CO)_6]_n^{2-}$ clusters or Pt ions [14] can enhance the photoconversion yield by inhibition of the electron hole recombination. Sclafani et al. [15] investigated the influence of Fe^{3+}, Fe^{2+} and Ag^{+} on the photocatalytic degradation of phenol in aqueous anatase and rutile TiO_2 dispersions. However, metal ion addition to the semiconductor does not provide permanent contact between the two, but it can be explained in terms of space-charge layer formation at interface which improves charge separation under band gap excitation, when both

the reacting species come in contact under continuous stirring. Platinum metal, on the other hand, introduces ohmic contact facilitating a quick transfer of electrons to the electrolyte [3]. Composite films based on TiO_2 and metal (Au, Pt, Ir) nanostructures have shown higher photocurrent and photovoltage and increasing charge separation. Despite a large number of investigations reported in the literature, the factors responsible for improved performance in metal-semiconductor nanocomposites are yet to be understood fully.

Among these metals, cost effective Ag nanoparticles (NPs) are of particular interest due to its applications [5,10,16,17] as an antimicrobial, antifungal and effective co-catalyst with favorable Fermi level. If such metal (Ag) nanoparticles suspended with a charged semiconductor nanostructure, the Fermi levels of the two systems will equilibrate. One factor that can potentially influence the electronic properties of the nanocomposite is the dimensionality of the metal nanoparticle that has not been studied well. The influence of particle shape on the catalytic activity depends on the density of the active corner/edge which correlates with strong surface activity such as binding/adsorption of substrate over the active sites. This correlation is attributed to the fact that nanocrystals of different morphologies have different facets with different fractions of atoms located at different corners, edges, and different defect sites.

While most of the reported studies characterize the TiO_2-core metal-shell composites [1-4], i.e., large sized catalyst and smaller sized co-catalyst (8 to 10 times smaller than catalyst) which leaves the majority of metal surfaces unused. *Therefore, it is important to develop ways of tailoring the design of new nanocatalyst systems with controlled sizes and shapes that result in high catalytic activity.* Among these factors, the nature of the substrate species (either neutral or ionic) are also expected to play a major role by giving the tendency to efficiently adsorb over the catalytic moieties and resulting in the overall photocatalytic rate. Therefore, in this regard, salicylic acid (SA) with polar –COOH and –OH groups and benzoic acid (BA) with –COOH group has been chosen as model compound to investigate the comparative co-catalytic effectiveness of morphologically varied Ag nanostructures imparted to TiO_2 for their photooxidation (under UV irradiation). *Ag polygonal nanospheres (Ag-PNS), nanorods (Ag-NR) and truncated triangles (Ag-TT) of much larger size (70-140 nm) than TiO_2 photocatalyst (25-40 nm) and small Ag nanospheres (Ag-NS of size = 4-8 nm) are prepared and employed as co-catalyst for the improvement of TiO_2 photocatalysis.* Scheme 1 demonstrated how various shapes

and sizes of Ag co-catalysts (larger as well as smaller than TiO_2) with different surface area per particle will interact with TiO_2 catalyst for the optimum photocatalytic activity.

6.2 Experimental section

6.2.1 Materials

Silver nitrate ($AgNO_3$) was purchased from Fischer Scientific. Polyvinyl pyrollidone (PVP), dimethylformamide (DMF), salicylic acid (SA) and benzoic acid (BA) were obtained from Loba chemie, India. P25-TiO_2 photocatalyst (size 30-50 nm, 70% anatase and 30 % rutile) is provided as a gift sample from Degussa Company, Germany. All the chemicals were used as-received without any further purification. De-ionized water was obtained using an ultra filtration system (Milli-*Q*, Millipore) with measured conductivity above 35 mho cm^{-1} at 25 °C.

6.2.2 Synthesis of Ag nanoparticles of different shapes and sizes

6.2.3 Ag nanosphere preparation

The silver nanoparticles of different shapes and sizes were synthesized by employing one-step seedless solvothermal reduction route [18] with a little modification. The silver nanospheres were prepared by introducing 6.9 mg $AgNO_3$ and 1 mg PVP in a round-bottom flask containing 5 ml DMF with stirring at room temperature for 10 min. The color of the solution turns yellow indicating the formation of silver nanospheres. These Ag-NS were separated from DMF and PVP by centrifugation and washed with water for five times and finally dispersed in 3 ml deionized water.

6.2.4 Preparation of Ag polygonal nanospheres, nanorods and truncated triangles

The Ag-NS colloidal solution (5 ml, without being washed) as formed above was refluxed for 1 h at 160 °C, where nanospheres act as seeds and resulted into the formation of large polygonal nanospheres through Ostwald ripening process. These Ag-PNS serve as a medium and changed to NR and TT on further increasing the refluxing time for two and four hour by keeping the reaction temperature constant (160 °C), respectively. The samples were cooled at room temperature and washed with water to separate from DMF and PVP during centrifugation for five times. The supernatant was then removed, and the solid was dispersed in 3 ml of deionized water. This 3 ml colloidal solution of Ag nanoparticles was used for the optical and structural characterization.

6.2.5 Photocatalytic activity study

The comparative co-catalytic activity of AgNPs as a function of their shape is investigated utilizing the same amount of Ag atoms, irrespective of their shapes. In this perspective, the above synthesized AgNPs of various shapes (3 ml) were centrifuged separately to remove the excess water followed by vacuum evaporation. Finally re-dispersed in the 500 µl of deionized water that contains an equal number of Ag atoms (ca. 2.39×10^{19}, calculated by the amount of Ag (mg) taken for the synthesis of NPs) in all the various AgNPs shapes. The co-catalytic activity of the different shapes and sizes of AgNPs was assessed by mixing (500 µl = 2.39×10^{19} Ag atoms) them with 50 mg TiO_2 (P25, size 30-50 nm having 70% anatase and 30 % rutile) for the photodegradation of aqueous solution of 5 ml (0.5 mM) salicylic acid (SA) and 5 ml (0.5 mM) benzoic acid (BA), separately. Furthermore, the effect of varying amount (100 to 700 µl) of Ag co-catalysts loading (4.7×10^{18}-3.36×10^{19} atoms) was also carried out quantitatively. The reaction mixture was then irradiated under UV irradiation (125 W Hg-arc lamp, 10.4 mW/cm^2 and λ_{max} = 253.6 nm) with constant magnetic stirring for different time periods. The reaction samples (SA and BA) were then analyzed by UV-Vis spectrophotometer (λ_{max} = 298 nm for SA and 223 nm for BA) after filtration with 0.22 µm cellulose filter.

6.2.6 Optical, structural and zeta potential analysis

Zeta potential measurement for AgNPs were conducted (Brookhaven 7610) on introducing 500 µl Ag nanoparticles (2.39×10^{19} atoms) in 1.5 ml water. Similarly, zeta potential measurement of the photocatalytic reaction mixture (1 mM, 5 ml SA + 50 mg TiO_2, with or without 500 µl Ag-NS addition) was carried out by taking 200 µl of reaction mixture in 1.3 ml of water.

6.3 Results and discussion

6.3.1 Optical properties of Ag nanoparticles of various morphologies

Figure 1 showed the surface plasmon resonance (SPR) band of AgNPs as a function of their particle size and shape. The as synthesized yellow colored particles of Ag-NS displayed their SPR band at 413 nm corresponds [19-21] to spherical shape. It was reported that a single SPR band was observed for the nanospheres whereas anisotropic particles could give rise to two or more SPR bands in accordance with the Mie's theory [22]. The SPR band at 454 nm has been accounted for anisotropic shaped polygonal nanospheres and the red shift in the SPR band from 413 nm to 454 nm was implied to the increase in particle size [21-26]. It has been found that for the larger nanospheres, the resonance continues to show red shift, and the absorption spectra becomes significantly broadened, which is attributed to scattering cross section due to the

different radiative damping of the plasmon resonance with increasing size of Ag-NS particles [21,24,25]. Furthermore, the rod-shaped nanostructures were also characterized by two SPR bands, namely transverse (422 nm) and longitudinal (524 nm) absorption band as shown in figure 1.

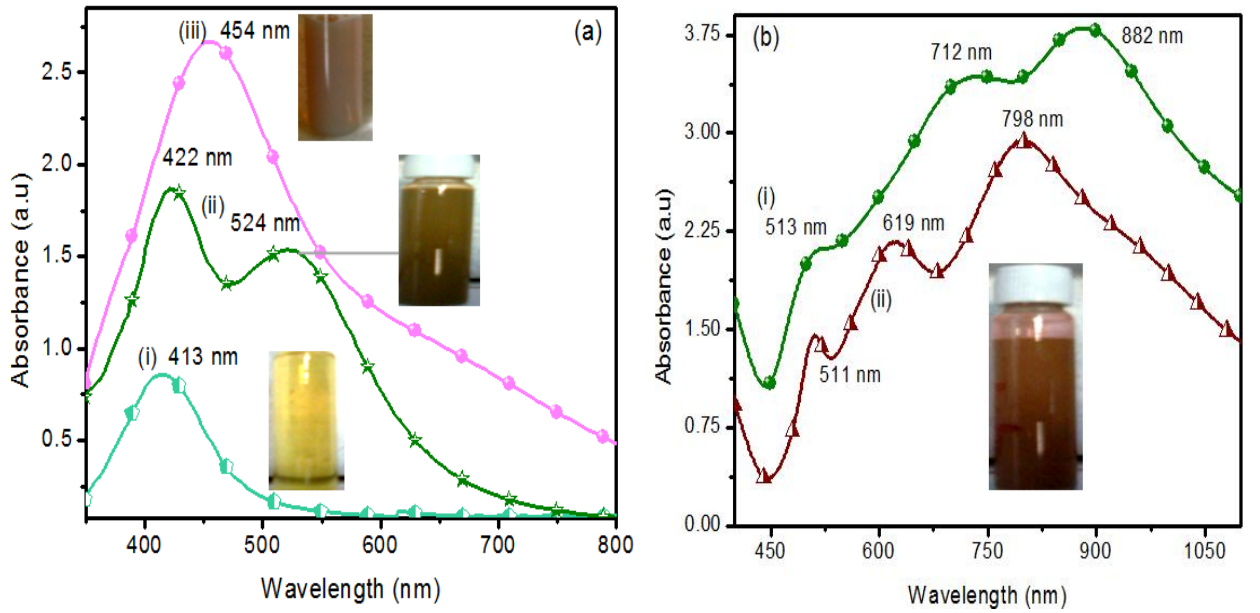

Figure 1. (a) Surface plasmon absorption spectra of Ag nanoparticles (i) small nanospheres, (ii) nanorods (iii) polygonal nanospheres, (b) Ag truncated triangles of different (i and ii) aspect ratio.

It was observed [26] that majority of larger silver particles were directed to grow into nanorods with uniform diameters during their early stage of the ripening process. Figure 1b represents the absorption spectra of two different sizes of Ag-TT morphology. The theoretical calculation by Jin and Schatz [27,28] has predicted that such type Ag-TT nanostructure typically exhibits three peaks ascribed to the out-of-plane quadrupole resonance, the in-plane quadrupole resonance, and the in-plane dipole plasmon resonance, respectively. The shoulder peaks for two different Ag-TT particles at 511 and 513 nm are attributed to the out-of-plane resonance and the second peak at the longer wavelength at 619 and 712 nm corresponding to the in-plane quadrupole resonances which is very sensitive about the size and aspect ratio. The appearance of third peak at the longest wavelength ca. 798 and 882 nm occurs due to the in-plane dipole-plasmon resonance. This is in accordance with the report of Jin et al. [28], they observe the decrease in intensity of the characteristic SPR band for the spherical particles at λmax = 400 nm with a simultaneous growth of three new SPR bands at λmax = 335 nm (weak), 470 nm (medium) and 670 nm (strong), respectively. Similarly, Santos et al. [29] observed UV-visible spectra of the

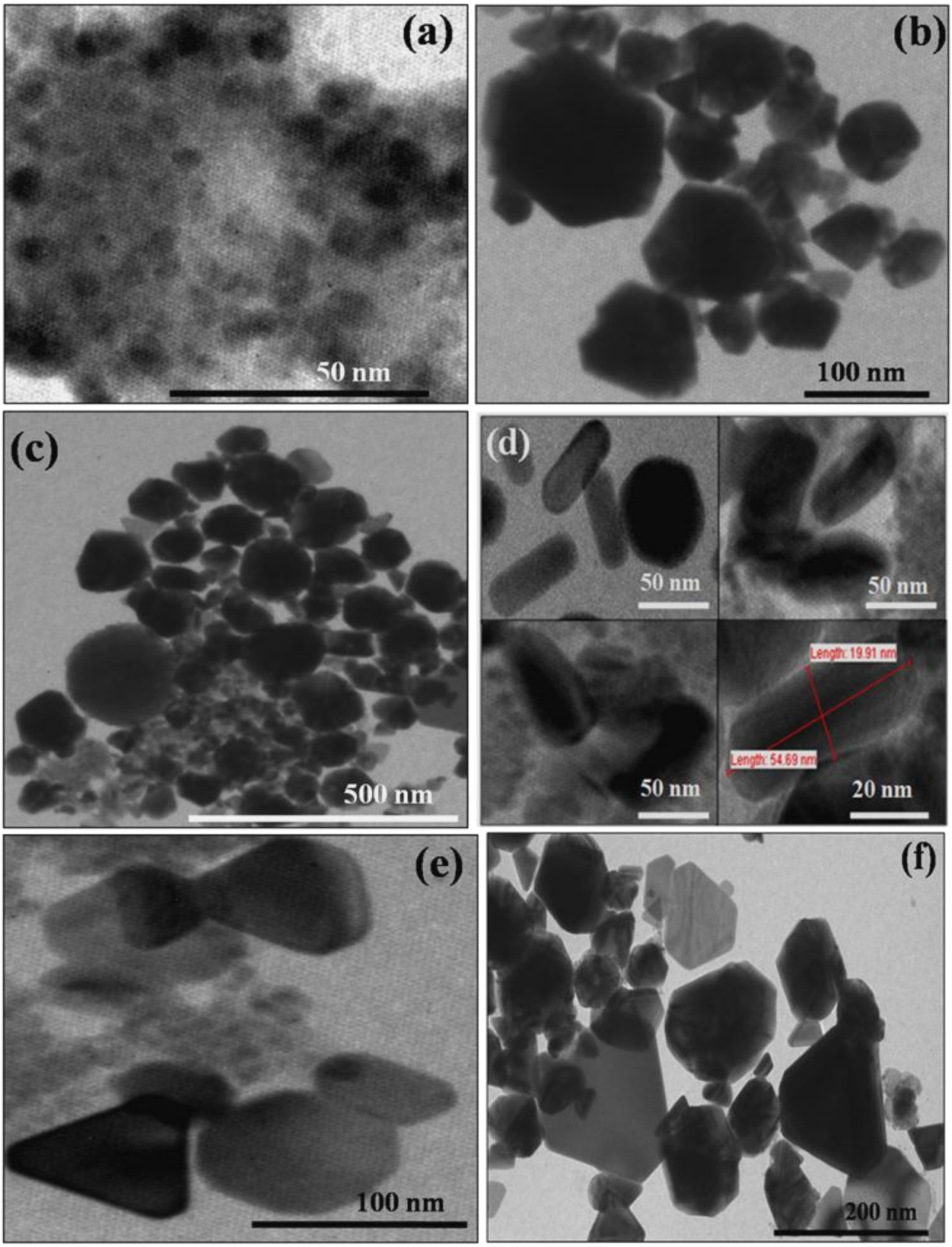

Figure 2. TEM images of (a) PVP coated small Ag nanospheres (size - 3.4 nm), (b and c) polygonal nanospheres (size - 96 nm) of different sizes, (d) Ag nanorods, (e and f) truncated Ag nanotriangles in the growth stage.

nanoprisms that display an intense in-plane dipolar plasmon resonance band, as well as weak bands for in-plane and out-of-plane quadrupolar resonances.

6.3.2 Structural characterization

The TEM image in figure 2a reveals the formation of almost spherical Ag-NS of size 4-8 nm having SPR absorption band at 413 nm. These Ag-NS particles are found to lie separate from

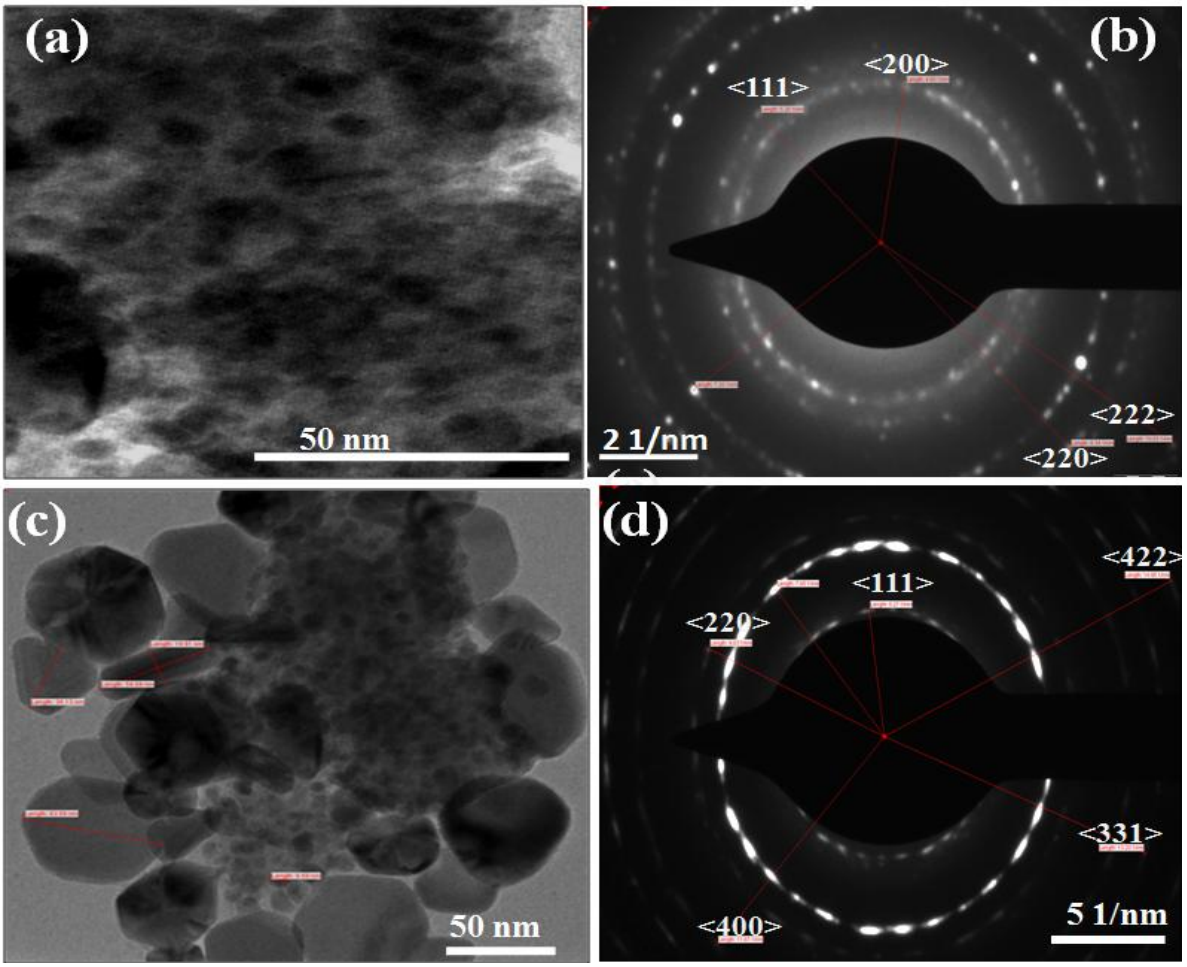

Figure 3. TEM images of (a) PVP coated small Ag nanospheres (size ≈ 3.4 nm), (b) SAED pattern of Ag nanospheres, (c) Ag nanostructures in the growth stage (after 1.5 h of refluxing) and (d) SAED pattern of Ag nanorods.

each other because of PVP coating and most of them are embedded in PVP dispersion (figure 3a). The selected-area diffraction pattern (SAED) of Ag-NS has been shown in figure 3b, evidencing the crystalline face centered cubic FCC structure [30] with lattice planes (2 0 0), (1 1 1), (2 2 0), and (2 2 2) as calculated from the radius of circular rings. On refluxing these smaller Ag-NS at 160 ˚C for 1 h, larger anisotropic particles i.e., Ag-PNS of different sizes within the

range of ~ 80-120 nm has been formed as shown in the TEM images of figure 2b and 2c. The intermediate growth stage (after 1.5 h of refluxing) of AgNPs where Ag-NS has been seen embedded within the matrix of PVP, a large number of Ag-PNS, few Ag-TT and Ag-NR are also present as shown in figure 3c. Figure 2d displayed the TEM images of many Ag-NR formations having a length within the range of ~ 70-75 nm and width of ~ 30-40 nm (aspect ratio = 2.39 ± 0.12) and most of the Ag-NR particles are seemed to be coated by a layer of PVP. The SAED pattern displayed (figure 3d) the characteristic diffraction rings for the lattice planes (1 1 1), (2 2 0), (4 0 0), (3 1 1) and (4 2 2) of FCC Ag nanocrystal in accordance with the reported [31] results. The Ag-TT nanostructures of side length ca. 70-140 nm were formed through Ostwald ripening process on further refluxing of Ag-NR for 4 h as can be observed in figure 2e and 2f.

6.3.3 Photocatalytic Activity

The co-catalytic activity of as synthesized Ag nanostructures of different morphology was evaluated by mixing 50 mg TiO_2 (3.77×10^{20} molecules) with them for the photooxidation of 5 ml salicylic (SA) and benzoic acid (BA) separately. The effective amount of TiO_2 used should be attuned primarily in order to obtain the maximum photocatalytic oxidation (PCO) rate with different shapes of AgNPs. Hence, influence of varying amount of TiO_2 addition (10 - 200 mg) has been carried out by a specific amount (500 µl Ag-NS = 2.39×10^{19}) of AgNPs co-catalyst for the photo-oxidation of SA and BA photodegradation (figure 4).

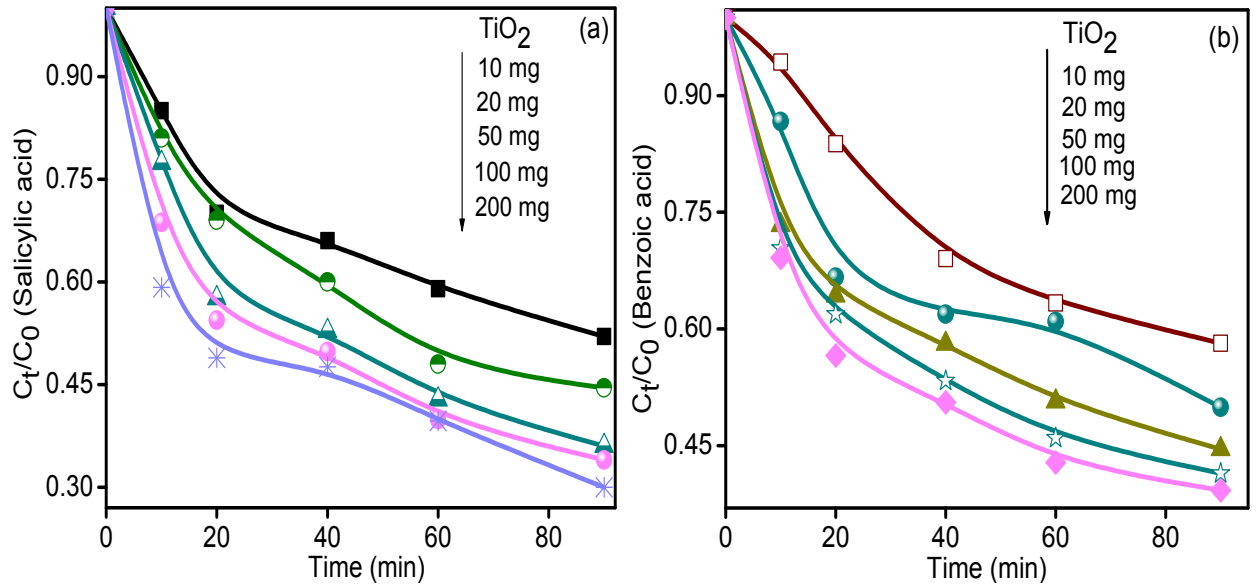

Figure 4. Effect of different concentration of TiO_2 (10 – 200 mg) on the photodegradation rate of (a) salicylic acid and (b) benzoic acid under UV irradiation.

It is observed that upto certain amount of TiO_2 (50 mg = 3.77×10^{20} molecules), the PCO rate of SA and BA is highly increased from 3.51 to 5.00 µmol/min and 1.47 to 2.62 µmol/min, respectively (table 1).

Table 1. Effect of TiO_2 concentration on the photooxidation rate of SA and BA.

S.No.	Amount of AgNPs (no. of Ag atoms)	Amount of Tio_2 (no. of TiO_2 molecules)	Rate of SA degradation (µ mol/min)×10^{-2}	Rate of BA degradation (µmol/ min)×10^{-2}
1.	500 µl (2.39×10^{19})	10 mg (0.754×10^{19})	1.3	1.2
2.		20 mg (1.508×10^{20})	1.5	1.4
3.		50 mg (3.77×10^{20})	1.8	1.6
4.		100 mg (7.54×10^{20})	1.8	1.6
5.		200 mg (15.08×10^{20})	1.85	1.64

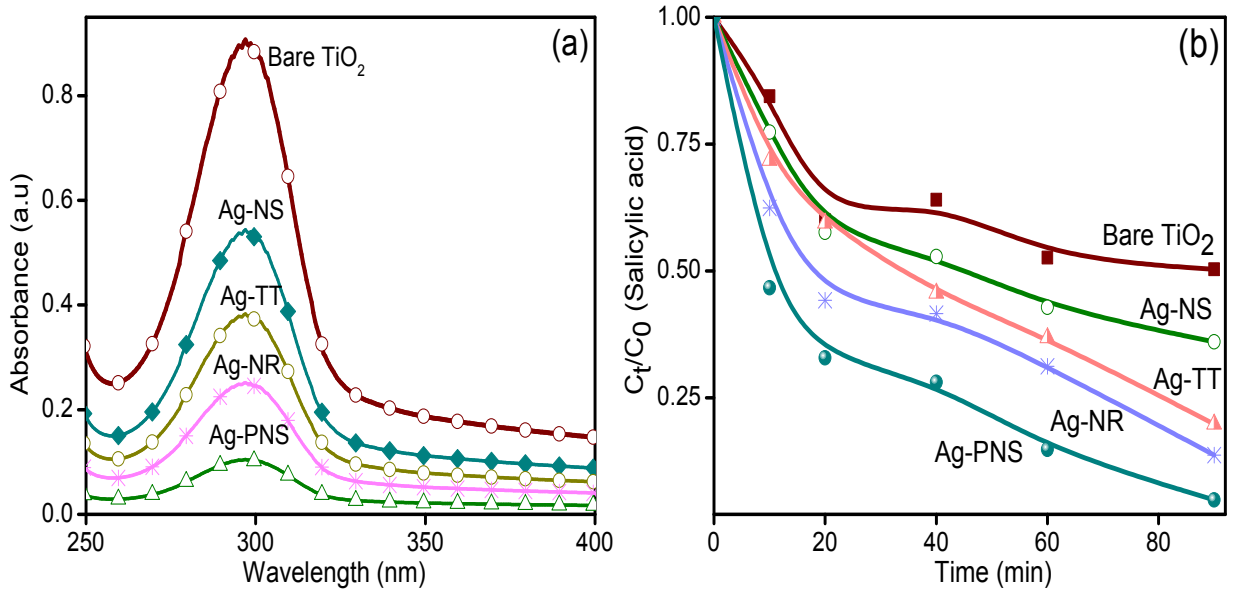

Figure 5. (a) Changes in the absorption spectra of salicylic acid (0.5 mM) and (b) time course of salicylic acid photodegradation by the addition of same amount (500 µl) of Ag co-catalysts of different shapes to 50 mg TiO_2 catalyst.

Thereafter, on increasing the dosage of photocatalyst (100-200 mg), the PCO rate remained almost constant. The observed enhancement in this range (10-50 mg) is probably due to an increased number of available adsorption and catalytic sites on TiO_2 [32]. On increasing TiO_2 concentration, increase in the surface layers of the TiO_2 particles on the AgNPs does not further

improve the PCO rate because of the denser TiO_2 suspension causes hindrance in light penetration and photoactivation for charge separation. Hence, 50 mg of TiO_2 catalyst was used for the optimum photocatalytic activity in all experiments.

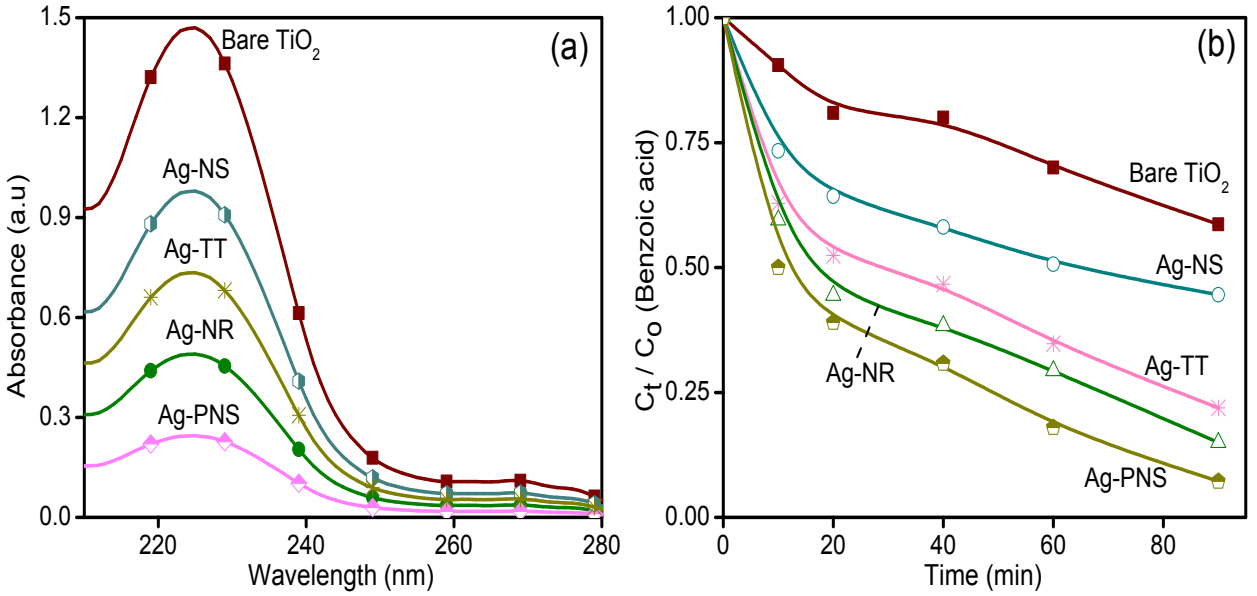

Figure 6. (a) Changes in the absorption spectra of benzoic acid (0.5 mM) and (b) time course of benzoic acid photodegradation by adding same amount (500 µl) of Ag co-catalysts of different shapes to 50 mg TiO_2 catalyst.

Figure 5a and 6a displayed the changes in the absorption intensity of SA (0.5 mM, abs. = 1.8 a.u.) and BA (0.5 mM, abs. = 2.1 a.u.) during its photooxidation by aqueous suspension of 50 mg TiO_2 and 500 µl (2.39×10^{19}atoms) AgNPs of different shapes under 1 h UV light irradiation**.** It is observed that Ag-PNS addition to TiO_2 exhibits highest photoactivity where almost complete degradation of SA (abs. 0.10 a.u.) occurs as compared to the lowest photoactivity (abs 0.54 a.u.) of PVP coated Ag-NS addition to TiO_2 particles under similar experimental conditions. The Ag-TT loading also significantly improved the TiO_2 photoactivity for SA degradation as evident from the decrease in SA absorbance. The co-catalytic ability of AgNPs of various shapes imparting to TiO_2 for the photooxidation of SA and BA is found to follow the same trend as PNS > NR > TT > NS (figure 5a and figure 6a). It is worthy to note that same amount of AgNPs addition to TiO_2 always enhanced the PCO rate of SA and BA in a varied extent as a function of the geometric shape of AgNPs co-catalysts as compared with bare TiO_2 photoactivity. The enhancement observed in the Ag-TiO_2 system (using different morphologies of AgNPs) as compared to bare TiO_2 is thought to be attributed to better electron capturing ability of Ag

deposits. These NP deposits generate greater number of strong oxidizing holes that assist the rapid photooxidation of adsorbed reacting species in solution [17] and also extend the lifetime of energetic charge carriers that reach the surface of the semiconductor by enhancing the rates of e^--h^+ separation at the AgNPs/semiconductor interface [33]. Further, the role of the AgNPs co-catalyst is to perform the catalytic function by providing active sites where chemical reactions can take place with lower activation barriers than on the semiconductor (TiO_2) [33].

Table 2. Structural, optical and co-catalytic properties of different Ag nanostructures.

Shape of Ag nanoparticles	SPR band	Average size of 15 particles	Surface area per particle (nm^2)	Rate of SA oxidation ($\mu mol/min)\times10^{-2}$	Rate of BA oxidation ($\mu mol/min)\times10^{-2}$
Nanosphere (Ag-NS)	413 nm	4 to 8 nm	157	1.8	1.5
Polygonal nanosphere (Ag-PNS)	454 nm	80 to 120 nm	30088	2.7	2.5
Nanorod (Ag-NR)	422 nm and 524 nm	length = 70 to 75 nm width = 30 to 38 nm		2.4	2.3
Truncated triangle (Ag-TT)	511 nm, 619 nm and 698 nm	one side length = 70 – 140 nm	5025	2.2	2.1

The plots shown in figure 5b and 6b showed the influence of Ag co-catalysts shapes (smaller as well as larger than TiO_2) on the PCO of SA and BA by mixing AgNPs (500 µl = 2.39×10^{19} atoms) of different morphologies such as Ag-NS, Ag-NR, Ag-TT and Ag-PNS with 50 mg TiO_2 at various time intervals of UV irradiation. The concentration of both the SA and BA is exponentially decreased by an increase in the irradiation time, indicating the first-order reaction kinetics as $C_t = C_o e^{-kt}$, where C_t is the amount degraded at time t, C_o is the initial concentration of SA or BA and k (min^{-1}) is the first-order rate constant. Figure 5b and 6b showed that the initial decrease in the oxidized amount of SA during first 20 min UV irradiation over bare or different AgNPs-TiO_2 (50 mg) suspension is always more than that of BA photodegradation under similar experimental conditions. Furthermore, with the gradual addition (500 µl = 2.39×10^{19} atoms) of AgNPs co-catalysts to TiO_2 (50 mg) reaction mixture, a sharp decrease in SA or BA concentration during first 20 min UV irradiation is observed with increasing geometric surface area per AgNPs particle ca. 157 nm^2 for Ag-NS < 5025 nm^2 for Ag-TT < 8553 nm^2 for Ag-NR,

and < 30088 nm^2 for Ag-PNS (table. 2). Also increased surface area of AgNPs exhibited more adsorption of SA and BA and Ag-PNS possessing highest surface area (30088 nm^2) displayed maximum adsorption and co-catalytic activity as follows Ag-NS < Ag-TT < Ag-NR < Ag-PNS.

The extent of SA or BA adsorption was confirmed by stirring the reaction mixture (with and without Ag-PNS) in the dark for 20 min and the changes in absorption intensity of SA or BA was recorded. Similarly, the comparative time course for the dark adsorption of SA and BA has been shown in figure 7a. It has been observed that SA concentration (0.5 mM) reduced to 0.38 mM on the addition of TiO_2 during dark reaction because of the SA adsorption over TiO_2 surface and the addition (500 µl = 2.39 × 10^{19} atoms) of Ag-PNS resulted to further reduction in SA concentration (0.32 mM), evidencing the existence of a strong ionic interaction between the SA,

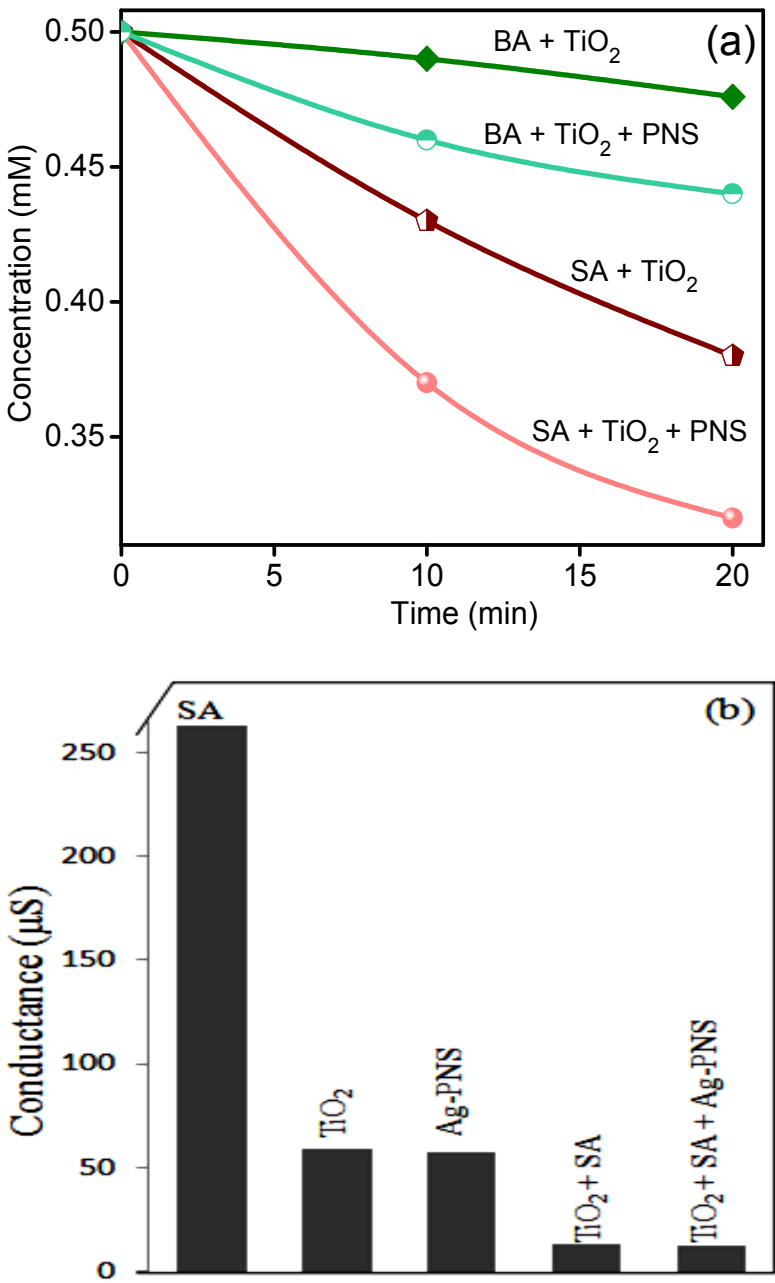

Figure 7. (a) Time course of dark adsorption for salicylic acid (0.5 mM) and benzoic acid (0.5 mM) over TiO_2 with or without Ag-PNS addition and (b) variation in conductance values of different reaction mixtures of TiO_2, SA and Ag-PNS.

Ag-PNS and TiO_2 in reaction mixture (figure 7a). In contrast, a slight decrease (0.5 mM to 0.44 mM) in the BA concentration was noticed on the addition of TiO_2 and Ag-PNS to reaction mixture (figure 7a). Tran et al. [17] reported that the enhancement provided by silver in the mineralization of the organic compounds is possibly related to the adsorption of carboxylic functional groups on the TiO_2 surface. Hence, the enhanced PCO of SA was ascribed to its strong affinity for adsorption onto TiO_2 surface through formation of inner-sphere titanium (IV)-salicylate complex with –COOH and –OH chelating groups [34]. But, no such complex being formed by the benzoic acid because of the absence of –OH group in its structural entity and hence the interaction between photocatalyst, and substrate was pretty low as reflected in their PCO rate of BA in comparison to SA. Various physical properties in correlation with the photocatalytic activity of different Ag co-catalysts-TiO_2 samples are summarized in table 2.

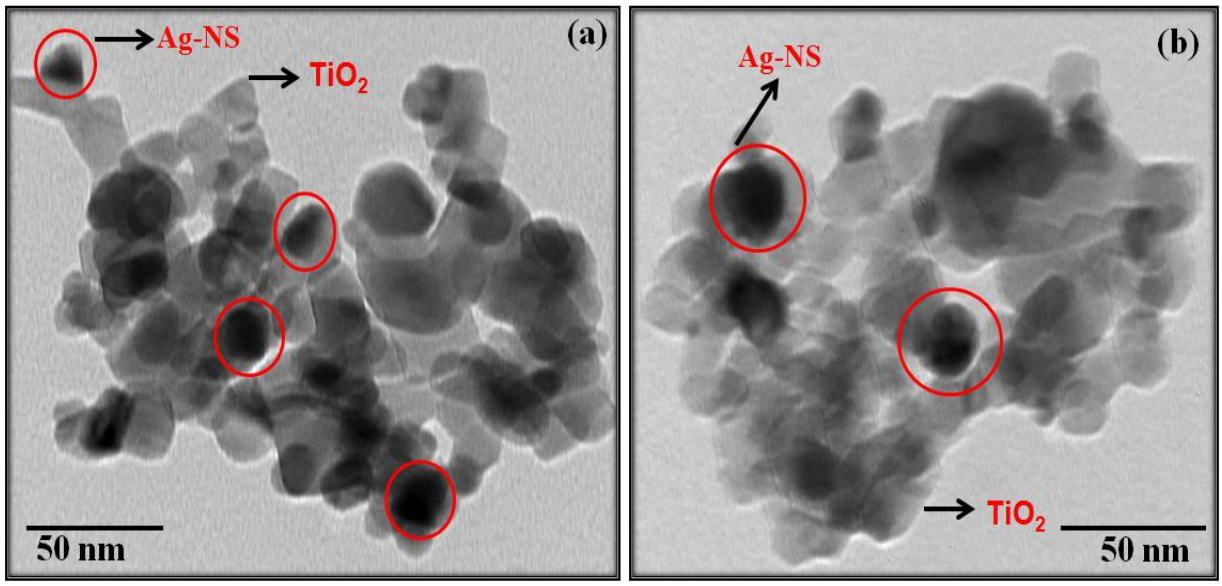

Figure 8. Changes in absorption spectra of (a) salicylic acid (b) benzoic acid on addition of Ag-PNS and 50 mg TiO_2 during 20 min of stirring in dark.

Zeta potential (ζ) and conductance measurements further supported the adsorption behavior among Ag-PNS, SA and TiO_2. The measured conductance (figure 7b) ca. 263 µS for SA, 57 µS for Ag-PNS and 59 µS for TiO_2 aqueous solution is highly reduced to 12 µS in TiO_2 + SA + Ag-PNS reaction mixture due to neutralization of electronic charge species (negatively charged -COOH and -OH) through complexation. In a similar way, the zeta potential ζ = -7.07 mV for SA and -2.80 mV for TiO_2 has been increased to + 43.51 mV in SA and TiO_2 aqueous mixture, which further reduced to -12.33 mV after addition of Ag-PNS, whose self ζ value is -

6.67 mV. This fact confirms the close interactions between TiO_2, SA and Ag-PNS particles in reaction mixture and formation of stable surface complex between the substrate species.

These close interaction/adsorption between aqueous mixture of Ag-NS, TiO_2 and SA is further verified by the TEM images (figure 8) that indicates proper attachment of AgNS (black colored) with TiO_2 particles (gray contrast) that may improve the TiO_2 photoactivity. This is in accordance with Ranjit et al. [35] results who reported the enhanced degradation of salicylic acid as compared to cinnamic acid due to the favorable stereo-configuration that coordinates the catalyst surface through COOH and -OH groups, resulting in efficient adsorption and interfacial charge transfer process, while the low adsorption of cinnamic acid on the catalyst surface resulted in a lower degradation rate.

The effect of varying amount (100-700 µl) of Ag-PNS (4.7×10^{18} – 3.36×10^{19} atoms) addition to TiO_2 for PCO of SA and BA has also been carried out (figure 9). It has been found that TiO_2 photoactivity first increased upto

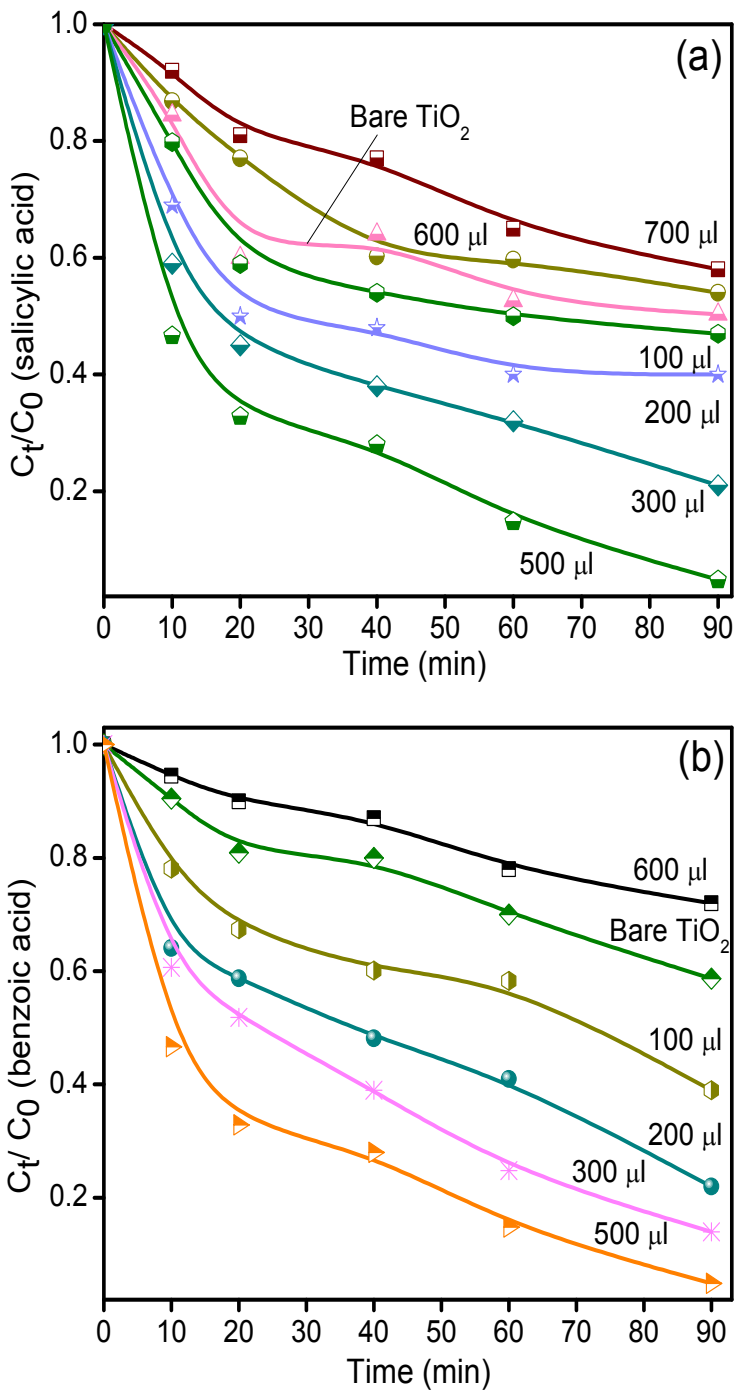

Figure 9. Effect of different amounts of Ag-PNS (100-700 µl) co-catalyst addition on the photodegradation rate of (a) salicylic acid and (b) benzoic acid by TiO_2 (50 mg) under UV irradiation.

300-500 µl (1.44 to 2.39 × 10^{19} atoms) Ag-PNS addition and thereby decreased [36] with increasing amount (600-700 µl) of Ag-PNS addition. The calculated geometric surface area of Ag nanoparticles and cross-sectional area of TiO_2 particles suggests that around 18-20 TiO_2 particles are desired for a single Ag-PNS particle coverage, 5-6 TiO_2 particles are needed for a Ag-NR coverage and 2-3 particles are required for a Ag-TT coverage due to the decrease in area of respective Ag nanostructures. However, one bigger TiO_2 particle may accommodate many smaller Ag-NS co-catalyst over its surface for photoreaction to occur.

Hence, for the maximum photocatalytic activity of Ag-TiO_2 system, an optimum amount of AgNPs co-catalyst and TiO_2 is very crucial. In fact, it was found that the ratio of AgNPs (500 µl) atoms to TiO_2 (50 mg) used for the highest photoactivity of Ag-TiO_2 system is 2.39 × 10^{19} Ag atoms: 3.77 × 10^{20} TiO_2 molecules = 2.39: 37.7 = 1:16 which is closely resembled with determined ratio of 18-20 TiO_2 to one Ag-PNS particle for highest photoactivity. The average surface to volume (S/V) ratio was gradually decreased as 0.981 nm^{-1} (Ag-NS) > 0.413 nm^{-1} (Ag-NR) > 0.069 nm^{-1}(Ag-PNS) cannot explain the high co-catalytic activity of Ag-PNS extended to TiO_2 catalyst. In contrary, Ag-NS being smaller in size (4-8 nm) having high surface to volume ratio were expected to be better co-catalyst than bigger size (80-120 nm) of Ag-PNS. As Ag-NS, particles being embedded in the PVP (Figure 2a) could not be able to make suitable electrical contact with TiO_2 and hence showed lowest co-catalytic activity.

One plausible reason could be the higher surface area of Ag-PNS particles led to better ohmic contact with TiO_2 surface and therefore, improves the charge transport across the Ag-TiO_2 interface for highest photocatalytic activity. The highest co-catalytic activity of Ag-PNS can also be explained on the basis of unsymmetrical nature having different crystalline faces act as active sites for the co-catalysis. Although AgNPs (SPR band > 400 nm) absorb visible light , here it is believed that the enhanced photoactivity of Ag-TiO_2 interface as compared to bare TiO_2 is probably due to the variation in co-catalytic effect of different AgNPs surface morphology because photoreaction was carried out solely under UV (125W Hg-arc lamp, 10.4 mW cm^{-2} and λ_{max} = 253.6 nm) light irradiation. During photoreaction, both the catalyst (TiO_2) and the co-catalyst (AgNPs) undergo Fermi level equilibration to attain an energy level close to the conduction band for the facile electron transfer from photoexcited TiO_2 to AgNPs and effectively increasing the lifetime of e^--h^+ pairs as a function of particle shape and interfacial contact area. Christopher and co workers [37] concluded that enhanced photoactivity is attributed to radiative

transfer of energy from Ag to the semiconductor leading to higher concentrations of charge carriers (e^--h^+ pairs) and hence, higher activity as a strong function of the size and shape of Ag nanostructures. Hirakawa et al. [38] demonstrates that the charge equilibration between the metal and semiconductor plays an important role in dictating the overall energetics of the composite. Such photoinduced charge carrier separation can be actually favored in semiconductor-metal nanocomposites [1-10,35-38] as proved by the improved photocatalytic and photoelectrochemical efficiency in many hybrid materials.

It is worthy to mention here that it is not obligatory for a nanoparticle to lie only in quantum sized range for illustrating highly active photoactivity. Our experimental results for Ag nanostructures showed an unexpected opposite trend in which the large polygonal nanospheres are more catalytically active than the smaller quantum sized nanospheres owing to the uneven surface, sharp edges, higher geometric surface area per particle and highly favorable AgPNS-TiO_2 interface.

6.4 References

[1] M. Bellardita, M. Addamo, A.D. Paola and L. Palmisano, Chem. Phys., 339 (2007) 94.

[2] M. Jakob, H. Levanon and P.V. Kamat, Nano Lett., 3 (2003) 353.

[3] A. Wood, M. Giersig and P. Mulvaney, J. Phys. Chem. B, 105 (2001) 8810.

[4] V. Subramanian, E.E. Wolf and P.V. Kamat, J. Am. Chem. Soc., 126 (2004) 4943.

[5] A. Takai and P.V. Kamat, ACS Nano, 5 (2011) 7369.

[6] H. Choi, W.T. Chen and P.V. Kamat, ACS Nano, 6 (2012) 4418.

[7] P. Wang, B. Huang, Y. Dai and M.H. Whangbo, Phys. Chem. Chem. Phys., 14 (2012) 9813.

[8] Z. Zheng, B. Huang, X. Qin, X. Zhang, Y. Dai and M.H. Whangbo, J. Mater. Chem., 21 (2011) 9079.

[9] R. Kaur and B. Pal, J. Mol. Catal. A: Chem., 355 (2012) 39.

[10] M.A. Behnajady, N. Modirshahla, M. Shokri and B. Rad, Global Nest J., 10 (2008) 1.

[11] M.J. Lopez-Munoz, J. Aguado and B. Ruperez, Res. Chem. Intermed., 33 (2007) 377.

[12] S.W. Lam, K. Chiang, T.M. Lim, R. Amal and G.K.C. Low, Appl. Catal. B: Environ., 55 (2005) 123.

[13] E. Pelizzetti, M. Borgarello, C. Minero, E. Pramauro, E. Borgarello and N. Serpone, Chemosphere, 17 (1988) 499.

[14] E. Kowalska, H. Remita, C. Colbeau-Justin, J. Hupka and J. Belloni, J. Phys. Chem. C, 112 (2008) 1124.

[15] A. Sclafani, L. Palmisano and E. Davi, J. Photochem. Photobiol. A: Chem., 56 (1991) 113.

[16] I. Sondi and B. Salopek-Sondi, J. Colloid Interf. Sci., 275 (2004) 177.

[17] H. Tran, K. Chiang, J. Scott and R. Amal, Photochem. Photobio. Sci., 4 (2005) 565.

[18] Y. Yang, S. Matsubara, L. Xiong, T. Hayakawa and M. Nogami, J. Phys. Chem. C, 111 (2007) 9095.

[19] E. Filippo, D. Manno, A. Buccolieri, M.D. Giulio and A. Serra, Superlattices Microstruct., 7 (2010) 66.

[20] P.Y. Silvert, R. Herrera-Urbinab and K. Tekaia-Elhsissena, J. Mater. Chem., 7 (1997) 293.

[21] A.S. Grijalva, R.H. Urbina, J.F.R. Silva, M.A. Borja, F.F.C. Barraza and A.P. Amarillas, Phys. E., 27 (2005) 104.

[22] C.M. Cobley, S.E. Skrabalak, D.J. Campbell and Y. Xia, Plasmonics, 4 (2009) 171.

[23] M. Futamata, Y. Maruyama and M. Ishikawa, J. Phys. Chem. B, 107 (2003) 7607.

[24] M. Moskovits and B. Vlckova, J. Phys. Chem. B, 109 (2005) 14755.

[25] M.G. Blaber, A.I. Henry, J.M. Bingham, G.C. Schatz and R.P.V. Duyne, J. Phys. Chem. C, 116 (2012) 393.

[26] Y. Sun, B. Mayers, T. Herricks and Y. Xia, Nano Lett., 3 (2003) 955.

[27] R. Jin, Y. Cao, C.A. Mirkin, K.L. Kelly, G.C. Schatz and J.G. Zheng, Science, 294 (2001) 1901.

[28] L.J. Sherry, R. Jin, C.A. Mirkin, G.C. Schatz and R.P.V. Duyne, Nano Lett., 6 (2006) 2060.

[29] I.P. Santos and L.M.L. Marzan, Nano Lett., 8 (2002) 903.

[30] A.S. Lanje, S.J. Sharma and R.B. Pode, J. Chem. Pharm. Res., 3 (2010) 478.

[31] D. Chen and L. Gao, J. Cryst. Growth, 264 (2004) 216.

[32] L. Rideh, A. Wehrer, D. Ronze and A. Zoulalian, Ind. Eng. Chem. Res., 36 (1997) 4712.

[33] S. Linic, P. Christopher and D.B. Ingram, Nat. Mater., 10 (2011) 911.

[34] A.E. Regazzoni, P. Mandelbaum, M. Matsuyoshi, S. Schiller, S.A. Bilmes and M.A. Blesa, Langmuir, 14 (1998) 868.

[35] K.T. Ranjit, I. Willner, S.H. Bossmann and A.M. Braun, J. Catal., 204 (2001) 305.

[36] M. Murdoch, G.I.N. Waterhouse, M.A. Nadeem, J.B. Metson, M.A. Keane, R.F. Howe, J. Llorca and H. Idriss, Nature Chem., 3 (2011) 489.

[37] P. Christopher, D.B. Ingram and S. Linic, J. Phys. Chem. C, 114 (2010) 9173.
[38] T. Hirakawa and P.V. Kamat, J. Am. Chem. Soc., 127 (2005) 3928.

Chapter 7

Copper Nanostructures of Various Morphologies for Superior Catalytic and Co-catalytic Activities

7.1 Introduction

Among the coinage metal (Au, Ag, and Cu) nanoparticles (NPs), substantial amount of research has been aimed towards the potential applications of Au and Ag metals in diverse disciplines as explained in the previous chapters. Whereas Cu metal, much economic relative to Au and Ag has received considerably less attention due to its oxidation viable nature under ambient conditions [1-4]. Moreover, it is well known that Cu plays a significant role in electronics circuits due to its excellent electrical conductivity [1-3]. Cu nanostructures have found potential applications in electrochemical sensors, lubrication, thermal conducting, nanofluids, surface-enhanced Raman scattering, etc. [1-8]. Abdulla-Al-Mamun et al. [9] evaluated the catalytic activity of Cu–TiO_2 nanocomposite to a photocatalytic cancer cell-killing under UV–visible light irradiation. Copper (Cu_2O, Cu^{2+}, etc.) based TiO_2 heterojunctions are proven to be the efficient photocatalysts for H_2 production and water splitting reactions [10]. Therefore, Cu owing to wide applications in various fields is an element of the choice and has been an alternate candidate for optical, electronic and catalytic applications.

In this respect, several methods have been mentioned in the literature for preparing stabilized CuNPs, such as chemical reduction route using sodium citrate, $NaBH_4$, N_2H_4 in combination with different surfactants and capping agents [11-21]. Other synthetic approaches involve solvothermal, hydrothermal, polyol, electrochemical and photochemical reduction ways, etc. for stabilizing the Cu nanostructures. CuNPs of size ≈ 2.8 nm has been synthesized in the gas phase using a sputtering-aggregation type source by Pedersen et al. [11]. Cu nanostructures were also prepared through hydrogenolysis of various organometallic copper precursors in an organic medium at moderate temperature [14]. The recent synthesis of Cu nanocubes, nanowires, and bipyramids, obtained in water by reduction with glucose and using hexadecylamine as a capping agent has also been reported [14]. Rathmell et al. [19,20] synthesized longer, thinner Cu nanowires (CuNW) and coated onto flexible plastic substrates to make transparent, conductive films that are equivalent to films of Ag nanowires in their performance.

Despite of all these synthetic approaches and applications, very few reports persist about the relative catalytic and co-catalytic activity of CuNPs as a function of their morphology. CuNPs of different dimensions and shapes would expect to interact in a varied way with the reactant moiety depending on their exposed surface active atoms, edges, corners, surface facets, adsorption behavior, surface charge, electronic movement within the nanostructures, etc. Moreover, the co-catalytic effect imparted by metal NPs co-catalyst onto semiconductor is highly dependent on interface contact between the two and influenced by the nanoparticle's morphology.

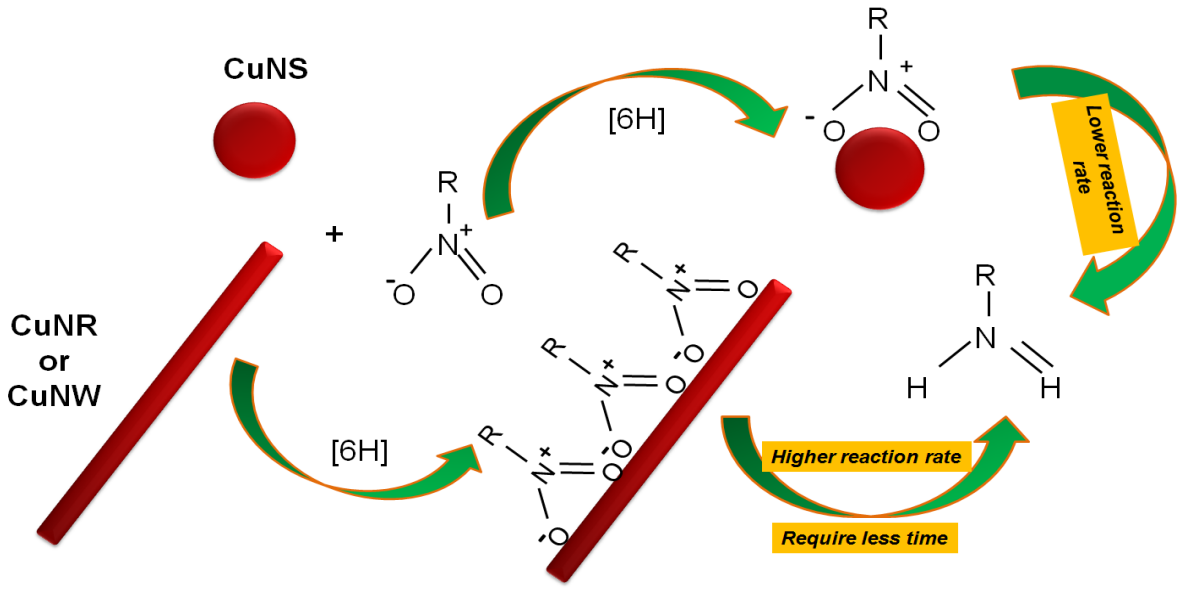

Scheme 1. Cu nanostructures of dissimilar shapes exhibiting nitroaromatic reduction.

So, this chapter addresses the synthetic approach for the synthesis of stable Cu nanomorphologies such as nanospheres of three different sizes (3-5 nm, 5-10 and 15-20 nm), 1 D NR (600-700 nm×15-20 nm) and NW (4-6 μm×60-80 nm) and their comparative catalytic efficacy was examined by carrying out the nitro aromatics reduction (nitrobenzene, m-chloronitrobenzene and m-nitrotoluene) to their respective amines as represented in scheme 1. Copper nanostructures were also employed as co-catalysts (CuNPs-TiO_2) for carrying out the photooxidation of acetic acid under UV light irradiation. Scheme 1 clearly illustrates that the lengthy copper nanowire (CuNW) and nanorods (NR) with higher exposed surface area aids great ease for the adsorption of reactant molecules and would expect to show pronounced catalytic effect compared to the spherical morphology.

7.2 Experimental Section

7.2.1 Materials

Poly(N-vinylpyrrolidone) (PVP, MW = 40,000), copper sulfate, copper(II) chloride, lauric acid, copper nitrate, aluminum chloride, ethylene glycol (EG), ethylenediamine (EDA), sodium hydroxide, acetic acid, sodium borohydride, ascorbic acid, hydrazine, nitrobenzene, m-chloronitrobenzene, m-nitrotoluene, aniline, m-chlororaniline and m-toludine were purchased from Loba chemie, India. P25-TiO_2 photocatalyst (size 30-50 nm, 70% anatase and 30 % rutile) is provided as a gift sample from Degussa Company, Germany. All the chemicals were used as-received without any further purification. De-ionized water was obtained using an ultra filtration system (Milli-*Q*, Millipore) with measured conductivity above 35 mho cm^{-1} at 25 °C.

7.2.2 Synthesis of CuNPs of different shapes and sizes

7.2.3 Cu nanospheres (CuNS) preparation

CuNS of various sizes were prepared by using different capping (PVP and EDA) and reducing agents (ascorbic acid and EDA) employing solvothermal and hydrothermal approach [21]. For the synthesis of extremely fine, homogenous and stable CuNPs, 2.00 g lauric acid was dissolved in 20 ml distilled water and mixed with 1.2 ml EDA under constant stirring for 30 min. Then 1.7 g Cu(II)chloride was dissolved in 5 ml distilled water which was then slowly introduced to the above solution and pH of the solution was adjusted upto 12–13 by the addition of aqueous NaOH (0.1 M). This solution was hydrothermally treated in Teflon-lined stainless steel at 170˚C for 20 h. After the hydrothermal treatment, 20 ml ethanol was added to the reaction mixture and sonicated for 15 min to dissolve the residual lauric acid and EDA. This mixture was allowed to settle for 15 min, during which CuNS with brown color were precipitated out and then dissolved in 20 ml water and this sample was coded as CuNS-1. CuNS using PVP as a capping agent was synthesized by mixing the solution of PVP (0.3 M, 10 ml), $CuSO_4$ (0.1 M, 6 ml) and ascorbic acid (0.25 M, 3 ml) in EG at 25˚C [16] and the sample was coded as CuNS-2. CuNS-3 sample was prepared similar to the CuNS-2 procedure expect the modification in the temperature condition. During the preparation of CuNS-3, solutions of $CuSO_4$ and ascorbic acid were drop-wise injected into the hot PVP solution (70˚C). Heating and stirring were maintained for 1 h and the solution finally turned reddish brown, it was then cooled and centrifuged (2500 rpm, 15 min) in order to remove the by-products and excess PVP.

7.2.4 Preparation of Cu nanorods (CuNR)

The CuNR were synthesized by mixing 2.00 g lauric acid, 1.2 ml EDA, 1.7 g copper(II)chloride and 1.3 g aluminium chloride in 25 ml distilled water [21]. The pH of this above formed deep blue colored solution was adjusted to 12-13 by the addition of aqueous NaOH (0.1 M). Then the solution was hydrothermally treated in Teflon-lined stainless steel autoclave at 200˚C for 24 h. The as prepared CuNR were collected by sonication followed by filtration and diluted to 20 ml with distilled water.

7.2.5 Preparation of Cu nanowires (CuNW)

CuNW were synthesized by hydrothermal approach utilizing the mixture of NaOH (200 ml, 1.5M), $Cu(NO_3)_2$ (10 ml, 0.2M), EDA (3 ml), and hydrazine (250 µl, 35 wt%) in a reaction flask at 80˚C for 1h [19,20]. 5 mg of PVP was then added instantly to this mixture to prevent the CuNW from aggregation and this mixture was quickly cooled in an ice bath. After the reaction, the CuNW were washed with aqueous solution of hydrazine and stored in aqueous solution.

7.2.6 Co-catalytic activity

The co-catalytic activity of various Cu nanostructures (3.73×10^{18} atoms) was comparatively studied by mixing 5 ml acetic acid (10 mM), 25 mg TiO_2 under UV irradiation (125 W Hg-arc lamp, and 10.4 mW/cm^2) with constant magnetic stirring for different time periods. The progress of reaction in terms of CO_2 evolution was measured by GC chromatogram studies. The CO_2 evolution was measured by injecting 1 ml of the gaseous mixture from the reaction vessel (gas tight test tube; 2 mg TiO_2-CuNPs, 5 ml acetic acid) into the gas chromatography (NUCON-5765) using Propak-Q column with nitrogen as carrier gas (30 ml/min) and Thermal Conductivity Detector (TCD). Column oven was maintained at 40˚C while injector and detector were at 70 and 80˚C, respectively.

7.2.7 Catalytic activity

Catalytic activity of Cu nanomorphologies ($\approx 3.73\times 10^{18}$ atoms) was examined by adding 1 ml of ice-cold $NaBH_4$ solution (0.84 M) to 5 ml nitro aromatic compounds (nitrobenzene, m-nitrotoluene, m-chloronitrobenzene, 5 mM), where the reduction of nitro compounds to their respective amines was monitored by measuring the absorption spectra of the reaction mixture at regular intervals and high–performance liquid chromatography (HPLC, Agilent, 1120 Compact LC, 254 nm, using C–18 column and MeOH:H_2O (70:30) as mobile phase) at a flow rate of 1ml/min. The intermediates were examined by GC-MS analysis.

7.2.8 Characterization

Optical property was analyzed by UV-vis absorption (Specord 205) spectrophotometer. Shape and size of the NPs were analyzed by SEM and TEM (Hitachi 7500 model) with resolution 2A° operating at voltage 120 kV measurements. Zeta potential (ζ) and dynamic light scattering (DLS) measurement was conducted using Brookhaven 7610 instrument. Samples for DLS and ζ examination were prepared by diluting CuNPs ca. 3.73×10^{18} atoms in 1.5 ml of water. Table 1 shows the optoelectronic and physical parameters of Cu nanostructures.

7.3 Results and discussion

7.3.1 Optical properties of Cu nanostructures

Figure 1 displayed the surface plasmon resonance band (SPR) of various copper nanostructures, whose position depends on the particle properties including size, shape, solvent used, capping agent employed, etc. The brown colored aqueous suspension of CuNS-1 particles (figure 1a) exhibit SPR at 590 nm, corresponds to spherical shape as in accordance with the reported results [21]. CuNS-2 and CuNS-3 particles with reddish brown colored appearance showed their SPR

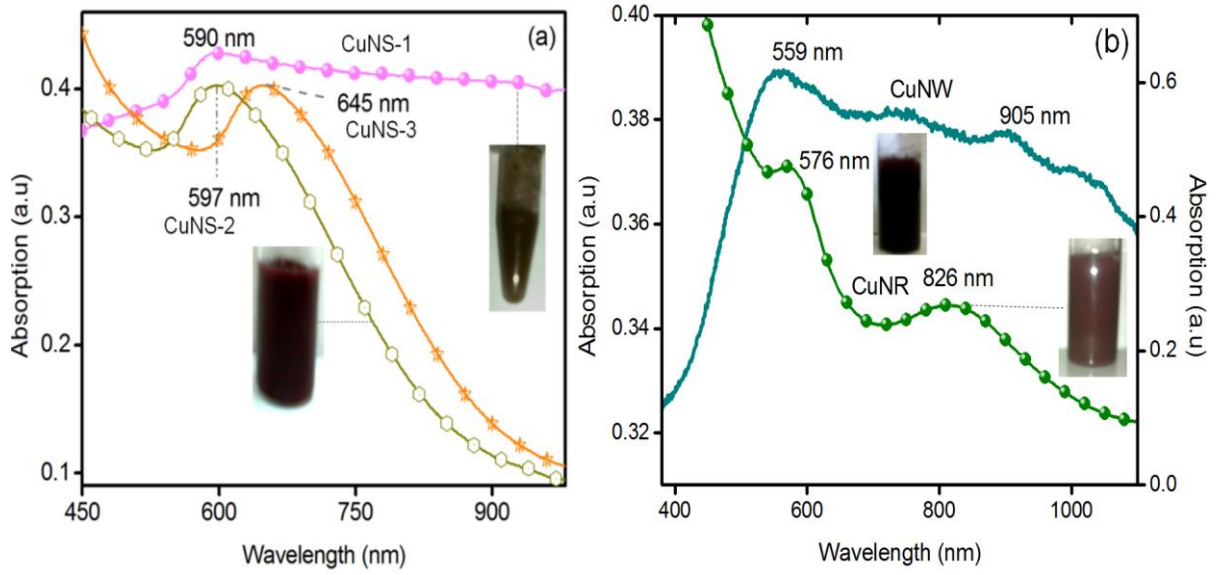

Figure 1. Optical absorption spectra of (a) copper nanospheres (CuNS) of three varied sizes, (b) copper nanorods (CuNR) and nanowires (CuNW).

band at 597 and 645 nm, respectively. The CuNS-1 particles are displaying weak and broader band as compared to highly intense and red shifted band of CuNS-2 and CuNS-3 particles. It is believed that red shift in the resonance band represents increase in the particle size while an increase in the bandwidth (CuNS-1) of the SPR may be due to electron scattering enhancement

at the surface of the particle signifies alteration in the particle size [22]. Two SPR bands at 576 and 826 nm have been observed for CuNR representing its transverse and longitudinal SPR modes as can be seen in figure 1b. The appearance of two SPR peaks for CuNR suggests the decrease in the symmetry of copper nanostructure, implies the formation of less symmetric or asymmetric shaped particle [22]. A very broad spectrum comprising two weakly intense peaks at 559 and 905 nm has been noticed for CuNW. The weak bands for lengthy structures (CuNR and CuNW) may result from the fact that the SPR of these nanomorphologies located in the region of the interband transitions because of the small diameter of CuNR and CuNW as already reported [23]. These variations in the SPR band of different Cu nanostructures can be ascribed to the variation in geometric facets which affects the scattering of light to diverse extent.

7.3.2 Dynamic light scattering studies

DLS is the preliminary study to investigate the NP size yet it does not provide the true size as it gives the information only about the hydrodynamic radius of particle [24]. The hydrodynamic radius is the radius of a sphere that has the same diffusion coefficient within the same viscous environment of the particles being measured. It is directly related to the diffusive motion of the particles. Figure 2 shows the hydrodynamic radius for the CuNS-1, CuNS-2 and CuNS-3 particles which lie in the range of 4-8 nm, 10-13 nm and 20-24 nm, respectively.

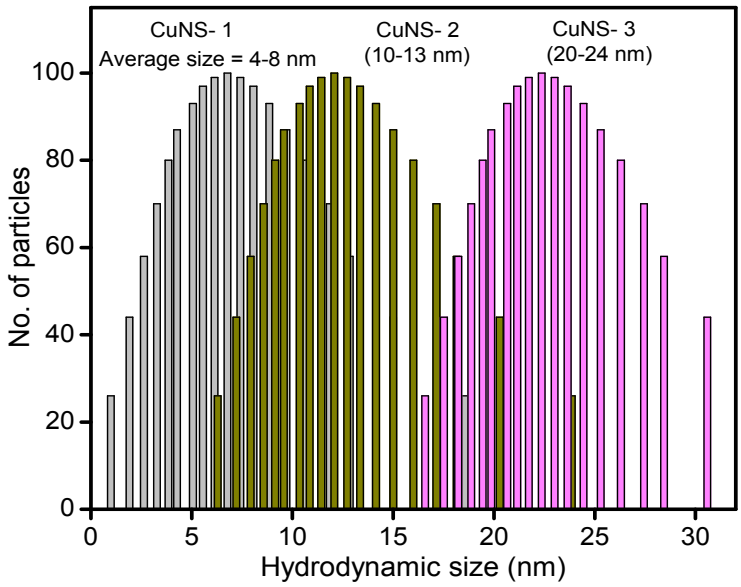

Figure 2. DLS particle size distribution of three different sizes of Cu nanospheres.

7.3.3 TEM analysis

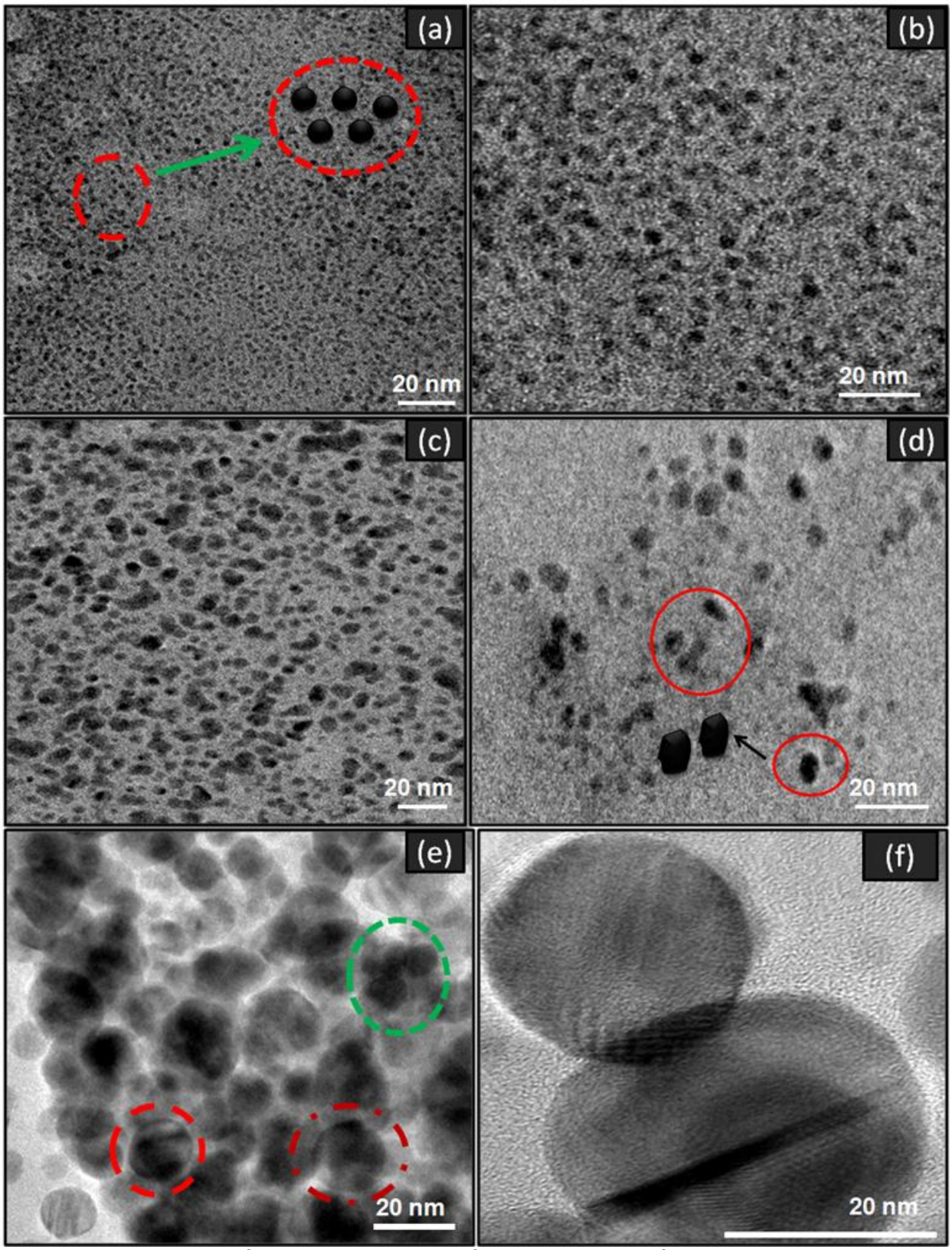

Figure 3. TEM images of aqueous suspension of Cu nanospheres of varied sizes (a, b) CuNS-1, size ≈ 3-5 nm, (c,d) CuNS-2, size ≈ 5-10 nm and (e, f) CuNS-3, size ≈ 15-20 nm.

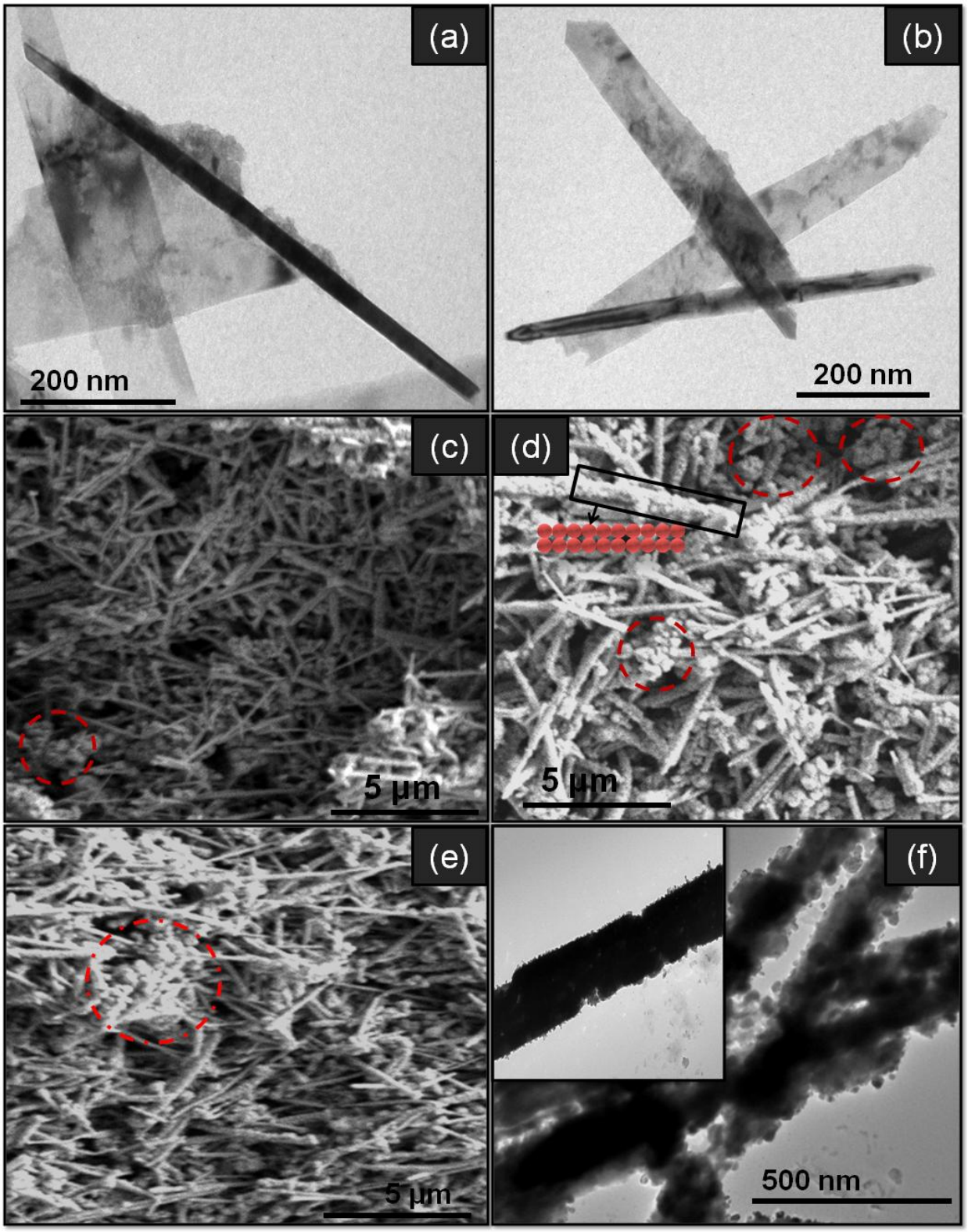

Figure 4. (a,b) TEM images of Cu nanorods of length = 600-700 nm, width = 15-20 nm, (c-e) SEM image of Cu nanowires with dimensions ≈ 4-6 µm×60-80 nm and (f) TEM image showing the Cu nanowire, inset showing an elaborated portion of nanowire.

A representative set of TEM images for three different sized Cu nanospheres synthesized under dissimilar conditions has been displayed in the figure 3. TEM image for the CuNS-1 (figure 3a and b) showed that the particles formed are of very small in size (≈ 3-5 nm), well separated, homogeneously distributed and are of spherical morphology as highlighted by a graphical image encircled in red.

Figure 3c and d showed the formation of 5-10 nm CuNS-2 particles, which are not so perfectly round in shape and some of the particles are seem to be elongated (encircled in red) and oval shaped. TEM image in figure 3e (CuNS-3) clearly highlights some irregular shaped particles such as polygonal morphology (encircled in red) along with the formation of spherical particles having size in the range of 15-20 nm. These CuNS-3 particles appear to be positioned in close proximity to each other and representing overlapped and disorganized behavior. Figure 3f reflects the image of fully grown spherical or polygonal shaped CuNS-3 particles.

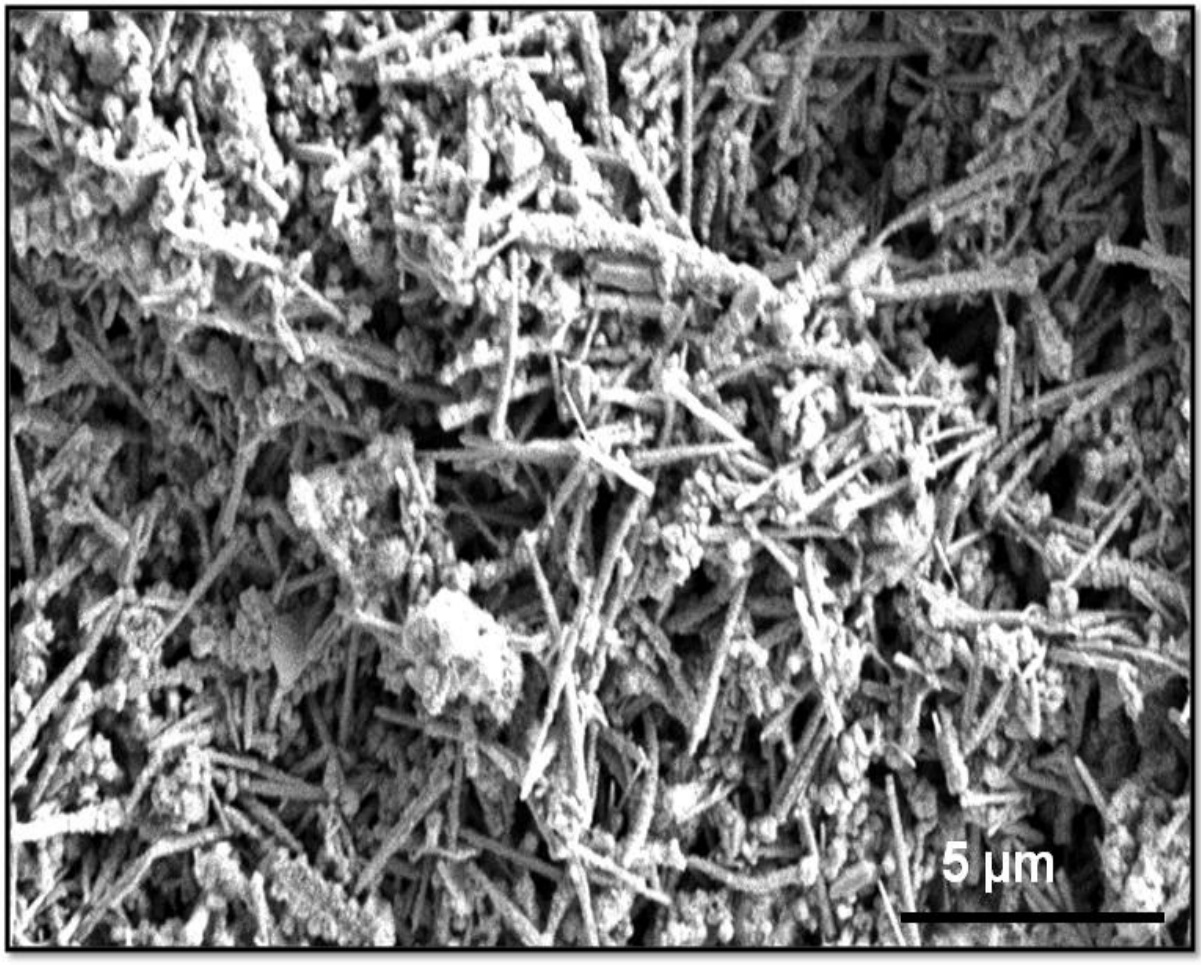

Figure 5. SEM image of Cu nanowires.

The uniform size and well orientation of CuNS-1 particles is due to the controlled growth carried out in the presence of long chain fatty acid surfactant (lauric acid) which allows the particles to grow in an appropriate manner and further stabilized by EDA [21]. The different geometric shapes of CuNS-2 and CuNS-3 particles arise because of the variance in the interaction among PVP, EG and Cu precursor ($CuSO_4$) at different temperature conditions (30˚C – 70˚C) that played an important factor in determining the morphology [16]. CuNS-3 particles synthesized using PVP as a capping agent at 70˚C, undergo an Ostwald ripening process [13] and result in larger sized asymmetric shaped particles in comparison to CuNS-2. It was suggested that large size particles (15-20 nm) begin to form at the expense of smaller particles on increasing the temperature. This nucleation growth phenomenon can be seen in figure 3e (encircled area in green) in which small sized spherical particles are appearing to merge and resulting in the formation of larger near-spherical shaped aggregates. Wang et al. [16] synthesized CuNPs of various morphologies at different temperature conditions. Moreover, it is believed that PVP

Table 1. Optoelectronic properties and physical parameters of copper nanostructures.

S.No.	Copper nanostructure	SPR band	Size TEM/(DLS)	Surface area (nm^2)	Surface/ volume ratio (nm^{-1})	Zeta potential (mV)	Conductance (μS)
1.	CuNS-1	590 nm	3-5 nm/ (4-8 nm)	50.29	1.73	-26.71	668
2.	CuNS-2	597 nm	5-10 nm/ (10-13 nm)	225.63	0.79	-12.28	454
3.	CuNS-3	645 nm	15- 20 nm (20-24 nm)	1076.02	0.34	-10.12	286
4.	CuNR	576 nm, 826 nm	Length=600-700 Width = 15-20 nm	352154	0.20	-30.08	1542
5.	CuNW	559 nm, 905 nm	Length= 4-6 μm Width =60-80 nm	1278295	0.05	-35.69	2364

macromolecule in solution adopts a pseudo-random coil conformation with metal atoms and thus increasing the probability of large sized and polymorphic shaped particle formation [25].

Fine CuNR with average length ≈ 600-700 nm and diameter ≈ 15-20 nm are clearly visible in the figure 4a and b. SEM images in the figure 4c-e revealed the presence of a vast number of CuNW with 60-80 nm in diameter and 4-6 µm length. CuNW are seem to be arranged in a randomly ordered manner and a few upright standing bundles exposing the closed ends of CuNW are also visible in figure 4c-e (encircled in red). A close glance at the SEM image (figure 4d, e and 5) is illustrating the presence of some small spheres on the NW surface which makes the appearance of NW surface rough. It suggests an idea as either NW grew from spherical seeds or it is being formed by the accumulation of small spherical particles as clearly demonstrated in the TEM image (figure 4f). Rathmell et al. [19,20] reported the growth mechanism for the synthesis of CuNW and suggested that these NW grew from spherical seeds.

7.3.4 Co-catalytic activity

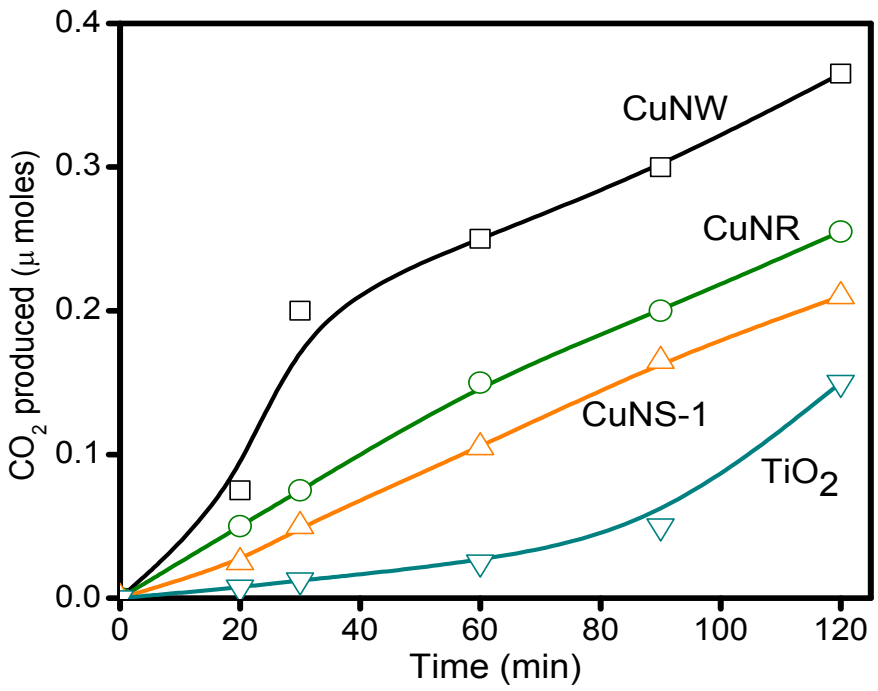

Figure 6. Time course of CO_2 evolution during acetic acid photodecomposition with various bare and Cu-TiO_2 nanostructures under UV light irradiation.

It is well known that that metal-TiO_2 system displayed higher photoactivity as compared to bare TiO_2 due to better electron capturing ability of metal NPs and leaving the holes free for oxidation

[26,27]. Figure 6 displayed the time dependent carbon dioxide evolution on the photodestruction of acetic acid carried out by using the mixture of TiO_2 (25 mg) and various Cu nanostructures (ca. 3.73×10^{18} atoms) under UV irradiation.

Calculations of CO_2 measurement by photooxidation of CH_3COOH with 25 mg TiO_2 and various Cu nanostructures (ca. 3.73×10^{18} atoms).

$$CH_3COOH + 2O_2 \rightarrow 2CO_2 + H_2O$$

It means complete mineralization of CH_3COOH evolved 2 molecules of CO_2

Initial concentration of CH_3COOH = 50 µM

5ml of CH_3COOH 50 µM contains = 50/1000 × 5 = 0.25 µmol

Its complete mineralization gives = 2 × 0.25 = 0.5 µmol

It is observed (figure 6) that CuNW addition to TiO_2 produced the highest amount of CO_2 i.e. ≈ 70 % (0.37 µmol) in 2 h in contrast to 50 % (0.25 µmol), 42 % (0.21 µmol) and 30 % (0.15 µmol) by CuNR-TiO_2, CuNS-1-TiO_2 and bare TiO_2, respectively. The difference in the co-catalytic activity is due to the varied morphology of CuNS-1, CuNR and CuNW which could alter the interfacial properties of CuNPs-TiO_2 junction for the photodestruction of acetic acid.

7.3.5 Catalytic activity

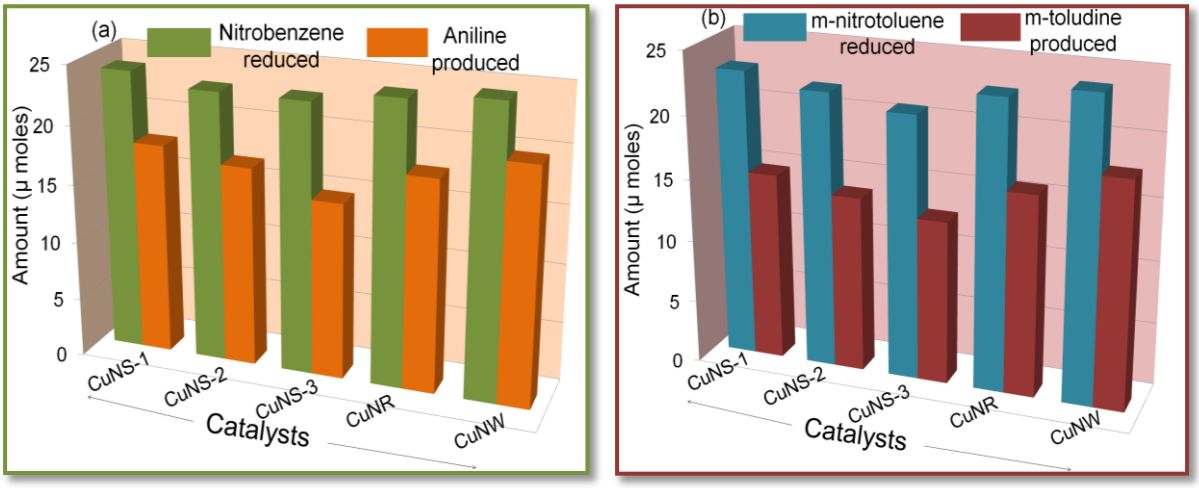

Figure 7. Comparative catalytic activity of various Cu nanostructures for (a) amount (µ moles) of nitrobenzene reduced to aniline and (b) m-nitrotoluene to m-toludine.

Size and shape dependent catalytic activity of Cu nanostructures (ca. 3.73×10^{18} atoms) has been assessed by the reduction of nitro aromatics in the presence of reducing agent ($NaBH_4$) and the progress of the reaction has been monitored through UV-visible spectrophotometer, HPLC and GC-MS analysis. The reaction was primarily carried by the addition of reducing agent only, but a

negligible change in the concentration of reactants has been observed, confirming the essentiality of CuNPs for the reaction [29-31]. Extent of reduction of nitrobenzene and m-nitrotoluene to aniline and m-toludine has been shown in figure 7 and quantified by HPLC analysis. Since, the reduction progress has been observed in the presence of $NaBH_4$, the concentration (0.82 M) of

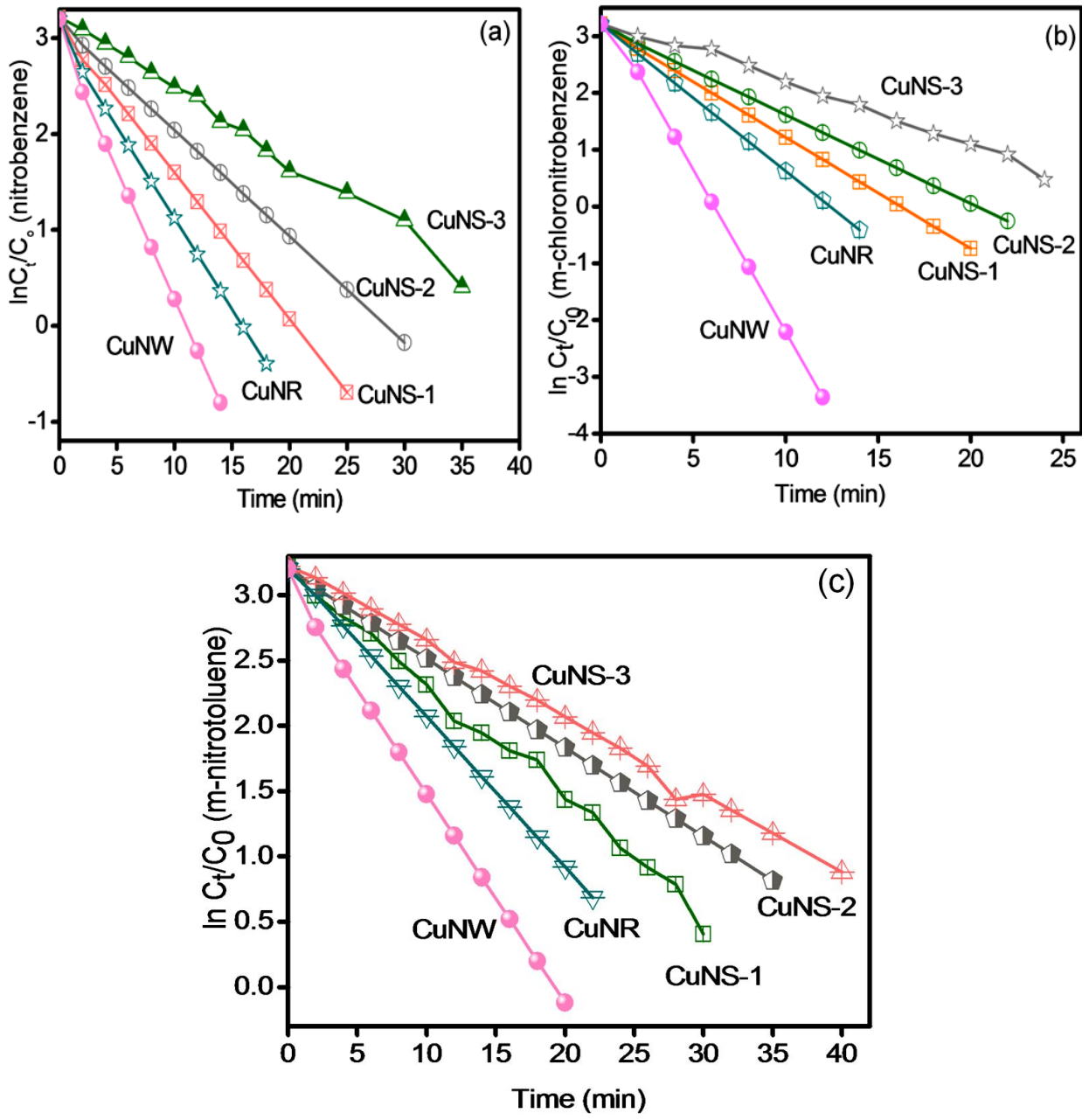

Figure 8. Plot of ln C_t/C_0 versus time for the reduction reaction of (a) nitrobenzene (b) m-chloronitrobenzene, and (c) m- nitrotoluene carried by various Cu nanomorpholgies.

Table 2. Observed rate constant (k) and percentage conversion for nitroaromatic reduction reaction.

S.No.	Catalyst	Nitrobenzene		m-chloronitrobenzene		m-nitrotoluene	
		K (min^{-1})	Conversion	K (min^{-1})	Conversion	K (min^{-1})	Conversion
1.	CuNS-1	1.5×10^{-1}	72 %	1.9×10^{-1}	75 %	0.8×10^{-1}	60 %
2.	CuNS-2	1.1×10^{-1}	68 %	1.5×10^{-1}	72 %	0.6×10^{-1}	55 %
3.	CuNS-3	0.7×10^{-1}	65 %	1.1×10^{-1}	69 %	0.5×10^{-1}	59 %
4.	CuNR	1.9×10^{-1}	75 %	2.5×10^{-1}	80 %	1.1×10^{-1}	65 %
5.	CuNW	3.8×10^{-1}	86%	5.0×10^{-1}	96 %	1.6×10^{-1}	78 %

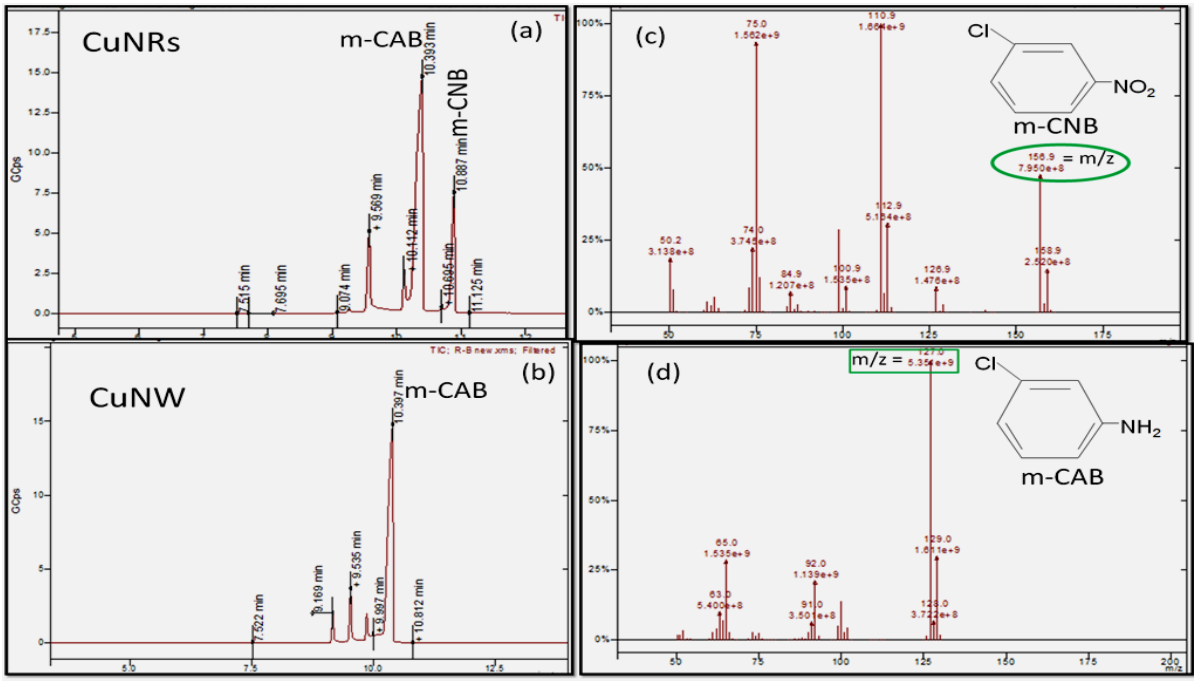

Figure 9. GC chromatograph for the reduction of m-chloronitrobenzene (m-CNB) to m-chloroaminobenzene (m-CAB) using (a) CuNR, (b) CuNW and (c,d) corresponding mass spectrum of identified compounds, inset showing structural formula of the compounds.

which exceeds the concentration of nitro aromatics (5mM, nitrobenzene, m-nitrotoluene, m-chloronitrobenzene), which implies that the reaction rate follows first order kinetics ($C = C_0e^{-kt}$).

The logarithm of concentration of reactant compounds has been found to decrease linearly with reaction time (figure 8) and from slope of ln C_t/C_0 versus time, apparent rate constant (k) of the reaction was estimated and has been displayed in table 2. These results signify that all the Cu nanostructures are successfully catalyzing the chemical reduction of nitro aromatic compounds.

Moreover, it is essential to mention here that the constant amount of CuNPs (3.73×10^{18} atoms) addition to reaction media exhibits catalytic effect in a varied extent as a function of their shape and size, reflected through the percentage yield and reduction rate, and follows the trend CuNW > CuNR > CuNS-1 > CuNS-2 > CuNS-3 (table 2). Most importantly, the above mentioned trend was also evidenced through the GC-MS analysis, that reveals the complete conversion of m-chloronitrobenzene (m/z =157, R_t = 10.8 min) to m-chloroaminobenzene (m/z = 127.57, R_t = 10.3 min) using CuNW in relation with CuNR (Figure 9a and b), confirming the incomplete reduction of the same for other Cu nanomorphologies. Similar, behavior was found for reduction of m-nitrotoluene to m-touldine (data not shown).

It was believed that the reduction proceeds via. utilizing the nanocatalyst surface efficiently through adsorbing reactant molecule followed by interfacial electron transfer and finally, desorption of the product as shown in the scheme 1. The 1 D lengthy Cu nanowires (CuNW, length = 4-6 μm, width = 60-80 nm) with highest surface area per particle (≈1278295 nm^2, table 1) provides much exposed surface for the reactant molecules and hence, resulting in immense yield in a very short period of time. On considering the size factor alone, CuNS-1 with smallest size (3-5 nm) are found to be more effective catalysts than the CuNS-2 (5-10 nm) and CuNS-3 (15-20 nm) because the decrease in the particle size results in an increase in the effective surface to volume ratio (table 1) and higher d-electron density of the Cu atoms, which leads to an increased reactivity towards hydrogen atoms [29]. The CuNS-3 and CuNR with comparable diameter (≈15-20 nm) were expected to show similar reduction rate, but contrary to this, CuNR with large surface area allow more interactions of reactant molecules with catalyst surface and therefore, show pronounced effect over the three dimensional nanostructure (CuNS-3). Moreover, distortion in the symmetry from spheres to rods and then to wires leads to more unbalanced forces on the particle surface and more exposed surface atoms which results in the higher reaction rate. One more plausible reason for effectiveness of the NWs is their rough surface (figure 4d) which promotes more interactions amongst reacting species and hence results in effective reduction. It has also been reported that lengthy nanostructures (CuNW) display

more co-catalytic effect to TiO_2 in comparison to spherical particles because of their high potential to act as an electron sink which in-turn increase lifetime of charge carriers recombination [32]. Moreover, the highest conductance of CuNW (2364 μS, table 1) relative to CuNS-1 (668 μS) and CuNR (1542 μS) evidenced the distinct effect of NW for fast transference of the electronic species from TiO_2 to lengthy NW.

7.3.6 Influence of functional group

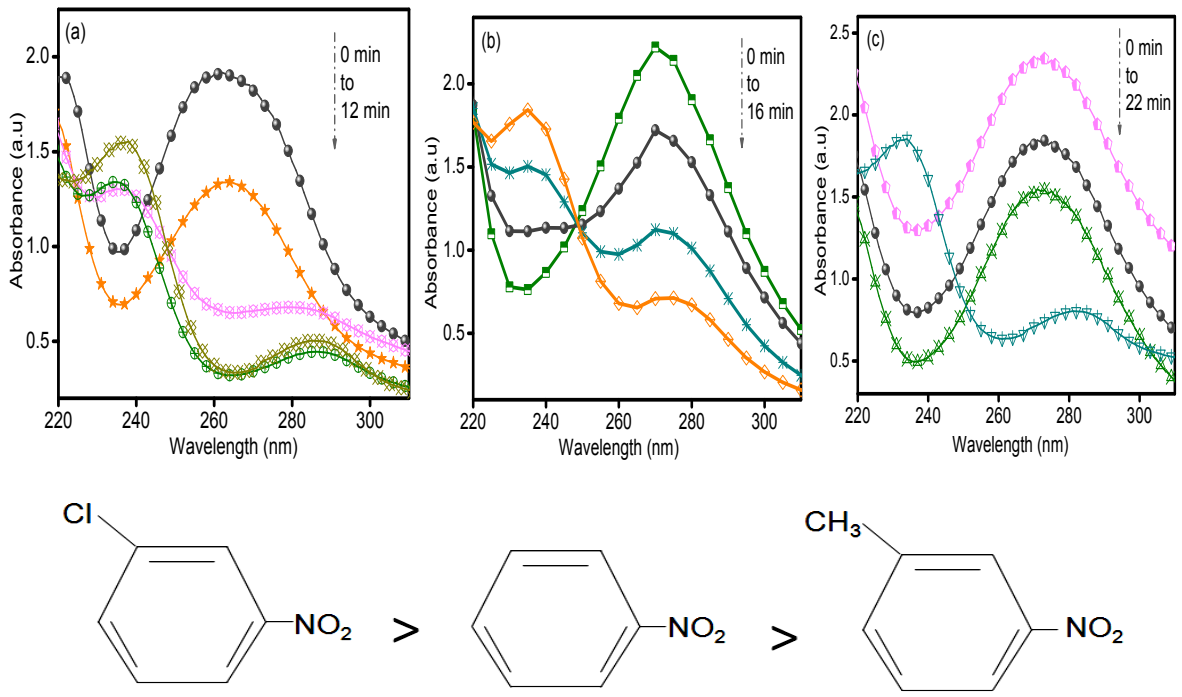

Figure 10. UV-vis absorption spectra recorded for the chemical reduction of (a) m-chloronitrobenzene, (b) nitrobenzene, and (c) m-nitrotoluene catalyzed by CuNW and the respective structures of nitrocompounds are drawn below.

The above results clearly demonstrate that CuNW are considered to be the best catalyst in comparison with NR and NS. One more important point here to be considered is the nature of the substrate, i.e., reduction rate also depends on the nature of the substituent group on aromatic ring. Lesser reduction rate is observed for compound substituted with electron-donating group ($^{-}CH_3$) in comparison with compound substituted with electron-withdrawing group (^{-}Cl) as can be seen from figure 10 and 11. Figure 10 shows the comparative UV-visible absorption spectra for the reduction of three compounds namely nitrobenzene, m-chloronitrobenzene and m-nitrotoluene employing CuNW as a catalyst. These experiments showed that aromatic compounds reduce in a very short time (≈12 min) interval substituted with electron-withdrawing radical ($-Cl^{-}$) than

compounds with electron-donating radicals (-CH_3, ≈ 20-25 min). These effects can be explained in the terms of localized (inductive) and delocalized (resonance) electronic effects of substituent.

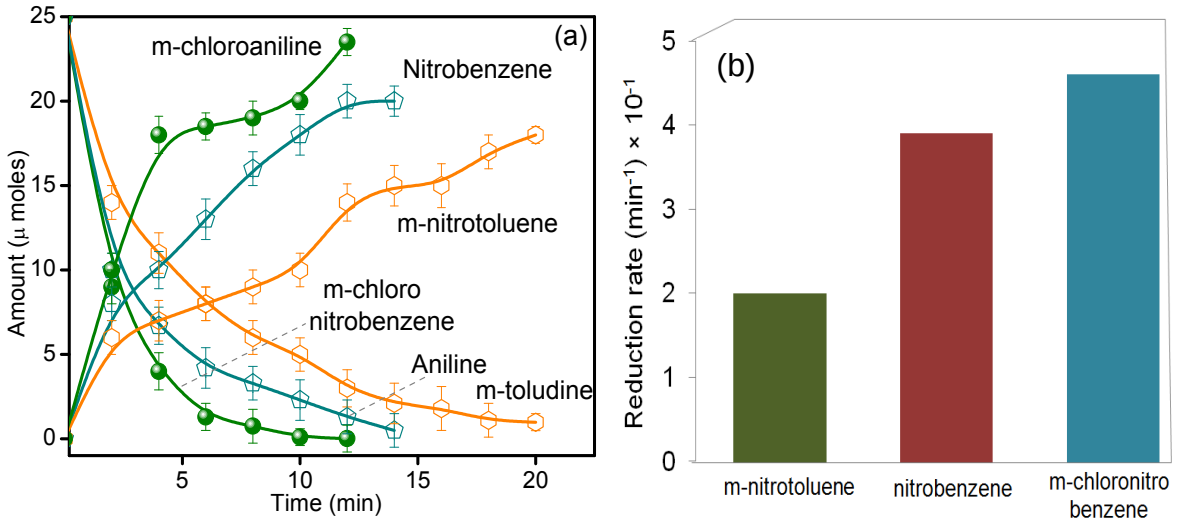

Figure 11. (a) Rate of change in the reduction of nitroaromatics (amount in μ moles) to their respective products utilizing CuNW catalyst as a function of functional group entity and (b) relative reduction rate of three nitroaromatic compounds.

The higher inductive (+ 0.34) and lower resonance stabilization value (-0.07) of chloro group relative to low inductive (-0.04) and high stabilization parameters (-0.11) of methyl group reflect fast rate of reduction for chloro group [33]. The resonance stabilized methyl substituted nitro aromatic compound would not respond fast toward the acceptance of electron and thus show low reduction rate in longer duration (figure 10). As expected, rate constant varies with the character of the radical and the reaction was found to follow apparent first-order kinetics (table 2).

In conclusion, we can say that the both catalytic and co-catalytic activities exhibited by the Cu nanostructures vary as a function of their morphology. Lengthy nanowires showed profound effect in catalyzing the reactions relative to spherical morphology owing to its highly exposed rough surface, more surface area and higher conductance value.

7.4 References

[1] B. Luo, X. Li, X. Li, L. Xue, S. Li and X. Li, Cryst. Eng. Comm., 15 (2013) 5654.

[2] T. Montini, V. Gombac, L. Sordelli, J.J. Delgado, X. Chen, G. Adami and P. Fornasiero, ChemCatChem., 3 (2011) 574.

[3] A.K. Schaper, H. Hou, A. Greiner, R. Schneider and F. Philips, Appl. Phys. A Mater. Sci. Process, 78 (2004) 73.

[4] S.K. Mehta, R. Kaur and G.R. Chaudhary, Colloids Surf. A, 403 (2012) 103.

[5] B. Pergolese, M. Muniz-Miranda and A. Bigotto, J. Phys. Chem. B, 110 (2006) 9241

[6] C.J. Flytzanis, Physics B At. Mol. Opt. Phys., 38 (2005) S661.

[7] M. Samim, N.K. Kaushik and A. Maitra, Bull. Mater. Sci., 30 (2007) 535.

[8] S.U. Son, I.K. Park, J. Park and T. Hyeon, Chem. Commun., (2004) 778.

[9] Md. A.Al-Mamun, Y. Kusumoto, B. Ahmmad and M.S. Islam, Top. Catal., 53 (2010) 571.

[10] W. Siripala, A. Ivanovskaya, T.F. Jaramillo, S.H. Baeck and E.W. McFarland, Sol. Energy Mater. Sol. Cells, 77 (2003) 229.

[11] Q. Liu, D. Zhou, K. Nishio, R. Ichino and M. Okido, Mater. Trans., 51 (2010) 1386.

[12] D.B. Pedersen and S. Wang, J. Phys. Chem. C, 111 (2007) 17493.

[13] C. Barriere, K. Piettre, V. Latour, O. Margeat, C. Turrin, B. Chaudret and P. Fau, J. Mater. Chem., 22 (2012) 2279.

[14] A. Sarkar, T. Mukherjee and S. Kapoor, J. Phys. Chem. C, 112 (2008) 3334.

[15] N.V. Surmawar, S.R. Thakare and N.T. Khaty, INT. J. Green Energy, 3 (2011) 302.

[16] Y. Wang, P. Chen and M. Liu, Nanotechnology, 17 (2006) 6000.

[17] B.J. Wiley, Y. Sun, B. Mayers and Y. Xia, Chem. Eur. J., 11 (2005) 454.

[18] H.H. Huang, F.Q. Yan, Y.M. Kek, C.H. Chew, G.Q. Xu, W.Ji, P.S. Oh and S.H. Tang, Langmuir, 13 (1997) 172.

[19] A.R. Rathmell, S.M. Bergin, Y.L. Hua, Z.Y. Li and B.J. Wiley, Adv. Mater., 22 (2010) 3558.

[20] A.R. Rathmell and B.J. Wiley, Adv. Mater., 23 (2011) 4798.

[21] A.K. Patra, A. Dutta and A. Bhaumik, Catal Comm., 11 (2010) 651.

[22] M.K. Oh, H.J. Baik, S.K. Kim and S. Park, J. Mater. Chem., 21 (2011) 19069.

[23] H. Guo, N. Lin, Y. Chen, Z. Wang, Q. Xie, T. Zheng, N.Gao, S. Li, J. Kang, D. Cai and D. L. Peng, Scientific Reports, 3 (2013) 2323.

[24] S. Park and K.H. Schifferli, J. Phys. Chem. C, 112 (2008) 7611.

[25] P.Y. Silvert, R.H. Urbina, and K. Tekaia-Elhsissena, J. Mater. Chem., 7 (1997) 293.

[26] F. Boccuzzi, A. Chiorino, G. Martra, M. Gargano, N. Ravasio, and B. Carrozzini, J. Catal., 165 (1997) 129.

[27] N.R. Khalid, E. Ahmed, Z. Hong, M. Ahmad, Y. Zhang and S. Khalid, Ceram. Int., 39 (2013) 7113.

[28] M. You, T.G. Kim, and Y.M. Sung, Cryst. Growth Des., 10 (2010) 983.

[29] P. Veerakumar, M. Velayudham, K.L. Lu and S. Rajagopal, Appl. Catal. A: Gen., 439 (2012) 197.

[30] Z. Duan, G. Ma, and W. Zhang, Bull. Korean Chem. Soc., 33 (2012) 4003.

[31] M. Chirea, A. Freitas, B.S. Vasile, C. Ghitulica, C.M. Pereira, and F. Silva, Langmuir, 27 (2011) 3906.

[32] R. Singh and B. Pal, J. Mol. Catal. A: Chem., 371 (2013) 77.

[33] C. Bougheloum and A. Messalhi, Physics Procedia, 2 (2009) 1055.

Chapter 8

Comparative Co-catalytic Account of Coinage Metal Nanoparticles (Au, Ag and Cu) for TiO_2 Photocatalysis under Visible Light Irradiation

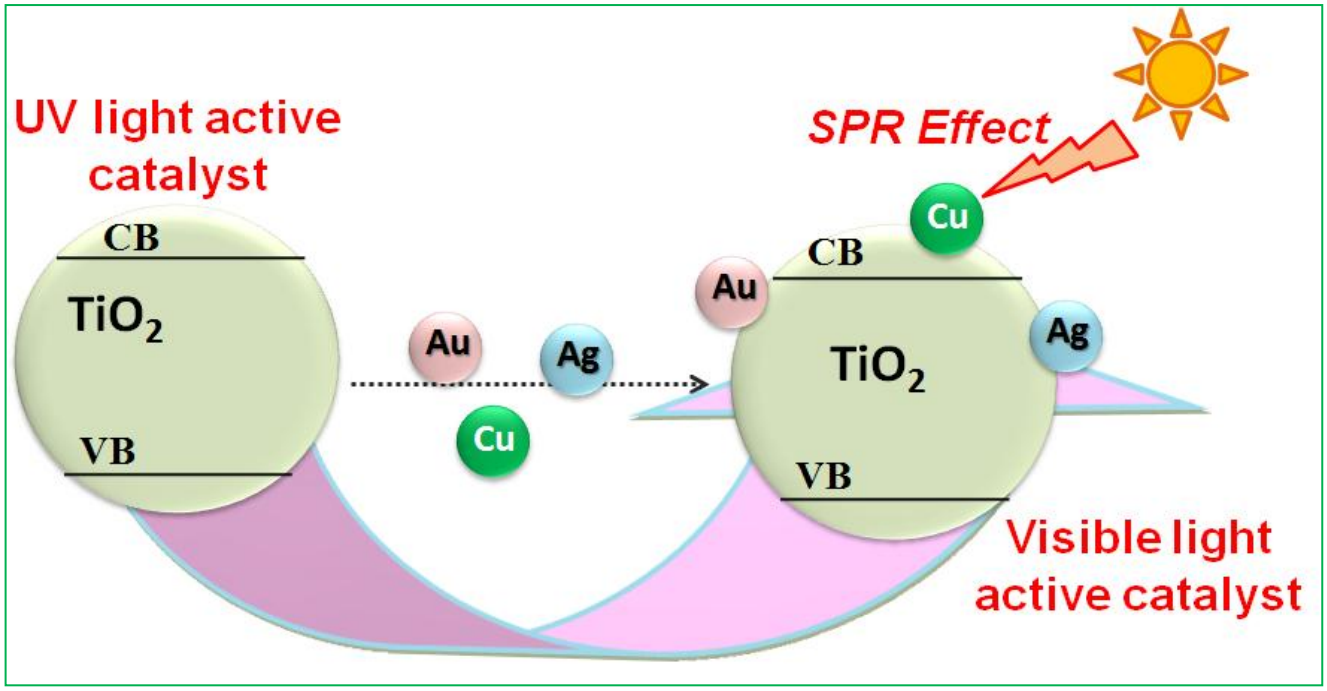

8.1 Introduction

Coinage metal (Au, Ag and Cu) nanoparticles (NPs) are known as plasmonic materials because they strongly absorb visible light due to surface plasmon resonance (SPR), in which conducting electrons undergo a collective oscillation induced by the electric field of visible light. These plasmonic nanostructures act primarily as an antenna to concentrate the light, convert the light energy to heat that enables them to serve as principle candidates for photovoltaic's, colorimetric sensors, photochromic devices, surface-enhanced Raman spectroscopy, photocatalysis, etc. [1-13]. Hence this light absorption property of the metallic nanostructures is presenting an opportunity to design a new class of efficient sunlight harvesting photocatalysts and have opened up a new direction in the field of photocatalysis. For example, Au and AgNPs supported on insulators such as ZrO_2 and SiO_2 were found to be highly efficient photocatalysts under visible light for the reduction of nitrobenzene to azobenzene and for the oxidation of benzyl alcohol [9,13-15]. In such systems, the insulator support does not play an active role in the catalysis as there is no electron transfer from the photo-excited metal NPs to insulator supports due to the wide band gap and high-lying conduction band edges [13-15].

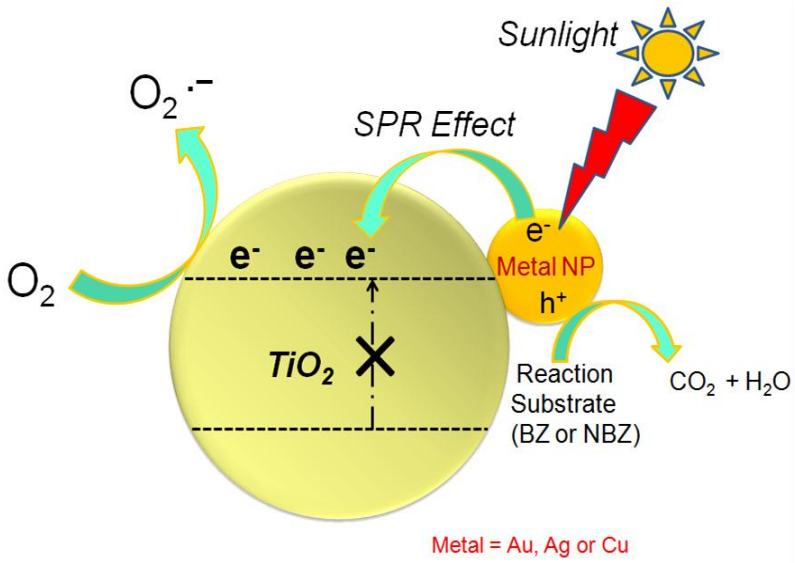

Scheme 1. Surface plasmon resonance effect of metal nanoparticles (Au, Ag or Cu) for TiO_2 photocatalysis under sunlight irradiation.

In this way, metal NPs can be utilized to enhance the photoactivity of UV light active photocatalysts (such as TiO_2) to visible or far-infrared region by altering the shape, size and nature of NP. Although TiO_2 semiconductor is known as a benchmark material for photocatalysis, yet the wide band gap restricts its absorption only to UV light (λ = 388 nm), which accounts for less than 5% of solar light [16-19]. The metallic nanostructures in close

proximity with TiO_2 would result in the reduction of band gap and enhancement in the visible light absorption [1-11]. When metal NPs are homogeneously distributed on the surface of TiO_2, the visible-light irradiation would stimulate a fast and efficient transfer of the photo-excited electrons from the metal NPs to the conduction band of TiO_2 [20-24]. This would result in electron-deficient metal NPs and electron-rich TiO_2, so that the photocatalytic oxidation of organic molecules over M-TiO_2 should occur on the metal NP surface rather than on the TiO_2 surface (scheme 1). Literature reveals that the presence of AuNPs on TiO_2 results in fast transference (less than 240 fs) of photo-excited electrons into the TiO_2 support [22,24-26]. This metal-TiO_2 (M-TiO_2) heterocomposite system is suitable to study the intrinsic association between the two because different types of interfacial contacts would result in varied photophysical, optoelectronic, chemical and catalytic properties depending on the morphology, composition and nature of the metal.

While several reports showed the visible light enhancement in TiO_2 photocatalyst employing various metallic nanostructures, but a comparative account of the co-catalytic activity imparted by coinage metal NPs is still need to be conferred at a glance. *In our previous chapters, we have already dealt with the morphological dependent co-catalytic effect of coinage metal NPs for the enhancement of TiO_2 photoactivity. So irrespective of shape and size effect, this chapter solely represents a comparative report on the nature of the coinage metal NPs (Au, Ag and Cu) for enhancement of the catalytic activity of TiO_2 utilizing visible light for the photodegradation of benzaldehyde and nitrobenzaldehyde. The difference in work function, redox potential, electron storage capacity, the nature of electronic charge and conduction ability of coinage metal NPs would dictate their varied co-catalytic activity.*

8.2 Experimental section

8.2.1 Materials and methods

Chloroauric acid ($HAuCl_4.3H_2O$), copper sulphate, trisodium citrate, benzaldehyde (BZ), nitrobenzaldehyde (NBZ) was purchased from Loba chemicals. Silver nitrate ($AgNO_3$) was purchased from Fischer scientific and commercially available P25-TiO_2 was obtained from Degussa Corporation, Germany, respectively. Deionized water was obtained using an ultra filtration system (Milli-Q, Millipore) with a measured conductivity 35 mho cm^{-1} at 25 ◦C.

8.2.2 Synthesis of Au, Ag and Cu nanospheres

Nanospheres (NS) of coinage metals (Au, Ag and Cu) have been prepared through reduction route using trisodium citrate as a reducing as well as capping agent [27]. The synthetic procedure involves the addition of 140 µl (0.01 M) aqueous solution of $HAuCl_4$, $AgNO_3$, and $CuSO_4$ in three respective beakers containing 14 ml boiling solution of trisodium citrate (50 mg/ ml). The obtained solution was allowed to boil till the light pink, yellow and brown color appears for the Au, Ag and Cu nanospheres, respectively.

8.2.3 Synthesis of M-TiO_2 nanocomposites (M = Au, Ag and Cu)

Metal loaded titania nanocomposites (M-TiO_2) were synthesized through wet impregnation method followed by calcination. In a typical experiment, 500 mg of TiO_2 was mixed with 50 ml distilled water by adding requisite amounts (1 wt%) of metal nanospheres (Au, Ag and Cu) individually, stirred for 12 h, followed by drying at 100 ˚C. The dried powder catalyst was then repeatedly washed with water and all the prepared samples were then sintered in muffle furnace at 80˚C for 10 h. The M-TiO_2 (M= Au, Ag or Cu) nanocomposites displayed a variety of colors dependent on the nature of metal NPs present.

8.2.4 Photocatalytic activity

The photocatalytic activity was tested for the photooxidation of 10 ml, 0.1 mM BZ and NBZ with 20 mg catalysts (bare TiO_2, Au-TiO_2, Ag-TiO_2 and Cu-TiO_2) under sunlight (intensity 40 mW/cm^2 using a 25 ml beaker) irradiation with constant magnetic stirring. The reaction samples were analyzed by UV–vis spectrophotometer (λ_{max} = 260 nm for NBZ and 242 nm for BZ) after filtration with 0.22 µm cellulose filter.

8.2.5 Characterization

The as prepared aqueous colloidal solution of metal NS (Au, Ag and Cu) and powdered M-TiO_2 composites were characterized by UV-vis absorption and diffuse reflectance spectrophotometer, respectively. Morphological study of size analysis was done by dynamic light scattering (DLS) and TEM. BET surface area was measured by N_2 adsorption technique. X-ray diffraction study was carried out for phase identifications. XPS was done for surface elemental studies. Current voltage characteristics and Time resolved spectroscopy were also investigated. Intermediates formed during the photodegradation process were analyzed through GC-MS. Amount of CO_2 produced on mineralization of BZ and NBZ was measured by GC with a TCD as a detector. All these techniques have been mentioned in detailed in chapter 1.

8.3 Results and discussion

8.3.1 Optical characteristics and DLS studies

Figure 1 displayed the surface plasmon resonance (SPR) bands for Au (≈ 520 nm), Ag (≈ 425 nm) and CuNS (≈ 612 nm). Highly intense and sharp band has been observed for the Ag and AuNS whereas weak and broadened band was depicted for CuNS. The sharp band for Au and AgNS clarifies the presence of homogenous and well separated particles while broadening in the SPR band for CuNS signifies its larger size.

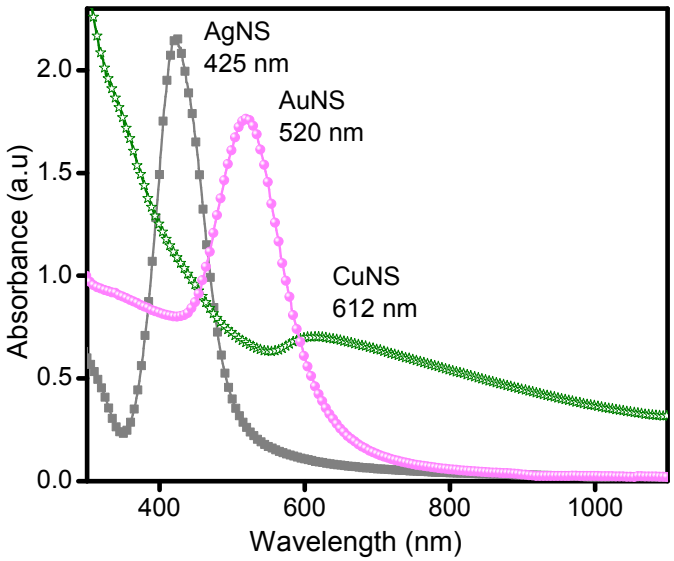

Figure 1. Surface palsmon resonance bands of Au, Ag and Cu nanospheres.

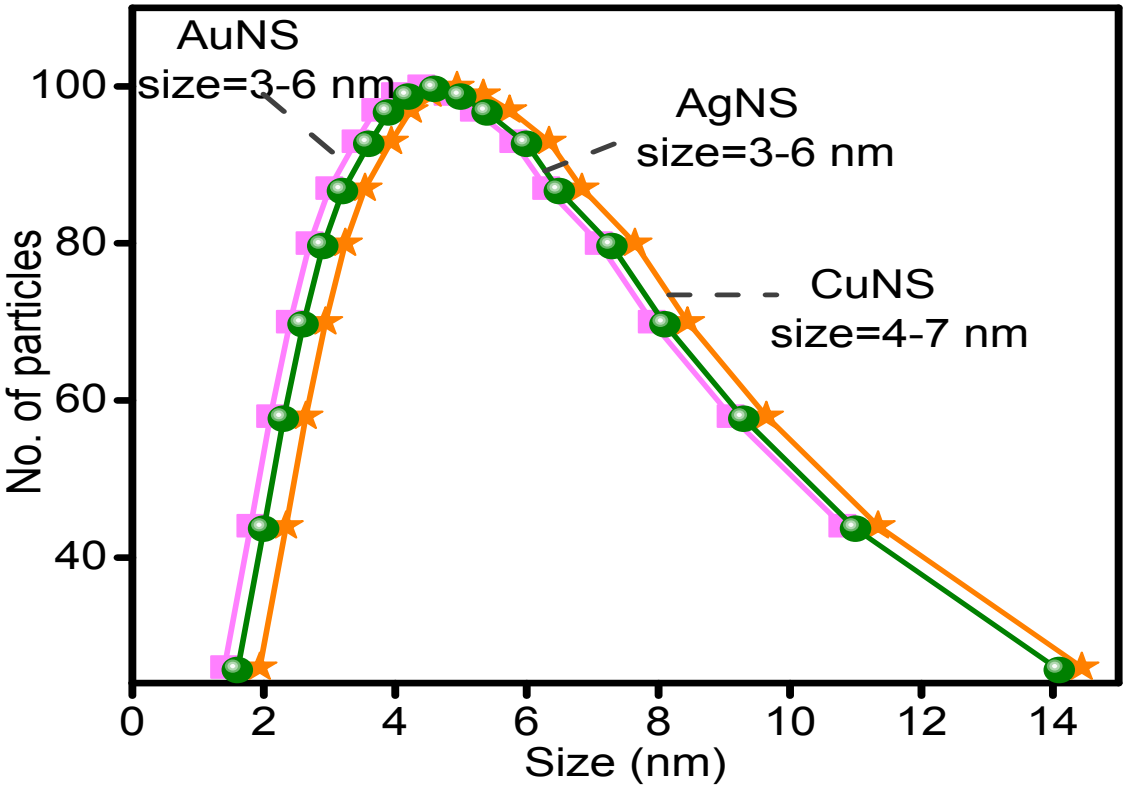

Figure 2. Partcle size distribution for Au, Ag and Cu nanospheres.

Such SPR band for AgNS at 420 nm has also been observed by Ratyakshi et al. [28] by employing trisodium citrate as a reducing agent, showing the size range ≈ 10-20 nm. AuNS of size ≈ 3-5 nm (SPR band ≈ 520 nm) has been prepared by well known Turkevich method [29], using citrate as a reducing and capping agent. Samim et al. [30] reported the preparation of CuNS of various sizes by citrate reduction route. These nanocolloidal suspensions of metal NS remain stable for a long time as being stabilized by trisodium citrate. Further, the particle size of the prepared metal NS has been characterized through dynamic light scattering studies which provide the information on the hydrodynamic radius of NS. Results clearly revealed that the particle size distribution for all the prepared coinage metal (Au, Ag and Cu) NS were found to lie in the ≈ 3-7 nm size range as shown in figure 2.

8.3.2 Diffuse reflectance studies of M-TiO_2 composites

These plasmonic metal NS operates as visible light sensitizers and their impregnation onto TiO_2 (P25, size = 30-50 nm) result in the M-TiO_2 composites (discussed in experimental section) which would show visible light sensitivity. The UV–vis diffuse reflectance spectrum of M-TiO_2 composites relative to P25-TiO_2 is being represented in figure 3a. Titania NPs are characterized by sharp absorption edge around ~390 nm (band gag, E_g = 3.12 eV, inset figure 3a). The assimilation of coinage metal NS of similar sizes on TiO_2 cause a red shift in the absorption edge of TiO_2 (≈ 390 nm) from the UV to visible region (≈ 415-420 nm) as can be seen in figure 3a and

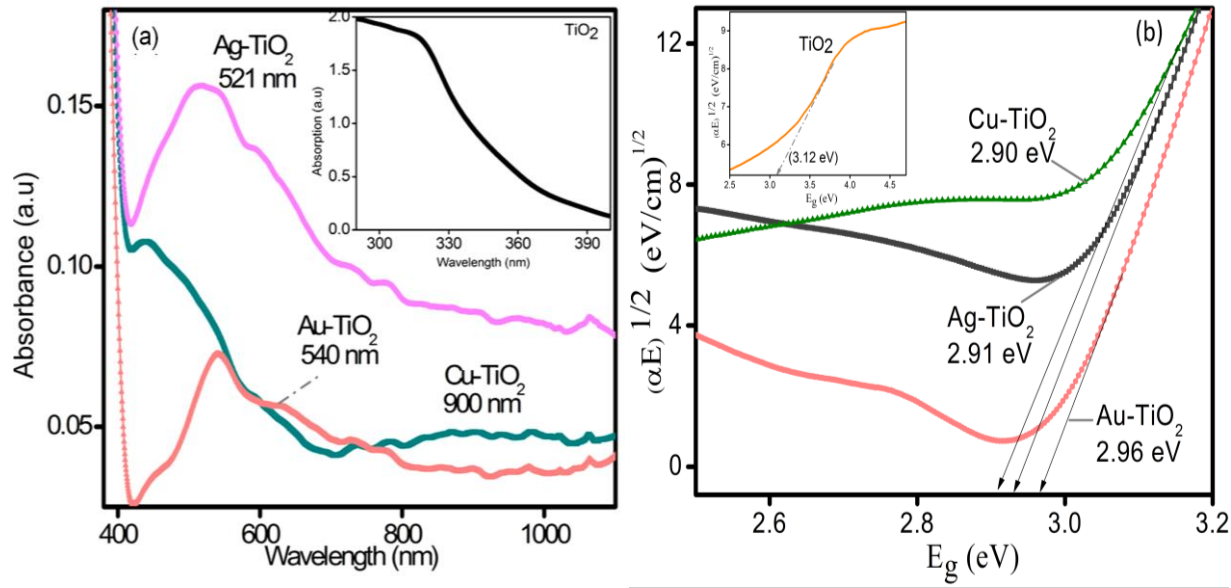

Figure 3. (a) Solid state absorbance spectra of M-TiO_2 (M=Au, Ag and Cu) composites with 1 wt% metal NP loading and P25-TiO_2 (inset) nanoparticles and (b) their corresponding bandgap.

can be explained in terms of the electron transfer from Au, Ag and CuNPs to TiO_2 [1-10,14,17,31]. The coinage metal NPs displayed their characteristic surface plasmon absorption band at ~521 nm for Ag-TiO_2, ~540 nm for Au-TiO_2 and >700 nm for Cu-TiO_2, respectively. One can observe that SPR band of citrate-capped Ag and AuNPs is around 425 and 520 nm (figure 1), whereas in composite form (Ag-TiO_2 and Au-TiO_2), the SPR band has been considerably red-shifted to 521 nm and 540 nm, respectively. This shift in the SPR towards longer wavelength can be attributed to the higher refractive index of the titania shell as already reported [32]. Zheng et al. [9] also observed red shift in SPR peaks for Au-TiO_2 and Ag-TiO_2 at 540 and 451 nm, respectively. The intensity and wavelength of SPR band are highly dependent on the size, shape, nature of the metal NP and composition of M-TiO_2 composite.

Red shift in the absorption edge of M-TiO_2 composites is an indication of narrowing of the TiO_2 band gap. The band gap (Eg) of the M-TiO_2 has been determined from the Tauc plot by extrapolating the linear portion of the plot of $(\alpha h\nu)^2$ versus $h\nu$, showed in figure 3b. The Eg aids in determining the energy necessary to create electron-hole (e^--h^+) pairs in the semiconductor to initiate photocatalytic processes. Eg calculated using Tauc's equation was found to be ca. 2.96 eV, 2.91 eV and 2.90 eV for Au-TiO_2, Ag-TiO_2 and Cu-TiO_2, respectively (table 1). It has been reported that the observed absorption edge shifting and band gap reduction in M-TiO_2 can be controlled as a function of surface morphology or by introducing lattice strain and vacancies [33,34]. Thus differences in the optical characteristics arise due to the variation in the size, shape, amount, surrounding environment, distribution factor and nature of the metal NPs.

8.3.3 XRD analysis

The structural analysis of the synthesized M-TiO_2 nanocomposite in comparison to bare TiO_2 (P25) particles has been carried out by XRD measurements as shown in figure 4. The XRD pattern indicates the mixture of anatase and rutile phase for all the synthesized M-TiO_2 samples and does not show any peak corresponding to metal NS. The non-existence of XRD peak for metal NS may be due to their lesser amount (1 wt%) and very small size (3-5 nm) which is below the detectability limit of XRD. Similar observation has been reported by Zheng et al. [9] on loading 1 wt% Au, Pt, Ag on TiO_2. Moreover, these results suggest that the coinage metal NS have been integrated into the basic structure of TiO_2 and have not induced the formation of any

discrete impurity phase. However, the EDX of M-TiO_2 composites taken during the TEM measurements (figure 8 and 9) and XPS analysis (table 1) confirmed the presence of metal NPs.

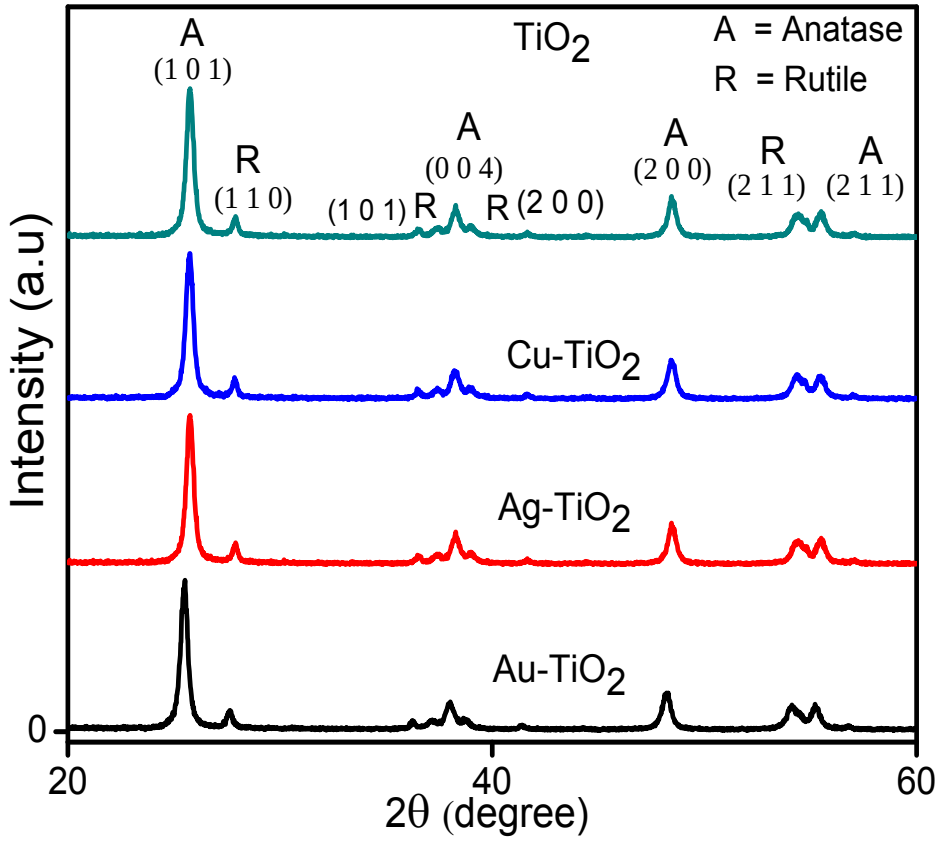

Figure 4. XRD patterns of TiO_2 (P25) and M-TiO_2 composites with loading of 1 wt% coinage metal nanoparticles.

Table 1. Elemental composition and physical parameters of M-TiO_2 composites.

Catalyst	*Atomic % (XPS data)*				*Band gap (eV)*	*S_{BET} (m^2g^{-1})*
	C1s	O1s	Ti2p	Respective metal (%)		
TiO_2	-	-	-	-	3.12	50
Au-TiO_2	35.71	50.13	14.11	Au4f (0.06)	2.96	29
Ag-TiO_2	35.47	51.04	13.14	Ag3d (0.35)	2.91	33
Cu-TiO_2	39.78	50.98	8.89	Cu2p (0.35)	2.90	20

8.3.4 BET analysis

The BET surface area (S_{BET}) of M-TiO_2 heterocomposites, ca. 29, 33 and 20 m^2g^{-1} for Au-TiO_2, Ag-TiO_2, and Cu-TiO_2 has been found to be decreased relative to bare TiO_2 (50 m^2g^{-1}), respectively (table 1). This large reduction in S_{BET} value may be due to the partial surface coverage of titania porous sites with metal NPs (≈1 wt%). Alteration in surface area of M-TiO_2 relative to TiO_2 (P25) signifies the presence of metal NS in TiO_2 matrix. Such results for the decrease in S_{BET} after deposition of metal particles over titania nanostructures were in agreement with the already reported results [34].

8.3.5 XPS characterization

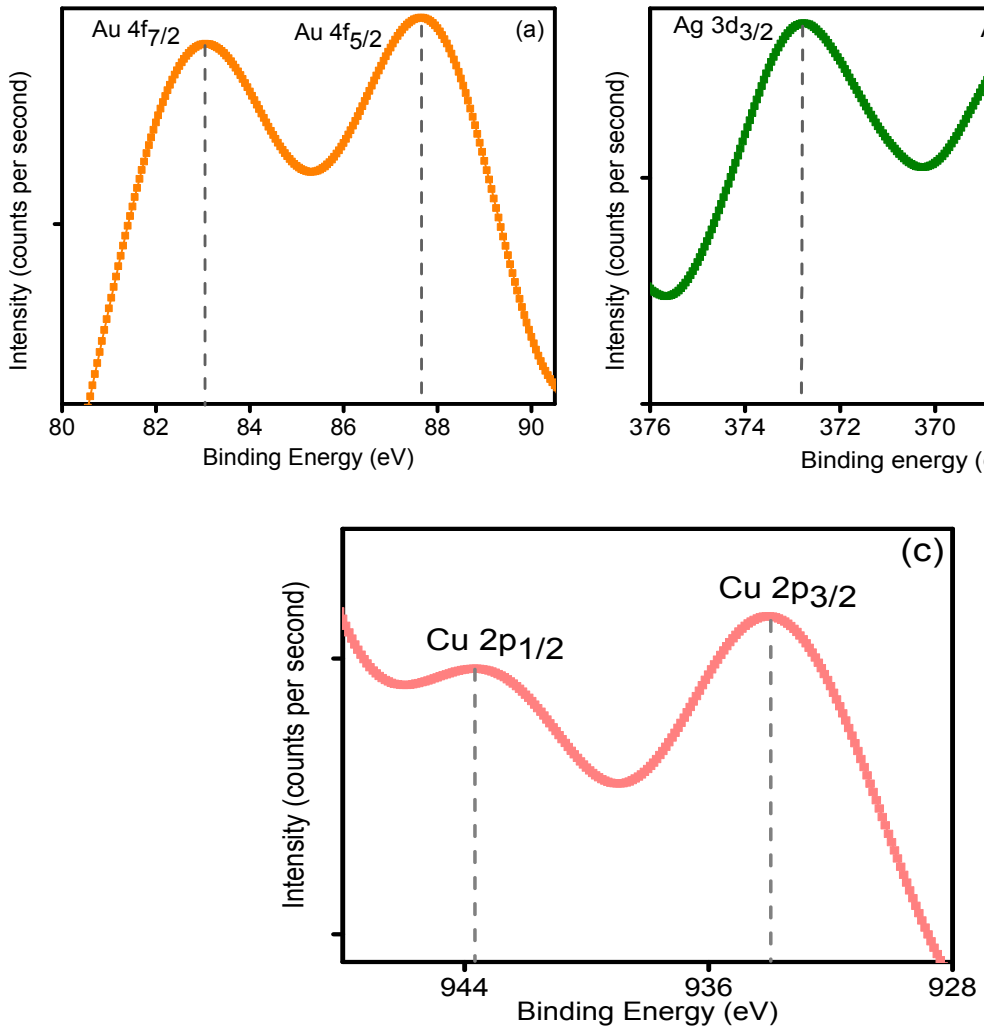

Figure 5. XPS spectra of (a) Au4f region for Au-TiO_2, (b) Ag3d region for Ag-TiO_2 and (c) Cu2p region for Cu-TiO_2 nanocomposite.

XPS, a valuable surface analyzing technique is helpful for characterizing atomic composition and chemical states of elements incorporated in the surface layer of materials [23,36]. The presence of metal NPs was further confirmed by XPS analysis and the respective surface chemical composition (atomic %) of representative M-TiO_2 photocatalysts determined by XPS analysis is being given in table 1. It has been observed that Ag-TiO_2 and Au-TiO_2 samples maintained O/Ti atom ratio very close to 3.5, indicating no variation in the metal oxide composition. However, for Cu-TiO_2, the O/Ti atom ratio is found close to ≈ 6 depicting the presence of some impurities in composite. The elemental composition also represented C1s which may due to the adventitious hydrocarbon from the XPS instrument itself [37]. Figure 5a shows binding energy of $Au4f_{7/2}$ at 83.4 and $Au4f_{5/2}$ at 87.7 eV, which are significantly different from $Au^{+}4f_{7/2}$ (84.6 eV) and $Au^{3+}4f_{7/2}$ (87.0 eV), respectively. The result suggests that the Au species in Au-TiO_2 are in the metallic state as well stated in the reported results [23,38,39]. The peaks observed at 373.6 eV and 368 can be ascribed to $Ag3d_{3/2}$ and $Ag3d_{5/2}$ of the metallic silver (figure 5b), respectively [23,40]. The XPS spectrum for Cu2p (figure 5c) gives the binding energy of Cu2p at 933eV and 943.4 eV corresponding to $Cu2p_{3/2}$ and $Cu2p_{1/2}$ characteristics of Cu^{2+} state [41].

8.3.6 TEM size and shape analysis

Figure 6-9 showed the TEM images of aqueous suspension of metal NS and M-TiO_2 nanocomposites. TEM micrographs of AuNS (figure 6) revealed that all the particles are spherical in shape, well dispersed having average size ≈ 3-5 nm. The inset figure 6 showed the magnified image of AuNS which insure their rounded/spherical shape. The homogenously dispersed NS of Ag were seen in figure 7a, all the NS were well separated from each other and displaying size range ≈ 3-5 nm. CuNS of similar size ≈ 3-5 nm with spherical morphology has been clearly visible in figure 7b. DLS measurements also verified that uniform size distribution of all the metal NS (figure 2).

The persistence of metal NS in M-TiO_2 composites and the way of their attachment to TiO_2 was examined through TEM analysis that yield valuable and direct information on the dimension and the distribution of NPs on the TiO_2 surface. Many black colored, spherical shaped AuNS in the size range 3-8 nm are seen to be uniformly distributed over TiO_2 (gray color) as shown in figure 8. Similarly, AgNS and CuNS are seen scattered over the TiO_2 surface as can be

seen in figure 9. The size of the NS (Au and Ag) is found to be in good agreement with the average diameter of original colloidal solution (figure. 6 and 7a) before impregnating to TiO_2, verifying their non-aggregation behavior. One can observe from the image (figure 8 and 9) that metal nanospheres are lying in a close proximity to TiO_2 and forming M-TiO_2 interfaces. Although there is no any chemical bond between metal NS and TiO_2, yet the electrostatic attractions between the two because of opposite charges (discussed in chapter 2 and 3) bring them closer. The close contact formed at the interface of NPs and TiO_2 would facilitate the electron transfer in this composite photocatalyst and assist in the photoreaction systems. In Cu-TiO_2 composite, NS are not seen so well separated and would appear as small aggregates over TiO_2 surface, clearly seen from the image 9c and d. The elemental analysis carried out using EDX (figure 8 and 9) confirms the presence of 1.13, 0.85 and 0.81 atomic % of Au, Ag and Cu in 1 wt % impregnated M-TiO_2 samples.

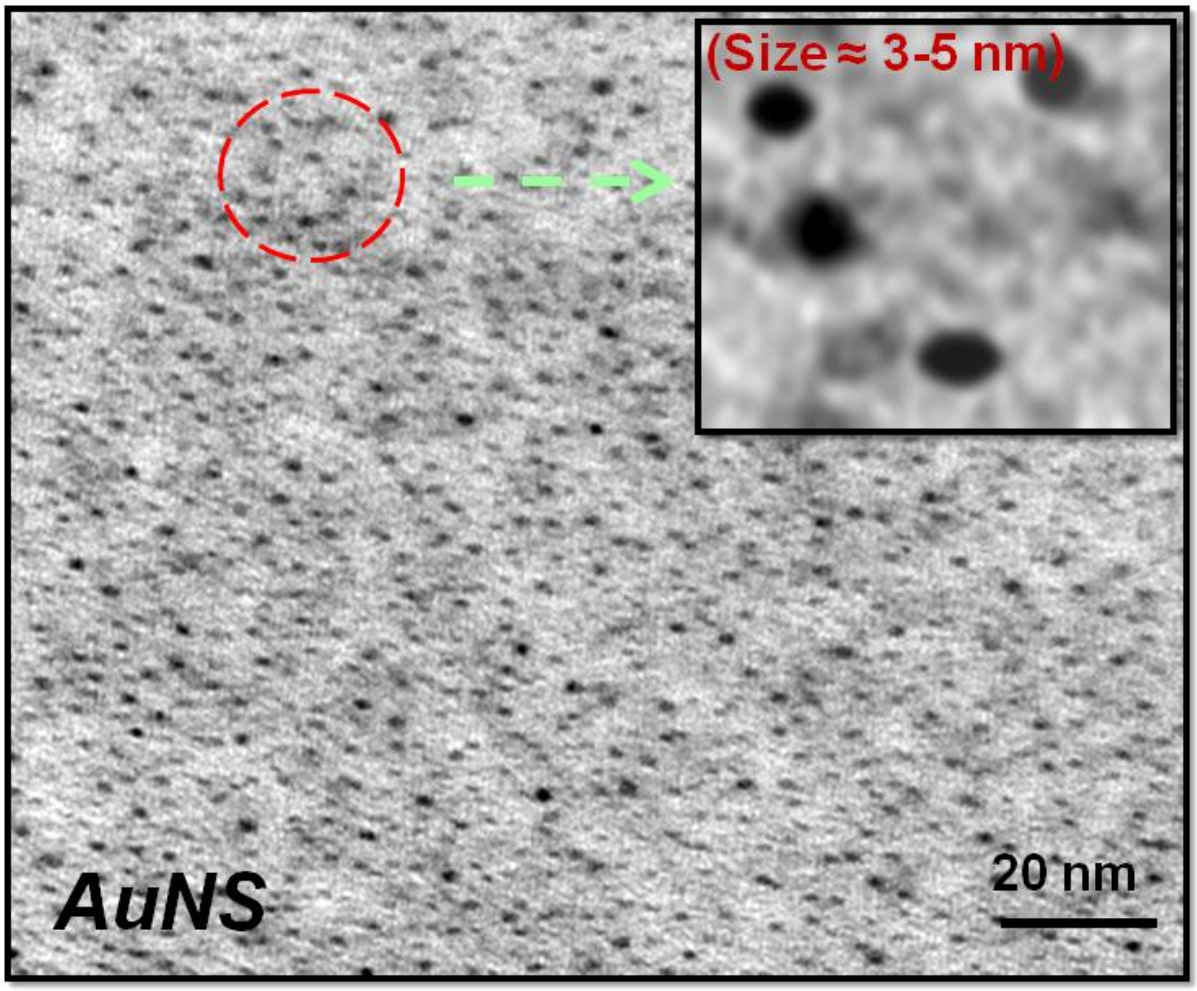

Figure 6. TEM images of AuNS having size = 3-5 nm.

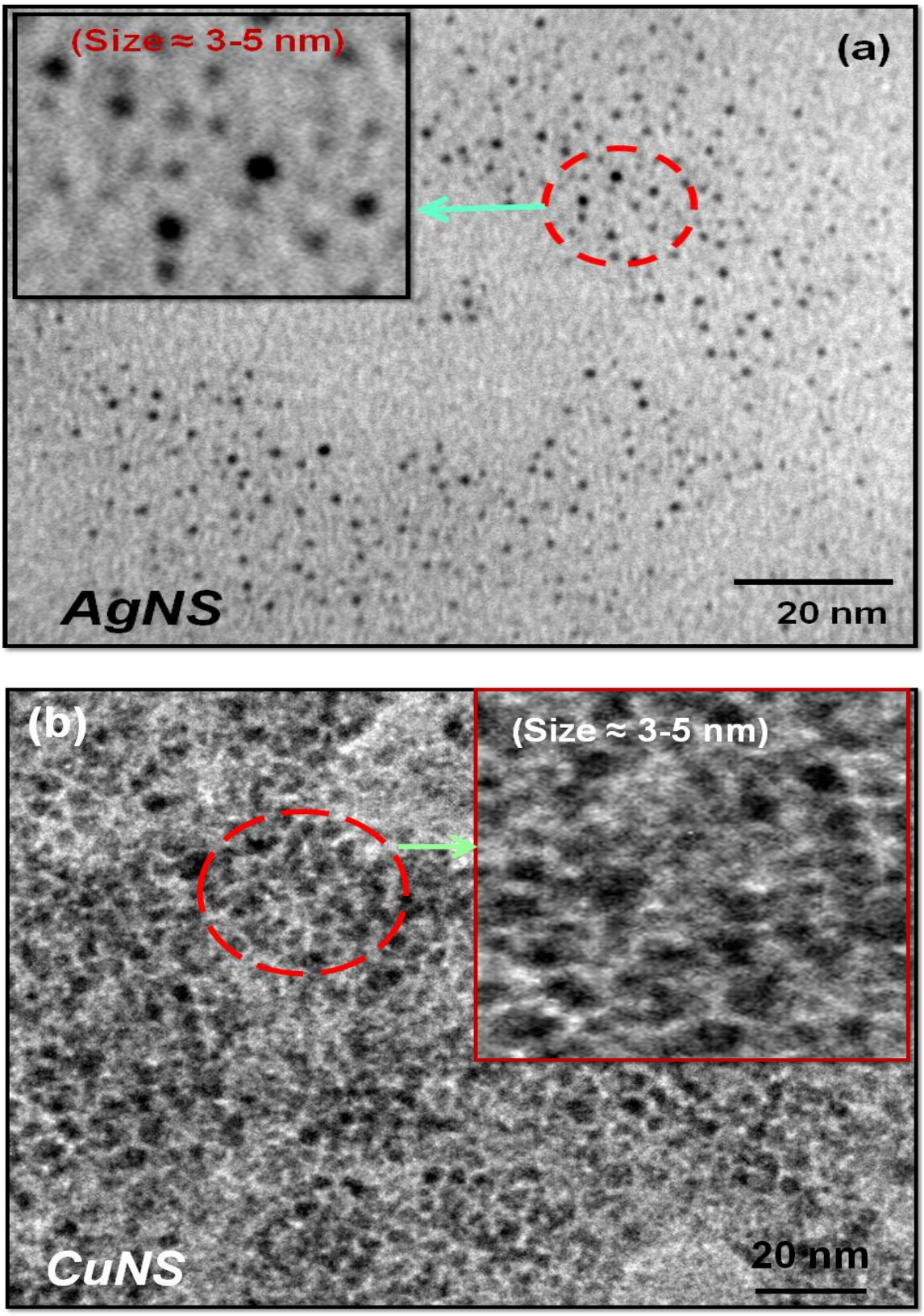

Figure 7. TEM image of (a) Ag and (b) CuNS having comparable sizes ≈ 3-5 nm.

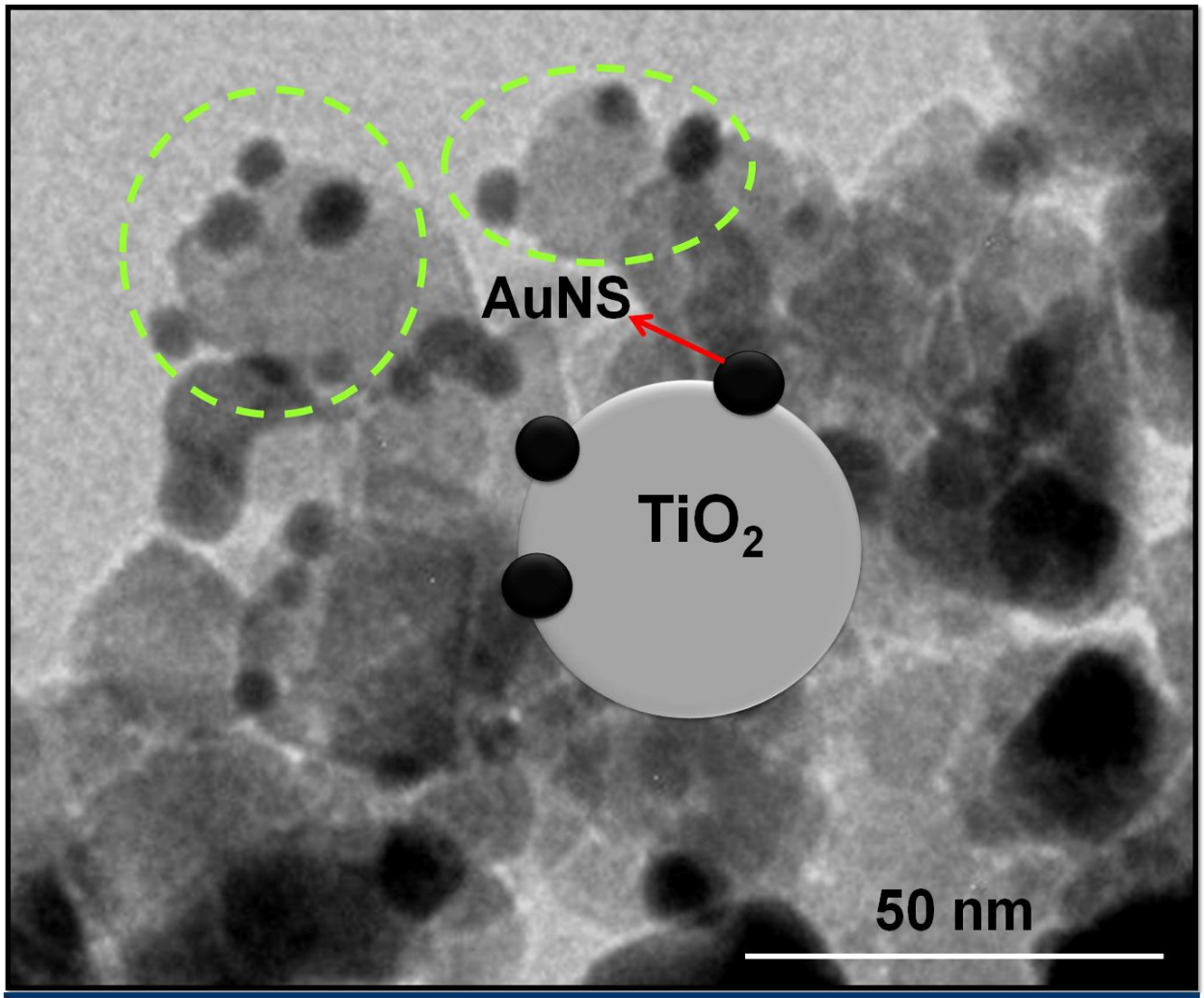

Element	Weight%	Atomic%
O K	45.55	70.87
Ti K	53.03	28.00
Au M	1.41	1.13
Totals	100.00	

Figure 8. TEM image of Au-TiO_2 composite, graphic representing the presence of AuNS (dark colored) over TiO_2 (gray colored) and its corresponding EDX profile.

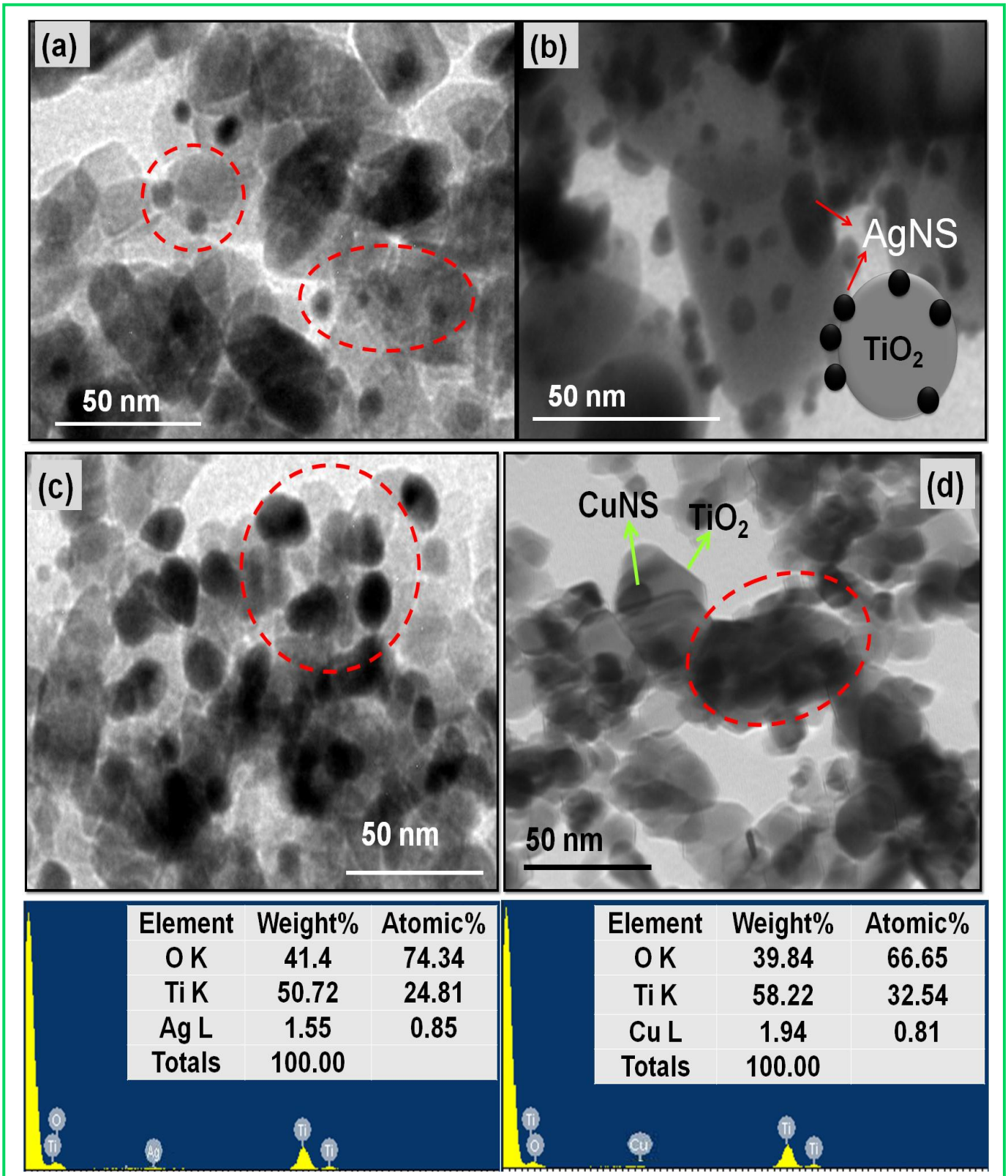

Figure 9. TEM images of (a, b) Ag-TiO_2, and (c, d) Cu-TiO_2 composites with loading amount of 1 wt % respective metal nanoparticles, given below their corresponding EDX profiles.

8.3.7 Current–voltage characteristics

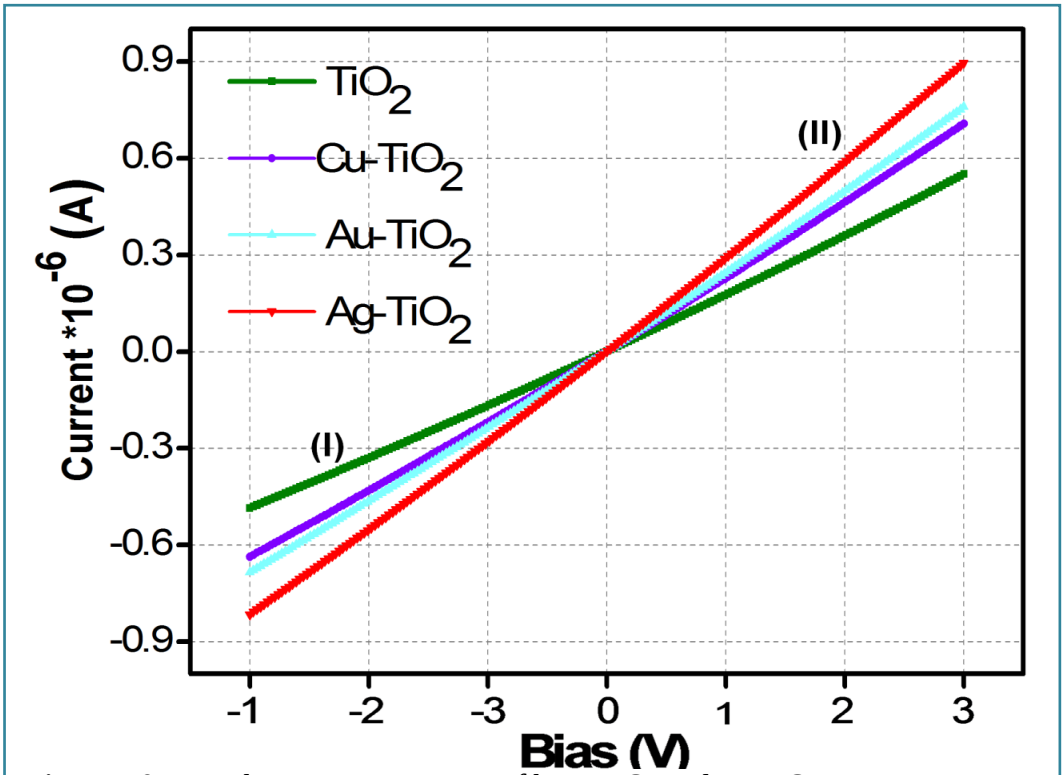

Figure 10. I–V characteristic curves of bare TiO_2 and M-TiO_2 nanojunctions.

Electrical conductivity is the ability of a material to conduct an electric current which helps to determine the extent of flow of electronically charged species along M-SC interface [42]. When electrical potential difference was placed across a conductor, movable charges start to flow and hence giving rise to an electric current. The current–voltage (I–V) characteristics of the bare TiO_2 and M-TiO_2 heterojunctions are shown in figure 10 which found to follow the Ohm's law (V=IR). The observed data shows that with increasing voltage, flow of the current through the heterojunctions is also increasing and, therefore, corresponding I–V curve approaches a straight line with a slope equal to the resistance of the M-TiO_2 interface. This resistance was determined using the differential voltage method at large bias I–V curve as R = dV/dI, where R is resistance, dV/dI differential voltage, this procedure gives resistances as 6.06, 3.70, 4.44 and 4.76 MΩ (at voltage = -2.0 V) and corresponding conductance values 1.65×10^{-7}, 2.7×10^{-7}, 2.25×10^{-7} and 2.1×10^{-7} S for bare, Ag-TiO_2, Au-TiO_2 and Cu-TiO_2 composites, respectively. This I–V curve can be divided into two or more segments, i.e., I and II, and respective to these segments, the voltage (V), current (I), resistance (R) and conductance (S) has been calculated (figure 10, table 2). The increase in conductance in M-TiO_2 composites in comparison to bare TiO_2 well

Table 2. Measurement of voltage (V), current (I), resistance (R), and conductance (S), corresponding to segments I and II of I–V characteristics.

Catalyst	Region	Voltage (V)	Current (nA)	Resistance (MΩ)	Conductance (S) $\times 10^{-7}$
TiO_2	I	-2.0	330	6.060	1.65
	II	2.0	500	5.555	1.8
Ag-TiO_2	I	-2.0	540	3.703	2.7
	II	2.0	600	3.333	3.0
Au-TiO_2	I	-2.0	450	4.444	2.25
	II	2.0	500	4.000	2.5
Cu-TiO_2	I	-2.0	420	4.761	2.1
	II	2.0	360	4.000	2.5

rationalizes the role of nature of metal for conduction developed by formation of Schottky barriers between different M-TiO_2 nanocomposites.

8.3.8 Time resolved spectroscopy

The dynamics of charge recombination time and interparticle electron transfer between metal and semiconductor is a very important criterion to be considered which can be easily understood through time-resolved spectroscopy. Though reports are available regarding the electron charge carrier time of nanocomposites as a function of shape and size of the semiconductors [43], still the influence of nature of metal onto the band edge and trapping states still remains a challenge. The charge carrier's relaxation dynamics of M-TiO_2 relative to P25-TiO_2 are shown in figure 11, which is measured by pulse excitation method. Samples were exposed to nitrogen laser (wavelength = 390 nm) and time resolved decay curves are obtained from where lifetime values of the various excited states have been calculated. The average lifetime τ_{av}, is related to band edge lifetime τ_1 and trapping or defect states given by the following equation:

$$\tau_{av} = (a_1\tau_1 + a_2\tau_2)/a_1 + a_2$$

where a_1 and a_2 represent the amplitude of band edge and trapping state emission, respectively.

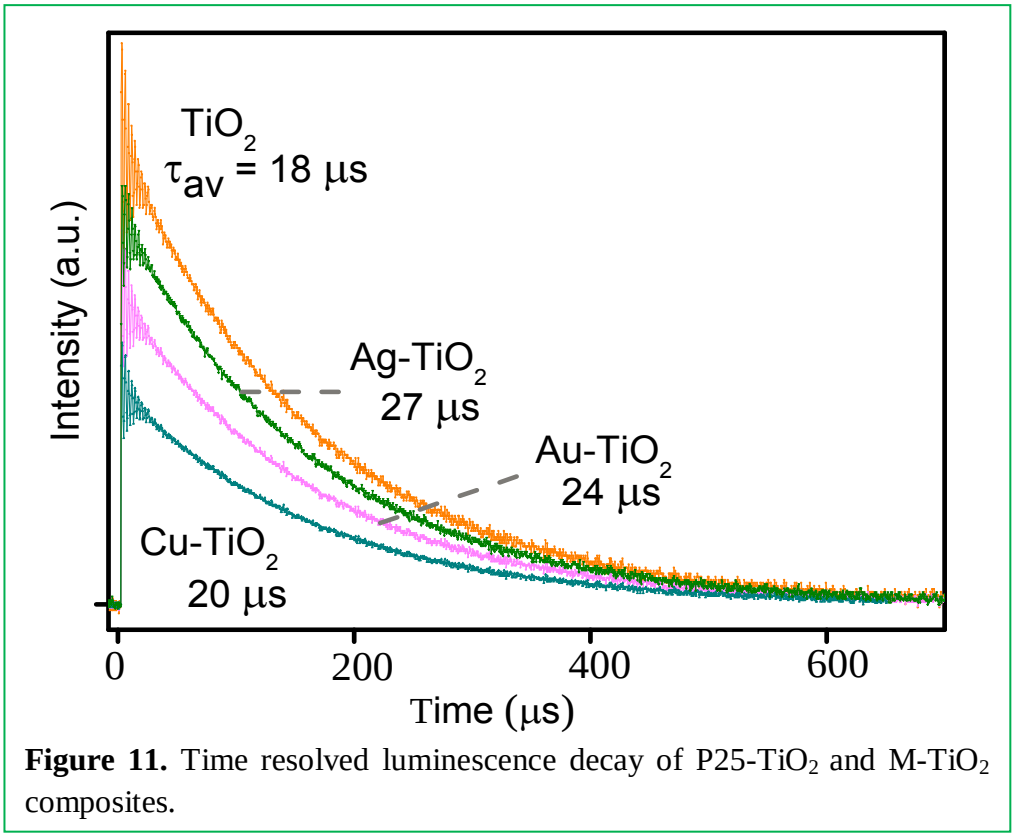

Figure 11. Time resolved luminescence decay of P25-TiO_2 and M-TiO_2 composites.

The estimated average lifetimes are ≈ 18, 20, 24 and 27 μs for bare P25-TiO_2, Cu-TiO_2, Au-TiO_2 and Ag-TiO_2, respectively. An increase in relaxation time of photoexcited electron–hole pairs is observed with the change in the nature of the metal NPs. It has been reported that Ag metal has a maximum capacity to capture and store electrons and acts as a better electron sink [8].

8.3.9 Photocatalytic activity

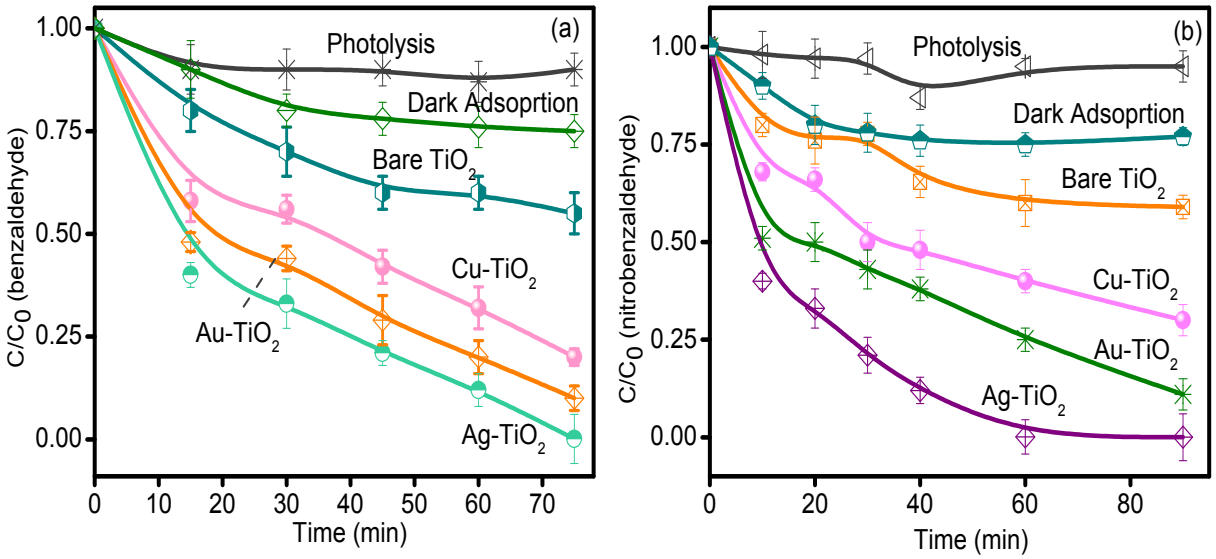

Figure 12. Time course of photodegradation of (a) benzaldehyde and (b) nitrobenzaldehyde using various M–TiO_2 composites under direct sunlight irradiation.

The plots for the extent of degradation (C/C_0) versus irradiation time using various M-TiO_2 composites have been displayed in figure 12 in which C is the absorbance of substrate solution at each time interval of irradiation and C_0 is the absorbance of the initial concentration. Irrespective of size and shape, the comparative photocatalytic activity of M-TiO_2 composites in aqueous suspensions under sun light irradiation has been investigated by employing BZ and NBZ substrates, as a function of nature of metal. The stability of both substrates was primarily tested under sunlight irradiation without the addition of any catalyst which confirms the non-degradable nature of substrate. Moreover, substrates showed a negligible loss in the concentration during dark reaction catalyzed by TiO_2 and M-TiO_2 composites.

The photooxidation was found to follow pseudo first-order kinetics using a simplified Langmuir–Hinshelwood model, $r = -dC/dt = k(KC)/(1 + KC)$ where r is the initial rate of photocatalytic degradation (mol $l^{-1}min^{-1}$), C is the concentration of the reactant (mol l^{-1}), t is the irradiation time (min), k is the rate constant and K is the Langmuir–Hinshelwood adsorption constant. At low concentration, KC can be neglected with respect to 1 and one gets the simplified equation: $r = -dC/dt = kKC$ or $C/C_o = e^{-kKt} = e^{-kt}$ where k is the apparent rate constant of the pseudo-first order (min^{-1}) reaction. The observed rate constant (k) calculated from figure 12a was found to be highest for Ag-TiO_2 (4×10^{-2} min^{-1}) as compared to 2.7×10^{-2} min^{-1} for Au-TiO_2 and 1.93×10^{-2} min^{-1} for Cu-TiO_2 during BZ photooxidation. In a similar manner, the photodegradation percentage for the NBZ was highest for Ag-TiO_2 (≈ 99%) relative to lowest ≈ 40% for P25-TiO_2. Results indicate that M-TiO_2 composites always exhibit higher photocatalytic efficiency than commercial P25-TiO_2 of the same total mass (≈ 20 mg), specifying enhanced photocatalytic activity due to the presence of plasmonic metals (figure 12). The enhancement in the M-TiO_2 composites relative to TiO_2 in visible light can be explained as per reported mechanisms [1-10,21] and displayed in scheme 1. The noble metal NPs act as sensitizers, absorb visible light due to their plasmon resonance, results in the formation of the electrons and holes on the surface of the metal NPs which assist in the oxidation of reactant substrates. The electrons are transferred to the adsorbed oxygen molecules via the conduction band of TiO_2 resulting in the formation of superoxide radicals. These radicals upon assistance with CB electrons combine to produce H_2O_2 that ultimately producing hydroxyl radicals. Both hydroxyl and superoxide radicals are strong oxidants, and therefore oxidize BZ and NBZ, resulting in the formation of intermediate organic

species (figure 13) and subsequently mineralize to water and CO_2. Therefore, lowest photocatalytic efficiency of bare TiO_2 (anatase:rutile ≈ 70:30) relative to M-TiO_2 nanocomposites can be accounted to its insufficiency of absorbing visible light. The resultant plots (figure 12) obtained from UV-vis studies represent almost complete photodegradation of substrate and to insure the same, GC-MS analysis of BZ was carried out (figure 13). GC-MS reveals the incomplete mineralization of BZ as various intermediates such as benzoic acid (m/z = 122, R_t = 12.5), 2-hydroxybenzaldehyde (m/z = 122.12, R_t = 14.1) and salicylic acid (m/z = 138, R_t = 18.3) are found to form (figure 13).

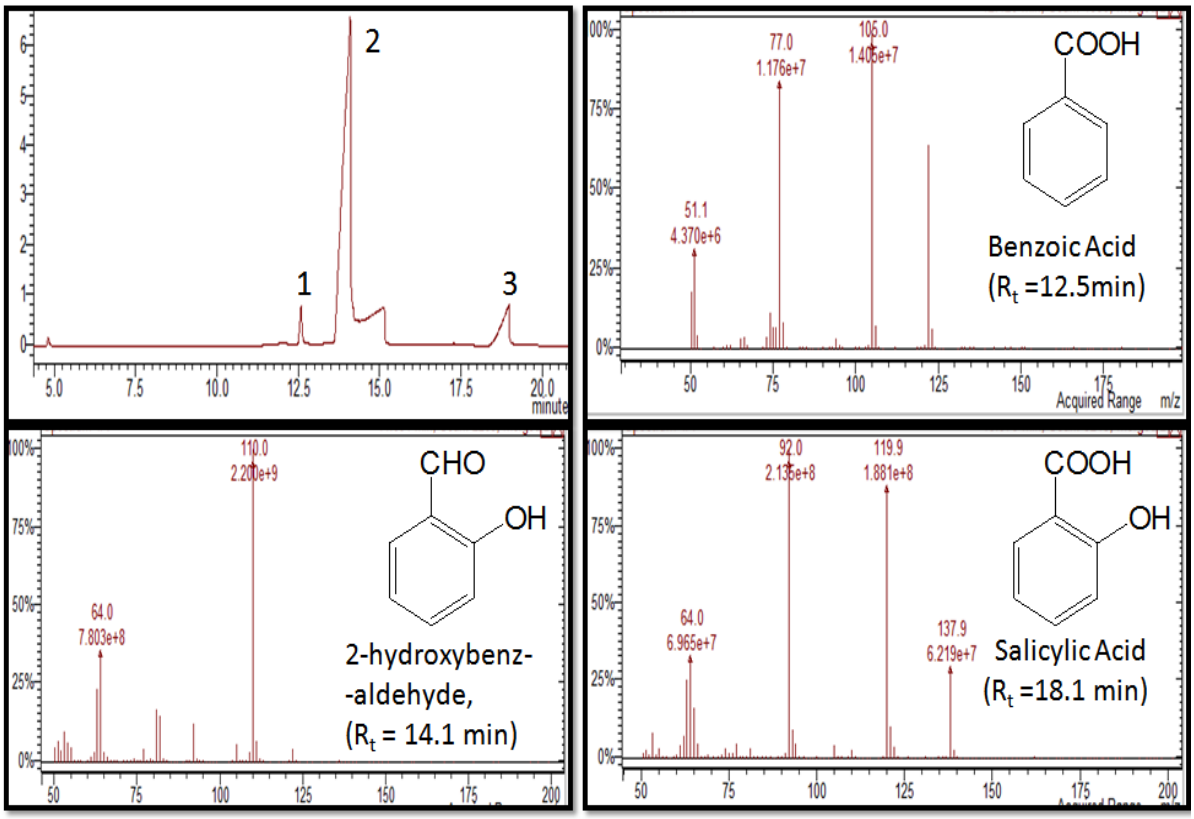

Figure 13. GC chromatograph for oxidation of benzaldehyde using Au-TiO_2 composite after 75 min of irradiation and mass spectra of identified compound; inset structural formula and retention times of identified compounds.

Therefore, exact % age of mineralization of BZ and NBZ was perceived through quantitative determination of the CO_2 evolution (figure 14), which is found to corroborate with their respective photodegradation. It has been suggested that if the molecule of BZ (C_6H_5CHO) and

NBZ ($C_7H_5NO_3$) was completely mineralized, it will give CO_2 and water as per following equation:

$$C_6H_5CHO + 8O_2 \rightarrow 7CO_2 + 3H_2O;$$

$$2C_7H_5NO_3 + 7/2O_2 \rightarrow 14CO_2 + 5H_2O + N_2$$

Although other species like nitrogen (for NBZ) was not measured but the measured CO_2 formation confirmed the photodegradation of BZ and NBZ by various M-TiO_2 nanocomposites under visible light irradiation. Figure 14a shows the relative percentage of CO_2 formation depending on the extent of photocatalytic activity of various catalysts. It was found that Ag-TiO_2 catalyst produced the highest amount of $CO_2 \approx 38\%$ in 3 h in contrast to 29.8% and 21.5% by Au-TiO_2 and Cu-TiO_2, respectively. Similar trend has been seen for NBZ photodecomposition as displayed in figure 14a, represented in table 3. The GC data supports the GC-MS analysis that also exhibits the photoconversion of BZ to other compounds (figure 13) and rendering its complete mineralization.

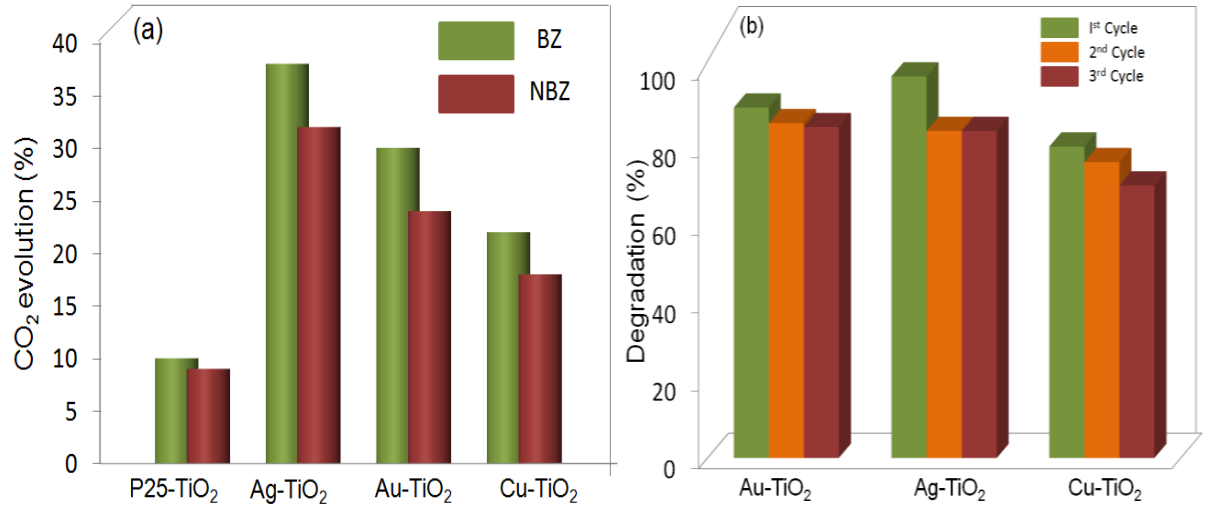

Figure 14. Percentage of CO_2 evolution on photodegradation of benzaldehyde (BZ) and nitrobenzaldehyde (NBZ) by using various M-TiO_2 nanocomposites after 3 h of sunlight irradiation and (b) nitrobenzaldehyde degradation (%) after recycling with M-TiO_2 composites under visible light irradiation.

As a comparison of all M-TiO_2 composites, Ag-TiO_2 composite showed profound photodegradation efficiency (38%) relative to Au-TiO_2 (30%) and Cu-TiO_2 (22%). Such distinguished behavior of as mentioned catalysts in the photocatalytic activity as a function of nature of metal can be explained in terms of work function, charge carrier relaxation time,

reduction potential, conductance and oxidation state of the metal NPs, expressed in table 3. The highest conductance of Ag-TiO_2 (2.7×10^{-7} μS, table 3), least work function of Ag metal (table 3) and relative near Fermi level position to CB of TiO_2 favors quick transference of electrons from silver to TiO_2 than other composites. Most importantly, its highest recombination time of photoproduced charge carriers (table 3) brings more formation of highly oxidative superoxide and hydroxyl radicals and hence, highest photooxidation ability. Undoubtedly, the observed (Ag> Au> Cu) photocatalytic behavior of metal-NPs is opposite to that expected from their reduction potentials. This surprising trend can be explained from XPS data (table 3) that reveals +2 oxidation state for Cu in Cu-TiO_2 composite, while zero for Ag and gold, due to which Cu first acquires photoproduced electrons from TiO_2 making availability of holes for production of only OH radicals. Whereas, for Ag and Au-TiO_2 (zero oxidation state) composites, there is formation of two highly oxidative species viz., hydroxyl and superoxide radicals that brings higher photoactivity for these composites.

Table 3. Chemical, elemental, electronic and catalytic parameters of M-TiO_2 composites.

Catalyst	Conductance $\times 10^{-7}$ (S)	e^- - h^+ recombination time (μs)	Oxidation state (from XPS analysis)	Respective metal (Au, Ag and Cu)		CO_2 evolution (%)	
				Work function (V)	Reduction Potential (V)	BZ	NBZ
TiO_2	1.65	18	--	-	-	10	9
Au-TiO_2	2.5	24	Au^0	5.32	1.5	30	22
Ag-TiO_2	2.7	27	Ag^0	4.30	0.80	38	30
Cu-TiO_2	2.1	20	Cu^{+2}	4.70	0.34	22	18

The reusability and stability of the prepared M-TiO_2 composites were examined by photodegradation of NBZ for the three cycles to ensure any loss in the activity (figure 14b). The photocatalytic activity of Au-TiO_2, Ag-TiO_2 and Cu-TiO_2, of the last cycle maintained 88%, 85%, and 72% of the original photocatalytic activity, respectively. It confirms that the metal NPs are homogeneously embedded in the TiO_2 matrix and would not lost even after reusing three times.

Hence, it has been revealed that irrespective of shape and size, nature of the metal also displays a great impact for the advancement in the heterogeneous photocatalytic systems. The Ag-TiO_2 junction has shown the best photoactivity relative to Au and Cu-TiO_2 hetero-junction as a function of electron-charge recombination time, diffusive electron movements, work function and reduction potential values. Therefore, the knowledge of such photocatalytic systems could be beneficial in designing highly active photocatalysts.

8.4 References

[1] S.T. Kochuveedu, Y.H. Jang and D.H. Kim, Chem. Soc. Rev., 42 (2013) 8467.

[2] P. Wang, B. Huang, Y. Daia and M.H. Whangbo, Phys. Chem. Chem. Phys., 14 (2012) 9813.

[3] M.M. Khan, S.A. Ansari, J. Lee and M.H. Cho, J. Ind. Eng. Chem., 19 (2013) 1845.

[4] S. Sarina, E.R. Waclawik and H. Zhu, Green Chem., 15 (2013) 1814.

[5] S.F. Chen, J.P. Li, K. Qian, W.P. Xu, Y. Lu, W.X. Huang and S.H. Yu, Nano Res., 3 (2010) 244.

[6] S. Linic, P. Christopher and D.B. Ingram, Nat. Mater., 10 (2011) 911.

[7] J.C. Scaiano and K. Stamplecoskie, J. Phys. Chem. Lett., 4 (2013) 1177.

[8] W.T. Chen, Y.J. Hsu, and P.V. Kamat, J. Phys. Chem. Lett., 3 (2012) 2493.

[9] Z. Zheng, B. Huang, X. Qin, X. Zhang, Y. Dai and M.H. Whangbo, J. Mater. Chem., 21 (2011) 9079.

[10] X. Zhou, G. Liu, J. Yu and W. Fan, J. Mater. Chem., 22 (2012) 21337.

[11] A. Pearson, S. Bhosale, S.K. Bhargava and V. Bansal, Appl. Mater. Interfaces, 5 (2013) 7007.

[12] Y. Ishii, Y. Kanamori, T. Kawashita, I. Mukhopadhyay and S. Kawasaki, J. Phys. Chem. Solids, 71 (2010) 511.

[13] H.Y. Zhu, X.B. Ke, X.Z. Yang, S. Sarina and H.W. Liu, Angew. Chem., Int. Ed., 49 (2010) 9657.

[14] H.Y. Zhu, X. Chen, Z.F. Zheng, X.B. Ke, E. Jaatinen, J.C. Zhao, C. Guo, T.F. Xie and D.J. Wang, Chem. Commun., (2009) 7524.

[15] X. Chen, Z.F. Zheng, X.B. Ke, E. Jaatinen, T.F. Xie, D.J. Wang, C. Guo, J.C. Zhao and H.Y. Zhu, Green Chem., 12 (2010) 414.

[16] H. Li, Z. Bian, J. Zhu, Y. Huo, H. Li, and Y. Lu, J. Am. Chem. Soc., 129 (2007) 4538.

[17] X.H. Yang, H.T. Fu, K. Wong, X.C. Jiang and A.B. Yu, Nanotechnology, 24 (2013) 41560-1.

[18] K.Y. Song, Y.T Kwon, G.J. Choi and W.I. Lee, Bull. Korean Chem. Soc., 20 (1999) 957.

[19] L. Liu, S. Ouyang and J. Ye, Angew. Chem., 125 (2013) 6821.

[20] N. Zhou, L. Polavarapu, N. Gao, Y. Pan, P. Yuan, Q. Wang and Q.H. Xu, Nanoscale, 5 (2013) 4236.

[21] R. Sellappan, M.G. Nielsen, F.G. Posada, P.C.K. Vesborg, I. Chorkendorff and D. Chakarov, J. Catal., 307 (2013) 214.

[22] Y. Tian and T. Tatsuma, J. Am. Chem. Soc., 127 (2005) 7632.

[23] A.Z. Jurek, E. Kowalska, J.W. Sobczak, W. Lisowski, B. Ohtani and A. Zaleskaa, Appl. Catal. B: Environ., 101 (2011) 504.

[24] Y. Tian and T. Tatsuma, Chem. Commun., (2004) 1810.

[25] A. Furube, L. Du, K. Hara, R. Katoh and M. Tachiya, J. Am. Chem. Soc., 129 (2007) 14852.

[26] G.L. Zhao, H. Kozuka and T. Yoko, Thin Solid Films, 277 (1996) 147.

[27] C. Li, D. Li, G. Wan, J. Xu and W. Hou, Nanoscale Res. Lett., 6 (2011) 440.

[28] Ratyakshi and R.P. Chauhan, Asian J. Chem., 21(2009) 113.

[29] J. Kimling, M. Maier, B. Okenve, V. Kotaidis, H. Ballot and A. Plech, J. Phys. Chem. B, 110 (2006) 15700.

[30] M. Samim, N.K. Kaushik and A. Maitra, Bull. Mater. Sci., 30 (2007) 535.

[31] N. Gupta and B. Pal, J. Mol. Catal. A: Chem., 371 (2013) 48.

[32] I. Tunc, M. Bruns, H. Gliemann, M. Grunze and P. Koelsch, Surf. Interface Anal., 42 (2010) 835.

[33] M. Sahu and P. Biswas, Nanoscale Res Lett., 6 (2011) 441.

[34] B. Choudhury, M. Dey and A. Choudhury, Int. Nano Lett., 3 (2013) 25.

[35] I.S. Grover, S. Singh and B. Pal, Appl. Surf. Sci., 280 (2013) 366.

[36] N. Kruse and S. Chenakin, Appl. Catal. A: Gen., 391 (2011) 367.

[37] B. Cheng, Y. Le and J. Yu, J. Hazard. Mater., 177 (2010) 971.

[38] M. Ganguly, A. Pal and T. Pal, J. Phys. Chem. C, 115 (2011) 22138.

[39] T. Bala, A. Singh, A. Sanyal, C.O. Sullivan, F. Laffir, C. Coughlan, and K.M. Ryan, Nano Res., 6 (2013) 121.

[40] S.S. Mandal and A.J. Bhattacharyya, J. Chem. Sci., 124 (2012) 969.

[41] C.Y. Tsai, H.C. Hsi, T.H. Kuo, Y.M. Chang, J.H. Liou, Aerosol Air Qual. Res., 13 (2013) 639.

[42] G.S. Lotey and N.K. Verma, J. Nanopart. Res., 13 (2011) 5397.

[43] I.S. Grover, S. Singh and B. Pal, J. Nanosci. Nanotecnol., doi:10.1166/jnn.2014.9072.

Summary and Conclusions

Chapter 1 provides an introductory note on the importance of coinage metal nanoparticles (NPs) as co-catalysts in TiO_2 photocatalyzed reactions. A general scheme of photocatalytic reaction and the ways towards the improvement in the yield of the photocatalytic systems by the loading of metal NPs has been discussed. It gives an idea that how the energetics of the photocatalytic system can be improved through changing shape and size of the metal NPs, which cannot be achieved through the earlier conventional approaches. A concise overview of the various studies carried out earlier in the field of presenting work and the research gaps which have been found during literature surveys are also presented. A short description of characterization techniques for the determination of optoelectronic, structural, photophysical and catalytic properties are also represented.

Chapter 2 summarizes the morphological effect of AuNPs co-catalysts for the relative enhancement in TiO_2 photocatalysis. The TiO_2 photoactivity has been found to be drastically enhanced with the decreasing size of AuNPs loading. It is interesting to know that the effective amount of Au atom required for maximum photocatalytic activity (PCA) of TiO_2 is 100 times less than the traditional prerequisite of 1-2 wt% metal deposition. The Au nanorod, aggregated nanospheres, and photodeposited particles addition considerably decreased the PCA of TiO_2 due to the difference in their co-catalytic efficiency that depend on the percentage of surface active atoms and Fermi energy shifts because of the notable change in their size, shape and S/V ratio. The Au nanorods may lower the substrate adsorption and hinder the direct light absorption on the oxide surface and thus reduced the photogeneration of charged species and the photoactivity. Moreover, the surface area/charge and zeta-potential measurements of each Au-TiO_2 junction of different conformations and the effects of aspect ratio of AuNR loading onto TiO_2 photoactivity are needed to investigate for better understanding the relative co-catalytic activity of various Au nanostructures.

Chapter 3 and 4 emphasizes the comparative study for the effect of surface charge and zeta potential of Au nanostructures (nanospheres and nanorods) in various polar and non-polar solvents as a function of their dipole moment on the stability, surface plasmon absorption, catalytic and co-catalysis ability of AuNPs. The dipolar interactions due to solvent polarity

induce the formation of AuNPs agglomerated morphologies which is significantly different from typical surface passivation by thiol (–SH) and amino acids (-NH_2, -SH and –COOH) functional moieties that generally results in the end-to-end or parallel self-assemblies. The interactions between solvent and NP distinctly modifies the adsorption behavior of polar molecules like p-nitrophenol and salicylic acid on AuNPs surface and thus resulted in varied catalytic and co-catalytic efficiency, respectively. The observed co-catalytic activity and catalytic activity of aggregated Au nanostructures (formed in polar solvents) varied in a diverse extent depending on its degree of agglomeration. As most of the Au catalyzed synthetic reactions are being carried out in common organic polar solvents, this obtained surface structural and electro-kinetics properties exhibited by aggregated AuNPs can influence the adsorption interaction and catalytic properties as a function of the ionic nature of the reacting substrates. Therefore, it is necessary to choose correct solvent for controlling the kinetics for Au catalyzed reactions as true catalytic ability is basically masked because of the aggregated morphology. Hence, this work may contribute towards better understanding of solution behavior of Au nanostructures in different solvents in comparison with conventional aqueous suspension and their colloidal stability can be tuned for the optimum catalytic activity of such metal nanoparticles in heterogeneous catalysis.

Chapter 5 explores the cost effective single step technique for the preparation of multiple shaped Au nanostructures by exposing Au nanorods with different energy laser irradiations (2.71, 2.54 and 2.41 eV). This laser-induced melting provides an intriguing way in tuning the surface morphology of irregular shaped multifaceted Au nanostructures in single quick pathway by different energy of laser irradiation without employing any typical synthetic routes. These photoetched Au nanostructures possess thermodynamically high-energy active surface atoms, enlarged per-particle surface area and more exposed fresh crystal planes that significantly affect the effective surface charge and zeta potential, and thus greatly altered the adsorption behavior of reacting substrate and thereby highly improve the catalytic activity and selectivity for the reduction of p-nitrophenol and m-dinitrobenzene relative to bare Au nanosphere and nanorod prior to laser treatment. Such easily prepared anisotropic Au nanostructures have the potential to become efficient and promising catalyst to be used in a wide range of industrially important chemical or biological systems.

Chapter 6 correlates the comparative co-catalytic effect of morphologically different large and small-sized AgNPs for superior electron storage in Ag-TiO_2 photocatalytic system and has been found to vary as: polygonal nanosphere > nanorod > truncated triangle > nanospheres. The variation in the co-catalytic activity is due to the difference in the number of active facets on the dissimilar shapes having different interfacial or contact area. Strong interaction among the catalyst surface, co-catalyst surface and the substrate is essential for better photocatalytic process. Furthermore, the PCA of the nanostructured Ag-TiO_2 hetero-interface could possibly be further enhanced by self-assembling AgNPs to TiO_2 for better electrical contact rather than simple addition. Exploring the catalytic activity of AgNPs-TiO_2 nanocomposite having an optimum amount of Ag co-catalyst could pave the way for designing novel catalysis systems.

Chapter 7 illustrates the improvement in the photocatalytic rate by utilizing different morphologies of Cu-TiO_2 nanocomposites in comparison with bare TiO_2. Catalytic efficiency of CuNPs for reduction of nitroaromatics and co-catalysis effect imparted to TiO_2 follows the trend as nanowires > nanorod > nanospheres. The excellent catalytic as well as co-catalytic activity exhibited by nanowires is due to its rough surface and much exposed surface area relative to nanorods and nanospheres, allows more adsorption interactions with the reactant substrate. The change in morphology from spherical to lengthy nanorod and nanowires results in the retardation of electron-hole recombination time and subsequently affects the photoactivity. Further this extremely economic and efficient photocatalytic system (Cu-TiO_2) could found its way for scaling up many industrially important reactions.

Chapter 8 provides a detailed study on the impact of nature of metal for the upgrading TiO_2 photocatalysis reaction rate under visible light irradiation. Irrespective of shape and size, similar sized nanospheres of coinage metals were impregnated on TiO_2 to compare the photocatalytic efficiency as a function of nature of metal. Results revealed that the stable Ag-TiO_2 heterojunction exhibits enhanced photoactivity relative to Au and Cu-TiO_2 governed by current-voltage characteristics, XPS data, electron charge recombination time, work function and reduction potential values. So, by manipulating the Ag-TiO_2 heterojunction (on employing various shapes and sizes of Ag nanoparticles), one can utilize the solar energy to much higher extent and achieve high quantum yield.

In brief, the whole work described in this thesis demonstrated a viable strategy for improving the photocatalytic reaction systems by introducing the separately synthesized coinage metal NPs co-catalysts of various morphologies in the semiconductor (TiO_2) matrix, which is an advancement over the conventional approach. It has been observed that with decreasing the size of the metal NPs, photocatalytic activity show pronounced effect as Fermi level shift towards the more negative potential which assists the rapid transference of electrons from semiconductor to metal NPs. Moreover, the information on the solution interaction behavior of metallic nanostructures is quiet valuable in order to tune the optimum catalytic activity as polar solvents interactions result in the aggregation moieties of various sizes depending on the solvent dipole moment. Variation in the morphology of NPs (such as spheres, rods, polygonal nanospheres, anisotropic shapes, truncated triangles and wires) displayed dissimilar catalytic activities, dictated in terms of their diverse surface structure, exposed surface atoms, surface to volume ratio, interfacial contact area between TiO_2 and metal particle, sharp edges and corners, etc. Cu nanowires were found to be highly efficient catalyst as well as co-catalyst in comparison with rod and sphere morphology for carrying out reduction and oxidation reactions, respectively. A comparative account on the nature of the coinage metal NPs irrespective of its shape reveals that the Ag-TiO_2 nanocomposites exhibit enhanced photoactivity relative to Au and Cu-TiO_2 composites.

Therefore, the interplay between materials properties i.e., by varying the shape, size and nature of metal NPs and their addition to TiO_2 would ultimately lead to the path for attainment of better heterogeneous photocatalysts. However, there are many other issues to look forward for the improvement in the co-catalysis effect such as it is desirable to synthesize such a shape of metal NP co-catalyst whose interaction with semiconductor would act as an efficient electron sink and assist in diminishing the electron-hole pair recombination and hence would result in 100% quantum efficiency. Designing the permanent assembly of metallic particles co-catalysts and TiO_2 is another point to be considered in the future studies. The reusability of the metal NPs in catalytic reactions is the major issue which needs to be resolved. However, efforts have to continue to synthesize novel materials with desirable characteristics which can resolve the as mentioned issues.

List of Publications

1. Rupinder Kaur and Bonamali Pal, Size and shape dependent attachments of Au nanostructures to TiO_2 for optimum reactivity of Au–TiO_2 photocatalysis, *Journal of Molecular Catalysis A: Chemical*, *355 (2012) 39-43* **Appeared as Editor Choice Paper.**

2. Rupinder Kaur and Bonamali Pal, Co-catalysis Effect of Different Morphological Facets of as prepared Ag Nanostructures for the Photocatalytic Oxidation Reaction by Ag-TiO_2 Aqueous Slurry, *Material Chemistry and Physics*, *143 (2013) 393-399.*

3. Rupinder Kaur and Bonamali Pal, Co-catalytic and Electro-kinetic Properties of Au Nanostructures dispersed in solvents of varying dipole moments. *Colloids and Surfaces A: Physicochemical and Engineering Aspects*, 441 (2014) 155–163.

4. Bonamali Pal, Sonia Rana and **Rupinder Kaur,** and Influence of Different Reducing Agents on the Ag Nanostructures and Their Electrokinetic and Catalytic Properties. *Journal of Nanoscience and Nanotechnology*, *(doi:10.1166/jnn.2014.9222).*

5. Rupinder Kaur and Bonamali Pal, Impact of polymorphic facets of Au nanostructures formed by variable energy laser exposure on its optical, electro-kinetic and catalytic properties. (Accepted in Journal of Molecular Catalysis A: Chemical).

6. Bonamali Pal and Rupinder Kaur, Facile synthesis of anisotropic Au nanostructures by laser irradiation and study their optical and electro-kinetic properties. (Accepted in Particulate Science and Technology).

7. Rupinder Kaur and Bonamali Pal, Plasmon, catalytic and electro-kinetic sensitivity during Au nanorods agglomeration in solvents of varying dipole moment and refractive index. **(**Under Review in Material Research Bulletin).

8. Rupinder Kaur and Bonamali Pal, Excellent catalytic activity imparted by various Cu morphologies for reduction reactions. (Submitted in Applied Catalysis A: General).

9. Rupinder Kaur and Bonamali Pal, Comparative co-catalytic account of coinage metal nanoparticles (Au, Ag and Cu) for TiO_2 photocatalysis under visible light irradiation**.** (manuscript under preparation).

Paper/Posters presented in Conferences

1. Rupinder Kaur and Bonamali Pal, "Excellent catalytic activity imparted by various morphologies of Cu-TiO_2 nanocomposites under sun light irradiation" Poster presented in National Conference on Innovative Molecules for Sustainable Future (NCIMSF-2013), Thapar University, Patiala.

2. Rupinder Kaur and Bonamali Pal, Shape and size dependent co-catalytic activity of Au nanostructures imparting to TiO_2 photoactivity. International Conference of Nanoscience and Technology (NanoSciTech-2012), Panjab University, Chandigarh, 15-18th February, 2012 ***(Awarded 2nd prize).***

3. Rupinder Kaur and Bonamali Pal, "Au and Ag nanoparticles mediated visible light photocatalytic activity of TiO_2 nanoparticles" Paper presented in International Conference on Nano Science And Technology (ICONSAT, 2014), INST, Mohali.

4. Bonamali Pal and Rupinder Kaur, "Facile synthesis of anisotropic Au nanostructures by laser irradiation and study their optical and electro-kinetic properties" Paper presented in International Conference on Powder, Granule and Bulk Solids: Innovations and Applications (PGBSIA– 2013), Thapar University, Patiala.

5. Rupinder Kaur and Bonamali Pal, "Influence of Solvent Polarity on the Optical, Electrokinetic and Co-catalytic Properties of Au nanorods" Presentation at Multani Mal Modi College, Patiala (RACES 2013).

6. Rupinder Kaur and Bonamali Pal, "Effect of Different Shapes and Sizes of Ag Nanoparticles as Co-catalysts for the Enhancement of TiO_2 Photoactivity" Punjabi University, Patiala (NFIC 2013).

7. Rupinder Kaur, Bonamali Pal "Shape and Size Dependent Catalytic Activity of Coinage Metal (Au, Ag and Cu) Nanoparticles for Nitro-aromatic reduction" BITS Pilani, Goa (ETNM-2013)

8. Rupinder Kaur and Bonamali Pal, Aggregation Effect of Gold Nanoparticles as Co-catalyst on TiO_2 Photocatalysis, National Symposium on Nanoscience and Nanotechnology (NANOSTECH 2011), Benchmarking- Science and Society.

9. Rupinder Kaur and Bonamali Pal, Effect of Gold (Au) Nanoparticles Addition on the Rate of TiO_2 Photocatalytic Reactions, Conference on Advance in Chemical Engineering (AChemE-2011), February 27-28, 2011, Thapar University, Patiala.

10. Rupinder Kaur, Nidhi Gupta, Rohit Singh, Bonamali Pal "Catalytic Activity of Coinage Metal Nanoparticles as Co- Catalyst for TiO_2 Photocatalysis" in International Conference of Nanotechnology and Its Application in Medical Sciences held at D.Y. Patil University, Kohlapur (Maharashtra) on 21^{st}- 23^{rd} October, 2010.